SIEMENS

MAGNETOM Flash

The Magazine of MRI

Issue Number 5/2014 | RSNA Edition

Not for distribution in the US

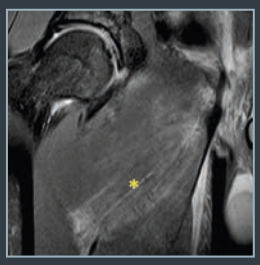

Athletic Pubalgia and Core Injury
Page 24

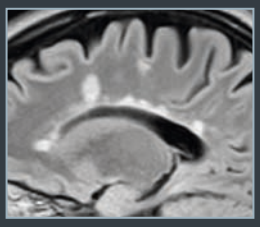

'White Dots' on Cranial MRI: MS and Differential Diagnosis
Page 32

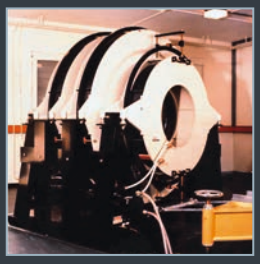

30 Years of Innovation at Siemens
Page 88

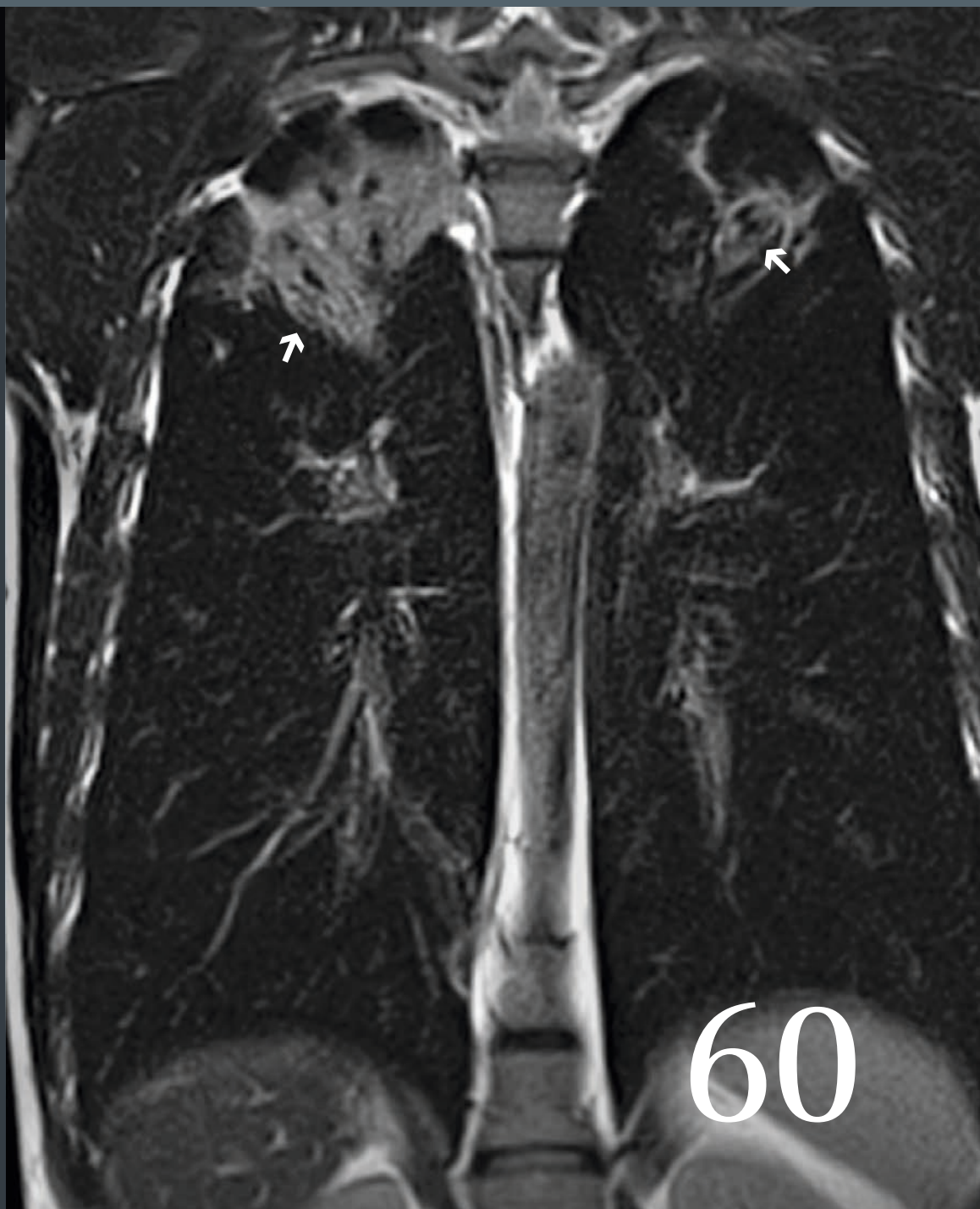

60

Professor Jeong Min Lee is Chief Radiologist of the section of Abdominal Radiology and Nonvascular Intervention at the Department of Radiology, Seoul National University, College of Medicine in Seoul, Korea. His radiology training was undertaken at Cheonbuk National University, College of Medicine. He was visiting Professor at Iowa University Hospitals & Clinics, before he moved to the Seoul National University in 2012.

His work on abdominal imaging and image-guided tumor ablation is of international renown. He is a co-applicant in a number of successful grant proposals in support of this research. He is a key opinion leader in gastrointestinal Radiology and body MR imaging.

Prof. Lee is scientifically very productive with currently 290 full scientific articles, over 500 research abstracts and chapters in numerous textbooks. He has co-edited the book "Radiology Illustrated: Hepatobiliary and Pancreatic Radiology" (Springer, Heidelberg) published in 2013.

Dear MAGNETOM Flash reader,

It is truly an honor and privilege for me to write this editorial for the 2014 RSNA edition of MAGNETOM Flash. The year will culminate with the 100th annual meeting of the RSNA on the theme of "A century of transforming medicine".

Indeed, diagnostic imaging has played an increasingly important role in the detection and diagnosis of diseases, staging of malignancies, and selection of appropriate treatment, transforming the way we approach medicine today. Among the diverse imaging modalities we have at our disposal, MRI has remained a cornerstone of neurologic, musculoskeletal, oncologic, and cardiovascular imaging owing to its inherent high soft tissue contrast. In fact, in recent years, body MR imaging has become one of the largest growth areas in radiology. Yet, compared with MDCT which has been shown to produce consistent image quality within a short examination time, body MR had demonstrated weaknesses in terms of inconsistency and a long examination time, particularly in patients who were obese or had limited breath-holding capacity. With recent technological advances in the MR system allowing enhanced imaged quality with faster acquisition times as well as multiparameteric capability, however, body MRI is now able to be performed in a fast, efficient, and comprehensive way, providing consistently high quality images and demonstrating disease processes effectively. Thus, although body MR is currently most often used for the purposes of "problem solving", there is a growing acceptance of MR as the primary imaging modality for liver, biliary and pancreas diseases. In addition, with the use of rapid imaging techniques and parallel imaging using high channel coils, the scanner time for body MR has been reduced so significantly that routine exam times are completed usually within 30 minutes. Furthermore, the exceptional contrast resolution and ability of MR to provide comprehensive information of abdominal organs and various diseases has allowed more definitive diagnoses, and the lack of radiation has motivated physicians and patients alike to consider MR over CT scans for follow-up exams, particularly in younger patients.

This is the current state and promising future of MR that we radiologists are forging today.

In this issue, detailing their experience on the National Jewish Health using thorax MRI, Chung et al. will show that proton MRI can be a viable means to image the chest including the lungs and pleura. This may be especially pertinent to patients with long life expectancies who may require frequent follow-up imaging of chronic lung diseases and infections [page 8].

Furthermore in this issue, Tobias Block et al. will show that radial scanning techniques, such as the Radial VIBE or StarVIBE sequence can be used to image the abdomen during free breathing, and that GRASP* can provide continuous data acquisition during free-breathing with consistently high quality volumetric T1-weighted image sets in the body [page 18]. Therefore, this approach may make abdominal dynamic contrast-enhanced MRI more accessible to patients who are unable hold their breath or for non-cooperative patients. In addition, owing to the use of the golden-angle scheme, the temporal resolution and desired image time points can be selected retrospectively, enabling reconstructing of both morphologic and perfusion imaging information from the same examination. They will also show that this technique can be utilized as a

robust imaging technique for bowel imaging and for the pediatric** population.

We will also read that the multi-parameteric capability of MRI may be valuable for not only neurologic or oncologic applications but also for musculoskeletal applications. In this issue, Muller-Lutz et al. will demonstrate that gagCEST* imaging can be a promising tool enabling non-invasive measurement of glycosaminoglycans *in vivo* [page 30]. In their study, they found that a decreased gagCEST effect was observed to be correlated with the degeneration of IVDs and disc herniation. Therefore, spine MRI may provide information on not only morphologic changes of intervertebral discs but also the compositional changes of the discs.

Moreover, regarding cardiovascular MR examinations, new approaches will be shown that may improve the efficiency as well as the safety of MRI. In this issue, there are three articles regarding non-enhanced MR angiography in the pediatric** population or in patients with peripheral arterial disease, using either the NATIVE TrueFISP [page 60] or QISS pulse sequence [page 66 and 74]. It was demonstrated that non-enhanced MR angiograph techniques can provide a robust, rapid, and easy-to-use technique for the imaging of renal or peripheral arteries. Given that many patients with peripheral arterial diseases suffer from renal dysfunction and are at risk of contrast-induced nephropathy or nephrogenic systemic fibrosis, these robust MRA techniques could provide additional value in terms of safety in these populations compared to both CT angiography and contrast-enhanced MRA. Furthermore, Pueyo et al. will show that the Cardiac Dot Engine can introduce patient benefit by allowing systematically reproducible and efficient studies which can consistently reduce the examination time [page 80].

Finally, Ingo Zenger and Antje Hellwich will review the success story of MRI at Siemens during the last 30 years, and detail the many innovations from Siemens that have changed the world [page 90].

In order to gain wide acceptance as a first-line diagnostic modality, MRI must be performed in a fast, efficient manner, and provide high quality images consistently while demonstrating disease processes in a comprehensive fashion including both morphological and functional information. I strongly believe that free breathing, radial gradient techniques with compressed sensing can consistently produce high quality post-contrast T1-weighted images, with suppression of motion artifacts, providing key morphologic information for the diagnosis of various disease entities. In addition, perfusion images which can be obtained additionally from the same dataset through GRASP reconstruction with variable temporal resolution may also show specific physiologic processes in normal and pathologic lesions in a quantitative way. Indeed, the future is bright.

I would like to thank the world-class, talented contributors to this issue for their outstanding and timely contributions and I am very confident that the readers will find this issue to be informative and relevant to daily clinical practice as I did.

Jeong Min Lee

* WIP, the product is currently under development and is not for sale in the US and in other countries. Its future availability cannot be ensured.

** MR scanning has not been established as safe for imaging fetuses and infants under two years of age. The responsible physician must evaluate the benefit of the MRI examination in comparison to other imaging procedures.

Editorial Board

Antje Hellwich
Editor-in-chief

Wellesley Were
MR Business Development Manager Australia and New Zealand

Ralph Strecker
MR Collaborations Manager, São Paulo, Brazil

Sven Zühlsdorff, Ph.D.
Clinical Collaboration Manager, Chicago, IL, USA

Gary R. McNeal, MS (BME)
Advanced Application Specialist, Cardiovascular MR Imaging Hoffman Estates, IL, USA

Peter Kreisler, Ph.D.
Collaborations & Applications, Erlangen, Germany

Review Board

Lisa Chuah, Ph.D.
Global Segment Manager Neurology, Neurosurgery, Pediatrics, and Orthopedics

Lars Drüppel, Ph.D.
Global Segment Manager Cardiovascular MR

Wilhelm Horger
Application Development Oncology

Michelle Kessler
US Installed Base Manager

Berthold Kiefer, Ph.D.
Head of Oncological and Interventional Applications

Sunil Kumar S.L., Ph.D.
Senior Manager Applications

Reto Merges
Head of Outbound Marketing MR Applications

Edgar **Müller**
Head of Cardiovascular Applications

Heiko Meyer, Ph.D.
Head of Neuro Applications

Heike Weh
Clinical Data Manager

Content

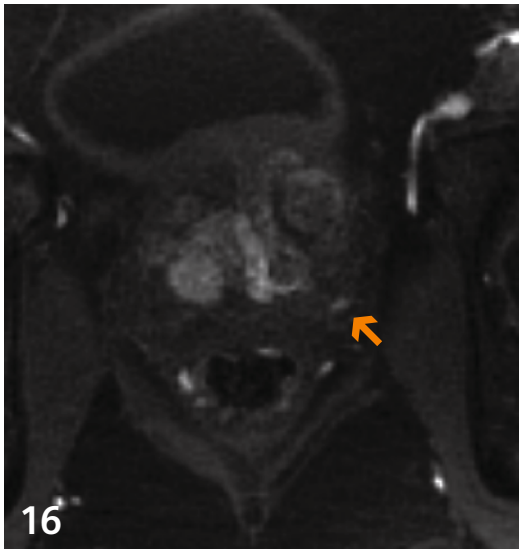

GRASP[1]: Tackling the Challenges of Abdominopelvic DCE-MRI

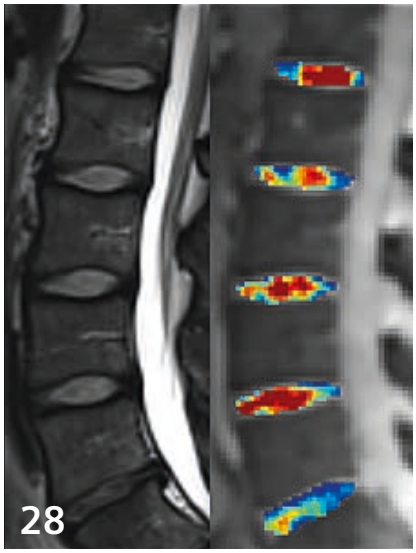

MR gagCEST[1] Imaging of the Lumbar Intervertebral Disc

Learn from the experience of other MAGNETOM users

The MAGNETOM World is the community of Siemens MR users worldwide, providing you with relevant clinical information. Here you will find application tips and protocols to optimize your daily work. Lectures and presentations from experts in the field will allow you to be exposed to new ideas and alternative clinical approaches.

Put the advantages of the MAGNETOM World to work for you!

www.siemens.com/magnetom-world

Body Imaging

6 Nonvascular Proton MRI of the Thorax: Pulmonary Utility and Beyond
Jonathan H. Chung, et al.

16 GRASP[1]: Tackling the Challenges of Abdominopelvic DCE-MRI
Kai Tobias Block, et al.

Orthopedic Imaging

24 Case Report: Athletic Pubalgia and Core Injury. Tear/Detachment of the Right Common Adductor Longus-Rectus Abdominis Aponeurosis
Coley C. Gatlin, Charles P. Ho

28 Magnetic Resonance gagCEST[1] Imaging of the Human Lumbar Intervertebral Disc
Anja Müller-Lutz, et al.

How to Reduce Sedation in Pediatric[2] MRI

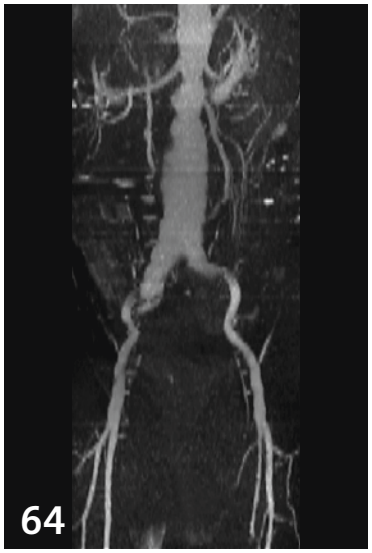

QISS[3] Non-Contrast MRA

Significant Time Reduction Using the Cardiac Dot Engine

Neurology

32 Pictorial Essay 'White Dots' on Cranial MRI: MS and Differential Diagnosis
Iris N. Kaschka, et al.

46 **How I do it:** Slice Order (Slice Timing) for fMRI Evaluation
Joachim Graessner

49 Case Report: Evaluation of Neurofibromas on ^{18}F-FDG PET/MRI in a Patient with Neurofibromatosis Type 1
Roy A. Raad, et al.

Pediatric Imaging

56 Why We Should Reduce Sedation in Pediatric[2] MRI and What We Need to Do It
Robert J. Min

58 **How I do it:** Renal Non-Enhanced MR Angiography (*syngo* NATIVE TrueFISP) in Pediatric[2] Patients
Jie Deng, et al.

Cardiovascular Imaging

64 Quiescent-Intervall Single-Shot[3] Magnetic Resonance Angiography
Robert R. Edelman, et al.

72 QISS[3] Non-Contrast MR Angiography: A Study of Three Cases with Peripheral Vascular Disease
Maria L. Carr, et al.

78 Cardiac Dot Engine: Significant Time Reduction at Cardiac Magnetic Resonance Imaging
Jesús Ciro Pueyo, et al.

How-I-do-it

82 How Modules of Imaging Sequences Fit Together: An Overview of Recent Advances in MR Imaging
Helmut Rumpel, et al.

30 Years of Innovation

88 Magnetic Resonance Imaging at Siemens: A Success Story
Ingo Zenger, Antje Hellwich

The information presented in MAGNETOM Flash is for illustration only and is not intended to be relied upon by the reader for instruction as to the practice of medicine.
Any health care practitioner reading this information is reminded that they must use their own learning, training and expertise in dealing with their individual patients. This material does not substitute for that duty and is not intended by Siemens Medical Solutions to be used for any purpose in that regard. The treating physician bears the sole responsibility for the diagnosis and treatment of patients, including drugs and doses prescribed in connection with such use. The Operating Instructions must always be strictly followed when operating the MR System. The source for the technical data is the corresponding data sheets.

[1]WIP, the product is currently under development and is not for sale in the US and in other countries. Its future availability cannot be ensured.

[2]MR scanning has not been established as safe for imaging fetuses and infants under two years of age. The responsible physician must evaluate the benefit of the MRI examination in comparison to other imaging procedures.

[3]QISS is pending 510(k) clearance and is not commercially available in the US.

Nonvascular Proton MRI of the Thorax: Pulmonary Utility and Beyond

Jonathan H. Chung, M.D.[1]; Jürgen Biederer, M.D.[2]; Michael Puderbach, M.D.[3]; Bradley D. Bolster, Jr., Ph.D.[4]; David A. Lynch, M.D.[1]

[1] Department of Radiology, National Jewish Health, Denver, CO, USA
[2] Radiologie Darmstadt, Gross-Gerau County Hospital, Gross-Gerau, Germany
[3] Deptartment of Diagnostic and Interventional Radiology, Hufeland Klinikum GmbH, Bad Langensalza, Germany
[4] Siemens Medical Solutions, Malvern, PA, USA

Introduction

Many still perceive thoracic MRI as an exotic tool. Radiography and CT are the accepted modalities to image lung disease. However, regular use of ionizing radiation must be minimized given the risk of radiation-induced malignancy. Patients with chronic pulmonary disease can be exposed to radiation doses exceeding 100 mSv if regularly imaged with chest CT. Though the risk of most radiation-induced malignancies is substantially decreased in older individuals, this decrease does not occur in the setting of lung cancer, as the risk of lung cancer induction from radiation exposure appears to increase with age up to at least middle age [1].

The potential of MRI for scientific and clinical applications within the thorax, even beyond being a radiation-free alternative to radiography and CT, is widely underestimated. Thoracic MRI has much untapped promise in the detection and diagnosis of both focal and diffuse thoracic conditions. In the recent past, pulmonary conditions were difficult to assess using proton MRI due to low pulmonary proton density and a large degree of susceptibility artifact. Improvements in MRI technology have obviated many of these obstacles; liberal use of parallel imaging, increased gradient strength, 3D imaging, and volume interpolation now allow for reliable and high-quality imaging of the lung parenchyma using proton MRI. Chest MRI is readily available for the initial evaluation of those most at risk for the stochastic effects of radiation (children, young adults, and pregnant women) and those in whom frequent follow-up examinations are anticipated (chronic lung diseases and infections).

MRI approach

The keys to wide-spread clinical use of any tool are practicality, speed, and robustness. Our general chest MRI protocol is listed in Table 1 and shown in Figure 1. Given the inherent high soft tissue contrast of MRI, intravenous Gadolinium contrast is only optional, though administration of contrast does aid assessment of pulmonary perfusion and focal lesion enhancement while improving the overall contrast in the chest. Available MRI sequence techniques include multiple MRI weightings (T1, T2, T2/T1 ratio) in the axial and coronal planes. Though most MRI acquisitions for thoracic assessment are of good quality, some series may not be of diagnostic quality in highly dyspneic or claustrophobic patients. Our protocol ensures that adequate imaging of the thorax will occur in at least one series, even in these challenging patients. Total scan time in most cases is less than 20 minutes; a focused examination may take as little as 5 minutes once the patient has been positioned in the MRI scanner.

The VIBE sequence is a rapid T1-weighted sequence which can be acquired in one breathhold. In the setting of lung pathology, VIBE is most useful for identification of conditions which increase proton density: Pulmonary nodules, masses, and consolidation. After contrast administration, this sequence also has excellent angiographic capacities. Well in line with the concept of a simple, fast, and robust protocol design, two fast breathhold-acquisitions in coronal and transverse orientation within the first 5 minutes after administration of the contrast material produce a high quality pulmonary angiogram. Besides excellent imaging of lung vascularity, post-contrast VIBE is useful for lung cancer staging and assessment of pleural disease.

Development of the VIBE sequence continues. The latest achievement is CAIPIRINHA (Controlled Aliasing in Parallel Imaging Results in Higher Acceleration) VIBE. CAIPIRINHA VIBE decreases acquisition time leading to decrease in

Table 1: Standard proton MRI chest protocol [2]

Sequence	Plane	Key Pathology and Uses	Spatial Resolution	Temporal Resolution
HASTE	Coronal	Consolidation, masses	Low	High
TrueFISP	Coronal	Pulmonary embolism, respiratory mechanics, gross pulmonary evaluation	Moderate	High
BLADE	Axial	Nodules and masses, bronchial mucous plugging, localized edema	Moderate	Moderate
VIBE	Axial +/- Coronal	Nodules, masses, and consolidation; +/- contrast; pulmonary embolism (+contrast)	High	Low
HASTE	Coronal	Consolidation, masses	Low	High

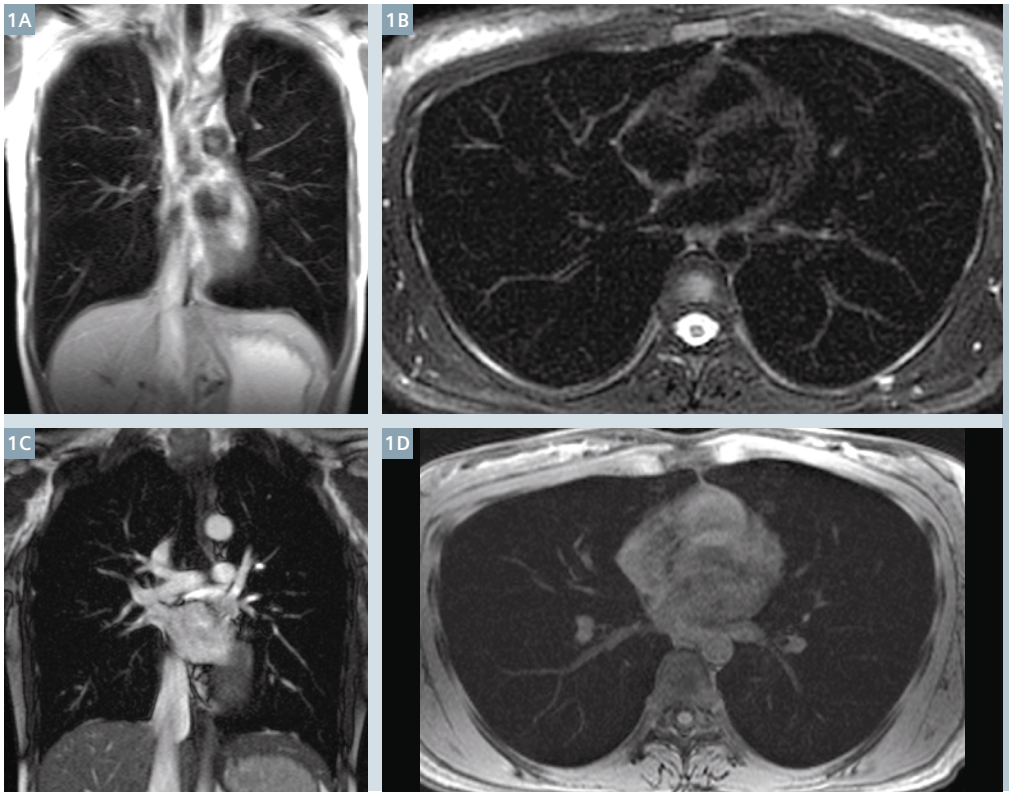

1 Non-contrast pulmonary MRI study in a normal volunteer shows the typical appearance of normal lung parenchyma on HASTE **(1A)**, BLADE **(1B)**, TrueFISP **(1C)**, and VIBE **(1D)** sequences.

breathhold time and increases signal in the mediastinum and central lung compared to standard VIBE. CAIPIRINHA VIBE is especially helpful in highly dyspneic patients in whom a long breathhold is not feasible.

The HASTE sequence is also helpful in detecting pulmonary conditions which increase proton density, and may also nicely show air-trapping due to small airway disease. TrueFISP is a 'white blood' cine sequence with high temporal resolution. In our protocol, the TrueFISP sequence is performed during free-breathing, which allows for assessment of respiratory mechanics; moreover, it is a useful sequence for gross pulmonary assessment in those who cannot hold their breath and as a gross screen for pulmonary arterial filling defects in cases of pulmonary embolism.

BLADE is a T2-weighted turbo spin echo sequence that collects data in radial 'blades' greatly decreasing sensitivity to motion. This sequence is helpful to detect fluid, edema, and/or inflammation (including bronchial inflammation, mucous plugging, and effusions) in addition to other proton-rich conditions of the thorax. As a variation to the protocol, navigator-triggered versions of this sequence are available for imaging of completely uncooperative subjects such a small children.

Proton MRI in chronic lung disease and chronic infection

Cystic fibrosis

Cystic fibrosis (CF) is a common autosomal recessive systemic condition which causes bronchiectasis and predisposes patients to recurrent pneumonia. Life expectancy in CF patients continues to increase with more aggressive therapy and now extends past middle age. Given their increased life expectancy, ionizing radiation should be minimized in CF patients. Proton MRI is a viable alternative to CT in these patients [3-5]. Bronchiectasis, mucous plugging, consolidation, cavities, and localized lung scarring are all evident using standard MRI sequences (Figs. 2, 3). Air-trapping is often evident on HASTE imaging given the relatively large contrast in proton density between normal lung and air-trapped lung in CF patients (Fig. 4).

Sarcoidosis

Sarcoidosis is a systemic illness which causes collections of noncaseating granulomas. The chest is affected in most cases. Pulmonary sarcoidosis manifests as perilymphatic diffuse nodular disease, often with symmetric mediastinal lymphadenopathy. In chronic cases, pulmonary involvement may evolve into frank fibrosis. Proton MRI may be a viable alternative to CT in the imaging of sarcoidosis (Figs. 5-7). Our data showed a strong correlation between MRI and CT, with a Spearman correlation coefficient of 0.774 ($p < 0.0001$) and a Cohen's weighted kappa score of 0.646 [6]. Correlation and agreement were highest for gross parenchymal opacification (consolidation and atelectasis) and lowest for nodular lung disease, though in our experience, significant nodular disease is readily detected using proton MRI, especially if IV contrast is used

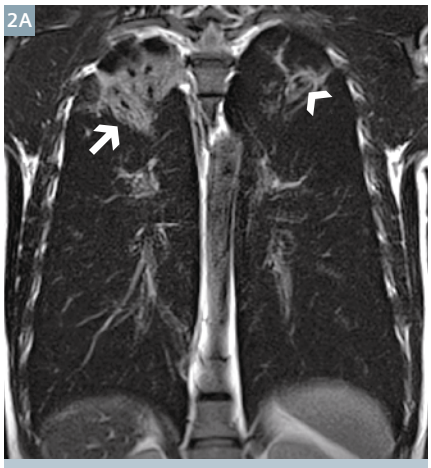

2 Coronal BLADE image in a patient with cystic fibrosis shows intermediate-density consolidation and volume loss in the right upper lobe (arrow). A small cavitary nodule is present in the left upper lobe (arrowhead).

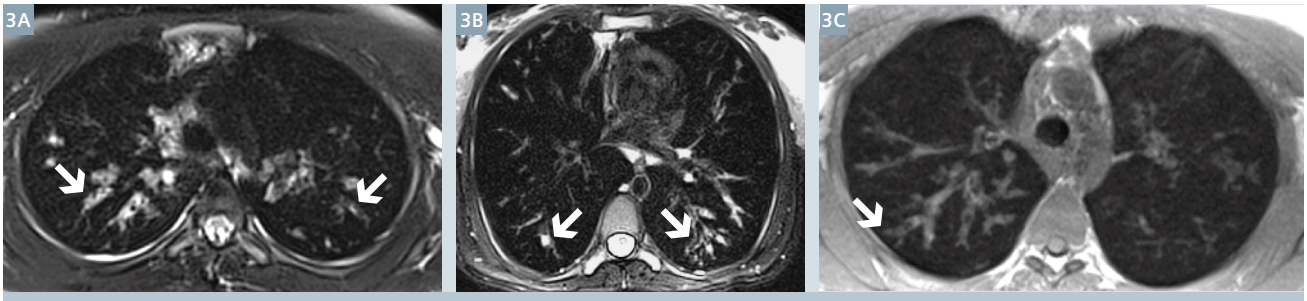

3 Axial BLADE images **(3A, B)** in a patient with cystic fibrosis show bilateral areas of bronchiectasis and mucus plugging (arrows). The T2-weighting of the BLADE sequence allows for accurate identification of inflammatory conditions within the lung parenchyma and airways. Axial VIBE image **(3C)** shows mucous plugging in areas of bronchiectasis out to the subpleural lung in the right upper lobe (arrow). The superior spatial resolution of the VIBE sequence compared to other MRI sequences is helpful in assessing smaller pulmonary structures.

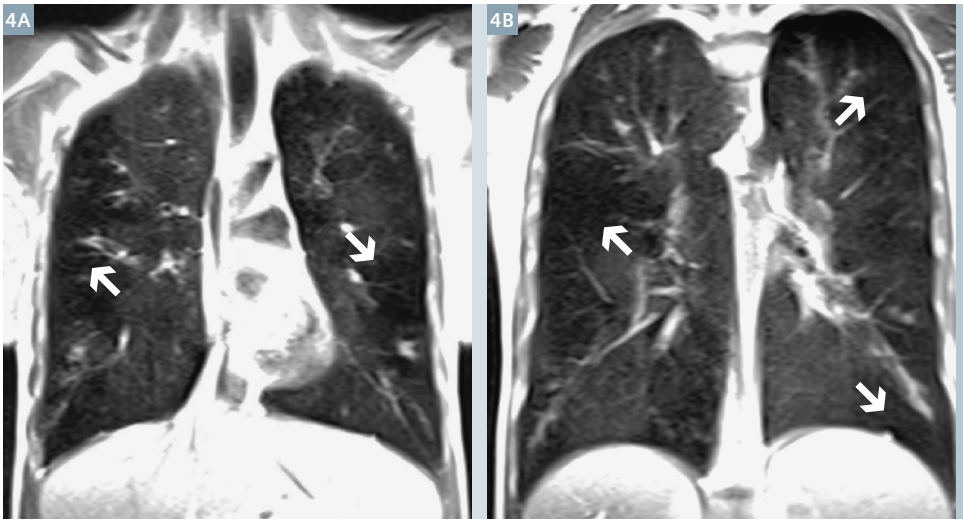

4 Coronal HASTE images **(4A, B)** in a patient with cystic fibrosis shows peripheral areas of relative hypointensity (arrows), consistent with air-trapping.

(Fig. 6). A potentially unique sign of sarcoidosis on proton MRI is the dark lymph node sign which is most evident on post-gadolinium VIBE and T2-BLADE images. This sign was present in approximately half of sarcoidosis cases in our series [7] (Fig. 7).

Nontububerculous mycobacterial pneumonia

Nontububerculous mycobacteria (NTM) are ubiquitously present in the environment including soil, water, and air. In contrast to Mycobacterium tuberculosis, NTM pneumonia is typically not transmissible from person-to-person. NTM presents with bronchiectasis, bronchial thickening, tree-in-bud nodules, cavities, consolidation, and ground-glass opacity on imaging; mirroring those of CF (Figs. 8-10). Patients with NTM pneumonia usually have long life expectancy though progressive disease may lead to significant pulmonary scarring or complete lung destruction. NTM pneumonia patients are imaged semi-annually at our clinical center. Given the high frequency of imaging, proton MRI is an especially attractive alternative to CT in these patients. Our initial data suggests that the correlation between CT and MRI for patients with Mycobacterium Avium Complex pneumonia (the most common type of NTM pneumonia) is strong (0.8252, p-value <0.001) even in the setting of nodular lung disease (Spearman 0.8122, p-value <0.001). Proton MRI's high performance in the setting of nodular disease was surprising as nodules in the setting of NTM pneumonia are quite small, on the scale of 2-4 mm (ATS 2014). We postulate that since nodules in this condition tend to cluster together in a tree-in-bud pattern or in adjacent centrilobular rosettes, the additive signal of adjacent nodules may aid in increasing conspicuity of the nodular disease on proton MRI. The same phenomenon of clustered nodular disease can be seen in many other conditions such as tuberculosis and fungal infection, implying that proton MRI may play a role in these diseases as well.

Miscellaneous

Hypersensitivity pneumonitis

Hypersensitivity pneumonitis is inflammatory disease caused by inhalation of organic or inorganic particles. Common antigenic agents include animal proteins, microbial agents, and low molecular weight chemicals. Imaging findings on chest CT include ground-glass nodules, classically, centrilobular in distribution [8-11]. Concomitant air trapping and mosaic attenuation is quite common occurring in up to 95% of cases. Given the relatively subtle imaging findings of hypersensitivity pneumonitis, one would not expect proton MRI to resolve the pulmonary mani-

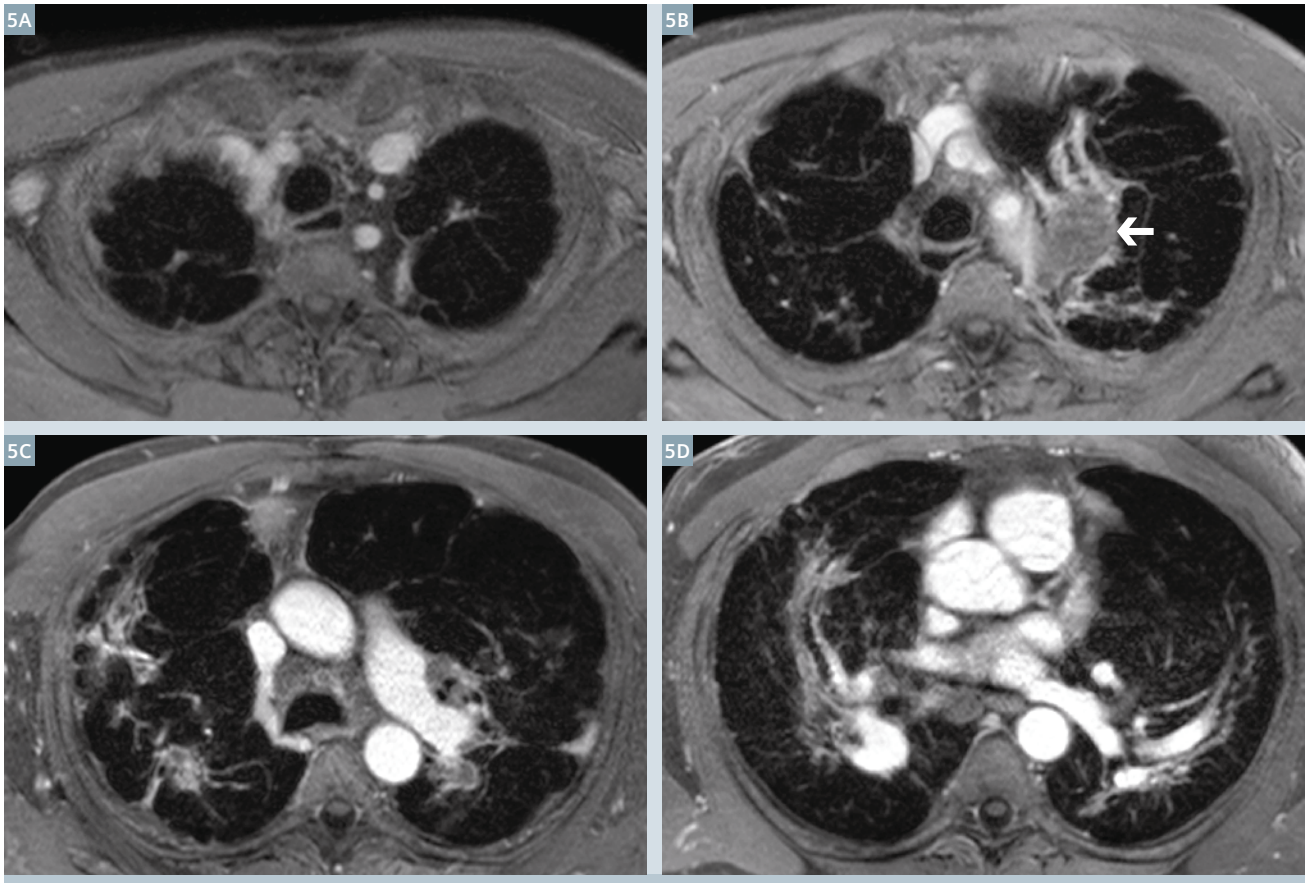

5 Axial post-gadolinium VIBE images **(5A-D)** in a patient with sarcoidosis show mid and upper lung fibrosis and subtle mid lung nodularity with an area of low-intensity, mass-like fibrosis (arrow) in the left upper lobe **(5B)**. Fibrosis is peribronchovascular in axial distribution, typical of chronic sarcoidosis. Low intensity within mediastinal lymphadenopathy likely represents fibrosis or calcification.

festations of this condition. However, with recent advances in MRI technology, even these subtle findings can be detected as shown in Figure 11.

Malignant disease

With the advent of hybrid PET/MRI, there has been renewed interest in whole-body MRI's role in metastatic disease work-up and characterization of specific lesions as benign or malignant. There is strong evidence that proton MRI has potential in differentiating benign from malignant disease in the lungs [12-15]. Given the superior soft tissue contrast of MRI as compared with CT, differentiation between tumor and lung atelectasis is better performed with MRI in cases of central lung masses and invasion of adjacent non-pulmonary structures is readily identified (Fig. 12) [14]. Furthermore, diffusion-weighted imaging (DWI) can help differentiate malignant from benign lung lesions, indicate the type of histology of primary lung cancer, and may increase sensitivity for small pulmonary lesions, for example, in the setting of metastatic disease [14, 16, 17] (Fig. 13). In screening for pulmonary malignancy, CT has superior spatial resolution compared to proton MRI. The lower limit of detectability for pulmonary nodules on proton MRI has been reported to be approximately 5 mm [18-20]. However, with current MRI technology, it may be as low as 4 mm based on our clinical experience; importantly, 6 mm is the threshold of actionable indeterminate pulmonary nodules in lung cancer screening as recommended by Lung-RADS (http://www.acr.org/Quality-Safety/Resources/LungRADS). Given the low signal background of MRI and DWI images, pulmonary nodules which are subtle on CT may be obvious on MRI (Fig. 13).

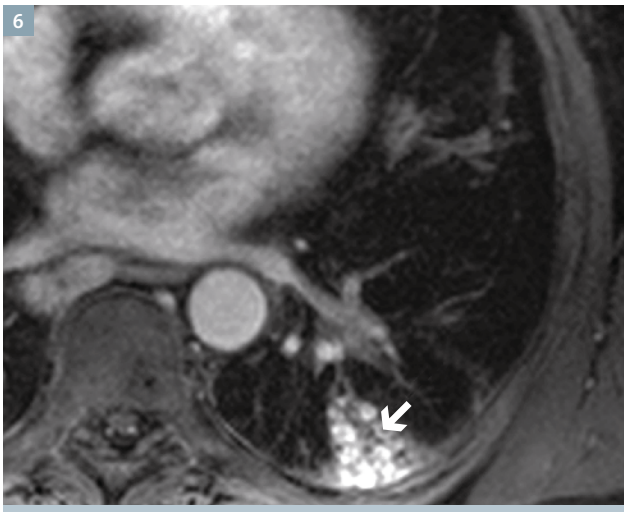

6 Axial post-gadolinium VIBE image clearly shows left lower lobe nodularity (arrow) in this patient with pulmonary sarcoidosis.

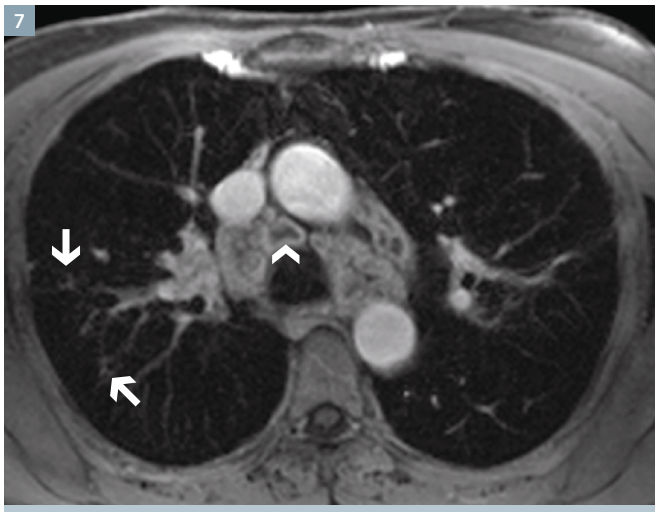

7 Post-gadolinium axial VIBE image shows mediastinal and right peribronchial lymphadenopathy as well as subtle right upper lobe bronchvascular nodularity (arrows) consistent with sarcoidosis. The non-homogeneous nodal enhancement pattern with central hypointensity and peripheral enhancement is known as the dark lymph node sign (arrowhead), which is quite common in lymphadenopathy from sarcoidosis and may potentially be a specific sign for sarcoidosis-related mediastinal lymphadenopathy.

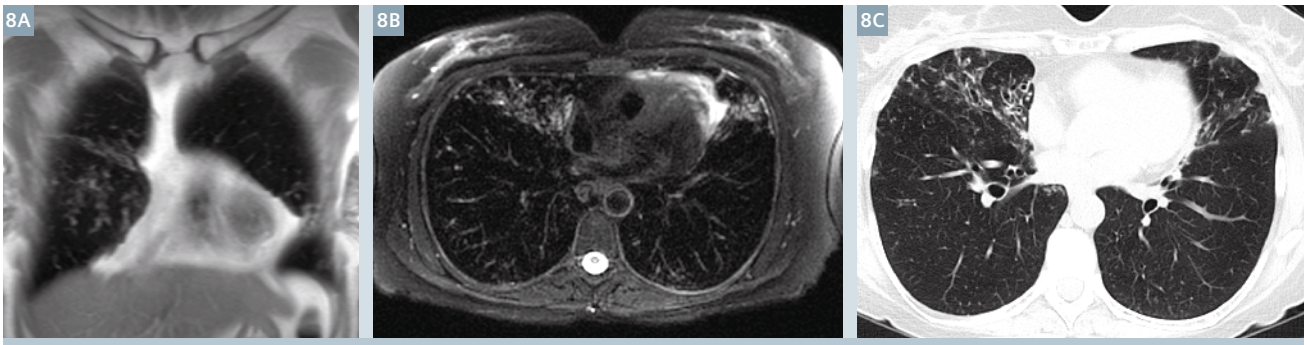

8 Coronal HASTE **(8A)** and axial BLADE **(8B)** MRI images show bronchiectasis in the paracardiac portions of the lungs in this patient with MAC pneumonia. Axial image from chest CT **(8C)** demonstrates bronchiectasis in the same distribution as on MRI.

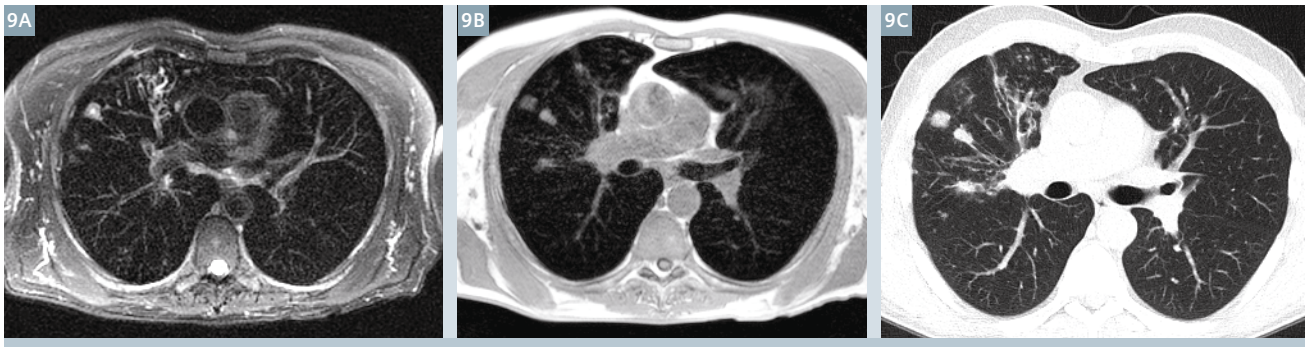

9 Axial BLADE **(9A)** and VIBE **(9B)** MRI images show nodular opacities and bronchiectasis in the right upper lobe in this patient with MAC pneumonia. Axial image from chest CT **(9C)** demonstrates similar imaging manifestations as shown on the MRI images.

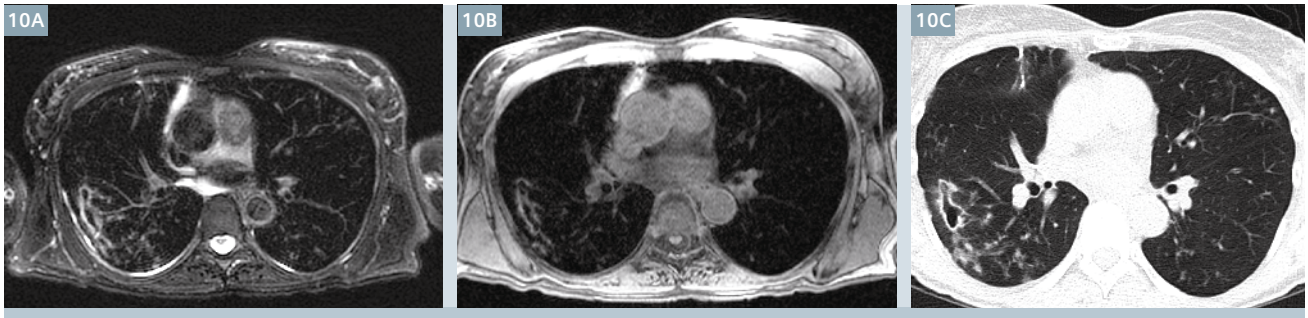

10 Axial BLADE **(10A)** and VIBE **(10B)** MRI images show a focal cavity in the superior segment of the right lower lobe in this patient with MAC pneumonia. Axial image from chest CT **(10C)** again redemonstrates the right lower lobe cavity.

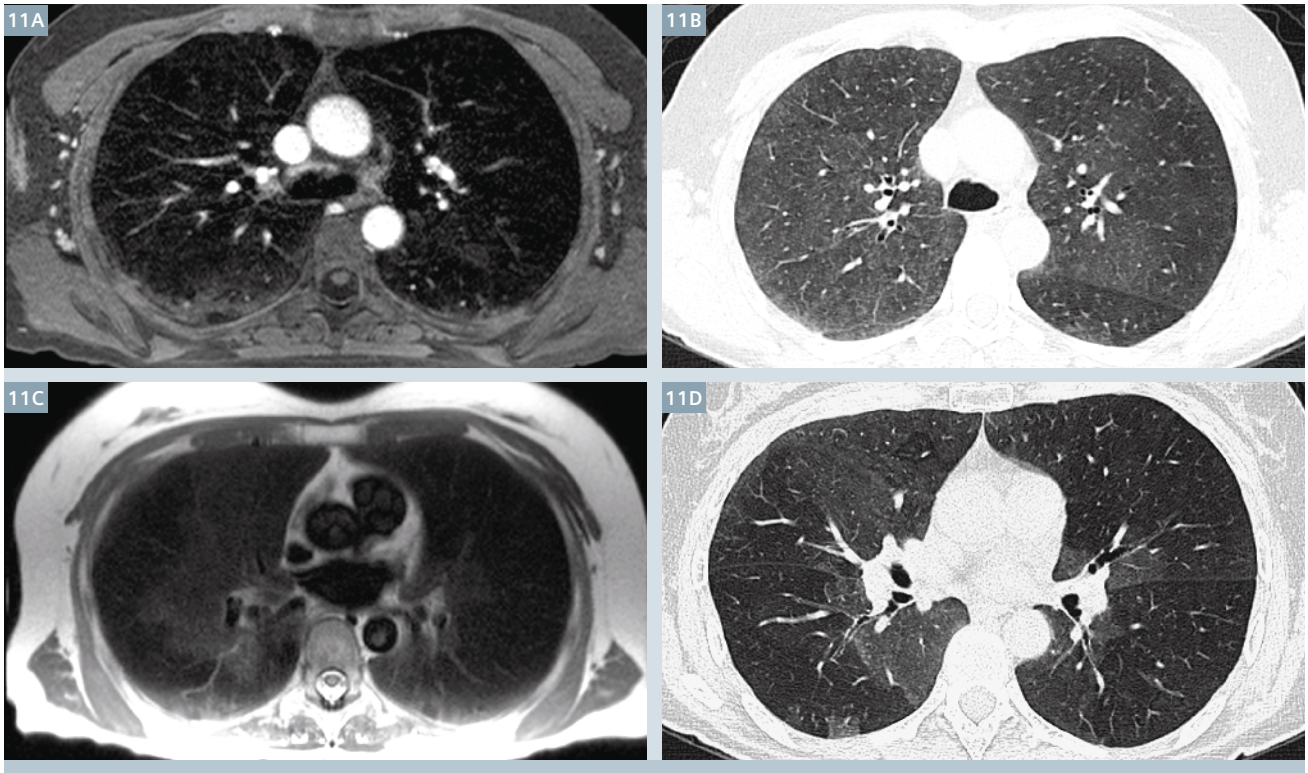

11 Axial post-gadolinium VIBE **(11A)** image shows subtle areas of asymmetric right-sided centrilobular nodularity corroborated on CT **(11B)**. Axial HASTE image **(11C)** from the same patient shows a mosaic pattern with areas of different intensity primarily in the right lung, in a similar distribution as on expiratory CT, consistent with air-trapping **(11D)** in this patient with hypersensitivity pneumonitis.

Pleural disease

Pleural scarring or thickening is most often due to evolution of previous empyema or hemothorax and is usually associated with parenchymal bands or focal rounded atelectasis. Pleural disease is also quite common in the setting of asbestos exposure along with more focal pleural plaques. As a tertiary and quaternary center for chronic lung diseases, our clinical center cares for a large population of patients with collagen vascular disease. Many patients with collagen vascular disease, specifically rheumatoid arthritis, develop pleuritis with resultant pleural scarring. Pleural scarring or thickening may result in restrictive respiratory physiology. Given the long life expectancy of patients with collagen vascular disease related pleural disease, longitudinal follow-up of these patients with CT is suboptimal given the cumulative radiation dose. MRI is a viable tool to follow patients with chronic pleural disease (Fig. 14).

Practical advantages and disadvantages compared to chest CT

The obvious strength of MRI compared to CT is the absence of ionizing radiation. Under the ALARA principle, physicians should do their best to reduce radiation dose to patients while still providing high quality care to patients. Therefore, if MRI can provide similar performance compared to CT in a specific disease setting, physicians should use proton MRI in place of CT. For example, in patients who are at risk for lung cancer, pneumonia should be followed to resolution given that adenocarcinoma may mimic bacterial pneumonia on imaging; MRI could be used to follow these patient rather than CT (Fig. 15). In young patients or in those with contraindication to iodinated contrast, MRA is an excellent means to detect pulmonary arterial thromboembolic disease [21]. As aforementioned, post-contrast VIBE produces excellent images with clear detection of pulmonary emboli (Fig. 16). TrueFISP has inherent white-

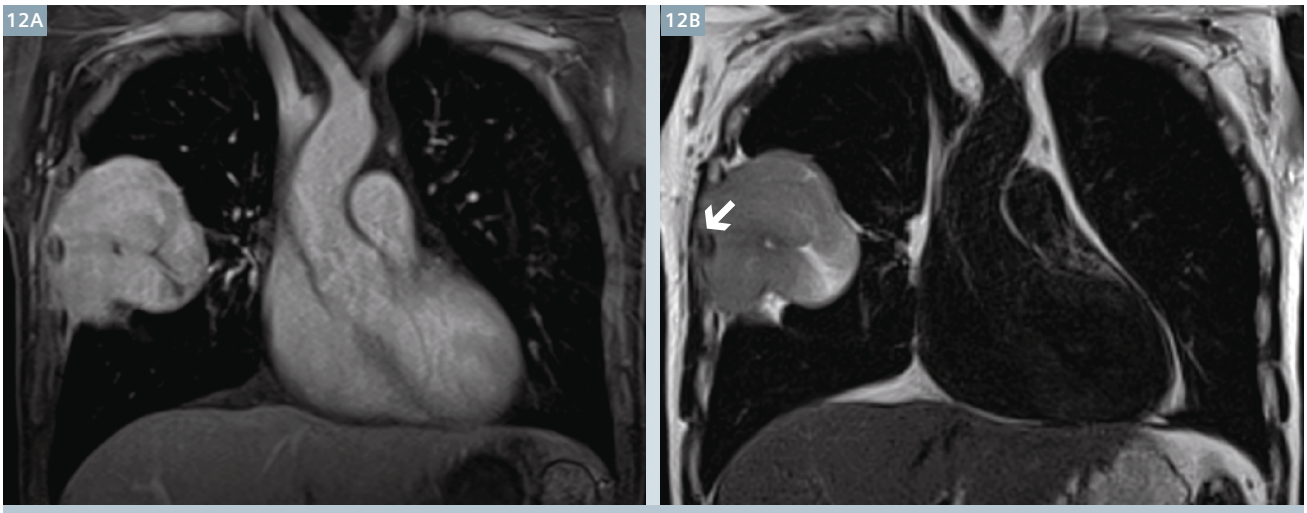

12 Post-gadolinium coronal VIBE **(12A)** and coronal BLADE **(12B)** images show a large mass in the lateral aspect of the right lung invading the adjacent chest wall in this patient with non-Hodkin lymphoma. The encased right lateral rib (arrow) shows abnormal low signal relative to other ribs diagnostic of bone invasion. *(Images courtesy of University Hospital Kiel, Germany.)*

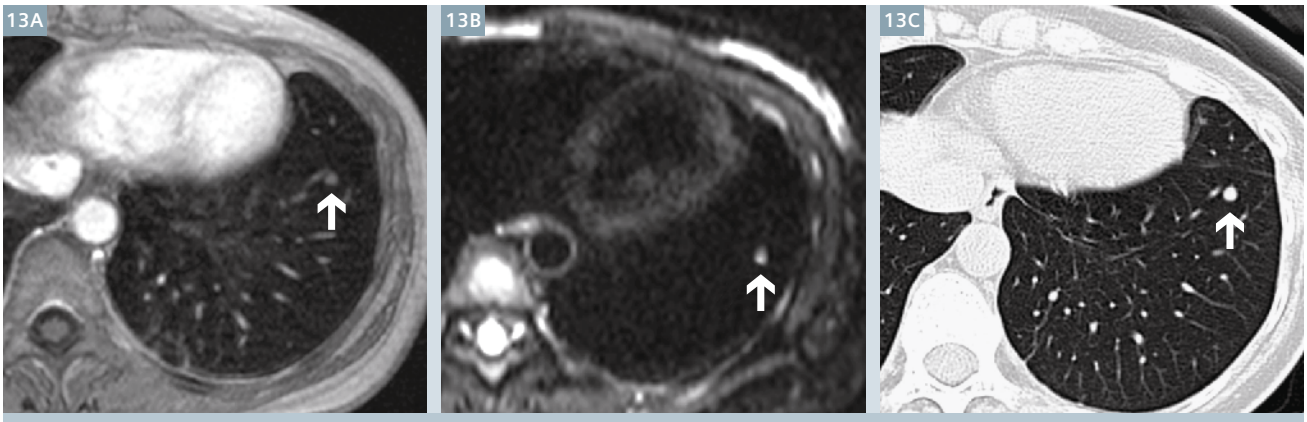

13 Post-gadolinium VIBE axial image **(13A)** shows a 4 mm left lower lobe nodule (arrow) in this patient with metastatic sarcoma. Navigator axial DWI image **(13B)** shows restricted diffusion in this nodule (arrow). The absence of substantial background signal on this sequence increases conspicuity of this lesion; the same lesion (arrow) was not prospectively identified on the axial CT image **(13C)** interpreted at an outside institution.

blood characteristics and can be used to evaluate for central pulmonary embolism in the setting of contrast allergy or renal failure.

However, the benefits of MRI extend beyond radiation reduction. MRI offers superior soft tissue contrast resolution as compared to CT. This stems from the fact that CT imaging is dependent on electron density primarily, whereas MRI imaging derives from proton density and the complex relationship of these protons in different tissues and in magnetic fields. T2-weighted imaging allows MRI to detect areas of localize edema, fluid, or inflammation which are often subtle or invisible on CT. In the setting of anterior mediastinal lesions, microscopic fat within focal tumor-like regions can confirm benign disease using in and out of phase imaging (Fig. 17). Also, MRI offers functional information such as real-time diaphragmatic functional analysis, temporal perfusion, and segmental ventilation, which would be untenable using CT given the resultant high patient radiation exposure.

Currently, MRI cannot match the spatial resolution of CT, though as previously stated, proton MRI can reliably detect nodules on the range of 4-5 mm. Nodules smaller than this are usually not actionable, given the high likelihood of benign disease in nodules smaller than 4 mm. Also, whether MRI can be a useful tool in interstitial lung disease (ILD) has yet to be determined, though isolated use of proton MRI in this setting is likely not currently feasible given the subtle manifestation of early ILD.

One of the biggest hurdles in widespread adoption of thoracic proton MRI is likely financial. Currently, most insurance companies do not explicitly cover proton MRI for general pulmonary assessment. Coverage for lung cancer staging, mediastinal mass, and pleural/chest wall assessment appears to be standard, however. Some would also argue that MRI is more expensive than CT, and therefore, even if MRI performs comparably to CT in pulmonary assessment, CT should be favored. Given that

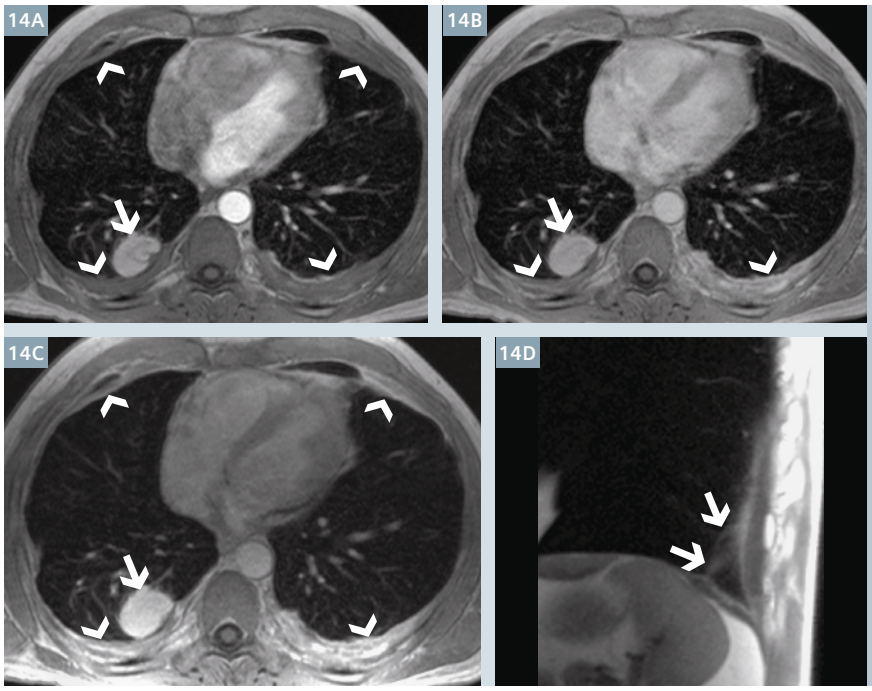

14 Post-gadolinium VIBE axial image at approximately 2, 5, and 7 minutes after contrast administration **(14A-C**, respectively) show progressive enhancement of bilateral pleural thickening (arrowheads) and a focus of rounded atelectasis (arrows) in the right lower lobe in this patient with rheumatoid arthritis. The area of rounded atelectasis can be definitely diagnosed on MRI given the underlying pleural thickening, localized and lobar volume loss, the subpleural location of the mass, and the swirling of the vasculature around this mass; swirling of lung parenchyma within this mass is clearly present on the 2-minute image **(14A)**. Sagittal HASTE image **(14D)** shows low-intensity left-sided pleural thickening with wispy parenchymal bands (arrows) extending centrally from the subpleural lung.

15 Axial T2 BLADE **(15A)**, axial non-contrast VIBE **(15B)**, axial CT **(15C)** images demonstrate left lower lobe consolidation consistent with pneumonia in this patient with fever and chills. Consolidation resolved with antibiotic treatment. For high-risk patients in whom consolidation must be followed to resolution, MRI is an ideal modality given its superior contrast resolution relative to radiography and its radiation-free technique.

most general pulmonary MRI studies can be performed in less than 15-20 minutes, one could make the argument that the cost of MRI should in fact be similar to that of CT in the thorax. In the long run, the strengths and relatively minor weaknesses of thoracic proton MRI suggest that increased coverage, support, and utilization of proton MRI in the thorax is inevitable.

Conclusion

Though CT is the current gold standard modality to image the chest; Proton MRI is a viable means to image the chest including the lungs and pleura. This is especially poignant in patients with long life expectancy who may require chronic follow-up imaging of the chest. As MRI technology progresses, more widespread utilization of proton MRI is expected.

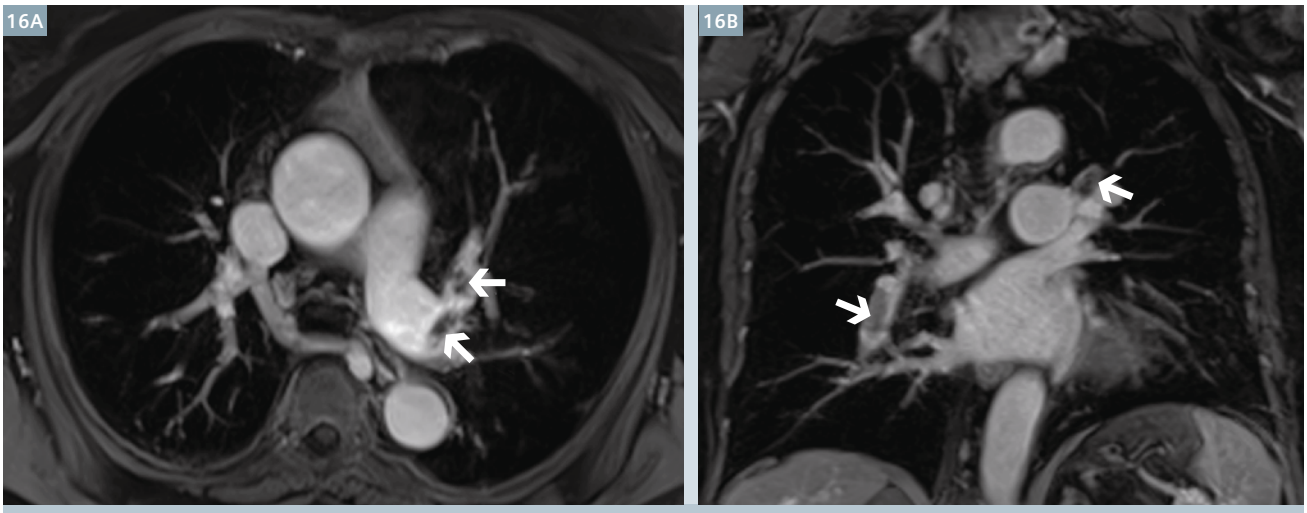

16 Post-gadolinium maximum intensity projection (MIP) VIBE axial **(16A)** and coronal **(16B)** images show filling defects within the pulmonary arteries consistent with pulmonary embolism. CT iodinated contrast was contraindicated as the patient was a candidate for radioiodine therapy for severe hyperthyroidism. In young patents, angiographic imaging using MRI is also valuable in that it allows for detection of pulmonary embolism without use of ionizing radiation.
(Images courtesy of Radiologie Darmstadt, Germany.)

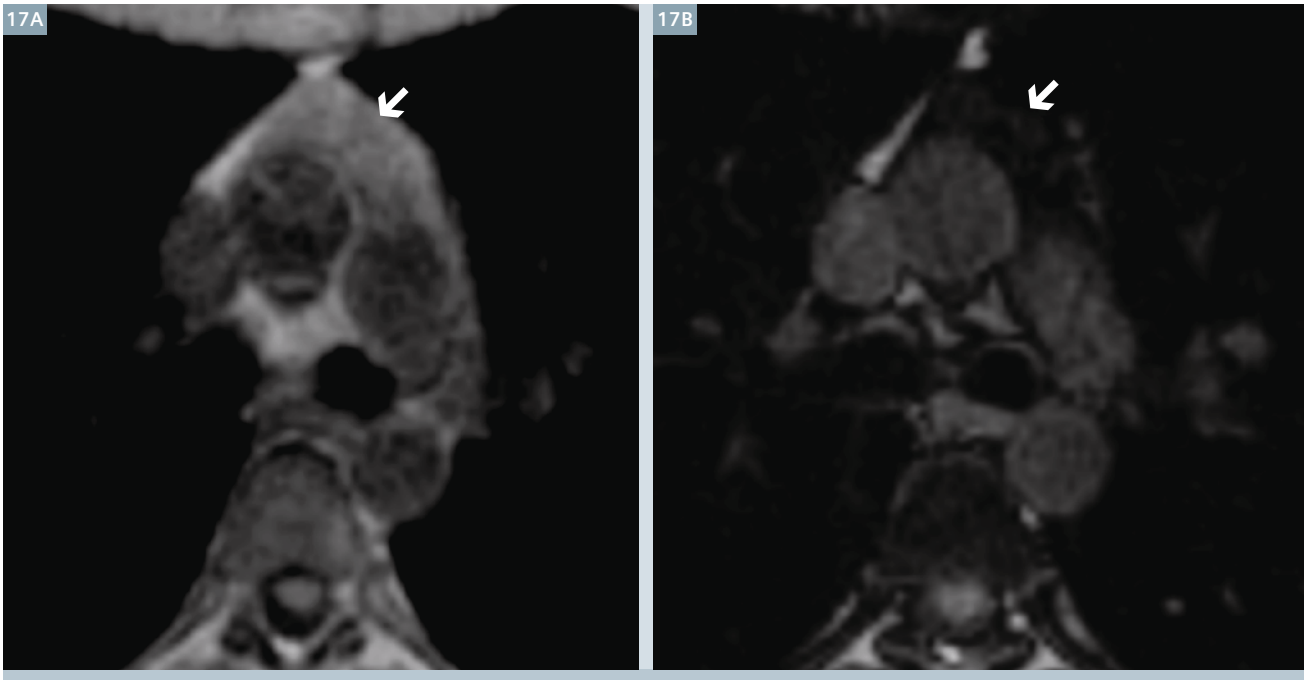

17 In phase **(17A)** and out of phase **(17B)** MR images show a mass lesion (arrows) in the anterior mediastinum. The intensity of the lesion decreases markedly on the out of phase image **(17B)** as compared to the in phase image **(17A)**, implying the presence of a large degree of microscopic fat within the lesion, highly suggestive of thymic hyperplasia as opposed to thymoma.
(Case courtesy of Jeanne B. Ackman, M.D.; Massachusetts General Hospital, Boston, MA, USA.)

References

1. Preston DL, Ron E, Tokuoka S, et al. Solid cancer incidence in atomic bomb survivors: 1958-1998. Radiat Res 2007;168:1-64.
2. Biederer J, Beer M, Hirsch W, et al. MRI of the lung (2/3). Why ... when ... how? Insights Imaging 2012;3:355-371.
3. Eichinger M, Optazaite DE, Kopp-Schneider A, et al. Morphologic and functional scoring of cystic fibrosis lung disease using MRI. Eur J Radiol 2011;81:1321-1329.
4. Failo R, Wielopolski PA, Tiddens HA, Hop WC, Mucelli RP, Lequin MH. Lung morphology assessment using MRI: a robust ultra-short TR/TE 2D steady state free precession sequence used in cystic fibrosis patients. Magn Reson Med 2009;61:299-306.
5. Puderbach M, Eichinger M, Haeselbarth J, et al. Assessment of morphological MRI for pulmonary changes in cystic fibrosis (CF) patients: comparison to thin-section CT and chest x-ray. Invest Radiol 2007;42:715-725.
6. Chung JH, Little BP, Forssen AV, et al. Proton MRI in the evaluation of pulmonary sarcoidosis: comparison to chest CT. Eur J Radiol 2013;82:2378-2385.
7. Chung JH, Cox CW, Forssen AV, Biederer J, Puderbach M, Lynch DA. The dark lymph node sign on magnetic resonance imaging: a novel finding in patients with sarcoidosis. J Thorac Imaging 2013;29:125-129.
8. Lynch DA, Rose CS, Way D, King TE, Jr. Hypersensitivity pneumonitis: sensitivity of high-resolution CT in a population-based study. AJR Am J Roentgenol 1992;159:469-472.
9. Remy-Jardin M, Remy J, Wallaert B, Muller NL. Subacute and chronic bird breeder hypersensitivity pneumonitis: sequential evaluation with CT and correlation with lung function tests and bronchoalveolar lavage. Radiology 1993;189:111-118.
10. Small JH, Flower CD, Traill ZC, Gleeson FV. Air-trapping in extrinsic allergic alveolitis on computed tomography. Clin Radiol 1996;51:684-688.
11. Silva CI, Churg A, Muller NL. Hypersensitivity pneumonitis: spectrum of high-resolution CT and pathologic findings. AJR Am J Roentgenol 2007;188:334-344.
12. Li B, Li Q, Chen C, Guan Y, Liu S. A systematic review and meta-analysis of the accuracy of diffusion-weighted MRI in the detection of malignant pulmonary nodules and masses. Acad Radiol 2013;21:21-29.
13. Coolen J, Vansteenkiste J, De Keyzer F, et al. Characterisation of solitary pulmonary lesions combining visual perfusion and quantitative diffusion MR imaging. Eur Radiol 2013;24:531-541.
14. Yang RM, Li L, Wei XH, et al. Differentiation of central lung cancer from atelectasis: comparison of diffusion-weighted MRI with PET/CT. PLoS One 2013;8:e60279.
15. Chen L, Zhang J, Bao J, et al. Meta-analysis of diffusion-weighted MRI in the differential diagnosis of lung lesions. J Magn Reson Imaging 2012;37:1351-1358.
16. Sommer G, Tremper J, Koenigkam-Santos M, et al. Lung nodule detection in a high-risk population: comparison of magnetic resonance imaging and low-dose computed tomography. Eur J Radiol 2013;83:600-605.
17. Tanaka R, Nakazato Y, Horikoshi H, et al. Diffusion-weighted imaging and positron emission tomography in various cytological subtypes of primary lung adenocarcinoma. Clin Imaging 2013;37:876-883.
18. Biederer J, Both M, Graessner J, et al. Lung morphology: fast MR imaging assessment with a volumetric interpolated breath-hold technique: initial experience with patients. Radiology 2003;226:242-249.
19. Heye T, Ley S, Heussel CP, et al. Detection and size of pulmonary lesions: how accurate is MRI? A prospective comparison of CT and MRI. Acta Radiol 2012;53:153-160.
20. Schroeder T, Ruehm SG, Debatin JF, Ladd ME, Barkhausen J, Goehde SC. Detection of pulmonary nodules using a 2D HASTE MR sequence: comparison with MDCT. AJR Am J Roentgenol 2005;185:979-984.
21. Biederer J, Mirsadraee S, Beer M, et al. MRI of the lung (3/3)-current applications and future perspectives. Insights Imaging 2012;3:373-386.

Contact

Jonathan Hero Chung, M.D.
Associate Professor, Department of Radiology
Director of Pulmonary MRI
Director of Radiology Professional Quality Assurance
Director of Cardiopulmonary Imaging Fellowship
National Jewish Health
1400 Jackson Street
Denver, CO 80206
USA
Chungj@njhealth.org

Further information

For protocols, clinical talks by renowned experts, articles and case studies, please visit us at

www.siemens.com/magnetom-world-lung

GRASP: Tackling the Challenges of Abdominopelvic DCE-MRI

Kai Tobias Block[1]; Li Feng[1]; Robert Grimm[2]; Hersh Chandarana[1]; Ricardo Otazo[1]; Christian Geppert[2]; Daniel K. Sodickson[1]

[1] Department of Radiology, NYU Langone Medical Center, New York, NY, USA
[2] Siemens Healthcare, Erlangen, Germany

Introduction

Dynamic contrast-enhanced (DCE) T1-weighted acquisition after injection of a gadolinium-based contrast agent is an integral part of most diagnostic abdominopelvic MRI examinations and essential for identifying and properly characterizing lesions and tumors, such as the hepatocellular carcinoma (HCC) or renal cancer [1]. Because tumors show a specific temporal contrast-enhancement pattern, it is necessary to obtain images of the whole region-of-interest at multiple short time points following the injection. While technically infeasible years ago, parallel-imaging acceleration techniques such as GRAPPA [2] have made it possible to achieve the required acquisition speed using standard clinical MRI systems, so that these scans can nowadays be performed at almost all imaging centers.

However, in routine practice abdominopelvic DCE-MRI exams remain challenging and the failure rates are undesirably high.

One main challenge is that the data has to be collected precisely at defined time points relative to the arrival time of the contrast agent in the aorta (see Fig. 1). To this end, usually a small test bolus is injected prior to the actual diagnostic scan and monitored using a bolus-tracking sequence to determine the patient-specific circulation delay [3]. Once estimated, the delay is then incorporated into the timing calculation of the dynamic scans, which are scheduled relative to the injection time of the contrast dose. This procedure is, of course, prone to inaccuracies and mistakes – with the potential risk of missing the important arterial phase (AP) of contrast enhancement. As additional complication, the dynamic acquisitions have to be performed during a strict breath hold of the patient and, thus, need to be properly synchronized with breath-hold commands. While the latter can be automated using computer-controlled voice instructions [3], it cannot be guaranteed that the patient is actually following these breath-hold instructions. Continued respiration occurs due to various reasons, including inability to hold breath for the scan duration (usually ~15 sec per acquisition), hearing or language problems, and uncertainty when exactly to stop breathing after hearing the command. Especially elderly or severely sick patients often struggle to properly suspend respiration, resulting in compromised or even fully non-diagnostic image quality. A particular problem here is that once the injection has been done, the acquisitions cannot be repeated before the contrast agent has been extracted from the body, which takes several hours and requires

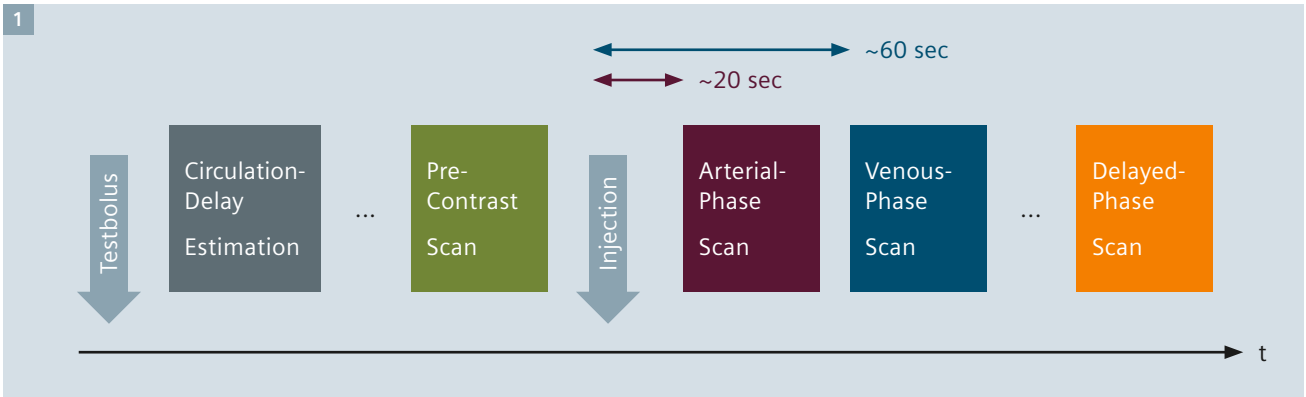

1 Conventional scheme for abdominopelvic DCE-MRI exams, starting with the injection of a test bolus to determine the circulation delay. Afterwards, a pre-contrast image is acquired as well as images in arterial, venous, and delayed phases of contrast enhancement. The acquisitions must be properly timed relative to the injection and accounting for the circulation delay, which makes the procedure prone to timing errors. Furthermore, the scans need to be performed during breath holding.

rescheduling of the examination on a different day. Strongly compromised image quality is also obtained when examining sedated or anesthetized patients, where suspending the respiration is not possible at all.

DCE-MRI with continuous radial acquisition

The requirement to perform abdominal scans during breath-holding results from the high motion sensitivity of conventional MRI techniques, as motion translates into appearance of numerous overlapping object copies known as ghosting artifacts. This problem can be ameliorated by using non-Cartesian acquisition techniques such as radial *k*-space sampling, which inherently prevent the appearance of motion-induced ghosting artifacts. Radial scanning techniques, such as the Radial VIBE or StarVIBE sequence [4], have recently become available for routine imaging, and it has been demonstrated that these sequences can be used to image the abdomen during free breathing [5]. However, the higher motion robustness of radial *k*-space trajectories comes at the price of lower scan efficiency. With typical scan durations of around 60 sec per image volume, sequences such as Radial VIBE are by itself too slow for dynamic abdominopelvic imaging as it would be impossible to separate the arterial and venous phases of enhancement.

To overcome this problem, our group has recently developed a technique called GRASP* that enables using the Radial VIBE sequence for DCE-MRI applications and that resolves many of the aforementioned challenges [6]. The key idea of GRASP is that, instead of performing several individual acquisitions for the required time points, data is acquired continuously throughout the whole exam while the contrast agent is injected (see Fig. 2). Image sets for the needed time points are then calculated from the continuously acquired data using an iterative reconstruction procedure (as described in the next section).

*WIP, the product is currently under development and is not for sale in the US and in other countries. Its future availability cannot be ensured.

This concept leads to a significant simplification of the overall clinical workflow. Because data is acquired all the time during the examination, it is not necessary anymore to determine the circulation delay using a test bolus. Also, the possibility of missing one of the important enhancement phases as a result of a timing or synchronization error is eliminated. Furthermore, because based on radial *k*-space acquisition, GRASP examinations can be performed during continued breathing [7], which removes the need for breath-hold commands, improves patient comfort, and makes the technique well-suited for patients where holding breath is impossible, such as pediatric** patients. Hence, with GRASP, the formerly complex and stressful abdominopelvic DCE-MRI exams now become a simple one-click procedure.

** MR scanning has not been established as safe for imaging fetuses and infants under two years of age. The responsible physician must evaluate the benefit of the MRI examination in comparison to other imaging procedures.

2

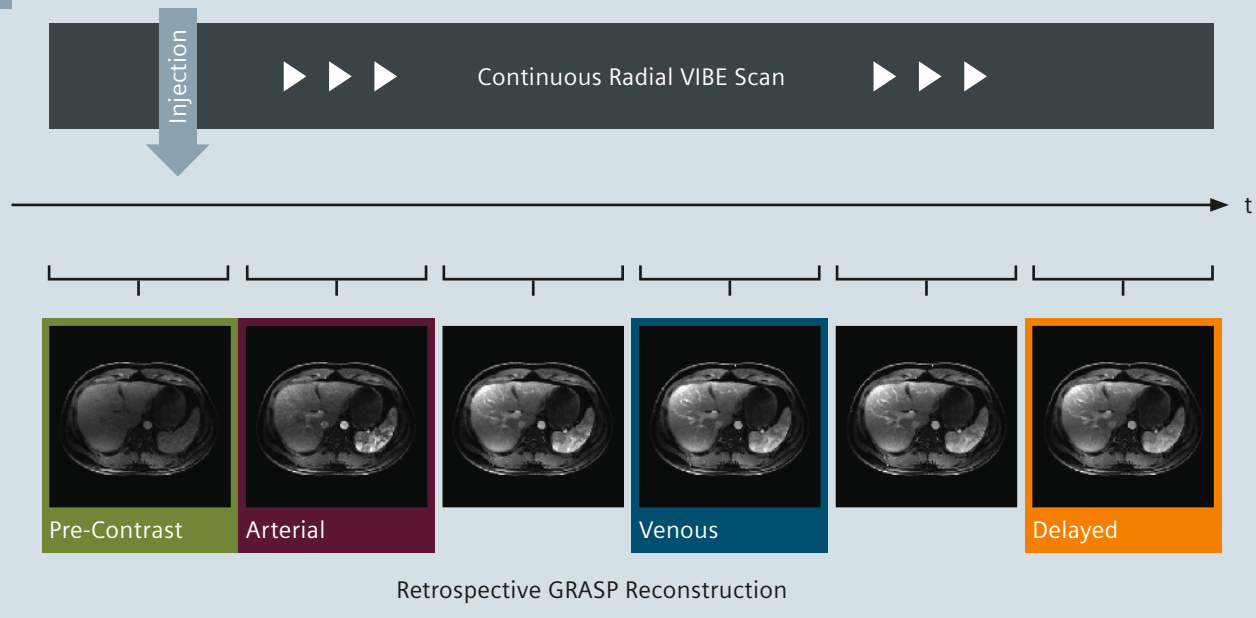

2 GRASP scheme for DCE-MRI, which uses a single continuous acquisition while the contrast agent is injected. Because radial sampling of k-space is used, the data can be acquired during free breathing. Images are calculated from the continuous data using an iterative reconstruction that allows selecting the desired time points and temporal resolution retrospectively. This eliminates the possibility of timing errors and leads to significant simplification of the workflow.

Technical background

On a technical level, GRASP combines several concepts for MRI scan acceleration that have been described previously as individual techniques. The data acquisition is based on the radial golden-angle ordering scheme, which was originally proposed by Winkelmann et al. [8]. When acquiring radial data with constant angular increment of 111.25 degrees (referred to as 'golden angle' because it corresponds to 180 degrees multiplied by the golden ratio), successively sampled radial spokes always add complementary *k*-space information to the previously acquired data, and any number of grouped spokes cover *k*-space approximately uniformly. This means that if data is acquired continuously over some time, any number of successively acquired spokes can be combined into an individual image (e.g., 144 spokes for low temporal resolution, or 21 spokes for high temporal resolution). Furthermore, the reconstruction window can be placed at any time point of the scan. In other words, it is possible to retrospectively decide which temporal resolution and which time points should be reconstructed.

When grouping only few spokes into each image to achieve high temporal resolution, as needed in DCE-MRI for separating the phases of enhancement, the data available for each time point is highly incomplete or, according to MR terminology, undersampled. For radial sequences, this means that the images are affected by severe 'streak' artifacts, which render the images diagnostically unusable. However, GRASP applies two known tricks to suppress this effect and to recover artifact-free images from the undersampled data: Compressed sensing [9] and parallel imaging [10]. The use of compressed sensing is motivated from the fact that the streak artifacts lead to strongly flickering patterns if viewed along time, whereas the true contrast enhancement occurs in a 'smooth' non-flickering fashion. In other words, flickering pixel intensities can be considered as artificial effects. Therefore, artifact-free images can be obtained by employing an iterative reconstruction procedure that, during each calculation step, matches the solution with the available undersampled data and, in addition, suppresses flickering pixels. Mathematically, this is achieved by calculating the total variation (TV) of each pixel along time and using this value as penalty measure during the iterations (because the true solution should have low total variation). By running the iterative procedure for a certain number of iterations, the streak artifacts disappear and the underlying true solution is recovered – even for severely undersampled data. As second mechanism, parallel imaging is integrated into the iterative scheme by using a CG-SENSE-type formalism [11], which contributes to the suppression of streaking artifacts by exploiting local coil sensitivities. Due to the synergistic combination of these two MR acceleration techniques, GRASP is able to compensate for the lower scan efficiency of radial sampling and achieves even higher temporal resolution than possible with most conventional DCE-MRI techniques. The key advantage, however, consists in the aforementioned workflow simplification.

Clinical integration and evaluation

The downside of using such an iterative reconstruction approach is that the image calculation involves a very computationally demanding numerical process (because the solution has to be mapped between image space and radial *k*-space over and over again). This property is not specific to GRASP and applies to other compressed-sensing techniques likewise. However, a difference is that the amount of data acquired during continuous GRASP acquisitions is enormous (up to 10 GB per scan). Processing such a vast amount of data with the described algorithm is not feasible using the computer components of current clinical MRI scanners, as the MRI systems would be blocked from clinical scanning for an unacceptable long time. Hence, for validating the feasibility of the GRASP technique in actual clinical practice, it was necessary for us to derive a workflow-friendly solution that completely circumvents the normal reconstruction pipeline. Therefore, we developed an offline-processing framework [12] that automatically transfers the acquired GRASP data from our various clinical MRI scanners to a central reconstruction server. Incoming reconstruction tasks are queued according to urgency (clinical vs. research scan) and processed with a parallelized and performance-optimized C++ implementation of the GRASP algorithm. Upon completion, the reconstructed images are sent into the clinical PACS without any user interaction. Our radiologists can then read the GRASP exams side-by-side with other scans that were reconstructed directly on the MRI scanner. Using our current reconstruction server with 64 CPU cores, GRASP images are available in the PACS within 5 to 45 minutes after the exam (depending on the exact scan/reconstruction protocol). With this seamless integration of the GRASP prototype into our routine clinical workflow, a stable solution is now in place to evaluate the technique in a large number of patients and across our different MRI systems. Over the last two years, already several thousand GRASP reconstructions have been performed at our institution, and the setup has recently also been disseminated to multiple collaboration sites for an independent evaluation.

Initial applications

As the development of GRASP was aimed at improving abdominal DCE-MRI, liver and kidney scans are logically among the main applications. Figure 3 shows exemplary images from a free-breathing GRASP liver exam of an adult patient, which are free from the typical MRI ghosting artifacts for continued respiration. In this reconstruction, 55 spokes were combined into each image, which yields a temporal resolution of 8.8 sec per image volume and fulfills the timing requirements for diagnostic abdominal DCE-MRI. However, a very powerful feature of GRASP is that the same dataset can be reconstructed with different temporal resolution as well.

When grouping only 13 spokes into each image, the resulting temporal resolution is 2.1 sec and, thus, fast enough for quantitative tissue-perfusion analysis. Researchers in our group are currently exploring this possibility for assessment of the liver function via dual-input dual-compartment modeling [13] and for assessment of the kidney function via estimation of the glomerular filtration rate (GFR). The key advantage here is that the perfusion information is obtained simultaneously without need for additional contrast injection or scan time. Thus, in the future, the GRASP concept might not only help to make abdominal examinations more robust but also provide new diagnostic measures.

Due to the high scan efficiency and simple workflow, GRASP is also very interesting for dynamic imaging of the prostate [14], which has become the GRASP application with the largest clinical scan volume at our institution. In prostate DCE-MRI, which is also with conventional techniques acquired during free breathing due to the required long readout (to properly capture the contrast washout), the main benefit of using GRASP consists in the higher achievable resolution (both spatially and temporally), which translates into an improved detectability and characterization of small tumors. Figure 4 shows images from our current GRASP protocol with 1.1 x 1.1 x 3.0 mm spatial and 2.2 sec temporal resolution, which represents a significant improvement in comparison to our former protocol and allows more precise assessment of the uptake/washout characteristics of suspicious lesions. In this application, data is acquired over a total duration of 5:38 min while the contrast agent is injected 20 sec after the start of the scan to ensure that sufficient pre-contrast data is available. In addition to the higher resolution, also the motion robustness of GRASP contributes to the achieved improvement in image clarity, as conventional prostate scans are often affected by ghosting artifacts caused by motion of the rectum or adjacent bowel loops.

Because GRASP handles such motion effects in a relatively benign manner, our clinical researchers have started

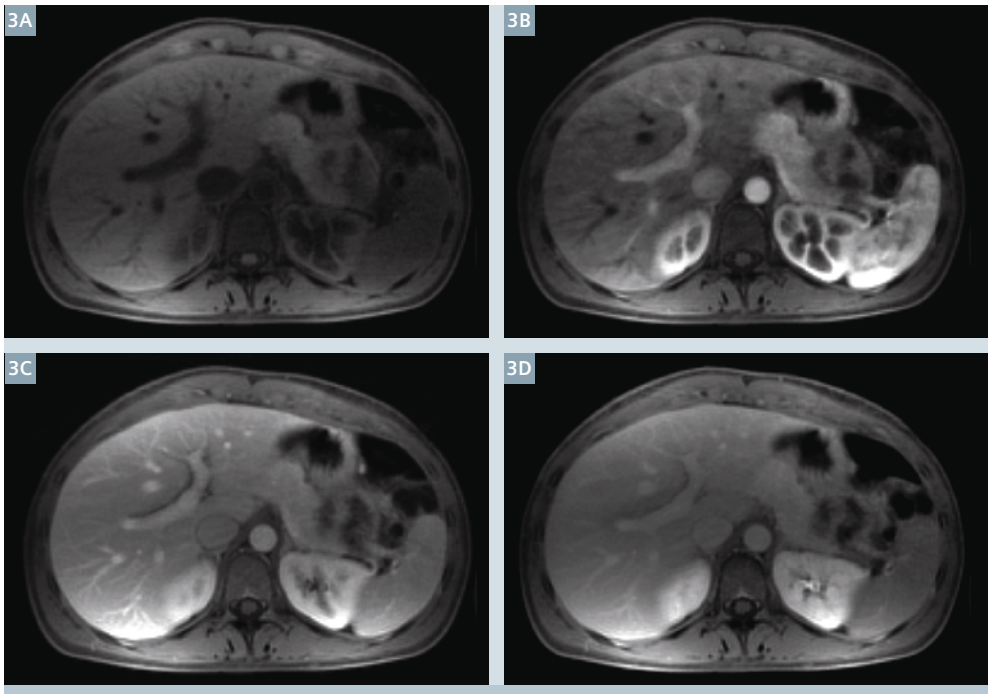

3 Free-breathing dynamic liver GRASP exam in an adult patient. Shown are images of the **(3A)** pre-contrast, **(3B)** arterial, **(3C)** venous, and **(3D)** delayed phase of enhancement. The reconstruction used 55 spokes per frame, corresponding to 8.8 sec per image (spatial resolution 1.5 x 1.5 x 3.0 mm, acquired at 1.5 Tesla).

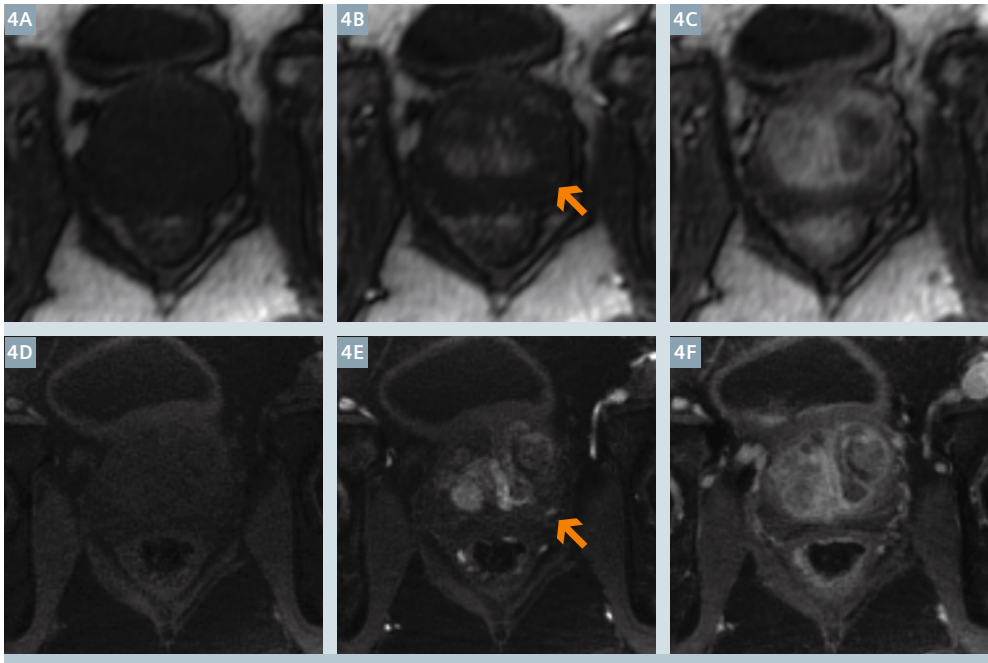

4 Dynamic prostate exam in a patient on active surveillance using **(4A, B, C)** conventional 3D FLASH with 5.5 sec temporal resolution and **(4D, E, F)** GRASP with 2.2 sec temporal resolution (both acquired at 3 Tesla). Images are shown from **(4A, D)** before the injection, **(4B, E)** the time of contrast arrival, and **(4C, F)** a late phase. Due to the higher spatial resolution (1.1 mm vs. 1.9 mm), a suspicious lesion in the peripheral zone with early enhancement and rapid washout (arrow) is more clearly visible on the GRASP scan. Note that the GRASP acquisition used fat suppression due to the off-resonance behavior of radial k-space sampling [4].

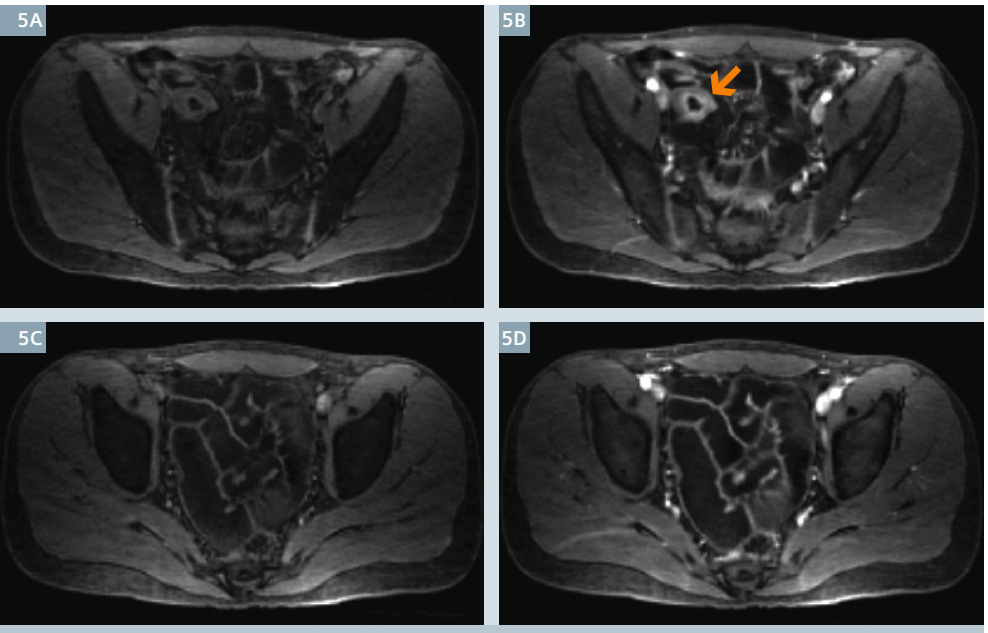

5 Bowel imaging using GRASP in a patient with Crohn's disease (acquired at 1.5 Tesla). Shown are time points **(5A, C)** before and **(5B, D)** shortly after the contrast injection. In the upper images **(5A, B)**, a bowel section with increased wall thickness and mucosal hyperenhancement can be seen (arrow), which indicates active inflammation. For comparison, the lower row **(5C, D)** shows a different slice with normal-appearing bowel sections.

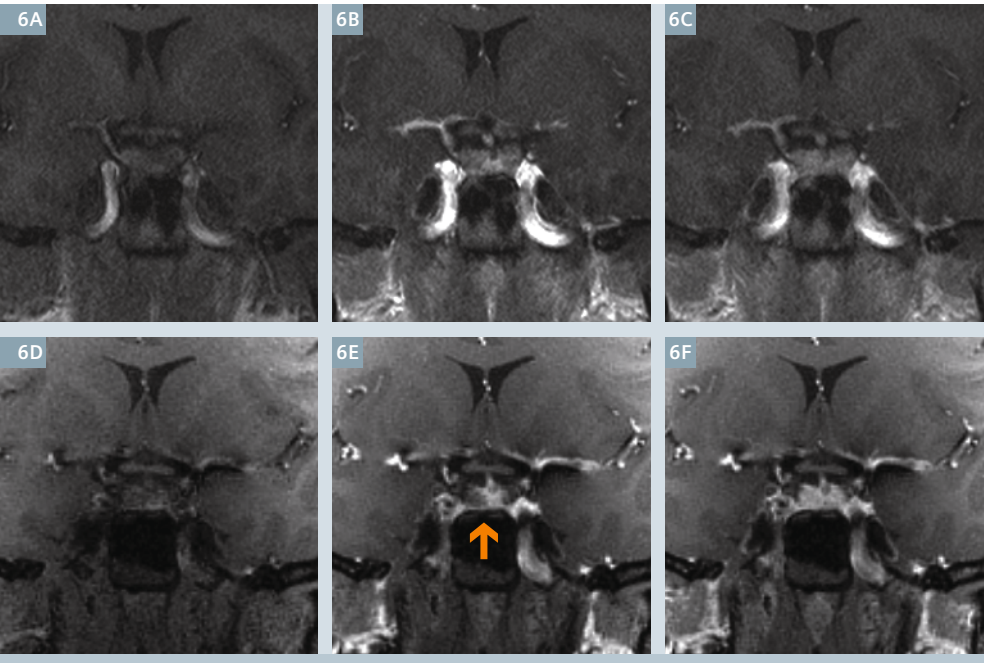

6 Dynamic imaging of the pituitary gland using **(6A, B, C)** a conventional 2D GRE sequence and **(6D, E, F)** GRASP (both acquired at 3 Tesla). Shown are images **(6A, D)** before the injection, **(6B, E)** shortly after contrast arrival, and **(6C, F)** at a later phase. A small area with delayed contrast uptake is visible in the inferior right gland (arrow), which likely reflects a microadenoma. Because of much thinner slices (1 mm vs. 3 mm) and higher overall image quality, such findings are easier to identify with GRASP.

using GRASP also for bowel imaging to investigate inflammatory bowel diseases such as Crohn's disease [15]. Inflamed bowel sections are characterized by increased wall thickness and reduced motility, as well as increased vascularity. Therefore, these bowel sections can be easily identified on GRASP scans, as shown in Figure 5. In addition, signal-enhancement curves can be generated from region-of-interests of the dynamic GRASP images and used to calculate quantitative perfusion measures that have been found to correlate with inflammation [15]. These parameters can potentially be used to non-invasively predict disease progression as well as response to treatments. Again, an advantage is that the perfusion images are obtained together with morphologic information from the same dataset through GRASP reconstruction with variable temporal resolution.

Finally, applications of GRASP are of course not confined to abdominopelvic imaging. GRASP can be used as robust imaging technique for any other dynamic T1-weighted examination as well, and a large portion of our recent GRASP scans are actually done in the head and neck region, including dynamic imaging of the orbits, the neck, and the pituitary gland. In the latter application, it is again the improvement in spatial resolution that makes GRASP attractive. When compared to our previously employed 2D GRE protocol (see Fig. 6), GRASP provides much higher spatial resolution along the slice direction and, thus, makes it easier to accurately localize tiny lesions such as microadenomas or small cysts. The possibility to incorporate also perfusion information into the diagnosis adds to its value [16].

Additional motion compensation

So, is GRASP now the ultimate solution for abdominopelvic DCE-MRI? Unfortunately, not quite yet. Our clinical evaluation showed that free-breathing abdominal GRASP exams work well in many patients with convincing results, but in a certain percentage of patients the image quality is still suboptimal. The problem here is that some patients perform deep respiration in

the moment when the contrast agent is injected, most likely because they are surprised by the sudden onset of the injection and the resulting sensation. Some patients even start to cough, so that the liver and adjacent organs rapidly move up and down by up to 10 cm during the initial circulations of the contrast agent. While GRASP handles moderate motion relatively well, compromised image quality is obtained if the data for each time point is affected by strong inconsistencies due to varying motion states. For example, if during 50% of the spokes the liver was in an end-expiratory position and during the other 50% of the data in an end-inspiratory position, GRASP will not be able to find one reconstruction that is consistent with both of these motion states. As a result, the images show motion blurring and streak artifacts.

However, since GRASP is based on radial sampling, it is possible to apply additional tricks to resolve this situation. Because all of the spokes pass through the center of *k*-space, it is possible to extract a respiration curve from the *k*-space center that indicates how the patient was breathing during the examination [17]. This is possible because the percentage of (dark) lung tissue in the field-of-view changes during respiration, which leads to a modulation of the total signal power. The latter is reflected by the signal intensity at the *k*-space center, which therefore can be used to generate the respiration curve. Once it is known from the curve what the respiratory state for each acquired spoke was, the data can be sorted according to the respiratory state and the GRASP reconstruction can be extended to treat the respiratory state as an extra dimension, which allows freezing the respiration in the reconstructed images [18]. This extended approach, which we call XD-GRASP*, is still under active development and accompanied by a further increase of the computational complexity. However, as shown in Figure 7, initial results look promising and we are convinced that the motion-compensated XD-GRASP approach is a leap towards the future of abdominopelvic DCE-MRI, soon delivering 100% reliability in every patient and at every imaging center, regardless of the patient's cooperation and regardless of the operator's training level.

Conclusion

GRASP is a new concept to simplify DCE-MRI exams by acquiring all information using a single continuous scan instead of several individual scans, which eliminates the possibility of timing or synchronization mistakes. Because GRASP is based on radial sampling, acquisitions can be performed during free breathing, thus making abdominal DCE-MRI accessible for patients unable hold breath. Sufficiently high acquisition speed is achieved by synergistically combining the compressed-sensing and parallel-imaging principles. Due to use of the golden-angle scheme, the temporal resolution and desired image time points can selected retrospectively, which enables reconstructing both morphologic and perfusion information from the same exam. GRASP has already been tested in thousands of patient exams in our routine practice, making it one of the first compressed-sensing techniques that have been evaluated on a large scale for clinical feasibility. While results are convincing for patients with regular breathing activity, limitations still exist for those patients performing deep respiration/coughing during the injection. This remaining issue is now being addressed by integrating active motion compensation based on the radial self-navigation principle.

References

1 Elsayes KM, Narra VR, Yin Y, Mukundan G, Lammle M, Brown JJ. Focal hepatic lesions: diagnostic value of enhancement pattern approach with contrast-enhanced 3D gradient-echo MR imaging. Radiographics. 2005 Sep-Oct;25(5):1299-1320.

2 Griswold MA, Jakob PM, Heidemann RM, Nittka M, Jellus V, Wang J, Kiefer B, Haase A. Generalized autocalibrating partially parallel acquisitions (GRAPPA). Magn Reson Med. 2002 Jun;47(6):1202-1210.

3 Martin DR, Sharma P, Kitajima H. Challenges and Clinical Value of Automated and Patient-Specific Dynamically Timed Contrast-Enhanced Liver MRI Examination. Siemens MAGNETOM Flash 3/2009:40-45.

4 Block KT, Chandarana H, Milla S, Bruno M, Mulholland T, Fatterpekar G, Hagiwara M, Grimm R, Geppert C, Kiefer B, Sodickson DK. Towards Routine Clinical Use of Radial Stack-of-Stars 3D Gradient-Echo Sequences for Reducing Motion Sensitivity. J Korean Soc Magn Reson Med. 2014 Jun;18(2):87-106.

5 Chandarana H, Block TK, Rosenkrantz AB, Lim RP, Kim D, Mossa DJ, Babb JS, Kiefer B, Lee VS. Free-breathing radial 3D fat-suppressed T1-weighted gradient echo sequence: a viable alternative for contrast-enhanced liver imaging in patients unable to suspend respiration. Invest Radiol. 2011 Oct;46(10):648-53.

6 Feng L, Grimm R, Block KT, Chandarana H, Kim S, Xu J, Axel L, Sodickson DK, Otazo R. Golden-angle radial sparse parallel MRI: Combination of compressed

*WIP, the product is currently under development and is not for sale in the US and other countries. Its future availability cannot be ensured.

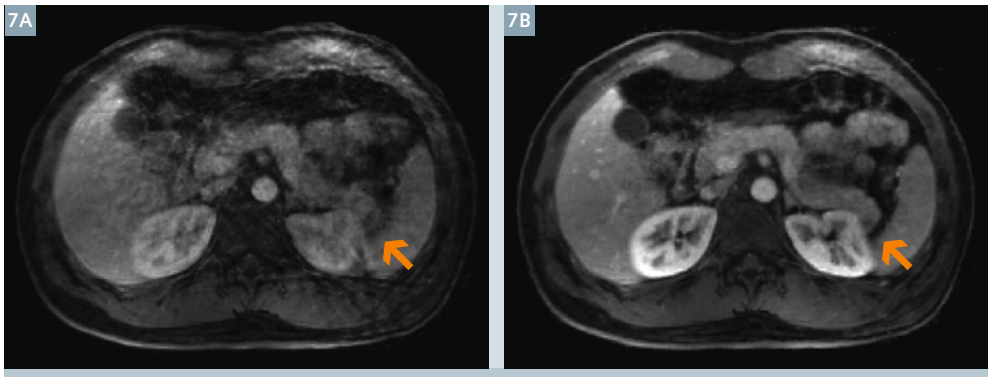

7 GRASP liver exam of a patient breathing deeply after the injection. Due to the inconsistent motion state of the acquired data, the normal GRASP reconstruction **(7A)** is affected by streak artifacts and motion blurring (arrow). These artifacts are clearly reduced when employing XD-GRASP with additional motion compensation **(7B)**.

sensing, parallel imaging, and golden-angle radial sampling for fast and flexible dynamic volumetric MRI. Magn Reson Med. 2014 Sep;72(3):707-717.
7 Chandarana H, Feng L, Block TK, Rosenkrantz AB, Lim RP, Babb JS, Sodickson DK, Otazo R. Free-breathing contrast-enhanced multiphase MRI of the liver using a combination of compressed sensing, parallel imaging, and golden-angle radial sampling. Invest Radiol. 2013 Jan;48(1):10-16.
8 Winkelmann S, Schaeffter T, Koehler T, Eggers H, Doessel O. An optimal radial profile order based on the Golden Ratio for time-resolved MRI. IEEE Trans Med Imaging. 2007 Jan;26(1):68-76.
9 Lustig M, Donoho D, Pauly JM. Sparse MRI: The application of compressed sensing for rapid MR imaging. Magn Reson Med. 2007 Dec;58(6):1182-1195.
10 Pruessmann KP, Weiger M, Börnert P, Boesiger P. Advances in sensitivity encoding with arbitrary *k*-space trajectories. Magn Reson Med. 2001 Oct;46(4):638-651.
11 Block KT, Uecker M, Frahm J. Undersampled radial MRI with multiple coils. Iterative image reconstruction using a total variation constraint. Magn Reson Med. 2007 Jun;57(6):1086-1098.
12 Information and free download available at http://ktblock.de/yarra
13 Chandarana H, Block TK, Ream J, Mikheev A, Sigal SH, Otazo R, Rusinek H. Estimating Liver Perfusion From Free-breathing Continuously Acquired Dynamic Gd-EOB-DTPA Enhanced Acquisition With Compressed Sensing Reconstruction. Invest Radiol. In press.
14 Rosenkrantz AB, Geppert C, Grimm R, Block TK, Glielmi C, Feng L, Otazo R, Ream JM, Romolo MM, Taneja SS, Sodickson DK, Chandarana H. Dynamic contrast-enhanced MRI of the prostate with high spatiotemporal resolution using compressed sensing,parallel imaging, and continuous golden-angle radial sampling: Preliminary experience. J Magn Reson Imaging. 2014 May 16. Epub ahead of print.
15 Ream JM, Doshi AM, Block KT, Kim S, Otazo R, Feng L, Chandarana H. High Spatiotemporal Dynamic Contrast-Enhanced MRI of the Small Bowel in Active Crohn's Terminal Ileitis using Compressed Sensing, Parallel Imaging, and Golden-Angle Radial Sampling. In Proc. Intl. Soc. Mag. Reson. Med. 22 (2014): 4292.
16 Espagnet CR, Bangiyev L, Block KT, Grimm R, Feng L, Ruggiero V, Babb J, Davis A, Sodickson DK, Fatterpekar G. High resolution DCE MRI of the Pituitary gland using Radial K space Aquisition with Compressed Sensing Reconstruction. In Proc. Intl. Soc. Mag. Reson. Med. 22 (2014): 4669.
17 Grimm R, Bauer S, Kiefer B, Hornegger J, Block KT. Optimal Channel Selection for Respiratory Self-Gating Signals. In Proc. Intl. Soc. Mag. Reson. Med. 21 (2013): 3749.
18 Feng L, Liu J, Block KT, Xu J, Axel L, Sodickson DK, Otazo R. Compressed Sensing Reconstruction with an Additional Respiratory-Phase Dimension for Free-Breathing Imaging. In Proc. Intl. Soc. Mag. Reson. Med. 21 (2013): 606.

Contact

Dr. Kai Tobias Block
Center for Biomedical Imaging
NYU Langone Medical Center
660 First Avenue
New York, NY 10016
USA
tobias.block@nyumc.org

Growth with Body MRI.

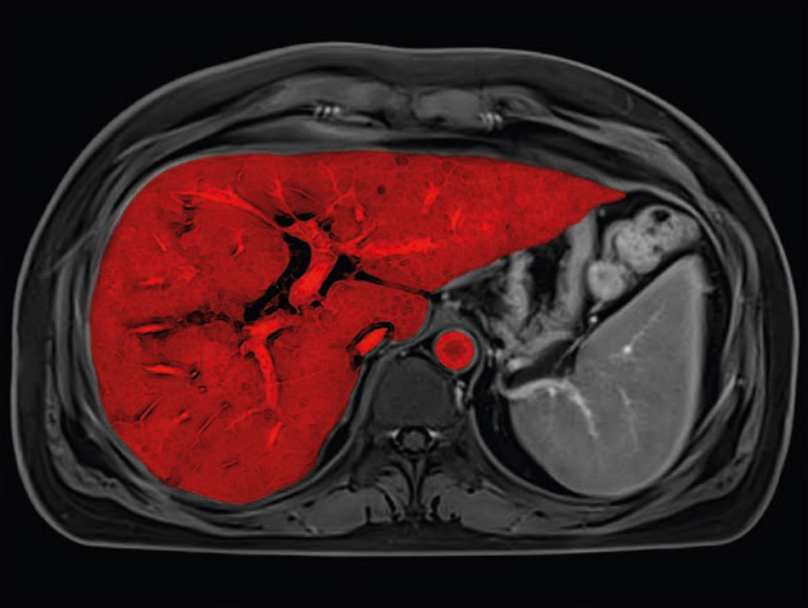

Are you facing challenges in Body MRI? With us you will be able to solve them!

Find out how we do that and see what other MAGNETOM users say:

www.siemens.com/body-mri

Save the Date

Heidelberg Summer School

Musculoskeletal Cross Sectional Imaging 2015

July 24th / 25th 2015
Heidelberg, Germany

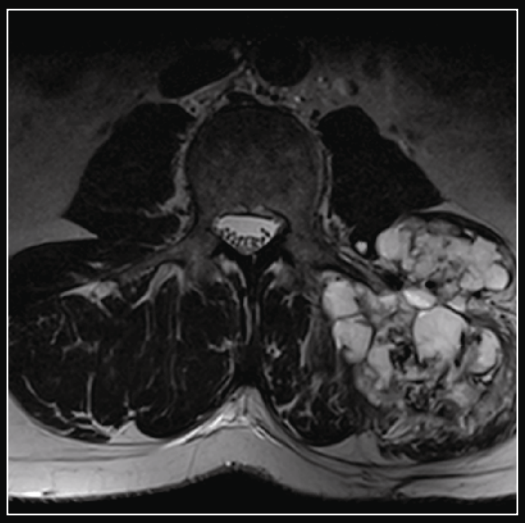

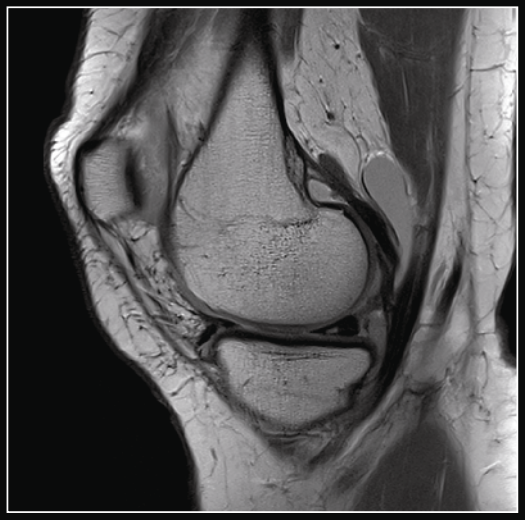

The Heidelberg Summer School offers advanced learning opportunities and promotes the academic exchange of knowledge, ideas, and experiences by bringing together physicians and professional staff from all over the world. Excellent speakers will cover a wide range of medical, physical, and technical topics in musculoskeletal imaging. All lectures are in English.

Course director

Marc-André Weber, M.D., M.Sc.

Professor of Radiology, Section Head Musculoskeletal Radiology at the University Hospital Heidelberg

CME Accreditation

The symposium will be accredited by the 'Landesärztekammer Baden-Württemberg' with CME credits (category A).
Also, the symposium is accredited for 1 category 3 credit point for the ESSR diploma by the European Society of Musculoskeletal Radiology.

Registration

Mrs. Marianne Krebs, Secretary of the Section Musculoskeletal Radiology

Marianne.Krebs@med.uni-heidelberg.de

For further information please visit:

www.heidelbergsummerschool.de

Case Report: Athletic Pubalgia and Core Injury. Tear/Detachment of the Right Common Adductor Longus-Rectus Abdominis Aponeurosis

Coley C. Gatlin, M.D.; Charles P. Ho, Ph.D., M.D.

Steadman Philippon Research Institute, Vail, CO, USA

History of present illness

The patient is a 24-year-old male skier who sustained a crash resulting in acute injuries to his left knee and right groin/lower abdomen. The patient complained of left knee pain, swelling, and instability. After his crash, he was unable to ski down due to a giving out sensation in his right hip/groin. He also noted right lower abdominal pain and groin pain and described a pinching sensation along his right hip and groin. The patient had a chronic history of right lower abdominal/groin pain dating back approximately 1.5 years prior to the acute injury.

Physical examination

He was noted on physical exam with tenderness to palpation along the origin of the adductors. He had pain with resisted hip adduction and hip flexion. He had a positive right anterior hip impingement sign, negative left anterior hip impingement sign, and negative bilateral hip posterior impingement testing. Negative bilateral hip log roll testing. Also, he noted mild lower abdominal pain with sit-ups.

Radiographs

AP pelvis and right hip radiographs were obtained. No acute pelvic fracture is identified. There was bilateral hip decreased offset at the head and neck junction. No evidence of heterotopic ossification or avulsion fracture at the adductor origins.

Clinical assessment

24-year-old male skier who sustained acute injuries to the right lower abdomen/groin and left knee. Injuries to the left knee based on physical exam and MRI include a complete ACL tear, lateral meniscus tear, and MCL sprain. In reference to the patient's right lower abdominal/groin pain, there is an acute injury superimposed upon chronic right groin symptoms.

Differential diagnosis for groin pain (limited)

- Rectus abdominis muscle strain
- Adductor muscle strain, tear, and/or chronic tendinopathy
- Rectus abdominis – adductor longus aponeurosis tear
- Pelvic bone fracture / stress fracture
- Acute labral tear
- Apophysitis
- Inguinal Hernia (indirect and direct)
- Femoral Acetabular Impingement (FAI)
- Iliopsoas tendinitis
- Iliotibial band syndrome

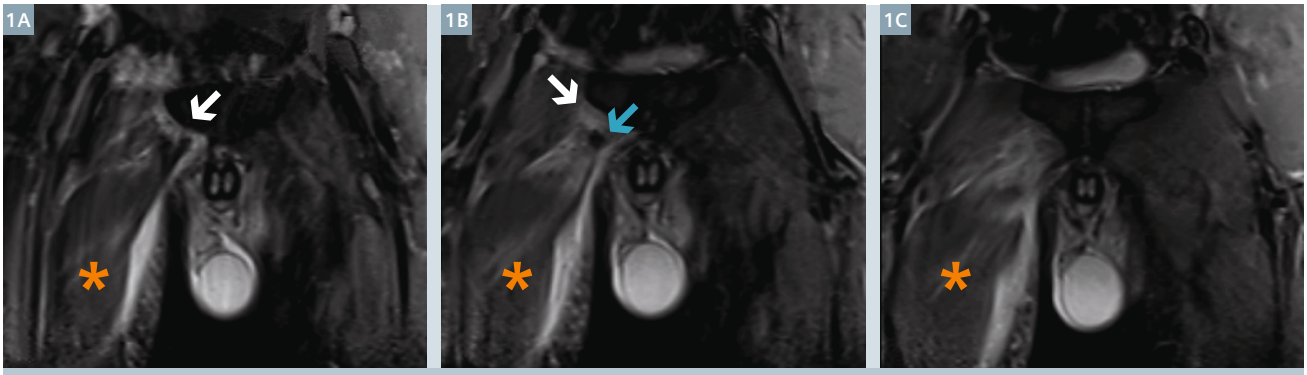

1 Sequential coronal STIR images (large FOV) from anterior to posterior **(1A-C)** demonstrating edema and hemorrhage in the right adductors (*), stripping/undermining of the common adductor longus-rectus abdominis aponeurosis (white arrow), and avulsion of the adductor longus from the pubic symphysis (blue arrow).

Plan

At the patient's initial presentation, it was determined that the patient would require left knee surgery to repair his ACL and lateral meniscus. In reference to his right lower abdominal/groin pain, the treatment options included conservative treatment versus conservative therapy and obtaining additional diagnostic imaging studies. After discussion with the patient, additional MR imaging of the pubic symphysis and right hip was performed to further assess the degree of injury and narrow the treatment options.

MR imaging findings

Sports Hernia Protocol:

1. Tearing and detachment of the common right adductor longus – rectus abdominis (AL-RA) aponeurosis with moderate adductor longus and distal rectus abdominis partial thickness tearing/muscle strains.
2. Moderate fluid and edema surrounding these areas along the anterior superficial soft tissues compatible with edema and contusion.

Discussion

Groin pain in athletes has long been a diagnostic and therapeutic challenge. Injuries to the groin region most commonly result from activities requiring rapid acceleration, deceleration, twisting, lateral motion, and abrupt changes in direction. Sports including soccer, American football, hockey, and baseball have been associated with particularly high rates of activity-induced groin pain, or athletic pubalgia. Up to 13% of soccer injuries involve the groin [1, 2]. Initially, sports related groin injuries were labeled 'sports hernias' secondary to the anatomic proximity to the superficial inguinal ring. However, the term 'sports hernia' is a misnomer as MRI has shown true hernias to be infrequent in this athletic population. The terms athletic pubalgia and core injury (more recently) have been used to describe this entity [6].

The pubic symphysis is an amphiarthrodial joint with an articular disc interposed between 2 pubic bones. The joint is stabilized by 4 ligaments and multiple tendon attachments. The arcuate (anterior inferior) and the superior, anterior, and posterior pubic ligaments encase the pubic articulation. The arcuate ligament and the superior pubic ligament are the strongest and most crucial for resisting shear forces. The arcuate ligament lines the inferior margin of the pubic symphysis in close association with the articular disc and the rectus abdominis/adductor longus aponeurosis. The pubic symphysis stabilizes the anterior pelvis while

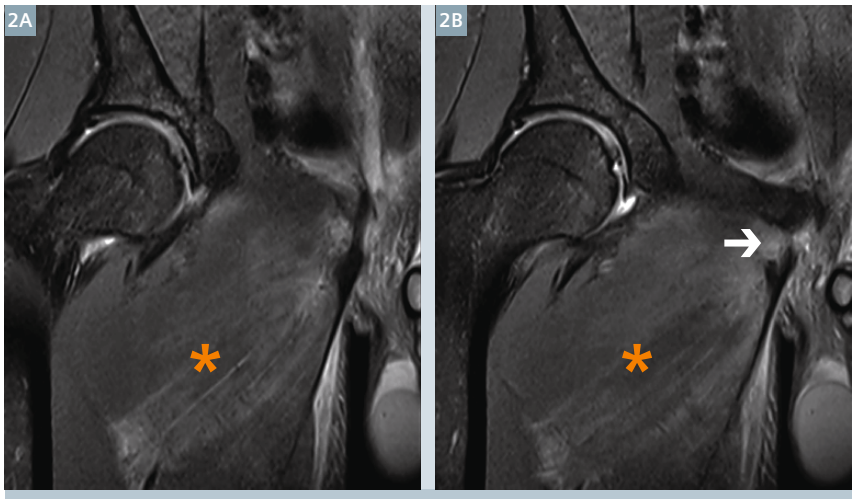

2 Coronal proton density TSE FS images of the right hip (small FOV) showing adductor interstitial strain/edema (*), stripping/undermining of the common adductor longus-rectus abdominis aponeurosis, and avulsion of the adductor longus from the pubic symphysis (arrow).

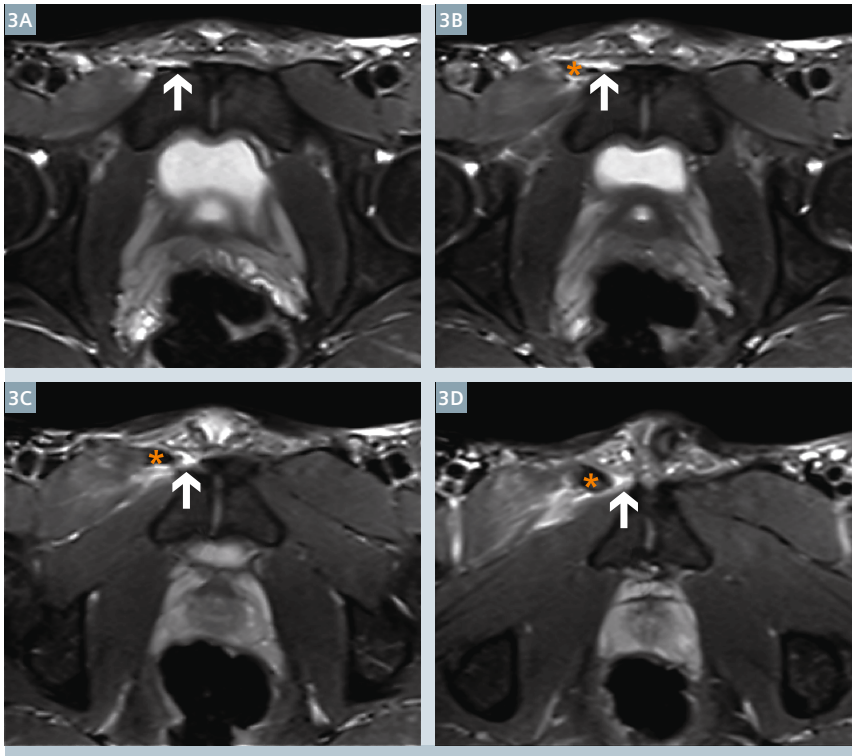

3 Axial T2-weighted TSE FS. Sequential images from superior to inferior **(3A-D)** showing stripping/undermining of the common adductor longus-rectus abdominis aponeurosis (denoted by the arrows) and avulsion of the adductor longus from the pubic symphysis (*).

still allowing a small degree of craniocaudal movement at the joint [3, 5].

The lower abdominal wall muscles attach to the pubic symphysis, including the rectus abdominis, internal and external obliques, and the transversus abdominis. The adductor muscles in the medial thigh also attach to the pubis and include the pectineus, adductor longus, adductor brevis, adductor magnus, and gracilis. Functionally, the rectus abdominis and the adductor longus are the most critical for stability at the anterior pelvis [3, 6]. Along the lateral margin of the pubis, the adductor longus blends with the inferior rectus abdominis attachment. At the midline, the inferior rectus abdominis, adductor fibers, arcuate ligament, and anterior pubic periosteum form the aponeurotic plate [6]. During core rotation and extension, the rectus abdominis and the adductor longus are relative antagonists. While the rectus elevates the anterior pelvis, the adductor longus depresses it. Injury of one of the these two components causes abnormal biomechanical forces on the opposing muscles and tendons leading to further injury at the aponeurosis and its attachments [7]. Continued athletic activity in the setting of pelvic instability may result in progressive/additional injury to the surrounding structures.

4 Sagittal T2-weighted TSE FS. Left common adductor longus-rectus abdominis aponeurosis shows continuity with overlying soft tissue swelling, edema, and contusion from the contralateral right common aponeurosis injury.

Imaging features

MR imaging:
Small field-of-view high resolution MR image acquisition of the pubic symphysis is obtained in the axial, sagittal, and coronal planes using a 3T MAGNETOM Verio system. Sagittal images are most helpful in depicting the adductor longus-rectus abdominis aponeurosis. Water-sensitive sequences, such as Proton Density TSE with fat saturation, are used to detect abnormal bone marrow signal within the pubis associated with stress-related changes, avulsion injuries, bone contusion, fracture, and other inflammatory, infectious, or infiltrative processes.

Strains or small tears of the muscles and tendons are most common and demonstrate increased intramuscular and intra-tendinous signal on water-sensitive sequences. Isolated tears of the adductor longus or rectus abdominis tendons present as high MR fluid-signal filled defects in the tendons. In the acute phase, surrounding hemorrhage and edema are present. Myotendinous injuries at the pubis most commonly involve the adductor muscle group, with the adductor longus being the most commonly injured. Proximal adductor longus tendon tears at the pubis frequently extend into the common aponeurosis [8].

In the distal rectus abdominis, the lateral attachment is most frequently injured [9]. Axial images best demonstrate interruption of the distal rectus abdominis tendon just superior to its attachment to the pubis. Chronic injuries of the rectus abdominis muscle or tendon may result in muscle atrophy and asymmetry in muscle bulk.

Avulsion injuries or tears of the common AL-RA aponeurosis are seen as fluid signal interposed between the aponeurosis and subjacent bone. These injuries are best seen on sagittal MR imaging and range from small microtears to complete disruption/detachment of the common aponeurosis.

The secondary cleft sign was originally described as an arthrographic finding following injection of the symphysis pubis with abnormal inferior extension of contrast from the central symphyseal fibrocartilaginous cleft. This was felt to represent a microtear of the adductor longus and gracilis tendon origins. An MRI equivalent of the secondary cleft is visible on fluid-sensitive sequences as a curvilinear fluid-signal interface that is continuous with the symphysis pubis and undermines the inserting structures at the pubis [10]. Although the exact etiology of the secondary cleft remains to be elucidated, this most likely represents a tear of the adductor longus origin and AL-RA aponeurosis and because of the interrelated anatomy may extend bilaterally [11].

Osteitis pubis is believed to result from instability of the pubic symphysis associated with repetitive shear and distraction injuries and an imbalance of the forces applied by the inserting abdominal wall and adductor muscle groups. The earliest MR sign of osteitis pubis is diffuse subarticular marrow edema bordering the symphysis pubis. The marrow edema is typically generalized and bilateral. Additional findings representative of osteitis pubis include periostitis, bony resorption, subchondral cysts and osteophytes [8].

Treatment and prognosis

Treatment strategies for patients with groin pain are evolving, guided by an improved understanding of the biomechanics of the anterior pelvis and a more focused imaging approach. Conservative treatment is often successful with isolated tendon or myotendinous strains. In more severe injuries, steroid injections in the region of the symphysis pubis or adductor tendon origin may be utilized. However, since steroid injections do not address the underlying injury, symptoms frequently recur with resumption of athletic activities. Surgery is considered if non-operative,

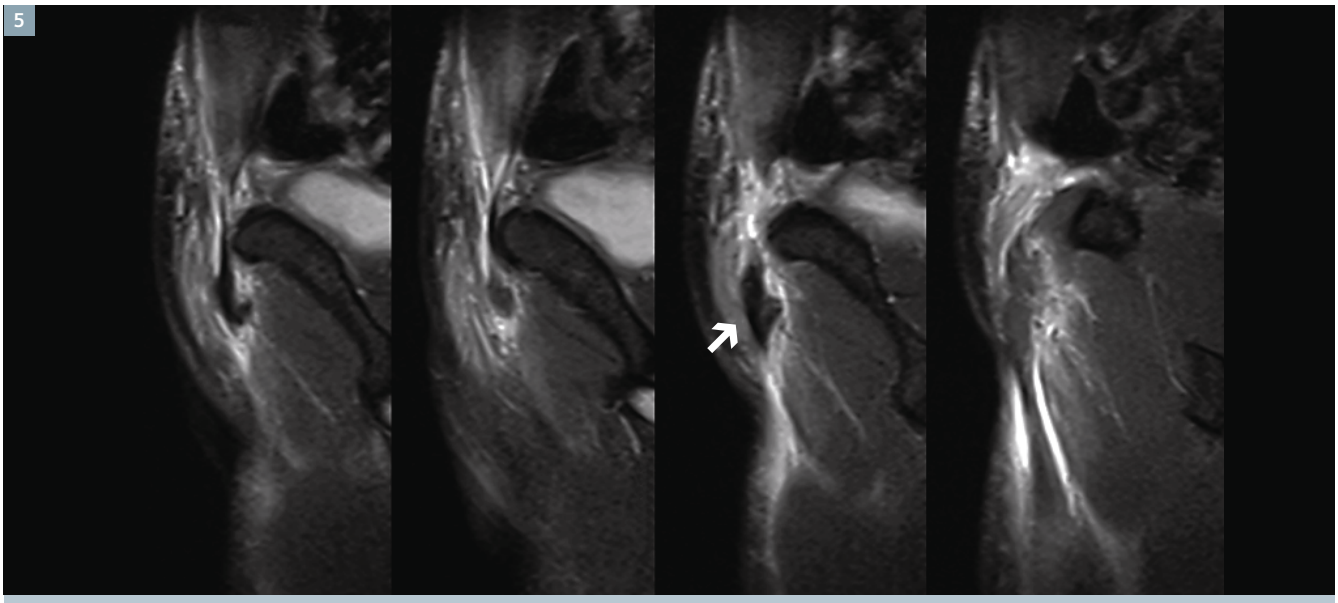

5 Sagittal T2-weighted TSE FS. Right common adductor longus-rectus abdominis aponeurosis avulsion with surrounding muscle strain/hemorrhage (medial to lateral).

conservative treatment fails after 6-8 weeks. Hernia repair without a detectable hernia has reported variable success rates with either a conventional or laparoscopic approach, commonly using mesh to repair and reinforce the abdominal wall. Some authors suggest that success in these patients may result from scarring of the inserting structures in the pubic region that secondarily stabilizes the unrecognized symptomatic anatomic defect [12]. Current surgical treatment is focused on correcting the underlying anatomic defect and stabilizing the anterior pelvis, and these targeted surgical repairs have resulted in improved outcomes [12, 13]. Pelvic floor repair with reattachment of the lateral margin of the rectus abdominis tendon at the pubis has been associated with some of the highest success rates. Depending on associated injuries, adductor tendon release or tenotomy may also be performed. Isolated full-thickness adductor tendon avulsions are typically surgically reattached.

Osteitis pubis is initially managed by non-steroid anti-inflammatory drugs (NSAID) therapy and physical rehabilitation. Steroid injections are considered as the next line of therapy. Symphyseal arthrodesis is reserved for patients failing conservative measures [7].

References

1 Ekstrand J, Gillquist J. The avoidability of soccer injuries. Int J Sports Med 1983;4(2):124–8.

2 Ekstrand J, Hilding J. The incidence and differential diagnosis of acute groin injuries in male soccer players. Scand J Med Sci Sports 1999; 9:98–103.

3 Omar IM, Zoga AC, Kavanagh EC, et al. Athletic pubalgia and "sports hernia": optimal MR imaging technique and findings. Radiographics 2008; 28: 1415–38.

4 Walheim GG, Selvik G. Mobility of the pubic symphysis: in vivo measurements with an electromechanic method and a roentgen stereophotogrammetric method. Clin Orthop Relat Res 1984; 191: 129–35.

5 Walheim G, Olerud S, Ribbe T. Mobility of the pubic symphysis: measurements by an electromechanical method. Acta Orthop Scand 1984; 55(2):203–8.

6 Khan W, et al. Magnetic Resonance Imaging of Athletic Pubalgia and the Sports Hernia. Current Understanding and Practice. Magn. Reson Imaging Clin N Am 21 (2013) 97-110.

7 Omar IM, et al. Athletic Pubalgia and "Sports Hernia": Optimal MR Imaging Technique and Findings. RadioGraphics2008; 28:1415-1438.

8 Stadnick ME. Athletic Pubalgia. MRI Web Clinic. February 2010.

9 Gamble JG, Simmons SC, Freedman M. The symphysis pubis: anatomic and pathologic considerations. Clin orthop Relat Res 1983; 203: 261-272.

10 Cunningham PM, et al. Patterns of bone and soft-tissue injury at the symphysis pubis in soccer players: observations at MRI. AJR 2007; 188:W291-W296.

11 Zoga AC, et al. Athletic Pubalgia and the "Sports Hernia": MR Imaging Findings. Radiology, 2008, 247 (3):797-807.

12 Meyers WC, et al. Management of severe lower abdominal or inguinal pain in high performance athletes. PAIN (Performing Athletes with Abdominal or Inguinal Neuromuscular Pin Study Group). Am J Sports Med 2000; 28: 2-8.

13 Taylor DC, et al. Abdominal musculature abnormalities as a cause of groin pain in athletes: inguinal hernias and pubalgia. Am J Sports Med 1991; 19: 239-242.

14 Koulouris G. Imaging Review of Groin Pain in Elite Athletes: An Anatomic Approach to Imaging Findings. AJR 2008; 191:962-972.

Contact

Charles P. Ho, Ph.D., M.D.
Steadman Philippon Research Institute
181 W. Meadow Drive, Suite 1000
Vail, CO 81657
USA
charles.ho@thesteadmanclinic.com

Magnetic Resonance gagCEST Imaging of the Human Lumbar Intervertebral Disc

Anja Müller-Lutz[1]; Christoph Schleich[1]; Gael Pentang[1]; Benjamin Schmitt[2]; Gerald Antoch[1]; Hans-Jörg Wittsack[1]; Falk Miese[1]

[1] University Dusseldorf, Medical Faculty, Department of Diagnostic and Interventional Radiology, Dusseldorf, Germany
[2] Siemens Ltd. Australia, Healthcare Sector, Macquarie Park, Australia

Abstract

Magnetic resonance gagCEST* imaging has helped to correlate with the content of glycosaminoglycans in joint cartilage. Therefore, this technique shows potential for the evaluation of biochemical composition of human lumbar discs. In this article we discuss the application of gagCEST imaging in four different cases: A healthy volunteer, a volunteer with disc bulging, a volunteer with disc herniation, and a volunteer with disc degeneration.

Introduction

Diseases of the intervertebral discs are frequent and have a high individual and socio-economic impact [1, 2]. The assessment of the composition of the intervertebral cartilage is a potential research tool for the assessment of these conditions. MR enables non-invasive and radiation-free imaging of the intervertebral disc. New imaging techniques such as sodium and chemical exchange saturation transfer (CEST) imaging allow for the evaluation of one key component of the intervertebral discs (IVD): The glycosaminoglycans (GAG).

GAGs are attached to aggrecan, which is a large proteoglycan molecule [3, 4]. GAG is important for the interstitial pressure of intervertebral discs, which are composed of the nucleus pulposus (NP) and annulus fibrosus (AF). The two compartments differ in their biochemical content: The nucleus pulposus contains more aggrecan than the annulus fibrosus, leading to a higher glycosaminoglycan content in this structure [3, 5, 6]. A decrease of glycosaminoglycan content with IVD degeneration, hydration deficit and reduced disc height has been reported previously [3, 7, 8].

Among the GAG-sensitive MR imaging techniques, such as dGEMRIC and sodium imaging, one method is chemical exchange saturation transfer (CEST) imaging, which is a new biochemical contrast mechanism that exploits the exchange of solute protons with water. Previous studies have shown the feasibility of gagCEST imaging in the human lumbar intervertebral disc of volunteers and patients with lower back pain [1, 3].

In the current report we demonstrate examples of gagCEST imaging in four cases of volunteers with different conditions of the intervertebral discs, i.e. healthy, disc bulging or herniation, and disc degeneration.

Materials and methods

Study population

Four volunteers with different physiological and pathological conditions were enrolled in this gagCEST MRI study. The study was approved by the local ethics committee and was therefore conducted in accordance with the ethical standards laid down in the 1964 Declaration of Helsinki and its later amendments. Details on age, gender and physical conditions of the volunteers are listed in table 1.

Data acquisition

MR imaging was performed on a clinical whole-body 3T MRI system (MAGNETOM Trio, A Tim System, Siemens Healthcare, Erlangen, Germany) using the spine matrix coil for signal reception. After a localizer, T2-weighted imaging was acquired for conventional radiologic assessment of the disc condition. To estimate the glycosaminoglycan content, gagCEST (glycosaminoglycan chemical exchange saturation transfer) and WASSR (water saturation shift referencing [9]) datasets were acquired using prototype sequences*. Both acquisitions consisted of a CEST pre-saturation module followed by a 2D RF-spoiled gradient echo sequence.

Parameters of the CEST and WASSR protocols are summarized in table 2. In table 3 the parameters of the T2-weighted sequence are listed.

During the CEST and WASSR acquisitions, a saturation band was applied in order to supress the abdominal wall and corresponding artefacts based on bowel movement.

Statistical significance was evaluated using a two-sided student's t-test.

Data analysis

Pfirrmann scoring and evaluation of disc bulging and herniation was performed by a radiologist with three years' experience in musculoskeletal radiology.

Motion correction was applied to the gagCEST and WASSR data using the prototype software fMRLung* (Siemens Healthcare, Erlangen, Germany) [10, 11].

The evaluation of the gagCEST effect was measured by an in-house developed MATLAB software (The Mathworks, Inc., Natick, MA, USA, R2012b). To reduce image noise a 3 x 3 Gaussian filter was applied to each CEST and WASSR image. Based on the WASSR

*WIP, the product is currently under development and is not for sale in the US and other countries. Its future availability cannot be ensured.

Table 1

Volunteer	Age	Gender	Example of	Physiological or pathological condition				
				L1/L2	L2/L3	L3/L4	L4/L5	L5/S1
1	21	f	Healthy volunteer	1a	1a	1a	1a	1a
2	30	f	Bulging (L5/S1)	2a	2a	2a	2a	3b
3	29	m	Herniation (L5/S1)	2a	1a	1a	1a	5c
4	30	m	Decreased Pfirrmann score (L5/S1)	2b	2b	2b	2b	4a

Overview of the described volunteers and their physical condition. Four volunteers are presented: A healthy volunteer without degrading and any disc disease (volunteer 1), a volunteer with bulging (volunteer 2), a volunteer with herniation (volunteer 3) and a volunteer with decreased Pfirrmann socre in one disc (volunteer 4). The physical condition is denoted as follows: The Pfirrmann scores are presented as numbers. In addition, (a) corresponds to a disc without protrusion or any herniation, (b) to a disc with bulging, and (c) to a disc with herniation.

Table 2

Segmented GRE sequence			
		CEST	WASSR
TE/TR	ms/ms	3.01/1590	3.01/590
Shot-TR	ms	480	480
Resolution	mm^3	1.6 x 1.6 x 5	1.6 x 1.6 x 5
Flip angle	°	12	12
FOV	mm^2	300	300
Duration	min:sec	12:24	7:26
Number of segments		64	64
Signal averages		6	6

Presaturation Module			
		CEST	WASSR
Number of Gaussian pulses		6	1
Pulse duration	ms	100	100
Interpulse duration	ms	100	6
B_1-CWAE	µT	1.5	0.3
Frequency range	ppm	-4 to 4	-1 to 1
Frequency interval	ppm	$0.\overline{3}$	0.05

Sequence parameters of the prototype CEST and WASSR sequences.

Table 3

T2-weighted sequence		
TE/TR	ms/ms	105/3100
Resolution	mm^3	1.2 x 1.2 x 3
Flip angle	°	160
FOV	mm^2	300
Duration	min:sec	3:39
Signal averages		2

Sequence parameters of the T2-weighted sequence.

images an offset map was calculated using the WASSR maximum symmetry algorithm introduced by Kim et al. [9]. The CEST-curves were normalized to the signal from an acquisition without pre-saturation (S0) thus leading to the Z-spectrum. The offset map was used to correct the Z-spectrum on a pixel-basis, thus leading to a minimization of the influence of B_0 field inhomogeneities. The signal intensity of the corrected Z-spectrum, i.e. Z(Δω), was denoted as a function of the pre-saturation frequency offset Δω with respect to the bulk water resonance frequency in parts per million (ppm). To enable an assessment of the CEST effect an asymmetry analysis was performed leading to the asymmetric magnetization transfer ratio

$$MTR_{asym}(\Delta\omega) = Z(-\Delta\omega)-Z(\Delta\omega).$$

MTR_{asym} maps were generated based on the average MTR_{asym} value between 1.0 ppm and 1.5 ppm. This frequency range reflected the resonance frequencies of glycosaminoglycan hydroxyl protons.

Postprocessing steps for calculation of the MTR_{asym} map are displayed in Figure 1.

In the nucleus pulposus and annulus fibrosus a region-of-interest (ROI) based analysis was performed for the evaluation of gagCEST effects following the method of Haneder et al. [3]. After calculation of the mean value and standard deviation of each ROI, the results for each intervertebral disc were compared intra-subjectively and related to the physical condition.

The mean gagCEST effect in nucleus pulposus and annulus fibrosus over all discs and all volunteers were calculated.

Results

Volunteer 1 (the healthy volunteer) had no degradation (Pfirrmann score = 1 for all examined IVDs) and no disc bulging, disc herniation or intraspongious disc herniation. Volunteer 1 showed an average MTR_{asym} value of 4.90 ± 1.37% (range: 3.67% ± 0.41% to 6.65% ± 0.45%) in NP, whereas a lower value of 3.36% ± 1.24% (range: 1.70% ± 1.40% to 4.57% ± 1.53%) was obtained in AF.

Volunteer 2 suffered from bulging with Pfirrmann score 2 on the level L5/S1. The lowest NP-MTR_{asym} value was found on this disc location (MTR_{asym} = 2.43% ± 0.64%). The NP-MTR_{asym} values of the other lumbar discs ranged from 3.09% ± 0.74% to 3.91% ± 0.81%. In all but the disc with bulging, the gagCEST effect was lower in AF compared to NP.

Volunteer 3 had a disc herniation on the level L5/S1 with a Pfirrmann score of 5. The other lumbar discs do not have a disc herniation or protrusion and had Pfirrmann scores 1 or 2. In the nucleus pulposus the lowest gag effect was observed on level L5/S1 (L5/S1: MTR_{asym} = 1.92% ± 0.80%). The NP-MTR_{asym} values of the remaining discs ranged from 3.28% ± 1.18% to 6.72% ± 1.16%. For all but the herniation disc, the MTR_{asym} value in the AF was lower compared to the NP.

Volunteer 4 had a Pfirrmann score of 4 on the level L5/S1 and 2 in the remaining lumbar discs (Fig. 2). The L5/S1 disc did not have bulging or herniation. Bulging was recognized in the lumbar discs L1/L2, L2/L3, L3/L4 and L4/L5. A lower MTR_{asym} value was noted in the L5/S1 disc (NP: MTR_{asym} = -1.14% ± 0.59%) compared to the other discs, where the lowest NP-MTR_{asym} value was 1.85% ± 1.21% and the highest NP-MTR_{asym} value was 4.24% ± 1.28%. For all but the disc with Pfirrmann score 4, lower MTR_{asym} values were noted in the AF compared to the NP.

The results for all volunteers are depicted in Figure 2.

1

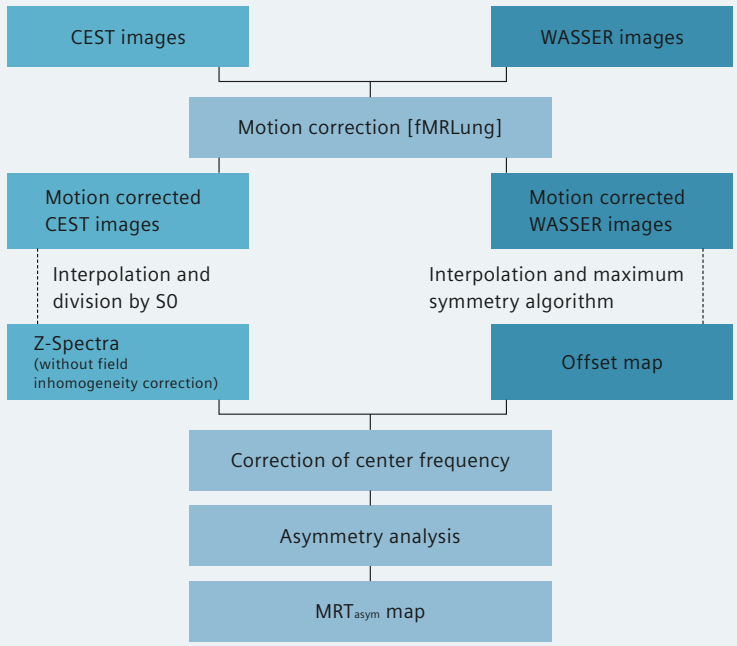

1 Postprocessing steps of CEST and WASSR images.

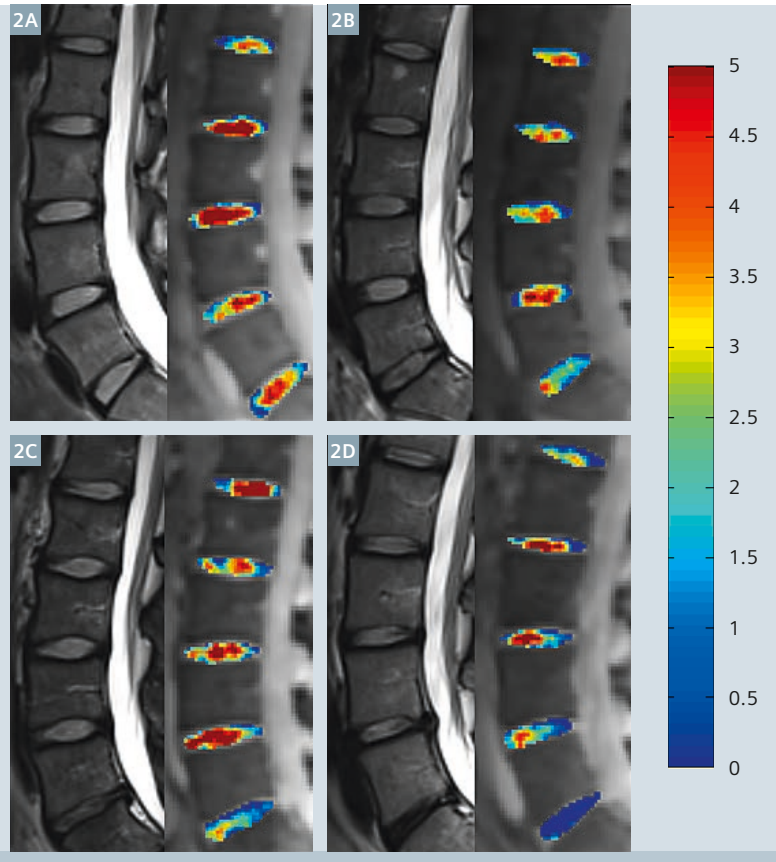

2 T2-weighted images and gagCEST images. The color coding in the discs shows the MTR_{asym} value in percent. Four different volunteers are displayed: **(2A)** A healthy volunteer, **(2B)** a volunteer with bulging (L5/S1), **(2C)** a volunteer with herniation (L5/S1), and **(2D)** a volunteer with a decreased Pfirrmann score (L5/S1).

Significantly higher glycosaminoglycan content was recognized in NP compared to AF (Fig. 3).

Discussion

This study showed a negative relation between conditions like degeneration or disc herniation and the gagCEST effect. The healthy volunteer showed MTR_{asym} values above 3.67% ± 0.41% in the nucleus pulposus, whereas all other volunteers showed lower values in the affected discs.

Decreased gagCEST values with degeneration according to the Pfirrmann score was previously reported by Haneder et al. in patients with back pain [3]. In the cases reported in this article disc degeneration is associated with a decreased CEST effect. In contrast to the study of Haneder et al. we suppressed bowel motion artefacts and increased the number of signal averages to improve the signal-to-noise ratio. However, future studies including more volunteers have to be performed to evaluate the influence of CEST acquisition parameters on the evaluated gagCEST effects and further validate our approach.

A relationship between gagCEST effects and proteoglycan content was previously reported by Saar et al. [6], who compared the CEST effect with sodium images and T2-mapping in porcine discs [6] and reported a positive correlation between T2 imaging, the sodium concentration and the CEST effect. Sodium imaging was not performed in our study due to hardware limitations.

Recently, Melkus et al. showed that the gagCEST effect also depends on pH value [12]. *In vivo*, the pH value in the human lumbar discs might be assessed using the contrast medium Iopamidol, which was previously applied in the human bladder to asses pH value [13]. Future studies are necessary to correlate pH and gagCEST effect *in vivo*.

Conclusion

gagCEST imaging is a promising tool which enables non-invasive measurement of glycosaminoglycans *in vivo*. A decreased gagCEST effect was observed to correlate with degeneration of IVDs and disc herniation. The measured gagCEST content was higher in the nucleus pulposus compared to the annulus fibrosus, which is in line with the physiologic biochemical constitution of human intervertebral discs.

3

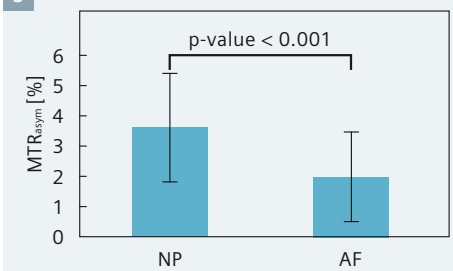

3 MTR_{asym} values in NP and AF. Significantly higher values were obtained in NP compared to AF.

References

1 Kim M, Chan Q, Anthony M-P, Cheung KMC, Samartzis D, Khong P-L. Assessment of glycosaminoglycan distribution in human lumbar intervertebral discs using chemical exchange saturation transfer at 3 T: feasibility and initial experience. NMR Biomed 2011;24:1137–44.

2 Hart LG, Deyo RA, Cherkin DC. Physician office visits for low back pain. Frequency, clinical evaluation, and treatment patterns from a U.S. national survey. Spine 1995;20:11–9.

3 Haneder S, Apprich SR, Schmitt B, Michaely HJ, Schoenberg SO, Friedrich KM, et al. Assessment of glycosaminoglycan content in intervertebral discs using chemical exchange saturation transfer at 3.0 Tesla: preliminary results in patients with low-back pain. Eur Radiol 2013;23:861–8.

4 Urban JPG, Winlove CP. Pathophysiology of the intervertebral disc and the challenges for MRI. J Magn Reson Imaging JMRI 2007;25:419–32.

5 Eyre DR, Muir H. Quantitative analysis of types I and II collagens in human intervertebral discs at various ages. Biochim Biophys Acta 1977;492:29–42.

6 Saar G, Zhang B, Ling W, Regatte RR, Navon G, Jerschow A. Assessment of glycosaminoglycan concentration changes in the intervertebral disc via chemical exchange saturation transfer. NMR Biomed 2012;25:255–61.

7 Urban JP, McMullin JF. Swelling pressure of the inervertebral disc: influence of proteoglycan and collagen contents. Biorheology 1985;22:145–57.

8 Miese F, Buchbender C, Scherer A, Wittsack H-J, Specker C, Schneider M, et al. Molecular imaging of cartilage damage of finger joints in early rheumatoid arthritis with delayed gadolinium-enhanced magnetic resonance imaging. Arthritis Rheum 2012;64:394–9.

9 Kim M, Gillen J, Landman BA, Zhou J, van Zijl PCM. Water saturation shift referencing (WASSR) for chemical exchange saturation transfer (CEST) experiments. Magn Reson Med 2009;61:1441–50.

10 Hermosillo G, Chefd'hotel C, Faugeras O. Variational Methods for Multimodal Image Matching. Int J Comput Vis 2002;50:329–43.

11 Chefd'Hotel C, Hermosillo G, Faugeras O. A Variational Approach to Multi-Modal Image Matching. Proc. IEEE Workshop Var. Level Set Methods VLSM01, Washington, DC, USA: IEEE Computer Society; 2001, p. 21f.

12 Melkus G, Grabau M, Karampinos DC, Majumdar S. Ex vivo porcine model to measure pH dependence of chemical exchange saturation transfer effect of glycosaminoglycan in the intervertebral disc. Magn Reson Med 2013.

13 Müller-Lutz A, Khalil N, Schmitt B, Jellus V, Pentang G, Oeltzschner G, et al. Pilot study of Iopamidol-based quantitative pH imaging on a clinical 3T MR scanner. Magma N Y N 2014.

Contact

Anja Müller-Lutz, Ph.D.
University of Dusseldorf
Department of Diagnostic and Interventional Radiology
Moorenstr. 5
D-40225 Düsseldorf
Germany
Phone: +49 (0) 211 - 81 17430
Fax: +49 (0) 211 – 81 16299
Anja.Lutz@med.uni-duesseldorf.de

Pictorial Essay
'White Dots' on Cranial MRI: MS and Differential Diagnosis

Iris N. Kaschka, M.D.; Tobias Engelhorn, M.D.; Arnd Doerfler, M.D

Department of Neuroradiology, University Hospital Erlangen, Germany

Introduction

Demyelinating disorders of the central nervous system (CNS) have a variety of aetiologies and can be separated into primary (e.g. multiple sclerosis) and secondary (e.g. infectious, ischemic, metabolic or toxic) diseases. Providing high spatial and contrast resolution, cranial MRI is the imaging modality of choice to assess demyelinating disorders [1].

Multiple sclerosis is the most common primary demyelinating disease of the CNS. However, differentiation from other demyelinating disorders might be challenging since clinical findings can be subtle and imaging is not always specific [2, 3]. Hence, precise assessment of lesion localization and morphology (over time) as well as clinical and laboratory results are essential for the correct diagnosis [1].

This pictorial essay is intended as an overview of the spectrum of demyelinating disorders and their typical and atypical imaging findings.

Multiple Sclerosis (MS)

MS is a chronic, immune-mediated demyelinating degenerative disease of the CNS and the leading cause of non-traumatic neurological disability in young and middle aged adults. Dissemination of disease in space and time proved by either clinical, paraclinical or laboratory assessments is an essential diagnostic criterion for MS [1, 4]. Differential diagnosis for the clinical presentation must be considered and excluded before MS can be diagnosed [2, 5]. Cranial MRI shows lesions in at least 95% of MS patients and plays a key role in diagnosis and follow-up. The 2010 revision of the McDonald Criteria defining dissemination in time (DIT) and space (DIS) has simplified the diagnostic criteria of MS and resulted in earlier and more reliable diagnosis [6]. As a consequence, therapy can be started earlier resulting in patients' improved quality of life.

McDonald criteria 2010

DIS:
≥ 1 T2 lesion in at least 2 of 4 areas of the CNS

- Periventricular
- Juxtacortical
- Posterior fossa
- Spinal cord

DIT:

1. A new T2 and/or gadolinium-enhancing lesion on follow-up MRI, with reference to a baseline scan, irrespective of the timing of the baseline MRI.
2. Simultaneous presence of asymptomatic gadolinium enhancing and non-enhancing lesions at any time.

Typical imaging findings of MS

The demyelinating lesions in MS are typically multiple, well-defined and ovoid, preferentially involving the corpus callosum (up to 93%), periventricular white matter, subcortical regions (including U-fibres), optic nerves (50%) and visual pathways, the posterior fossa (68% brain stem, up to 49% cerebellar lesions) and cervical spinal cord (56%) [1, 7, 8] (Fig. 1).

Typical signs of MS are (Fig. 2):

- 'Finger prints': Typical morphology of lesions of the corpus callosum in MS patients at the undersurface of the corpus callosum.
- 'Dawson's fingers': Ovoid lesions radially oriented perpendicular to the lateral ventricles, which represent the perivascular pattern of inflammation along the medullary veins.
- 'Open ring' sign: Lesions with an open ring enhancement, which are highly specific for demyelinating processes and may help in differentiating atypical demyelination from neoplasm or abscess.

Continued on page 35.

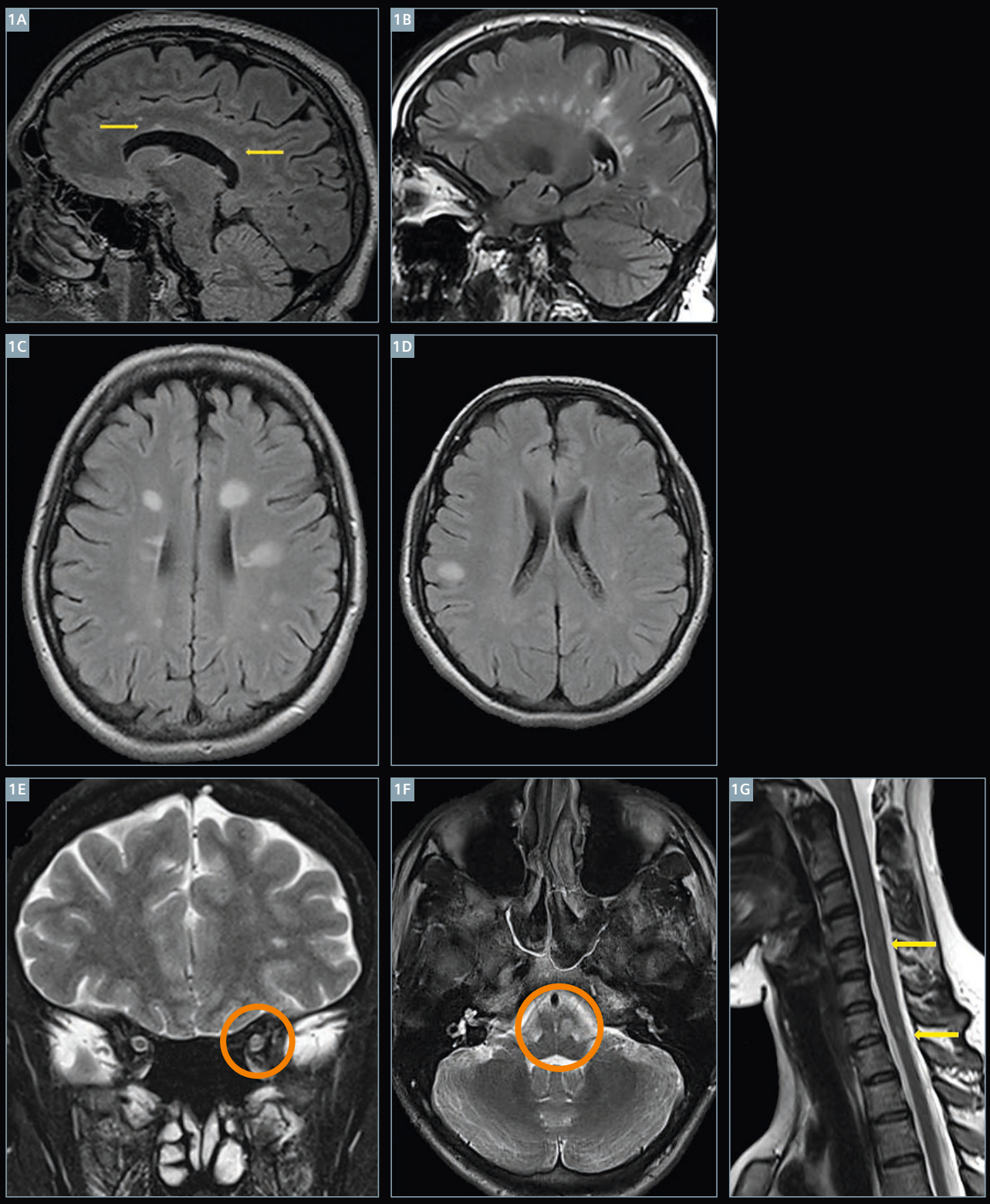

1 Typical locations of MS plaques.
(1A) Involvement of the corpus callosum; **(1B)** Lesions at the callososeptal interface; **(1C)** Ovoid, well-defined lesions in the periventricular and **(1D)** subcortical white matter; **(1E)** Affection of the optic nerve; **(1F)** Lesion in the brain stem; **(1G)** Small plaques in the cervical spinal cord.

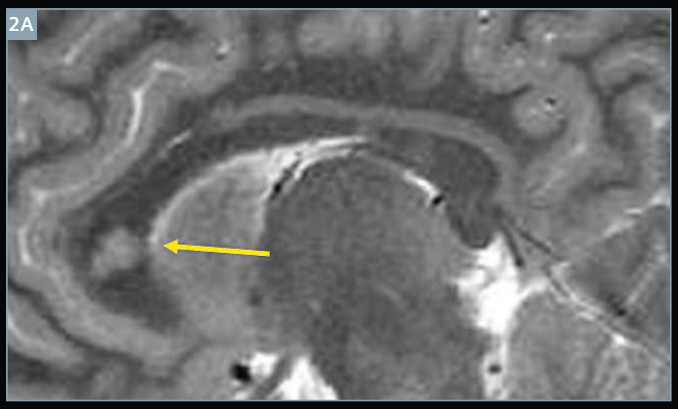

2 Typical imaging signs of MS.
(2A) Finger prints at the undersurface of the corpus callosum; **(2B)** Dawson-fingers reflecting the perivenular inflammation; **(2C)** Open ring sign of enhancing lesions.

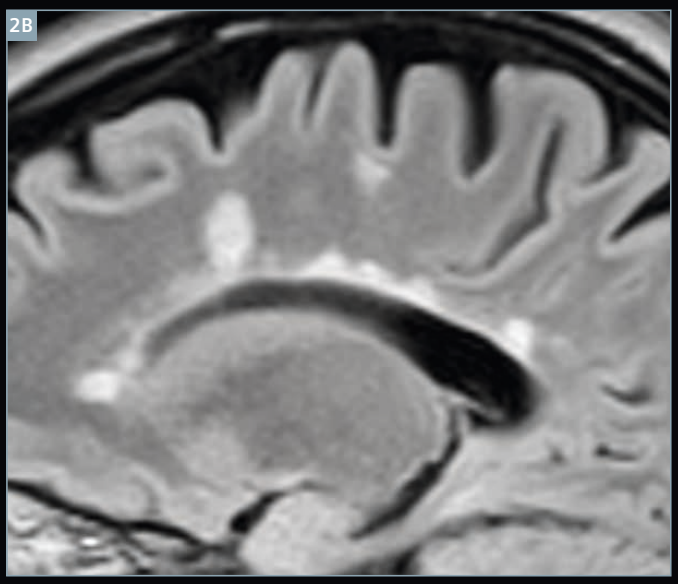

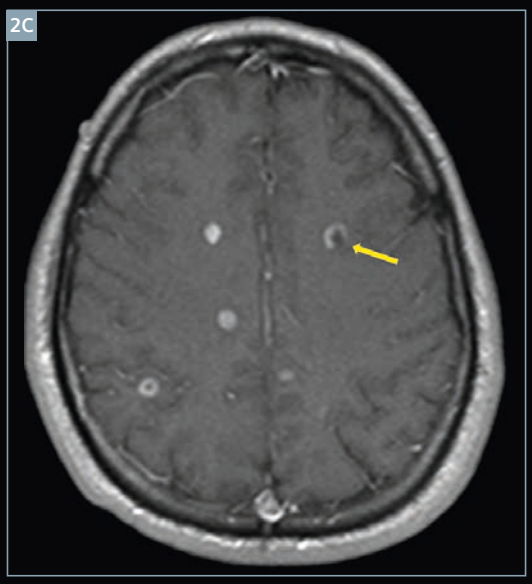

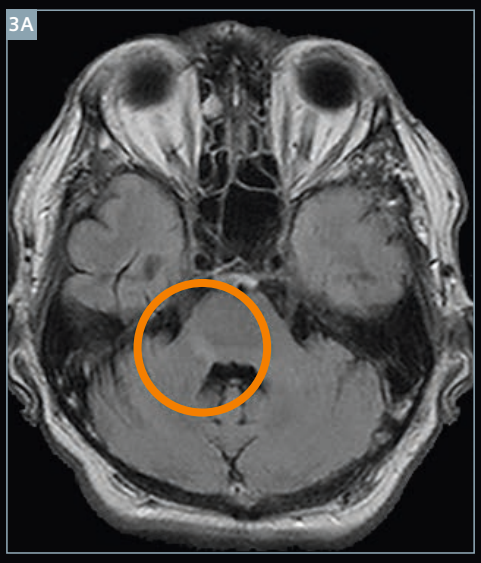

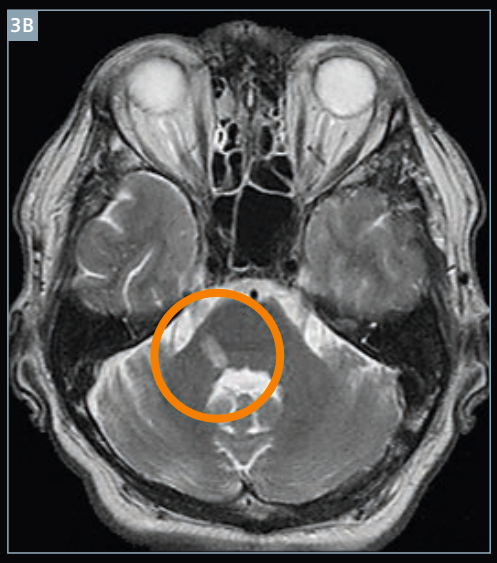

3 Assessment of lesion load in the posterior fossa.
(3A) FLAIR versus **(3B)** T2-weighted images.

Imaging appearance

MS plaques show high signal intensity on T2w and low signal intensity on T1w reflecting the loss of myelin and increase in water content. FLAIR is the preferred sequence for assessing lesions of the corpus callosum, often the first area involved. Suppression of the cerebrospinal fluid (CSF) signal makes periventricular lesions at the callososeptal interface more conspicuous [1]. For the assessment of lesions in the posterior fossa, however, T2w is superior to FLAIR [7] (Fig. 3). Active plaques with high cellular lymphocytic infiltrate may show reduced diffusivity in diffusion-weighted imaging (DWI) with corresponding low signal on apparent diffusion coefficient (ADC) maps [1]. Inactive lesions are hypocellular with increased ADC. Acute lesions may also show a halo of less striking hyperintensity, presumably as a result of transient edema [8] (Fig. 4). 5–10% of lesions also involve grey matter and are difficult to detect with conventional MRI [8]. Double inversion recovery sequences might be helpful to better assess cortical lesions. Some T1w hypointensities disappear as the edema resolves and remyelination occurs, while some remain and develop into ' black holes', reflecting more aggressive tissue destruction and axonal loss (Fig. 5). Active lesions may show contrast enhancement due to inflammation-related blood-brain barrier breakdown [1]. Enhancement patterns may be solid, ring or arc like and persist for 4–6 weeks. Open ring enhancement is highly specific for demyelinating lesions [9]. Corticosteroids obturate the blood-brain barrier so that enhancement stops 48 hours after therapy starts. Similar to brain metastases, the use of double dose contrast media and an increased time delay between contrast application and scanning both improve the detection rate of enhancing lesions.

Spinal cord plaques occur in 83% of MS patients and can help to narrow differential diagnosis where there is uncertainty. The preferential location is the peripheral cervical and also thoracic cord. Acute plaques cause cord swelling and may show contrast enhancement. Cord atrophy may be seen in advanced MS, probably reflecting axonal loss.

Red flags

Red flags are clinical, laboratory or imaging findings that should alert clinicians to consider alternative diagnoses [10].

Major imaging red flags include:

- Cortical infarctions *(consider embolic disease, vasculitis)*
- Lacunar infarctions *(consider hypertensive ischemic disease, CADASIL, Susac's syndrome)*
- Haemorrhages/microhaemorrhages *(consider amyloid angiopathy, CADASIL, vasculitis)*
- Mainly (sub)cortical location *(consider age-related change, small vessel disease, vasculitis, progressive multifocal leukoencephalopathy)*
- Symmetrical lesions *(consider leukodystrophy)*
- T2 hyperintensities of the temporal pole and external capsule/insula *(consider CADASIL)*
- Large lesions *(consider glioblastoma, lymphoma, progressive multifocal leukencephalopathy)*
- Central brainstem lesions *(consider central pontine myelinolysis, hypoxic-ischemic conditions, infarct)*
- Meningeal enhancement *(consider chronic meningitis, sarcoidosis, CNS vasculitis)*
- Persistent gadolinium enhancement (> 6 weeks) and continued lesion enlargement *(consider lymphoma, glioma, vasculitis, sarcoidosis)*
- Complete ring enhancement *(consider brain abscess, glioblastoma, brain metastasis)*
- Simultaneous enhancement of all lesions *(consider acute disseminated encephalomyelitis (ADEM), vasculitis, lymphoma, sarcoidosis)*

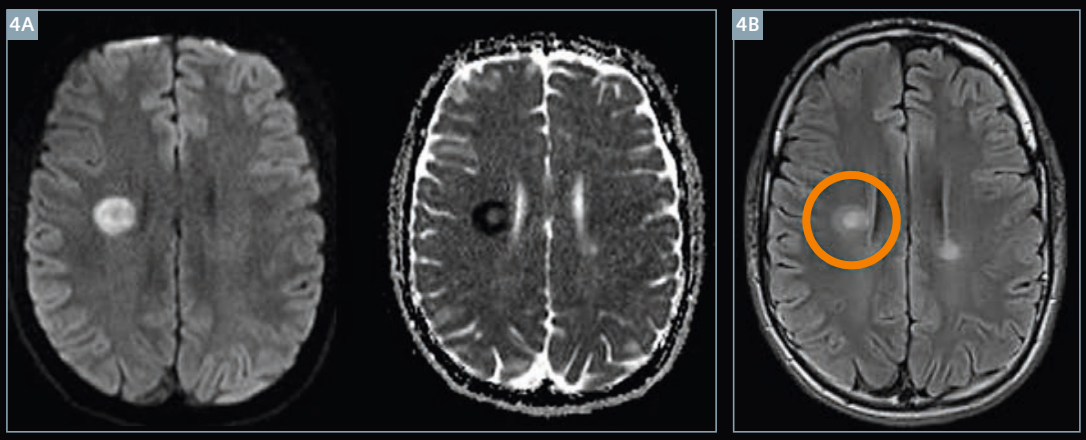

4 Active lesion in the right periventricular white matter with **(4A)** decreased diffusivity on ADC map and **(4B)** a halo of less striking hyperintensitiy on axial FLAIR.

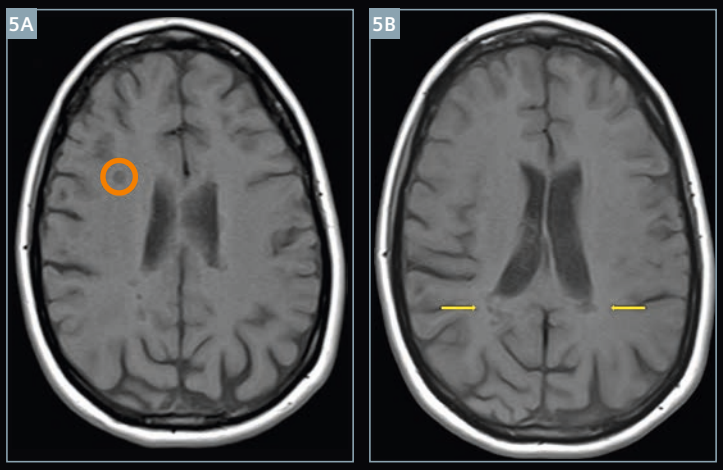

5 'Black holes' as a sign of advanced tissue destruction. **(5A)** 'Black hole' in the white matter of the right frontal lobe **(5B)** 'Black holes' at the occipital horns of the lateral ventricles.

Tumefactive demyelinating lesions (TDLs)

TDLs are solitary lesions, which may simulate neoplasms or abscesses. Clues to the diagnosis include less mass effect than expected for their size, an arc-like incomplete ring enhancement, no increased perfusion and visualisation of veins coursing through the lesion – all untypical of tumor or abscess [9, 11]. On the contrary, abscesses and highly cellular tumors like CNS lymphomas show restricted diffusivity with low ADC values.

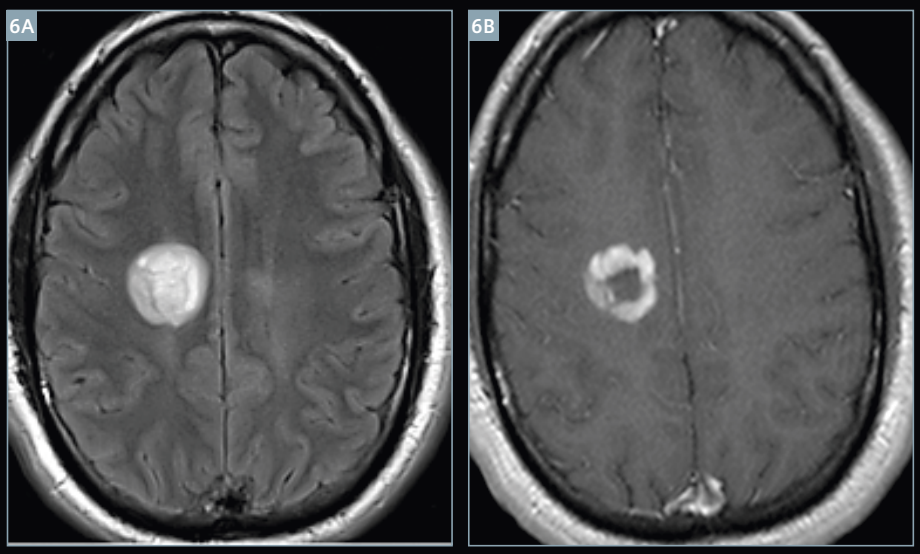

6 37-year-old woman presenting with a progressive left-side hemiparesis. **(6A)** Large hyperintense lesion in the deep white matter of the right praecentral area with only a little mass effect and **(6B)** ring enhancement.

Radiologically isolated syndrome (RIS)

This syndrome refers to incidentally identified cerebral lesions on MRI meeting the characteristic imaging criteria of MS in subjects without any clinical symptoms. Up to half of the patients, however, develop neurological symptoms on follow-up, around two-thirds show radiological progression within 5 years. Clinical conversion is more likely in patients with a high number of MRI lesions (> 9), gadolinium enhancing lesions, and especially the presence of asymptomatic cervical cord lesions. Some clinicians advocate a 'wait and see' strategy, while others propose MRI and clinical follow-up examinations. However, treatment with disease-modifying drugs is not advisable at this stage [12, 13].

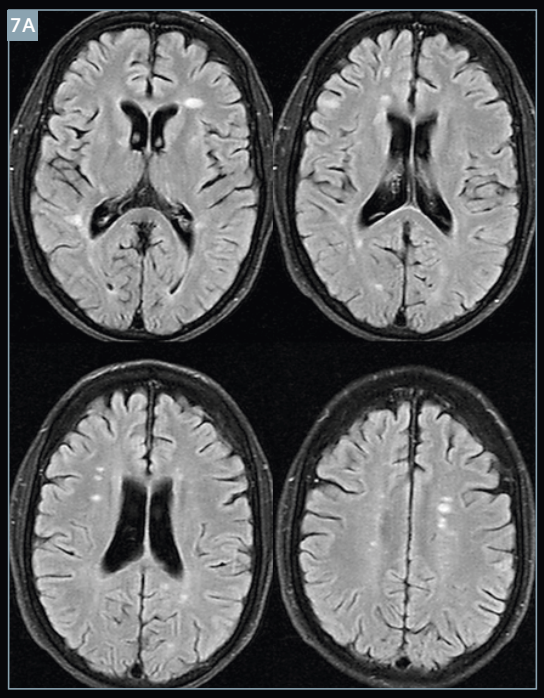

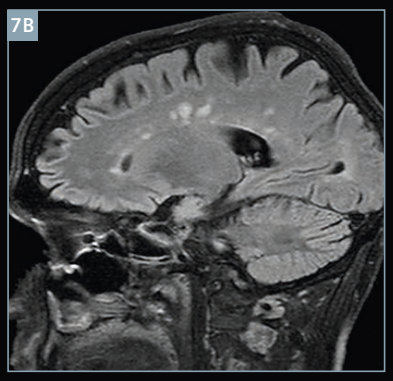

7 31-year-old man with incidentally recognized MS-like lesions on cranial MRI. He had no clinical history and there were no abnormal findings on examination. **(7A)** Small, ovoid hyperintensities especially in the periventricular white matter **(7B)** Radially oriented lesions perpendicular to the lateral ventricles on sagittal FLAIR.

Neuromyelitis optica (NMO)

NMO or Devic disease is an autoimmune, inflammatory demyelinating disorder of the CNS with predominant affection of the optic nerve (optic neuritis) and spinal cord [14, 15]. Cord lesions on MRI are usually extensive (involving at least 3 vertebral segments) and centrally located, with or without enhancement. Optic nerve lesions may be uni- or bilateral with high T2 signal of the swollen optic nerve segment [16]. Although brain lesions do not normally show the MS-typical configuration, lesions are indistinguishable from MS in 10% of cases [17].

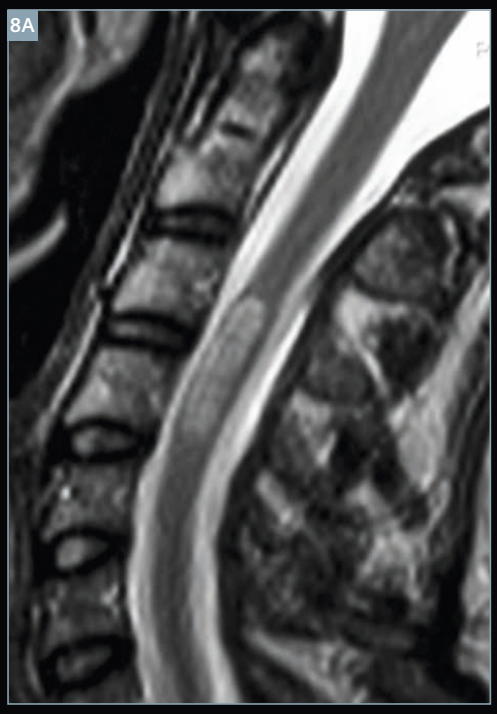

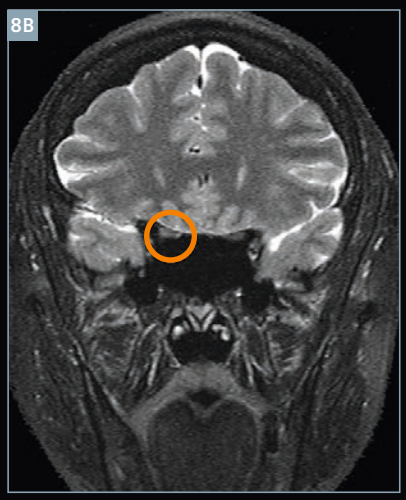

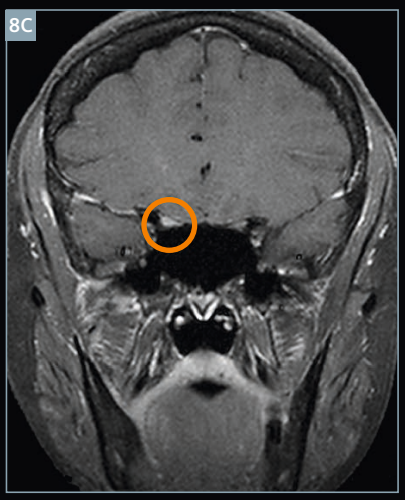

8 MRI findings in a middle-aged woman with anti-AQP-4 antibodies, lymphocystosis in the cerebrospinal fluid and symptoms of optic neuritis and acute myelitis. **(8A)** T2w sagittal with an extensive, centrally located area of high T2 signal within the cervical cord associated with cord swelling. **(8B)** High T2 signal of the right optic nerve in the intracranial part **(8C)** with corresponding contrast enhancement on T1w imaging.

Acute disseminated encephalomyelitis (ADEM)

Caused by an allergic or autoimmune cross-reaction with viral protein, this inflammatory, mostly monophasic demyelinating disease of the CNS usually appears days to several weeks after viral infection or immunisation with clinical symptoms of severe encephalopathy, fever, variable focal deficits and drowsiness. ADEM causes a diffuse perivenous inflammatory process with multiple poorly marginated confluent lesions, typically larger and without dissemination in time than those of MS (often > 1.5-2 cm) [16]. The subcortical and deep white matter is more often affected than periventricular regions, lesions are not oriented perpendicular to the lateral ventricles, and one third of cases show additional cord lesions [14]. The lesions usually resolve completely in up to 75% of the cases.

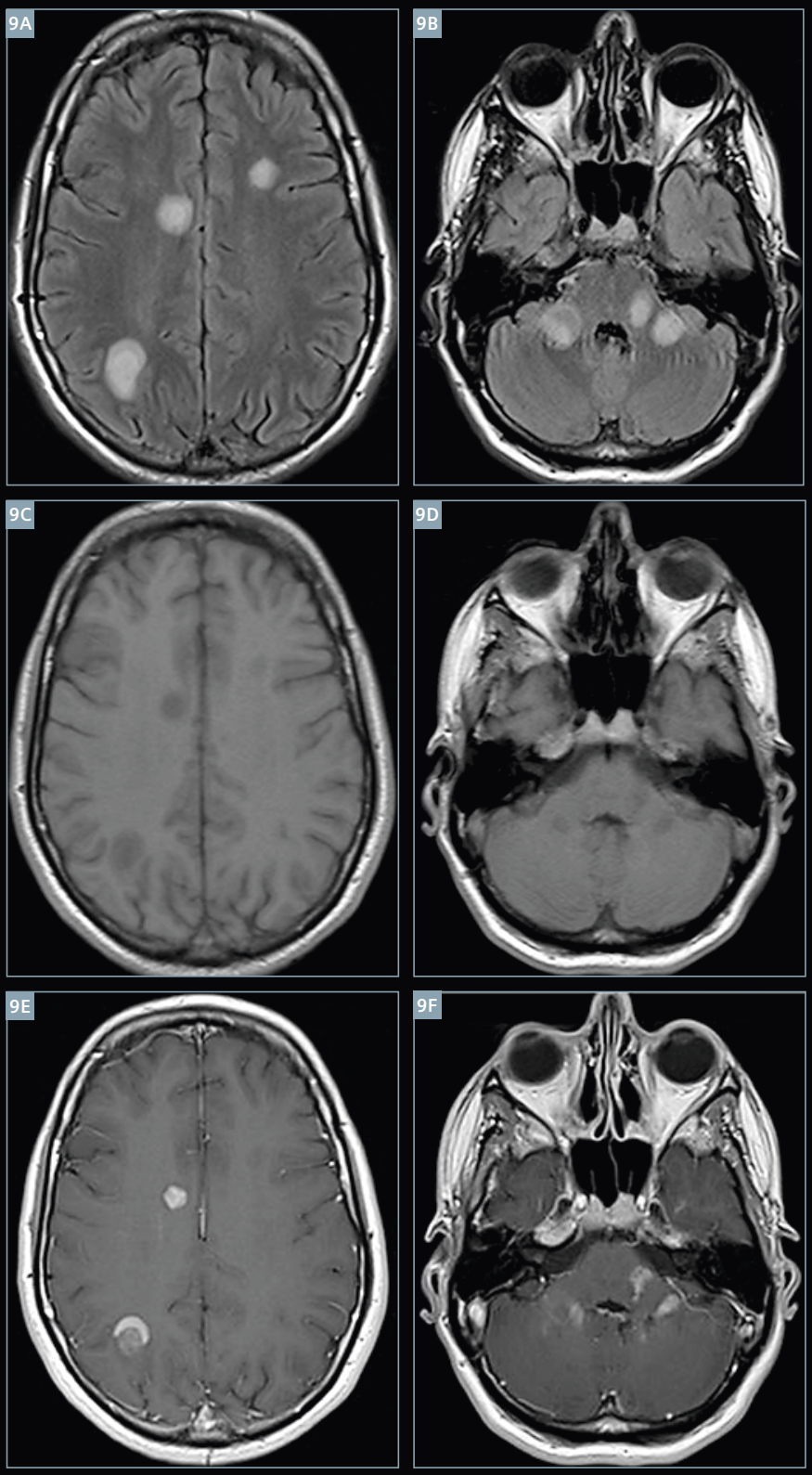

9 Acute demyelinating encephalomyelitis (ADEM) in a young woman. MR images show multiple, supra- and infratentorial, bilateral, poorly defined, large T2 hyperintense **(9A, B)**, T1 hypointense **(9C, D)** and contrast enhancing **(9E, F)** lesions. Few weeks before, the patient had a pulmonary infection.

Neuroborreliosis (Lyme disease)

Lyme disease is a multisystem inflammatory disorder caused by an infection with Borrelia burgdorferi. Patients usually present with severe headache and influenza-like illness. MRI shows hyperintense small periventricular white matter lesions (resulting from demyelination), which can mimic MS. Lesions may enhance or show decreased diffusivity. Also enhancement of the facial nerve, cauda equina and meninges can be found [14].

In addition, there are some other rare infections that might resemble MS, such as Whipple's disease, neurosyphilis, HIV encephalitis, Creutzfeldt-Jakob disease, brucellosis or HHV-6 infection [18].

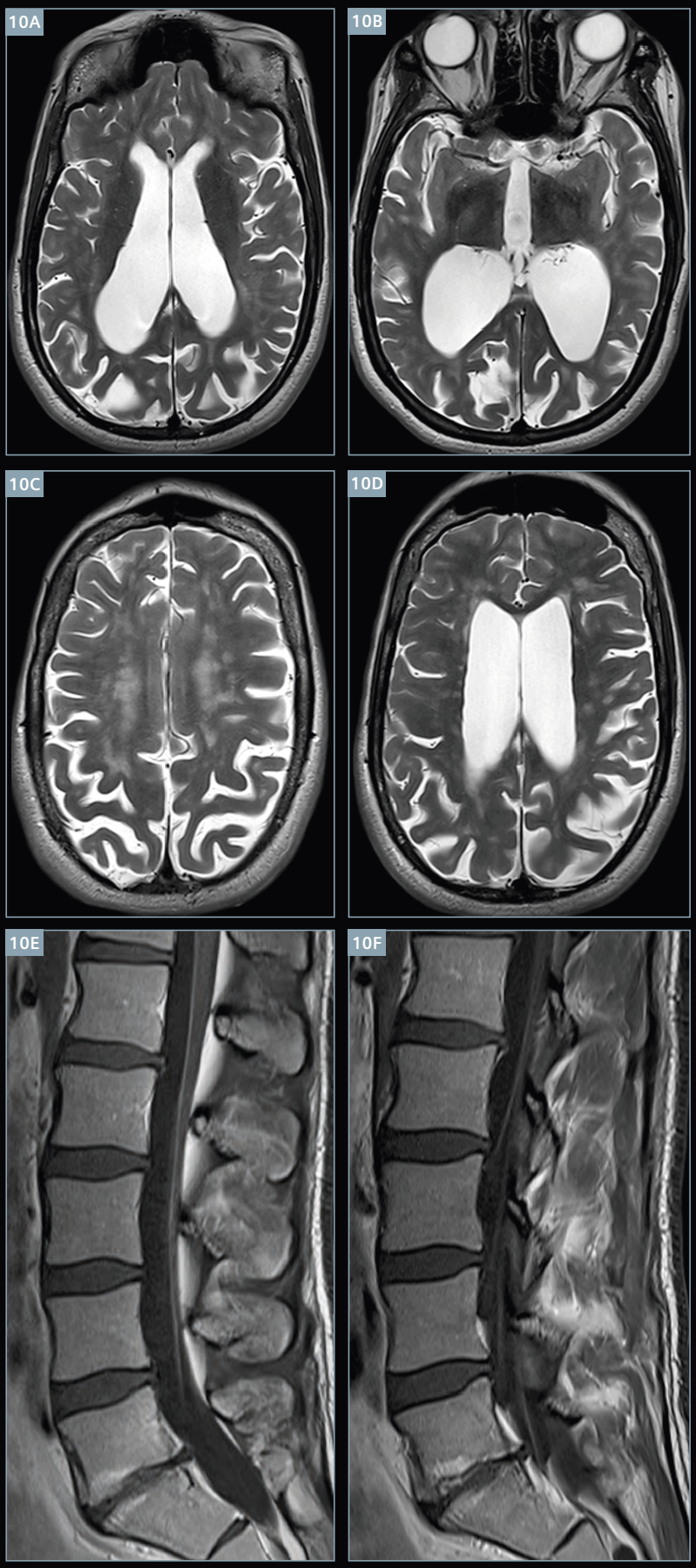

10 Lyme disease in a patient with hydrocephalus **(10A, B)** and foci of high T2 signal in the periventricular white matter, similar to MS plaques **(10C, D)**. Spinal MRI with T1w sagittal **(10E, F)** sequences show contrast enhancement of the pial surface of the conus medullaris and the cauda equina. CSF protein was elevated and Borrelia titres were high.

Neurosarcoidosis

Sarcoidosis is a multisystem granulomatous disease of unknown aetiology most frequently affecting the lungs. In 3-5% of patients with sarcoidosis the CNS is involved. Optic neuritis, acute transverse myelitis or brainstem syndromes may be present. Basal meningitis, hypothalamic involvement, hydrocephalus and manifestations around the pituitary fossa, however, are more common signs of Neurosarcoidosis, which help to differentiate between neurosarcoidosis and MS [14].

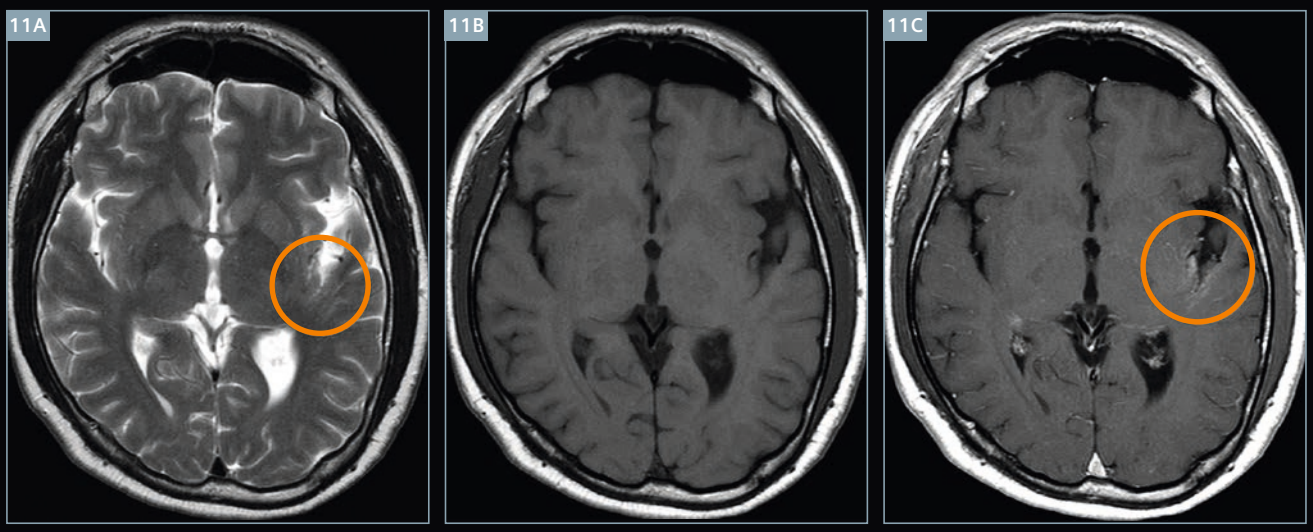

11 MRI findings in a patient with neurosarcoidosis. **(11A)** T2w axial MRI shows slight unilateral basal perisylvian parenchymal hyperintensities with contrast enhancement on T1w **(11B, C)**.

Susac's Syndrome

Susac's syndrome is characterized by the clinical triad of multifocal encephalopathy, branch retinal artery occlusion and hearing loss. Histopathologically, Susac's syndrome is based on a microangiopathy of the brain, retina and cochlea, suggested to be caused by an immune-mediated damage of the endothelial cells. MRI shows multiple small white matter lesions (corresponding to microinfarctions) preferentially involving the centre of the corpus callosum. These 'snowball' lesions are pathognomonic for Susac's syndrome. Microinfarctions may also extensively involve the internal capsule, basal ganglia and thalami in 70% of cases and additional leptomeningeal enhancement is seen in about 30% of cases [19].

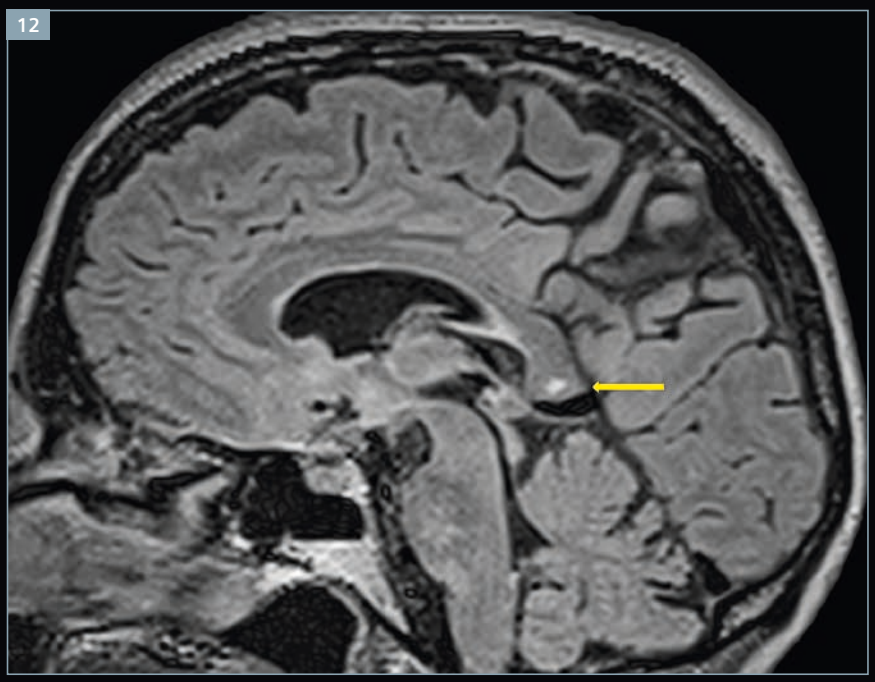

12 Susac's syndrome in a young woman who presented with encephalopathy and hearing problems. There is a circumscribed focus of high T2 signal in the centre of the splenium of the corpus callosum on saggital FLAIR imaging ('snowball' lesion).

Cerebral autosomal-dominant arteriopathy with subcortical infarctions (CADASIL)

CADASIL is a hereditary small-vessel disease of the brain associated with a mutation of a NOTCH 3 gene. Patients develop recurrent stroke-like episodes, migraine-like headaches and subcortical dementia [20]. Cranial MRI shows diffuse ischemic-derived T2 hyperintensities in deep white matter. Involvement of the anterior temporal lobes and external capsule are pathognomonic for CADASIL [21]. Common changes also include lacunar infarctions in the pons, internal capsule, thalami and basal ganglia, involvement of the U-fibres and multiple scattered microhaemorrhages. The corpus callosum and posterior fossa are rarely affected.

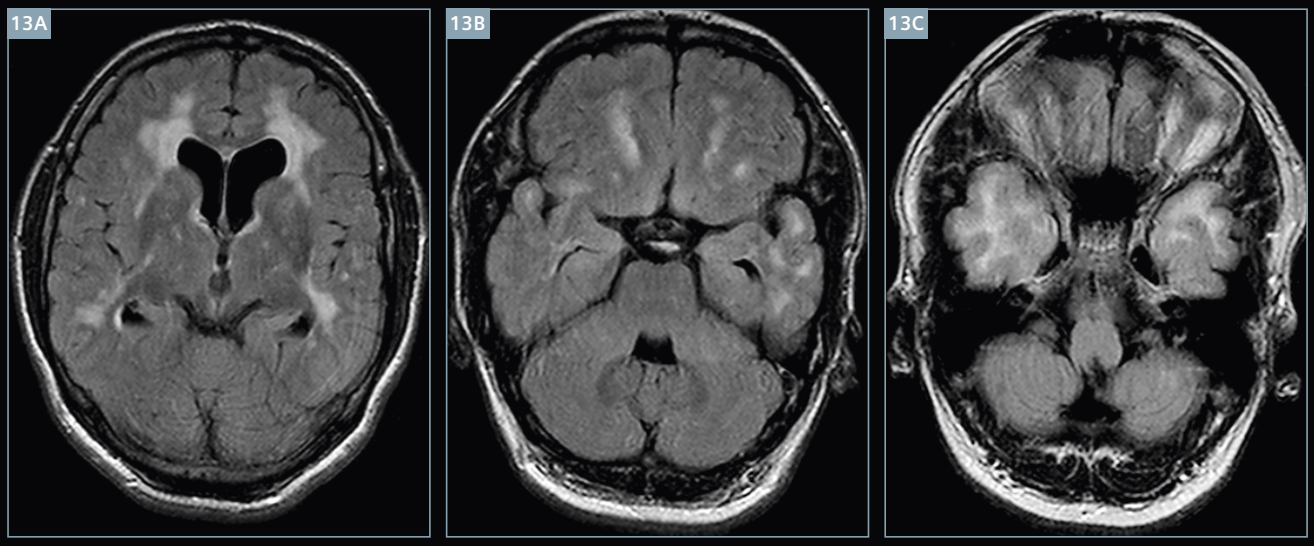

13 CADASIL with confluent areas of high T2 signal in the deep and subcortical white matter with involvement of the external capsule **(13A)** and predominant affection of the basal frontal and anterior temporal lobes **(13B, C)**.

Subcortical arteriosclerotic encephalopathy (SAE, Binswanger's disease)

Caused by ischemia of the deep central white matter, Binswanger's disease presents with extensive white matter changes that spare the periventricular region and extend into the corona radiata [14]. The age of the patients at clinical onset, sparing of U-fibres and missing involvement of the corpus callosum help to differentiate it from MS [16].

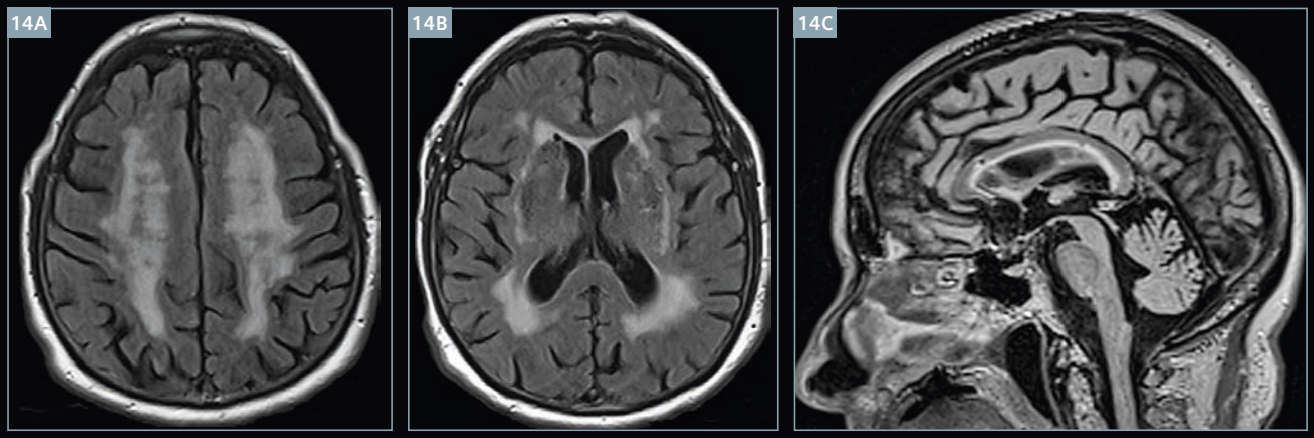

14 SAE with extensive confluent white matter changes in the centrum semiovale **(14A)** and around the frontal and occipital horns **(14B)** with moderate generalized cerebral atrophy, lacunar infarctions in the basal ganglia and affection of the corpus callosum **(14C)**.

Leukodystrophies

These are hereditary metabolic disorders with progressive white matter lesions, which tend to be bilateral and symmetrical with an antero-posterior gradient of progression [21]. With the exception of adrenoleucodystrophy, these disorders do not show contrast enhancement.

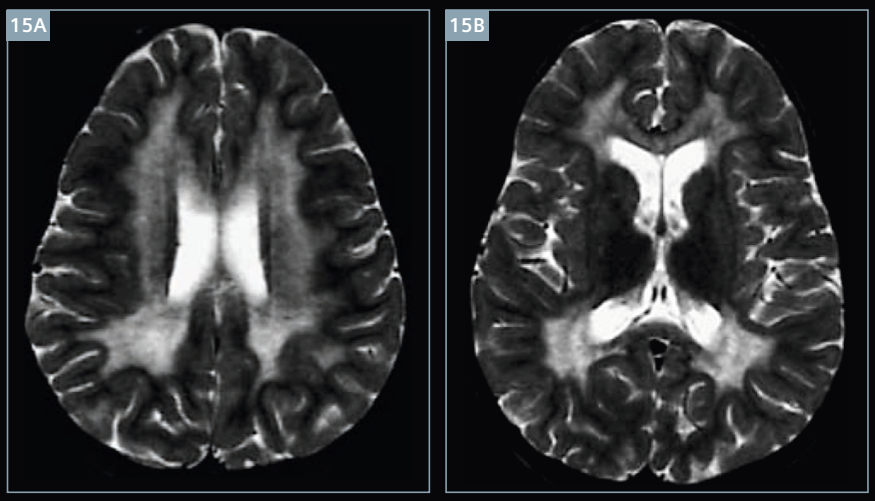

15 Leukodystrophy with diffuse, bilateral and symmetrical white matter changes on axial T2w MRI.

Mitochondrial diseases

This is a group of rare multisystem disorders caused by a variety of genetic defects affecting the mitochondrial metabolism. Especially Leber's hereditary optic neuropathy, chronic progressive ophthalmoplegia and mitochondrial encephalomyelopathy, lactic acidosis and stroke-like episodes (MELAS) might be difficult to distinguish radiologically from MS. Multisystem involvement, clinical presentation including a positive family history as well as calcified cerebral lesions might be the clue to the correct diagnosis [5].

*Siemens disclaimer: MR scanning has not been established as safe for imaging fetuses and infants less than two years of age. The responsible physician must evaluate the benefits of the MR examination compared to those of other imaging procedures.

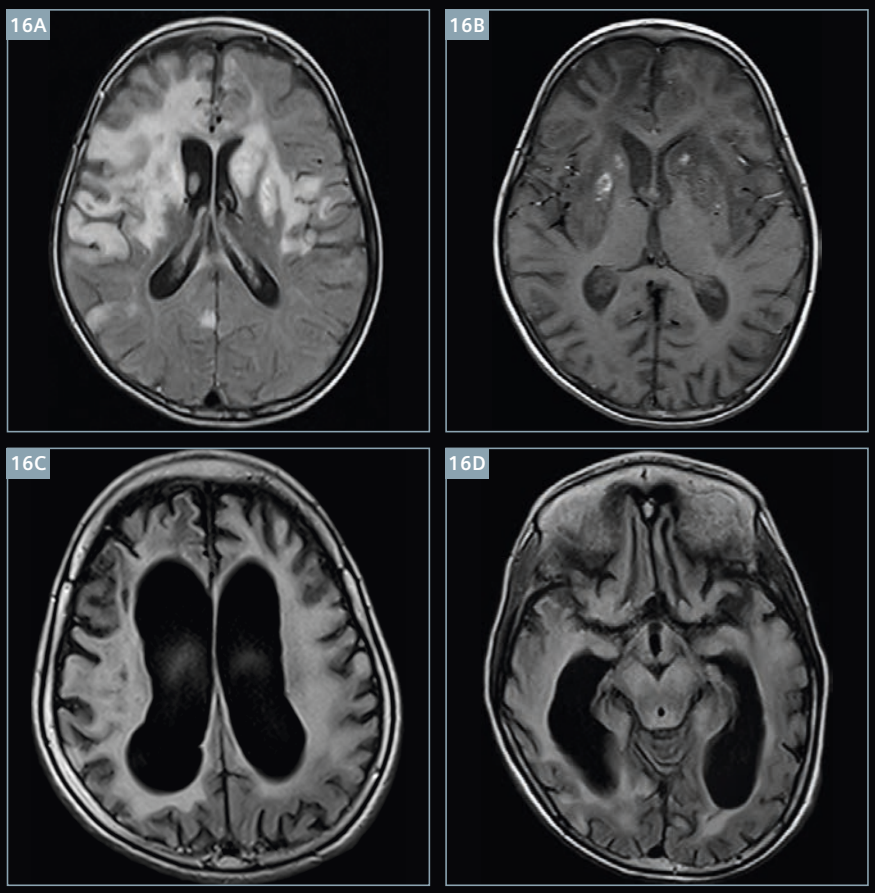

16 Follow-up MRI examinations in a child* with a mitochondrial disease and lactic acidosis. **(16A, B)** Examination at the age of 8 years old* with large, asymmetrical and multiple areas of high T2 signal in the deep periventricular and subcortical white matter and in the basal ganglia (a) with haemorrhages within the basal ganglia on native T1w (b). **(16C, D)** Follow-up examination at the age of 12 years old* after drastic progression with vast white matter changes, affection of the cerebral peduncles and mesencephalon and progressive atrophy with enlargement of the ventricles.

Vasculitis

Several vasculitic disorders may involve the brain, like systemic lupus erythematosus (SLE), Wegener's granulomatosis, Behçet's syndrome, polyarteritis nodosa or Sjögren's syndrome. Patients may present with cortico-subcortical or MS-like periventricular lesions on MRI. Isolated angiitis of the CNS is a rare disorder with granulomatous inflammation of small cerebral parenchymal or leptomeningeal vessels. Patients present with severe headache and focal neurological signs. MRI may show focal lesions similar to MS, diffuse white matter changes, involvement of grey matter structures, infarctions, haemorrhages and leptomeningeal or parenchymal enhancement [5]. High-resolution time-of-flight MR angiography is a reasonable initial modality in the investigation of suspected CNS vasculitis (demonstrating multiple stenosis also affecting peripheral arteries), but in case of normal MRA, catheter cerebral angiography should be considered.

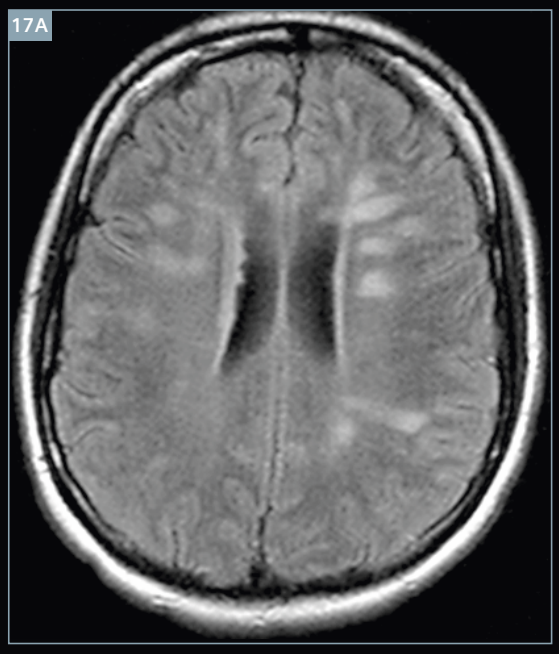

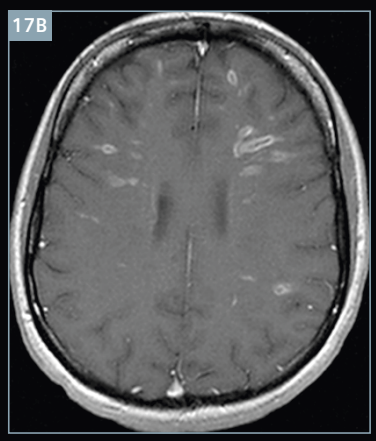

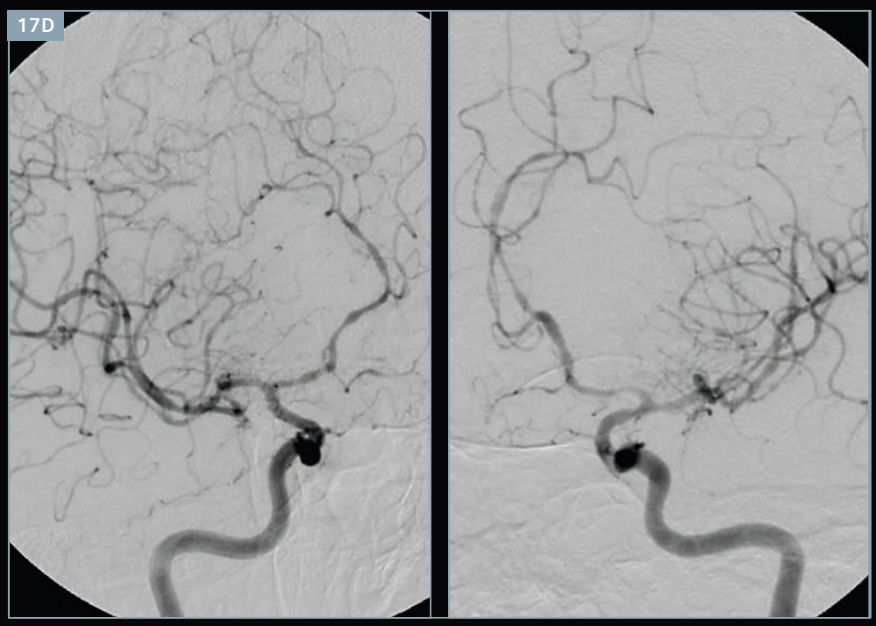

17

Cerebral vasculitis. FLAIR **(17A)** and contrast-enhanced T1w axial **(17B)** MR images show multiple contrast-enhancing foci of high T2 signal in the periventricular and subcortical white matter, similar to MS. **(17C)** TOF-MR angiography shows multifocal, segmental narrowing of the intracranial vessels mainly in the anterior circulation. **(17D)** Catheter cerebral angiography proves the finding of vasculitis.

Normal aging phenomena

Multifocal areas of T2 hyperintensity in the periventricular or deep white matter have been reported in around 35% of healthy individuals over the age of 60 years. Lesions may be small, multiple and punctuate or large and confluent. These non-specific, age-related, asymptomatic foci of ischemic demyelination may lead to misdiagnosis or underdiagnosis of MS especially in patients over 50 years old [14].

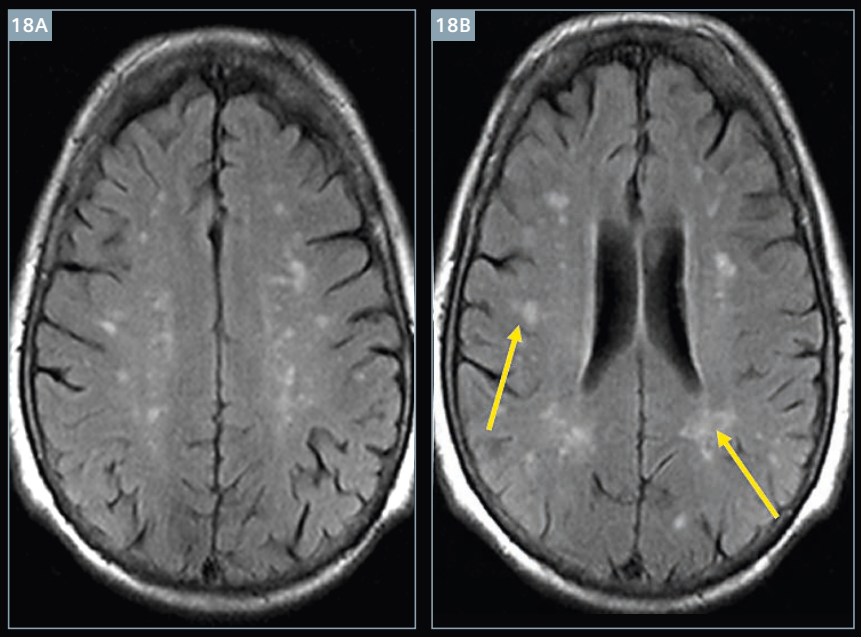

18 64-year-old healthy male with age-related, partially confluent periventricular foci of high T2 signal on axial FLAIR.

Conclusion

There is a variety of aetiologies for demyelinating processes of the CNS. MRI is the preferred imaging technique for diagnostic workup. Knowledge of the typical and rather unusual MR features of MS as well as consideration of the patient's age, clinical history and laboratory evaluation is essential to narrow the differential diagnosis.

References

1 Smith AB, Smirniotopoulos JG. Imaging evaluation of demyelinating processes of the central nervous system. Postgrad Med J 2010; 86:218-229. doi: 10.1136/pgmj.2009.087452.
2 Eckstein C, Saidha S, Levy M. A differential diagnosis of central nervous system demyelination: beyond multiple sclerosis. J Neurol. 2012; 259.801-816. doi 10.1007/s00415-011-6240-5.
3 Katz Sand IB, Lublin FD. Diagnosis and differential diagnosis of multiple sclerosis. Continuum (Minneap Minn) 2013; 922-43. doi: 10.1212/01.CON.0000433290.15468.21.
4 Deangelis TM, Miller A. Diagnosis of multiple sclerosis. Hand Clin Neurol. 2014; 122:317-42. doi: 10.1016/B978-0-444-52001-2.00013-3.
5 Trojano M, Paolicelli D. The differential diagnosis of multiple sclerosis: classification and clinical features of relapsing and progressive neurological syndromes. Neurol Sci 2001; 22:S98-S102.

Contact

Iris N. Kaschka, M.D.
Department of Neuroradiology
University Hospital Erlangen
Schwabachanlage 6
91054 Erlangen
Germany
Phone: +49 (0) 9131 85-39388
Fax: +49 (0) 9131 85-39179
iris.kaschka@uk-erlangen.de

6 Polman CH, Reingold SC, Banwell B, Clanet M, Cohen JA, Filippi M, Fujihara K, Havrdova E, Hutchinson M, Kappos L, Lublin FD, Montalban X, O'Connor P, Sandberg-Wollheim M, Thompson AJ, Waubant E, Weinshenker B, Wolinsky JS. Diagnostic criteria for Multiple Sclerosis: 2010 Revisions to the McDonald Criteria. ANN NEUROL 2011; 69-292-302.

7 Zivadinov R, Bakshi R. Role of Magnetic Resonance Imaging in the Diagnosis and Prognosis of Multiple Sclerosis. From: Current Clinical Neurology: Multiple Sclerosis. Edited by: Olek MJ. Humana Press Inc., Totowa, NJ 2005.

8 Sahraian MA, Radue E-W. MS lesions in T2-weighted images. MRI Atlas of MS lesions. 2008, Springer.

9 Javalkar V, Manix M, Wilson J, Nanda A. Open ring enhancement in atypical brain demyelination. J Clin Neurosci. 2012; 19(6):910-2. doi: 10.1016/j.jocn.2011.06.037.

10 Miller DH, Weinshenker BG, Filippi M, Banwell BL, Cohen JA, Freedman MS, Galetta SL, Hutchinson M, Johnson RT, Kappos L, Kira J, Lublin FD McFarland HF, Montalban X, Panitch H, Richert JR, Reingold SC, Polman CH. Differential diagnosis of suspected multiple sclerosis: a consensus approach. Mult Scler. 2008; 14(9): 1157-1174. doi: 10.1177/1352458508096878.

11 Yacoub HA, Al-Qudahl ZA, Lee H-J, Baisre A, Souayah N. Tumefactive Multiple Sclerosis presenting as Acute Ischemic Stroke. Journal of Vascular and Interventional Neurology 2011; 4(2): 21-23.

12 Granberg T, Martola J, Kristoffersen-Wiberg M, Aspelin P, Fredrikson S. Radiologically isolated syndrome - incidental magnetic resonance imaging findings suggestive of multiple sclerosis, a systematic review. MSJ 2012; 19(3) 271-280; doi: 10.1177/1352458512451943.

13 De Stefano N, Siva A. The radiologically isolated syndrome dilemma: just an incidental radiological finding or presymptomatic multiple sclerosis? MSJ 2012; 19(3) 257-258; doi: 10.1177/1352458512460418.

14 Kira J, Haller S, Kesselring J, Sahraian MA. Differential Diagnosis of Multiple Sclerosis. In Sahraian MA, Radue EW. MRI Atlas of MS lesions. 2008, Springer.

15 Lee D-H, Laemmer A, Waschbisch A, Struffert T, Maihöfner C, Schwab S, Linker RA. Neuromyelitis optica presenting with relapses under treatment with natalizumab: a case report. Journal of medical Case Report 2014, 8:155. doi: 10.1186/1752-1947-8-155.

16 Marcus JF, Waubant EL. Updates on clinically isolated syndrome and diagnostic criteria for multiple sclerosis. The Neurohospitalist 2013; 3(2) 65-80. doi: 10.1177/1941874412457183.

17 Ciccarelli O. Do cortical lesions help us to distinguish MS from NMO? Neurology 2012; 79;630-1631. doi: 10.1212/WNL.0b013e31826e9bbf.

18 Brinar VV, Habek M. Rare infections mimicking MS. Clin Neurol Neurosurg. 2010; 112(7):625-8. doi: 10.1016/j.clineuro.2010.04.011.

19 Engeholm M, Leo-Kottler B, Rempp H, Lindig T, Lerche H, Kleffner I, Henes M, Dihné M. Encephalopathic Susac's Syndrome associated with livedo racemosa in a young woman before the completion of family planning. BMC Neurology 2013, 13:185.

20 Bentley P, Wang T, Malik O, Nicholas R, Ban M, Sawcer S, Sharma P. CADASIL with cord involvement associated with a novel and atypical NOTCH3 mutation. J Neurol Neurosurg Psychiatry 2011; 82:855-860. doi: 10.1136/jnnp.2010.223297.

21 Bastianello S, Pichiecchio A, Spadaro M, Bergamaschi R, Bramanti P, Colonnese C, Sabatini U, Uggetti C, Luccichenti G. Atypical multiple sclerosis: MRI findings and differential diagnosis. Neurol Sci 2004; 25:S356-S360. doi: 10.1007/s10072-004-0340-2

T1w PSIR for Imaging MS Lesions in the Cervical Spinal Cord

The T1-weighted PSIR shows great potential in revealing MS lesions in the cervical spinal cord.

Visit us at
www.siemens.com/magnetom-world
to download

- the protocol for 3T MAGNETOM Skyra,
- 3T and 1.5T Phoenix images
- Bart Schraa's article on "T1-weighted Phase Sensitive Inversion Recovery for Imaging Multiple Sclerosis Lesions in the Cervical Spinal Cord".

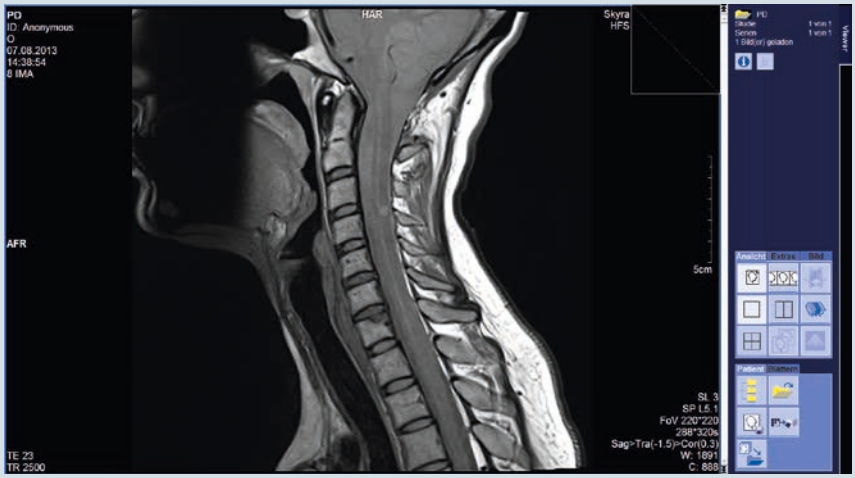

Slice Order (Slice Timing) for fMRI Evaluation

Joachim Graessner, Dipl. Ing.

Siemens Healthcare, Hamburg, Germany

This article focuses on the temporal order of slices in EPI-BOLD experiments such as slice timing, which is essential at least for event-related paradigms.

The first thing to keep in mind is the difference between the "Multi-slice mode" and "Series" parameters (Fig. 1). The latter requires our attention for our topic slice order.

The **Multi-slice mode** describes the way slices are excited within one TR interval:

- Interleaved measurement means line-by-line data acquisition of all slices in the repetition time TR starting with the first and ending with the last phase encoding step for normal sequences, such as spin echo or gradient echo.
- For an EPI sequence the Multi-slice mode = Interleaved is is actually a Single-Shot mode.

The **Series** parameter influences the excitation order of a stack of slices. You can select Ascending, Descending or Interleaved (Fig. 2).

The interleaved mode is usually chosen to minimize crosstalk between the slices.

In ascending and interleaved mode, the direction of transverse slice excitation is always from foot to head. In descending mode the direction changes to head to foot for axial slices. (Fig. 3)

All examples are valid for transverse slices only, meaning the orientation parameter with a leading "TRA > .... ".

In interleaved mode the number of slices determines which slice is excited first when image numbering feet to head is used:

- Even number of slices: slice number 2 first
- Odd number of slices: slice number 1 first

Example: Image numbering F>>H

- 36 slices: even number of slices (Fig. 4)
  – Order: **2**,4,6,8,10,...., 34,36,**1**,3,5,7,10,....,33,35
- 35 slices: odd number of slices (Fig. 5)
  – Order: **1**,3,5,7,10,...., 33,35,**2**,4,6,8,10,....,32,34

1 GEOMETRY/COMMON card; "Multi-slice mode" and "Series" parameters.

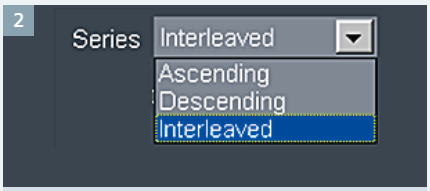

2 Choices for parameter "Series".

3

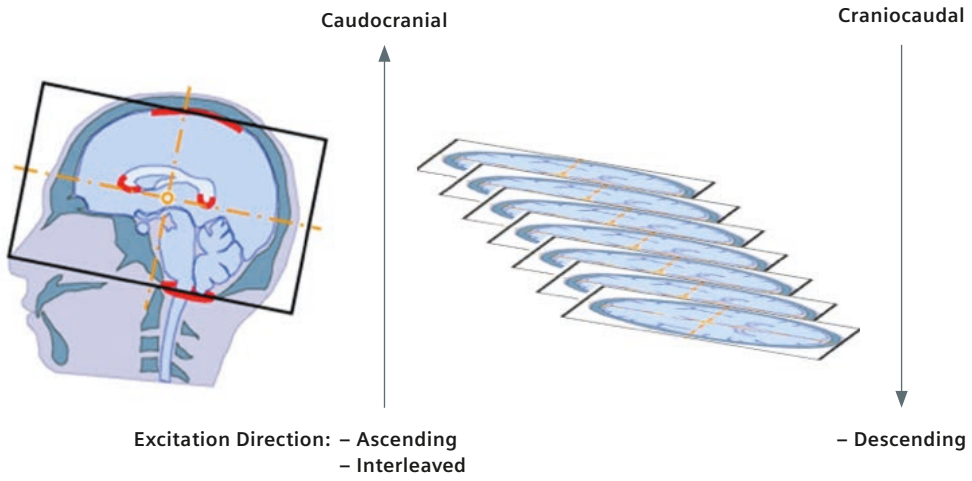

3 Slice excitation direction depending on "Series Mode" = Ascending; Descending; Interleaved.

4

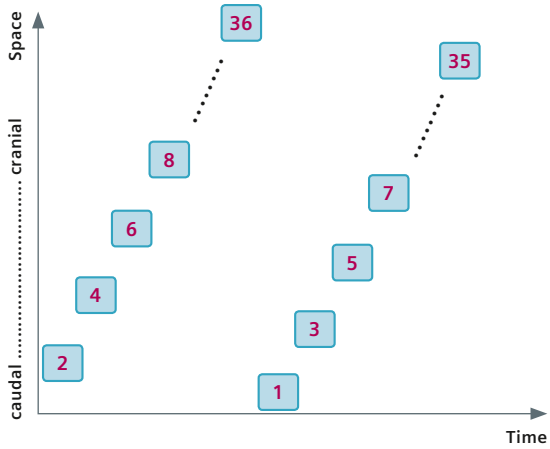

4 Even number of slices; Series = Interleaved; Image Numbering F>>H.

5

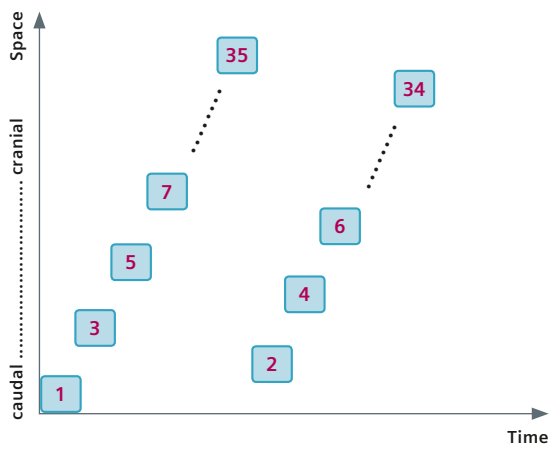

5 Odd number of slices; Series = Interleaved; Image Numbering F>>H.

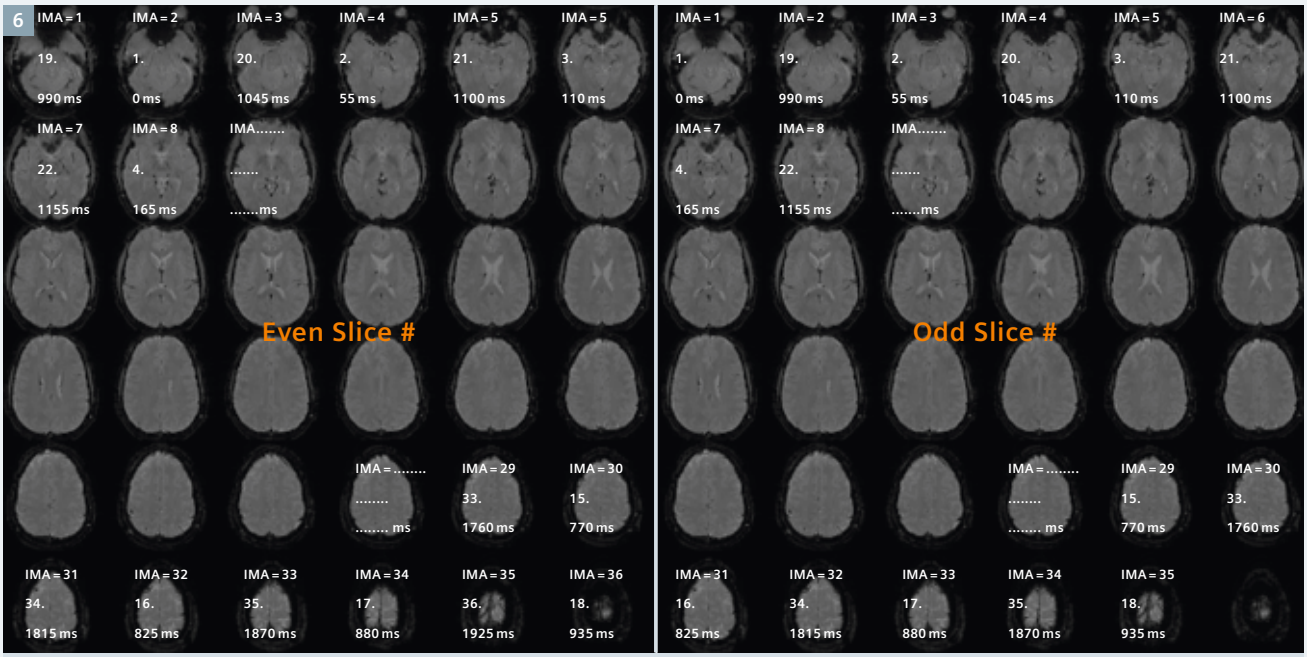

6 Mosaic images with even/odd number of slices; Series = Interleaved; Image Numbering F>>H.

The EPI mosaic in figure 6 shows a series containing 36/35 interleaved measured slices with text overlays for image numbers, excitation order number and relative offset time. The latter value can be extracted from the DICOM header in tag (0019,1029) „MosaicRefAcqTimes" together with tag (0008,0032) „Acquisition time" to calculate the absolute time of an image.

The displayed slice numbers in this example are identical to the image numbers of the series as long as the default setting for image numbering is used: Transversal F>>H on parameter card System/Miscellaneous (Fig. 7)

Do not use the mode H>>F because this complicates the numbering and you will have to sort images manually in most fMRI post-processing tools. The excitation of the slices in this case also starts caudally with the highest image numbers counting backwards! The rule with even or odd image numbers is not applicable. Furthermore, the images are displayed in a reverse order on the mosaic images. When used accidentally, the excitation order is shown below.

Example: Image numbering H>>F

- 36 slices: Even number
  – Order: **35**,33,31,29,...., 3,1,**36**,34,32,30,...4,2
- 35 slices: Odd number
  – Order: **35**,33,31,29,...., 3,1,**34**,32,30,28,...4,2

Please make sure that your evaluation software takes care of the slice order specified above.

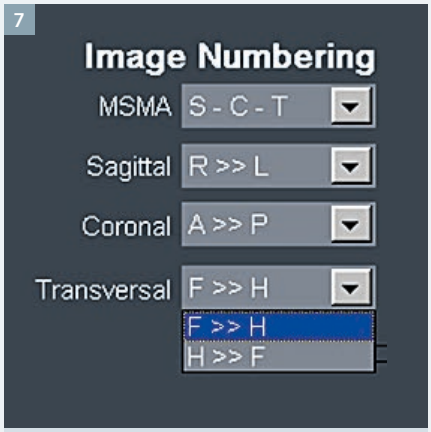

7 Parameter card SYSTEM/MISCELLANEOUS; Image Numbering Transversal F>>H.

Contact

Joachim Graessner, Dipl. Ing.
Siemens AG Healthcare
RC-DE COC NB CM
Lindenplatz 2
20099 Hamburg
Germany
joachim.graessner@siemens.com

Case Report: Evaluation of Neurofibromas on ^{18}F-FDG PET/MRI in a Patient with Neurofibromatosis Type 1

Roy A. Raad, M.D.[1]; Shailee Lala, M.D.[1]; Christopher Glielmi, Ph.D.[3]; Jeffrey C. Allen, M.D.[2] ; David Faul, Ph.D.[3]; Kent P. Friedman, M.D.[1]

[1] Department of Radiology, New York University School of Medicine, New York, NY, USA
[2] Departments of Pediatrics and Neurology, New York University School of Medicine, New York, NY, USA
[3] Siemens Healthcare Inc., USA

Introduction

Neurofibromatosis Type 1 (NF-1), a disease with autosomal dominant inheritance, has an incidence of 1 in 3000 [1]. NF-1 is characterized by various clinical manifestations, including café au lait spots, Lisch nodules, skeletal deformities, neurofibromas, and plexiform neurofibromas. Plexiform neurofibromas can undergo transformation into a malignant peripheral nerve sheath tumor (MPNST), the primary cause of mortality in this patient population [2]. It is an aggressive lesion, with a poor prognosis. Clinical findings such as pain and rapid enlargement sentinel signs of malignant transformation. Currently, 18-fludeoxyglucose* positron emission tomography/computed tomography (^{18}F-FDG PET/CT) is a sensitive imaging modality for detection of MPNSTs [3]. ^{18}F-FDG PET/MRI may be a better imaging modality for assessment of neurofibromas in this patient population, by combining metabolic data from PET with superior soft tissue contrast and radiation dose reduction of MRI by omitting the CT exam.

*The full prescribing information for the Fludeoxyglucose F^{18} injection can be found at the end of the article.

Patient history

20-year-old female with known NF-1 presented to the outpatient clinic with a palpable right axillary mass, progressively enlarging and increasingly painful over the past two years. She also complained of numbness and paresthesias in her right hand, mainly along the middle, fourth and fifth fingers, as well as right hand weakness. She denied any family history of neurofibromatosis. Physical examination revealed a large tender mass in the right axilla with associated right hemihypotrophy, as well as an additional superficial smaller mass overlying the right scapula, multiple café au lait spots, and bilateral axillary freckling. Neurologic examination revealed cognitive impairment, mild atrophy and mild flexor/extensor motor weakness in both hands, right greater than left.

Sequence details

Simultaneous PET and MRI were acquired (Biograph mMR, Siemens Healthcare, Erlangen, Germany) using the same tracer injection from a PET/CT (Biograph™ mCT) exam performed on the same day. Diagnostic MR sequences included axial STIR, coronal STIR and diffusion-weighted imaging (DWI) using 3 b-values (0, 350, 750 s/mm^2). PET was acquired simultaneously covering 4 beds from upper legs through thorax (6-minute sinogram acquisition).

Imaging findings

Initial MRI of the cervical spine and right arm reportedly demonstrated a dominant large soft tissue mass in the right axilla extending into the brachial plexus, as well as extensive bilateral plexiform neurofibromas. At the time of initial presentation around 2 years prior, a biopsy of the right axillary mass was done and showed a "WHO 1 low-grade plexiform neurofibroma without evidence of malignancy". Subsequent ^{18}F-FDG MR/PET examination was performed showing focal intense FDG uptake in the dominant enlarging well-circumscribed right axillary mass with a maximal standardized uptake value (SUV_{max}) of 5.7, demonstrating heterogeneous increased T2 signal intensity with a central cystic area, as well as diffusion restriction at the periphery of the mass (Fig. 1). Additional neurofibromas with low-grade metabolism without diffusion restriction were also detected in the left gluteus maximus muscle with SUV_{max} of 3.7 (Fig. 2) as well as in the right iliacus muscle with SUV_{max} of 3.3 and right gluteus maximus muscle with SUV_{max} of 2.1 (Fig. 3). Based on the significant progression of clinical symptoms and worrisome imaging features of enlargement, elevated SUV_{max} value, and peripheral diffusion restriction, patient underwent ultrasound-guided biopsy of the right axillary mass. Histopathology was consistent with a MPNST.

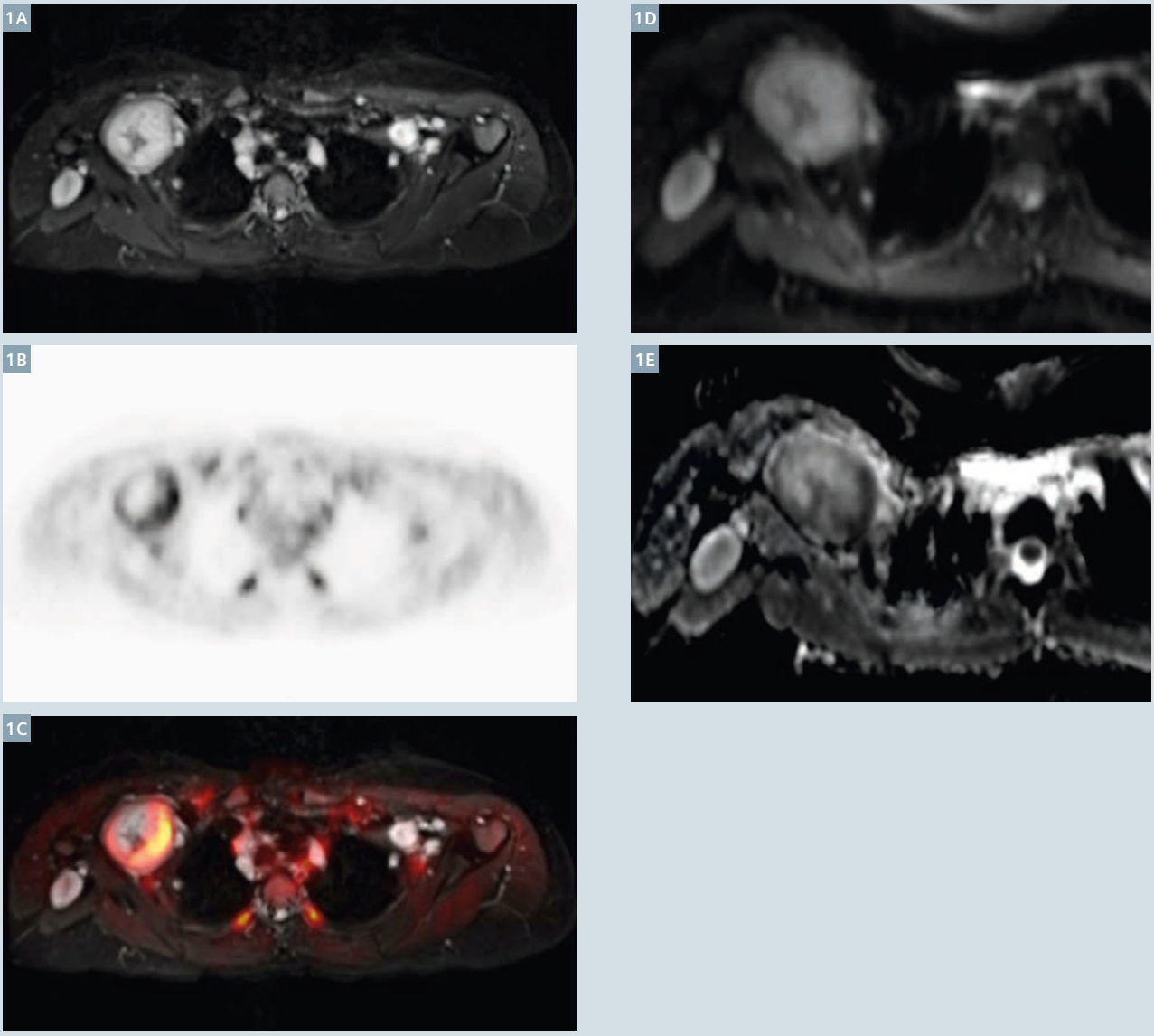

1 Axial STIR **(1A)**, PET **(1B)**, fused post-hoc **(1C)**, DWI **(1D)** and ADC **(1E)** images demonstrate a hyperintense right axillary mass with central cystic component, intense peripheral FDG uptake (SUV_{max} 5.7) and diffusion restriction. Tumor was malignant at surgery.

Indications

Fludeoxyglucose F^{18} Injection is indicated for positron emission tomography (PET) imaging in the following settings:

- **Oncology:** For assessment of abnormal glucose metabolism to assist in the evaluation of malignancy in patients with known or suspected abnormalities found by other testing modalities, or in patients with an existing diagnosis of cancer.
- **Cardiology:** For the identification of left ventricular myocardium with residual glucose metabolism and reversible loss of systolic function in patients with coronary artery disease and left ventricular dysfunction, when used together with myocardial perfusion imaging.
- **Neurology:** For the identification of regions of abnormal glucose metabolism associated with foci of epileptic seizures.

Important Safety Information

- **Radiation Risks:** Radiationemitting products, including Fludeoxyglucose F^{18} Injection, may increase the risk for cancer, especially in pediatric patients. Use the smallest dose necessary for imaging and ensure safe handling to protect the patient and healthcare worker.
- **Blood Glucose Abnormalities:** In the oncology and neurology setting, suboptimal imaging may occur in patients with inadequately regulated blood glucose levels. In these patients, consider medical therapy and laboratory testing to assure at least two days of normoglycemia prior to Fludeoxyglucose F^{18} Injection administration.
- **Adverse Reactions:** Hypersensitivity reactions with pruritus, edema and rash have been reported; have emergency resuscitation equipment and personnel immediately available.

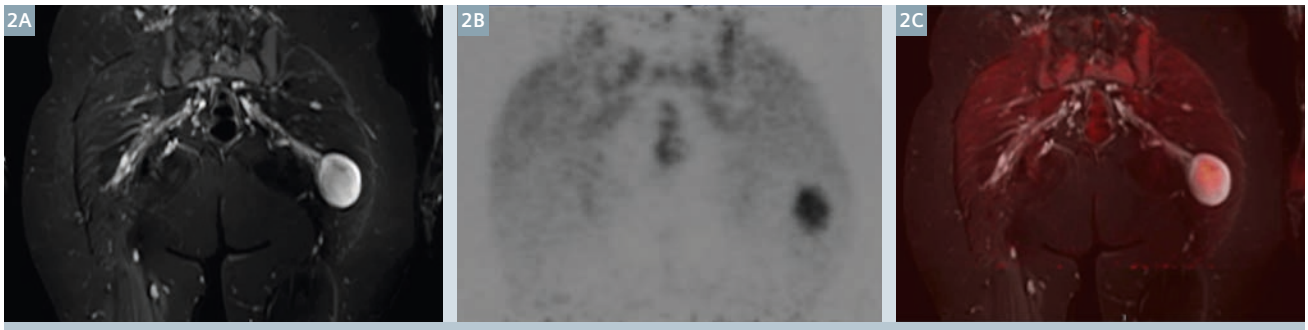

2 Coronal STIR **(2A)**, PET **(2B)**, and fused post-hoc **(2C)** images of a left gluteus muscle mass demonstrating high T2 signal intensity and mild FDG uptake (SUV_{max} 3.7).

Discussion

^{18}F-FDG PET/CT has developed into a well-recognized highly sensitive imaging modality for detection of MPNST, which is the leading cause of morbidity and mortality in patients with neurofibromatosis type 1 (NF1) [1-6]. Moreover, ^{18}F-FDG PET/CT may be potentially useful in preoperative tumor staging, guiding biopsies to the region of highest diagnostic yield within the tumor, or even directly influence management, either by reducing the number of unnecessary surgeries for benign plexiform neurofibromas or suggesting early intervention in tumors with imaging features suspicious for malignancy [7-9]. The most recognized parameter of PET/CT to differentiate between benign and malignant tumors in these NF1 patients is the maximum standardized uptake value (SUV_{max}). Despite the variation in the SUV_{max} cutoff value to differentiate between benign and malignant neurogenic tumors in patients with NF1, ranging between 1.8 [10] and 7.0 [1], the most widely used value is 3.5, where tumors with $SUV_{max} < 2.5$ are considered to be benign, tumors with $SUV_{max} > 3.5$ to be malignant, and those with values between 2.5 and 3.5 to be equivocal, in which case clinical correlation is suggested, and clinical/radiologic follow-up accordingly. Most studies have reported some degree of overlap between benign and malignant lesions on PET/CT, especially in the 2.5-3.5 SUV_{max} range.

Several MRI features have been described as favoring MPNSTs, such as ill-defined margins, irregular enhancement, intratumoral lobulation and perilesional edema, all of which however have much lower sensitivity compared to PET/CT [2, 11, 12]. Whole-body MRI has been used to determine the burden of disease and extent of tumors in patients with NF1, without proven accurate differentiation between benign and malignant lesions. Tumor density measured by ADC and quantitative measures of perfusion measured by dynamic contrast-enhanced MRI (DCE-MR) require further study as potential diagnostic biomarkers for MPNSTs.

The above literature demonstrates that PET/CT and MR alone are not sufficiently reliable in differentiating benign, atypical and malignant PNST histologies and there is a need to develop better non-invasive imaging signatures to guide patient management. This case is an example of the potential utility of MR/PET in these lesions, with an excellent correlation between worrisome imaging features including an elevated SUV_{max} value (> 3.5) and diffusion restriction, and the eventual pathologic diagnosis on MPNST. The additional lesions in the pelvis area were presumed to be benign, mainly based on their low-grade metabolism and absence of other worrisome imaging features, as well as the absence of clinical symptoms.

Conclusion

Hybrid MR/PET is a promising new imaging modality which can potentially address the current limitation of existing knowledge by combining two of the most advanced imaging modalities (MR and PET) in an attempt to better diagnose malignancy in patients with this very serious disease that causes significant morbidity and mortality among Americans, at a significantly reduced radiation exposure by omitting clinically unnecessary imaging such as CT.

*The statements by Siemens' customers described herein are based on results that were achieved in the customer's unique setting. Since there is no "typical" setting and many variables exist there can be no guarantee that other customers will achieve the same results.

3 Coronal STIR **(3A)**, PET **(3B)**, and fused post-hoc images **(3C)** of right gluteus maximus and right iliacus lesions also demonstrating high T2 signal intensity and mild ^{18}F-FDG uptake (SUV_{max} 3.3 and 2.1 respectively).

References

1 Ferner, RE, Golding, JF, Smith, M, Calonje, E, Jan, W, Sanjayanathan, V, and O'Doherty, M, *[18F]2-fluoro-2-deoxy-D-glucose positron emission tomography (FDG PET) as a diagnostic tool for neurofibromatosis 1 (NF1) associated malignant peripheral nerve sheath tumours (MPNSTs): a long-term clinical study*. Ann Oncol, 2008. **19**(2): p. 390-4.

2 Tsai, LL, Drubach, L, Fahey, F, Irons, M, Voss, S, and Ullrich, NJ, *[18F]-Fluorodeoxyglucose positron emission tomography in children with neurofibromatosis type 1 and plexiform neurofibromas: correlation with malignant transformation*. J Neurooncol, 2012. **108**(3): p. 469-75.

3 Treglia, G, Taralli, S, Bertagna, F, Salsano, M, Muoio, B, Novellis, P, Vita, ML, Maggi, F, and Giordano, A, *Usefulness of whole-body fluorine-18-fluorodeoxyglucose positron emission tomography in patients with neurofibromatosis type 1: a systematic review*. Radiol Res Pract, 2012. **2012**: p. 431029.

4 Karabatsou, K, Kiehl, TR, Wilson, DM, Hendler, A, and Guha, A, *Potential role of 18fluorodeoxyglucose-positron emission tomography/computed tomography in differentiating benign neurofibroma from malignant peripheral nerve sheath tumor associated with neurofibromatosis 1*. Neurosurgery, 2009. 65(4 Suppl): p. A160-70.

5 Warbey, VS, Ferner, RE, Dunn, JT, Calonje, E, and O'Doherty, MJ, *[18F]FDG PET/CT in the diagnosis of malignant peripheral nerve sheath tumours in neurofibromatosis type-1*. Eur J Nucl Med Mol Imaging, 2009. **36**(5): p. 751-7.

6 Bredella, MA, Torriani, M, Hornicek, F, Ouellette, HA, Plamer, WE, Williams, Z, Fischman, AJ, and Plotkin, SR, *Value of PET in the assessment of patients with neurofibromatosis type 1*. AJR Am J Roentgenol, 2007. **189**(4): p. 928-35.

7 Wegner, EA, Barrington, SF, Kingston, JE, Robinson, RO, Ferner, RE, Taj, M, Smith, MA, and O'Doherty, MJ, *The impact of PET scanning on management of paediatric oncology patients*. Eur J Nucl Med Mol Imaging, 2005. **32**(1): p. 23-30.

8 Brenner, W, Friedrich, RE, Gawad, KA, Hagel, C, von Deimling, A, de Wit, M, Buchert, R, Clausen, M, and Mautner, VF, *Prognostic relevance of FDG PET in patients with neurofibromatosis type-1 and malignant peripheral nerve sheath tumours*. Eur J Nucl Med Mol Imaging, 2006. **33(**4): p. 428-32.

9 Fisher, MJ, Basu, S, Dombi, E, Yu, JQ, Widemann, BC, Pollock, AN, Cnaan, A, Zhuang, H, Phillips, PC, and Alavi, A, *The role of [18F]-fluorodeoxyglucose positron emission tomography in predicting plexiform neurofibroma progression*. J Neurooncol, 2008. **87**(2): p. 165-71.

10 Cardona, S, Schwarzbach, M, Hinz, U, Dimitrakopoulou-Strauss, A, Attigah, N, Mechtersheimer section sign, G, and Lehnert, T, *Evaluation of F18-deoxyglucose positron emission tomography (FDG-PET) to assess the nature of neurogenic tumours*. Eur J Surg Oncol, 2003. **29**(6): p. 536-41.

11 Lodge, MA, Lucas, JD, Marsden, PK, Cronin, BF, O'Doherty, MJ, and Smith, MA, *A PET study of 18FDG uptake in soft tissue masses*. Eur J Nucl Med, 1999. **26**(1): p. 22-30.

12 Derlin, T, Tornquist, K, Munster, S, Apostolova, I, Hagel, C, Friedrich, RE, Wedegartner, U, and Mautner, VF, *Comparative effectiveness of 18F-FDG PET/CT versus whole-body MRI for detection of malignant peripheral nerve sheath tumors in neurofibromatosis type 1*. Clin Nucl Med, 2013. **38**(1): p. e19-25.

Contact

Roy A. Raad, M.D.
New York University School of Medicine
Department of Radiology
660 First Avenue, 3rd floor
New York, NY 10016
USA
Phone: +1 212-263-7410
Fax: +1 212-263-5567
roy.raad@nyumc.org

HIGHLIGHTS OF PRESCRIBING INFORMATION

These highlights do not include all the information needed to use Fludeoxyglucose F 18 Injection safely and effectively. See full prescribing information for Fludeoxyglucose F 18 Injection.
Fludeoxyglucose F 18 Injection, USP
For intravenous use
Initial U.S. Approval: 2005

RECENT MAJOR CHANGES

Warnings and Precautions (5.1, 5.2)	7/2010
Adverse Reactions (6)	7/2010

INDICATIONS AND USAGE

Fludeoxyglucose F18 Injection is indicated for positron emission tomography (PET) imaging in the following settings:

- Oncology: For assessment of abnormal glucose metabolism to assist in the evaluation of malignancy in patients with known or suspected abnormalities found by other testing modalities, or in patients with an existing diagnosis of cancer.
- Cardiology: For the identification of left ventricular myocardium with residual glucose metabolism and reversible loss of systolic function in patients with coronary artery disease and left ventricular dysfunction, when used together with myocardial perfusion imaging.
- Neurology: For the identification of regions of abnormal glucose metabolism associated with foci of epileptic seizures (1).

DOSAGE AND ADMINISTRATION

Fludeoxyglucose F 18 Injection emits radiation. Use procedures to minimize radiation exposure. Screen for blood glucose abnormalities.

- In the oncology and neurology settings, instruct patients to fast for 4 to 6 hours prior to the drug's injection. Consider medical therapy and laboratory testing to assure at least two days of normoglycemia prior to the drug's administration (5.2).
- In the cardiology setting, administration of glucose-containing food or liquids (e.g., 50 to 75 grams) prior to the drug's injection facilitates localization of cardiac ischemia (2.3).

Aseptically withdraw Fludeoxyglucose F 18 Injection from its container and administer by intravenous injection (2).

The recommended dose:

- for adults is 5 to 10 mCi (185 to 370 MBq), in all indicated clinical settings (2.1).
- for pediatric patients is 2.6 mCi in the neurology setting (2.2).

Initiate imaging within 40 minutes following drug injection; acquire static emission images 30 to 100 minutes from time of injection (2).

DOSAGE FORMS AND STRENGTHS

Multi-dose 30mL and 50mL glass vial containing 0.74 to 7.40 GBq/mL (20 to 200 mCi/mL) Fludeoxyglucose F 18 Injection and 4.5mg of sodium chloride with 0.1 to 0.5% w/w ethanol as a stabilizer (approximately 15 to 50 mL volume) for intravenous administration (3).

CONTRAINDICATIONS

None

WARNINGS AND PRECAUTIONS

- Radiation risks: use smallest dose necessary for imaging (5.1).
- Blood glucose adnormalities: may cause suboptimal imaging (5.2).

ADVERSE REACTIONS

Hypersensitivity reactions have occurred; have emergency resuscitation equipment and personnel immediately available (6).
To report SUSPECTED ADVERSE REACTIONS, contact PETNET Solutions, Inc. at 877-473-8638 or FDA at 1-800-FDA-1088 or www.fda.gov/medwatch.

USE IN SPECIFIC POPULATIONS

Pregnancy Category C: No human or animal data. Consider alternative diagnostics; use only if clearly needed (8.1).

- Nursing mothers: Use alternatives to breast feeding (e.g., stored breast milk or infant formula) for at least 10 half-lives of radioactive decay, if Fludeoxyglucose F 18 Injection is administered to a woman who is breast-feeding (8.3).
- Pediatric Use: Safety and effectiveness in pediatric patients have not been established in the oncology and cardiology settings (8.4).

See 17 for PATIENT COUNSELING INFORMATION

Revised: 1/2011

FULL PRESCRIBING INFORMATION: CONTENTS*

1 INDICATIONS AND USAGE
1.1 Oncology
1.2 Cardiology
1.3 Neurology
2 DOSAGE AND ADMINISTRATION
2.1 Recommended Dose for Adults
2.2 Recommended Dose for Pediatric Patients
2.3 Patient Preparation
2.4 Radiation Dosimetry
2.5 Radiation Safety – Drug Handling
2.6 Drug Preparation and Administration
2.7 Imaging Guidelines
3 DOSAGE FORMS AND STRENGTHS
4 CONTRAINDICATIONS
5 WARNINGS AND PRECAUTIONS
5.1 Radiation Risks
5.2 Blood Glucose Abnormalities
6 ADVERSE REACTIONS
7 DRUG INTERACTIONS
8 USE IN SPECIFIC POPULATIONS
8.1 Pregnancy
8.3 Nursing Mothers
8.4 Pediatric Use
11 DESCRIPTION
11.1 Chemical Characteristics
11.2 Physical Characteristics
12 CLINICAL PHARMACOLOGY
12.1 Mechanism of Action
12.2 Pharmacodynamics
12.3 Pharmacokinetics
13 NONCLINICAL TOXICOLOGY
13.1 Carcinogenesis, Muta-genesis, Impairment of Fertility
14 CLINICAL STUDIES
14.1 Oncology
14.2 Cardiology
14.3 Neurology
15 REFERENCES
16 HOW SUPPLIED/STORAGE AND DRUG HANDLING
17 PATIENT COUNSELING INFORMATION

* Sections or subsections omitted from the full prescribing information are not listed.

FULL PRESCRIBING INFORMATION

1 INDICATIONS AND USAGE

Fludeoxyglucose F 18 Injection is indicated for positron emission tomography (PET) imaging in the following settings:

1.1 Oncology

For assessment of abnormal glucose metabolism to assist in the evaluation of malignancy in patients with known or suspected abnormalities found by other testing modalities, or in patients with an existing diagnosis of cancer.

1.2 Cardiology

For the identification of left ventricular myocardium with residual glucose metabolism and reversible loss of systolic function in patients with coronary artery disease and left ventricular dysfunction, when used together with myocardial perfusion imaging.

1.3 Neurology

For the identification of regions of abnormal glucose metabolism associated with foci of epileptic seizures.

2 DOSAGE AND ADMINISTRATION

Fludeoxyglucose F 18 Injection emits radiation. Use procedures to minimize radiation exposure. Calculate the final dose from the end of synthesis (EOS) time using proper radioactive decay factors. Assay the final dose in a properly calibrated dose calibrator before administration to the patient [see Description (11.2)].

2.1 Recommended Dose for Adults

Within the oncology, cardiology and neurology settings, the recommended dose for adults is 5 to 10 mCi (185 to 370 MBq) as an intravenous injection.

2.2 Recommended Dose for Pediatric Patients

Within the neurology setting, the recommended dose for pediatric patients is 2.6 mCi, as an intravenous injection. The optimal dose adjustment on the basis of body size or weight has not been determined [see Use in Special Populations (8.4)].

2.3 Patient Preparation

- To minimize the radiation absorbed dose to the bladder, encourage adequate hydration. Encourage the patient to drink water or other fluids (as tolerated) in the 4 hours before their PET study.
- Encourage the patient to void as soon as the imaging study is completed and as often as possible thereafter for at least one hour.
- Screen patients for clinically significant blood glucose abnormalities by obtaining a history and/or laboratory tests [see Warnings and Precautions (5.2)]. Prior to Fludeoxyglucose F 18 PET imaging in the oncology and neurology settings, instruct patient to fast for 4 to 6 hours prior to the drug's injection.
- In the cardiology setting, administration of glucose-containing food or liquids (e.g., 50 to 75 grams) prior to Fludeoxyglucose F18 Injection facilitates localization of cardiac ischemia

2.4 Radiation Dosimetry

The estimated human absorbed radiation doses (rem/mCi) to a newborn (3.4 kg), 1-year old (9.8 kg), 5-year old (19 kg), 10-year old (32 kg), 15-year old (57 kg), and adult (70 kg) from intravenous administration of Fludeoxyglucose F 18 Injection are shown in Table 1. These estimates were calculated based on human[2] data and using the data published by the International Commission on Radiological Protection[4] for Fludeoxyglucose ^{18}F. The dosimetry data show that there are slight variations in absorbed radiation dose for various organs in each of the age groups. These dissimilarities in absorbed radiation dose are due to developmental age variations (e.g., organ size, location, and overall metabolic rate for each age group). The identified critical organs (in descending order) across all age groups evaluated are the urinary bladder, heart, pancreas, spleen, and lungs.

Table 1. Estimated Absorbed Radiation Doses (rem/mCi) After Intravenous Administration of Fludeoxyglucose F-18 Injection[a]

Organ	Newborn	1-year old	5-year old	10-year old	15-year old	Adult
	(3.4 kg)	(9.8 kg)	(19 kg)	(32 kg)	(57 kg)	(70 kg)
Bladder wallb	4.3	1.7	0.93	0.60	0.40	0.32
Heart wall	2.4	1.2	0.70	0.44	0.29	0.22
Pancreas	2.2	0.68	0.33	0.25	0.13	0.096
Spleen	2.2	0.84	0.46	0.29	0.19	0.14
Lungs	0.96	0.38	0.20	0.13	0.092	0.064
Kidneys	0.81	0.34	0.19	0.13	0.089	0.074
Ovaries	0.80	0.8	0.19	0.11	0.058	0.053
Uterus	0.79	0.35	0.19	0.12	0.076	0.062
LLI wall *	0.69	0.28	0.15	0.097	0.060	0.051
Liver	0.69	0.31	0.17	0.11	0.076	0.058
Gallbladder wall	0.69	0.26	0.14	0.093	0.059	0.049
Small intestine	0.68	0.29	0.15	0.096	0.060	0.047
ULI wall **	0.67	0.27	0.15	0.090	0.057	0.046
Stomach wall	0.65	0.27	0.14	0.089	0.057	0.047
Adrenals	0.65	0.28	0.15	0.095	0.061	0.048
Testes	0.64	0.27	0.14	0.085	0.052	0.041
Red marrow	0.62	0.26	0.14	0.089	0.057	0.047
Thymus	0.61	0.26	0.14	0.086	0.056	0.044
Thyroid	0.61	0.26	0.13	0.080	0.049	0.039
Muscle	0.58	0.25	0.13	0.078	0.049	0.039
Bone surface	0.57	0.24	0.12	0.079	0.052	0.041
Breast	0.54	0.22	0.11	0.068	0.043	0.034
Skin	0.49	0.20	0.10	0.060	0.037	0.030
Brain	0.29	0.13	0.09	0.078	0.072	0.070
Other tissues	0.59	0.25	0.13	0.083	0.052	0.042

[a] MIRDOSE 2 software was used to calculate the radiation absorbed dose. Assumptions on the biodistribution based on data from Gallagher et al.1 and Jones et al.2

[b] The dynamic bladder model with a uniform voiding frequency of 1.5 hours was used. *LLI = lower large intestine; **ULI = upper large intestine

2.5 Radiation Safety – Drug Handling

- Use waterproof gloves, effective radiation shielding, and appropriate safety measures when handling Fludeoxyglucose F 18 Injection to avoid unnecessary radiation exposure to the patient, occupational workers, clinical personnel and other persons.
- Radiopharmaceuticals should be used by or under the control of physicians who are qualified by specific training and experience in the safe use and handling of radionuclides, and whose experience and training have been approved by the appropriate governmental agency authorized to license the use of radionuclides.
- Calculate the final dose from the end of synthesis (EOS) time using proper radioactive decay factors. Assay the final dose in a properly calibrated dose calibrator before administration to the patient [see Description (11.2)].
- The dose of Fludeoxyglucose F 18 used in a given patient should be minimized consistent with the objectives of the procedure, and the nature of the radiation detection devices employed.

2.6 Drug Preparation and Administration

- Calculate the necessary volume to administer based on calibration time and dose.
- Aseptically withdraw Fludeoxyglucose F 18 Injection from its container.
- Inspect Fludeoxyglucose F 18 Injection visually for particulate matter and discoloration before administration, whenever solution and container permit.
- Do not administer the drug if it contains particulate matter or discoloration; dispose of these unacceptable or unused preparations in a safe manner, in compliance with applicable regulations.
- Use Fludeoxyglucose F 18 Injection within 12 hours from the EOS.

2.7 Imaging Guidelines

- Initiate imaging within 40 minutes following Fludeoxyglucose F 18 Injection administration.
- Acquire static emission images 30 to 100 minutes from the time of injection.

3 DOSAGE FORMS AND STRENGTHS

Multiple-dose 30 mL and 50 mL glass vial containing 0.74 to 7.40 GBq/mL (20 to 200 mCi/mL) of Fludeoxyglucose F 18 Injection and 4.5 mg of sodium chloride with 0.1 to 0.5% w/w ethanol as a stabilizer (approximately 15 to 50 mL volume) for intravenous administration.

4 CONTRAINDICATIONS

None

5 WARNINGS AND PRECAUTIONS

5.1 Radiation Risks

Radiation-emitting products, including Fludeoxyglucose F 18 Injection, may increase the risk for cancer, especially in pediatric patients. Use the smallest dose necessary for imaging and ensure safe handling to protect the patient and health care worker [see Dosage and Administration (2.5)].

5.2 Blood Glucose Abnormalities

In the oncology and neurology setting, suboptimal imaging may occur in patients with inadequately regulated blood glucose levels. In these patients, consider medical therapy and laboratory testing to assure at least two days of normoglycemia prior to Fludeoxyglucose F 18 Injection administration.

6 ADVERSE REACTIONS

Hypersensitivity reactions with pruritus, edema and rash have been reported in the post-marketing setting. Have emergency resuscitation equipment and personnel immediately available.

7 DRUG INTERACTIONS

The possibility of interactions of Fludeoxyglucose F 18 Injection with other drugs taken by patients undergoing PET imaging has not been studied.

8 USE IN SPECIFIC POPULATIONS

8.1 Pregnancy

Pregnancy Category C

Animal reproduction studies have not been conducted with Fludeoxyglucose F 18 Injection. It is also not known whether Fludeoxyglucose F 18 Injection can cause fetal harm when administered to a pregnant woman or can affect reproduction capacity. Consider alternative diagnostic tests in a pregnant woman; administer Fludeoxyglucose F 18 Injection only if clearly needed.

8.3 Nursing Mothers

It is not known whether Fludeoxyglucose F 18 Injection is excreted in human milk. Consider alternative diagnostic tests in women who are breast-feeding. Use alternatives to breast feeding (e.g., stored breast milk or infant formula) for at least 10 half-lives of radioactive decay, if Fludeoxyglucose F 18 Injection is administered to a woman who is breast-feeding.

8.4 Pediatric Use

The safety and effectiveness of Fludeoxyglucose F 18 Injection in pediatric patients with epilepsy is established on the basis of studies in adult and pediatric patients. In pediatric patients with epilepsy, the recommended dose is 2.6 mCi. The optimal dose adjustment on the basis of body size or weight has not been determined. In the oncology or cardiology settings, the safety and effectiveness of Fludeoxyglucose F 18 Injection have not been established in pediatric patients.

11 DESCRIPTION

11.1 Chemical Characteristics

Fludeoxyglucose F 18 Injection is a positron emitting radiopharmaceutical that is used for diagnostic purposes in conjunction with positron emission tomography (PET) imaging. The active ingredient 2-deoxy-2-[^{18}F]fluoro-D-glucose has the molecular formula of $C_6H_{11}{}^{18}FO_5$ with a molecular weight of 181.26, and has the following chemical structure:

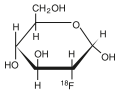

Fludeoxyglucose F 18 Injection is provided as a ready to use sterile, pyrogen free, clear, colorless solution. Each mL contains between 0.740 to 7.40GBq (20.0 to 200 mCi) of 2-deoxy-2-[^{18}F]fluoro-D-glucose at the EOS, 4.5 mg of sodium chloride and 0.1 to 0.5% w/w ethanol as a stabilizer. The pH of the solution is between 4.5 and 7.5. The solution is packaged in a multiple-dose glass vial and does not contain any preservative.

11.2 Physical Characteristics

Fluorine F 18 decays by emitting positron to Oxygen O 16 (stable) and has a physical half-life of 109.7 minutes. The principal photons useful for imaging are the dual 511 keV gamma photons, that are produced and emitted simultaneously in opposite direction when the positron interacts with an electron (Table 2).

Table 2. Pricipal Radiation Emission Data for Fluorine F18

Radiation/Emission	% Per Disintegration	Mean Energy
Positron (b+)	96.73	249.8 keV
Gamma (±)*	193.46	511.0 keV

*Produced by positron annihilation

From: Kocher, D.C. Radioactive Decay Tables DOE/TIC-I 1026, 89 (1981)

The specific gamma ray constant (point source air kerma coefficient) for fluorine F 18 is 5.7 R/hr/mCi (1.35 x 10-6 Gy/hr/kBq) at 1 cm. The half-value layer (HVL) for the 511 keV photons is 4 mm lead (Pb). The range of attenuation coefficients for this radionuclide as a function of lead shield thickness is shown in Table 3. For example, the interposition of an 8 mm thickness of Pb, with a coefficient of attenuation of 0.25, will decrease the external radiation by 75%.

Table 3. Radiation Attenuation of 511 keV Photons by lead (Pb) shielding

Shield thickness (Pb) mm	Coefficient of attenuation
0	0.00
4	0.50
8	0.25
13	0.10
26	0.01
39	0.001
52	0.0001

For use in correcting for physical decay of this radionuclide, the fractions remaining at selected intervals after calibration are shown in Table 4.

Table 4. Physical Decay Chart for Fluorine F18

Minutes	Fraction Remaining
0*	1.000
15	0.909
30	0.826
60	0.683
110	0.500
220	0.250

*calibration time

12 CLINICAL PHARMACOLOGY

12.1 Mechanism of Action

Fludeoxyglucose F 18 is a glucose analog that concentrates in cells that rely upon glucose as an energy source, or in cells whose dependence on glucose increases under pathophysiological conditions. Fludeoxyglucose F 18 is transported through the cell membrane by facilitative glucose transporter proteins and is phosphorylated within the cell to [18F] FDG-6-phosphate by the enzyme hexokinase. Once phosphorylated it cannot exit until it is dephosphorylated by glucose-6-phosphatase. Therefore, within a given tissue or pathophysiological process, the retention and clearance of Fludeoxyglucose F 18 reflect a balance involving glucose transporter, hexokinase and glucose-6-phosphatase activities. When allowance is made for the kinetic differences between glucose and Fludeoxyglucose F 18 transport and phosphorylation (expressed as the ‚lumped constant" ratio), Fludeoxyglucose F 18 is used to assess glucose metabolism. In comparison to background activity of the specific organ or tissue type, regions of decreased or absent uptake of Fludeoxyglucose F 18 reflect the decrease or absence of glucose metabolism. Regions of increased uptake of Fludeoxyglucose F 18 reflect greater than normal rates of glucose metabolism.

12.2 Pharmacodynamics

Fludeoxyglucose F 18 Injection is rapidly distributed to all organs of the body after intravenous administration. After background clearance of Fludeoxyglucose F 18 Injection, optimal PET imaging is generally achieved between 30 to 40 minutes after administration.

In cancer, the cells are generally characterized by enhanced glucose metabolism partially due to (1) an increase in activity of glucose transporters, (2) an increased rate of phosphorylation activity, (3) a reduction of phosphatase activity or, (4) a dynamic alteration in the balance among all these processes. However, glucose metabolism of cancer as reflected by Fludeoxyglucose F 18 accumulation shows considerable variability. Depending on tumor type, stage, and location, Fludeoxyglucose F 18 accumulation may be increased, normal, or decreased. Also, inflammatory cells can have the same variability of uptake of Fludeoxyglucose F 18.

In the heart, under normal aerobic conditions, the myocardium meets the bulk of its energy requirements by oxidizing free fatty acids. Most of the exogenous glucose taken up by the myocyte is converted into glycogen. However, under ischemic conditions, the oxidation of free fatty acids decreases, exogenous glucose becomes the preferred myocardial sub strate, glycolysis is stimulated, and glucose taken up by the myocyte i s metabolized immediately instead of being converted into glycogen. Under these conditions, phosphorylated Fludeoxyglucose F 18 accumulates in the myocyte and can be detected with PET imaging.

In the brain, cells normally rely on aerobic metabolism. In epilepsy, the glucose metabolism varies. Generally, during a seizure, glucose metabolism increases. Interictally, the seizure focus tends to be hypometabolic.

12.3 Pharmacokinetics

Distribution: In four healthy male volunteers, receiving an intravenous administration of 30 seconds in duration, the arterial blood level profile for Fludeoxyglucose F 18 decayed triexponentially. The effective half-life ranges of the three phases were 0.2 to 0.3 minutes, 10 to 13 minutes with a mean and standard deviation (STD) of 11.6 (±) 1.1 min, and 80 to 95 minutes with a mean and STD of 88 (±) 4 min.

Plasma protein binding of Fludeoxyglucose F 18 has not been studied.

Metabolism: Fludeoxyglucose F 18 is transported into cells and phosphorylated to [^{18}F]-FDG-6- phosphate at a rate proportional to the rate of glucose utilization within that tissue. [F18]-FDG-6-phosphate presumably is metabolized to 2-deoxy-2-[F18]fluoro-6-phospho-D-mannose([F 18]FDM-6-phosphate).

Fludeoxyglucose F 18 Injection may contain several impurities (e.g., 2-deoxy-2-chloro-D-glucose (ClDG)). Biodistribution and metabolism of ClDG are presumed to be similar to Fludeoxyglucose F 18 and would be expected to result in intracellular formation of 2-deoxy-2-chloro-6-phospho-D-glucose (ClDG-6-phosphate) and 2-deoxy-2-chloro-6-phospho-D-mannose (ClDM-6-phosphate). The phosphorylated deoxyglucose compounds are dephosphorylated and the resulting compounds (FDG, FDM, ClDG, and ClDM) presumably leave cells by passive diffusion. Fludeoxyglucose F 18 and related compounds are cleared from non-cardiac tissues within 3 to 24 hours after administration. Clearance from the cardiac tissue may require more than 96 hours. Fludeoxyglucose F 18 that is not involved in glucose metabolism in any tissue is then excreted in the urine.

Elimination: Fludeoxyglucose F 18 is cleared from most tissues within 24 hours and can be eliminated from the body unchanged in the urine. Three elimination phases have been identified in the reviewed literature. Within 33 minutes, a mean of 3.9% of the administrated radioactive dose was measured in the urine. The amount of radiation exposure of the urinary bladder at two hours post-administration suggests that 20.6% (mean) of the radioactive dose was present in the bladder.

Special Populations:

The pharmacokinetics of Fludeoxyglucose F 18 Injection have not been studied in renally-impaired, hepatically impaired or pediatric patients. Fludeoxyglucose F 18 is eliminated through the renal system. Avoid excessive radiation exposure to this organ system and adjacent tissues.

The effects of fasting, varying blood sugar levels, conditions of glucose intolerance, and diabetes mellitus on Fludeoxyglucose F 18 distribution in humans have not been ascertained [see Warnings and Precautions (5.2)].

13 NONCLINICAL TOXICOLOGY

13.1 Carcinogenesis, Mutagenesis, Impairment of Fertility

Animal studies have not been performed to evaluate the Fludeoxyglucose F 18 Injection carcinogenic potential, mutagenic potential or effects on fertility.

14 CLINICAL STUDIES

14.1 Oncology

The efficacy of Fludeoxyglucose F 18 Injection in positron emission tomography cancer imaging was demonstrated in 16 independent studies. These studies prospectively evaluated the use of Fludeoxyglucose F 18 in patients with suspected or known malignancies, including non-small cell lung cancer, colo-rectal, pancreatic, breast, thyroid, melanoma, Hodgkin's and non-Hodgkin's lymphoma, and various types of metastatic cancers to lung, liver, bone, and axillary nodes. All these studies had at least 50 patients and used pathology as a standard of truth. The Fludeoxyglucose F 18 Injection doses in the studies ranged from 200 MBq to 740 MBq with a median and mean dose of 370 MBq.

In the studies, the diagnostic performance of Fludeoxyglucose F 18 Injection varied with the type of cancer, size of cancer, and other clinical conditions. False negative and false positive scans were observed. Negative Fludeoxyglucose F 18 Injection PET scans do not exclude the diagnosis of cancer. Positive Fludeoxyglucose F 18 Injection PET scans can not replace pathology to establish a diagnosis of cancer. Non-malignant conditions such as fungal infections, inflammatory processes and benign tumors have patterns of increased glucose metabolism that may give rise to false-positive scans. The efficacy of Fludeoxyglucose F 18 Injection PET imaging in cancer screening was not studied.

14.2 Cardiology

The efficacy of Fludeoxyglucose F 18 Injection for cardiac use was demonstrated in ten independent, prospective studies of patients with coronary artery disease and chronic left ventricular systolic dysfunction who were scheduled to undergo coronary revascularization. Before revascularization, patients underwent PET imaging with Fludeoxyglucose F 18 Injection (74 to 370 MBq, 2 to 10 mCi) and perfusion imaging with other diagnostic radiopharmaceuticals. Doses of Fludeoxyglucose F 18 Injection ranged from 74 to 370 MBq (2 to 10 mCi). Segmental, left ventricular, wall-motion assessments of asynergic areas made before revascularization were compared in a blinded manner to assessments made after successful revascularization to identify myocardial segments with functional recovery.

Left ventricular myocardial segments were predicted to have reversible loss of systolic function if they showed Fludeoxyglucose F 18 accumulation and reduced perfusion (i.e., flow-metabolism mismatch). Conversely, myocardial segments were predicted to have irreversible loss of systolic function if they showed reductions in both Fludeoxyglucose F 18 accumulation and perfusion (i.e., matched defects).

Findings of flow-metabolism mismatch in a myocardial segment may suggest that successful revascularization will restore myocardial function in that segment. However, false-positive tests occur regularly, and the decision to have a patient undergo revascularization should not be based on PET findings alone. Similarly, findings of a matched defect in a myocardial segment may suggest that myocardial function will not recover in that segment, even if it is successfully revascularized. However, false-negative tests occur regularly, and the decision to recommend against coronary revascularization, or to recommend a cardiac transplant, should not be based on PET findings alone. The reversibility of segmental dysfunction as predicted with Fludeoxyglucose F 18 PET imaging depends on successful coronary revascularization. Therefore, in patients with a low likelihood of successful revascularization, the diagnostic usefulness of PET imaging with Fludeoxyglucose F 18 Injection is more limited.

14.3 Neurology

In a prospective, open label trial, Fludeoxyglucose F 18 Injection was evaluated in 86 patients with epilepsy. Each patient received a dose of Fludeoxyglucose F 18 Injection in the range of 185 to 370 MBq (5 to 10 mCi). The mean age was 16.4 years (range: 4 months to 58 years; of these, 42 patients were less than 12 years and 16 patients were less than 2 years old). Patients had a known diagnosis of complex partial epilepsy and were under evaluation for surgical treatment of their seizure disorder. Seizure foci had been previously identified on ictal EEGs and sphenoidal EEGs. Fludeoxyglucose F 18 Injection PET imaging confirmed previous diagnostic findings in 16% (14/87) of the patients; in 34% (30/87) of the patients, Fludeoxyglucose F 18 Injection PET images provided new findings. In 32% (27/87), imaging with Fludeoxyglucose F 18 Injection was inconclusive. The impact of these imaging findings on clinical outcomes is not known.

Several other studies comparing imaging with Fludeoxyglucose F 18 Injection results to subsphenoidal EEG, MRI and/or surgical findings supported the concept that the degree of hypometabolism corresponds to areas of confirmed epileptogenic foci. The safety and effectiveness of Fludeoxyglucose F 18 Injection to distinguish idiopathic epileptogenic foci from tumors or other brain lesions that may cause seizures have not been established.

15 REFERENCES

1. Gallagher B.M., Ansari A., Atkins H., Casella V., Christman D.R., Fowler J.S., Ido T., MacGregor R.R., Som P., Wan C.N., Wolf A.P., Kuhl D.E., and Reivich M. "Radiopharmaceuticals XXVII. 18F-labeled 2-deoxy-2-fluoro-d-glucose as a radiopharmaceutical for measuring regional myocardial glucose metabolism in vivo: tissue distribution and imaging studies in animals," J Nucl Med, 1977; 18, 990-6.
2. Jones S.C., Alavi, A., Christman D., Montanez, I., Wolf, A.P., and Reivich M. "The radiation dosimetry of 2 [F-18] fluoro-2-deoxy-D-glucose in man," J Nucl Med, 1982; 23, 613-617.
3. Kocher, D.C. "Radioactive Decay Tables: A handbook of decay data for application to radiation dosimetry and radiological assessments," 1981, DOE/TIC-I 1026, 89.
4. ICRP Publication 53, Volume 18, No. I-4,1987, pages 75-76.

16 HOW SUPPLIED/STORAGE AND DRUG HANDLING

Fludeoxyglucose F 18 Injection is supplied in a multi-dose, capped 30 mL and 50 mL glass vial containing between 0.740 to 7.40 GBq/mL (20 to 200 mCi/mL), of no carrier added 2-deoxy-2-[F 18] fluoro-D-glucose, at end of synthesis, in approximately 15 to 50 mL. The contents of each vial are sterile, pyrogen-free and preservative-free.

NDC 40028-511-30; 40028-511-50

Receipt, transfer, handling, possession, or use of this product is subject to the radioactive material regulations and licensing requirements of the U.S. Nuclear Regulatory Commission, Agreement States or Licensing States as appropriate.

Store the Fludeoxyglucose F 18 Injection vial upright in a lead shielded container at 25°C (77°F); excursions permitted to 15-30°C (59-86°F).

Store and dispose of Fludeoxyglucose F 18 Injection in accordance with the regulations and a general license, or its equivalent, of an Agreement State or a Licensing State.

The expiration date and time are provided on the container label. Use Fludeoxyglucose F 18 Injection within 12 hours from the EOS time.

17 PATIENT COUNSELING INFORMATION

Instruct patients in procedures that increase renal clearance of radioactivity.

Encourage patients to:

- drink water or other fluids (as tolerated) in the 4 hours before their PET study.
- void as soon as the imaging study is completed and as often as possible thereafter for at least one hour.

Manufactured by: PETNET Solutions Inc.
810 Innovation Drive
Knoxville, TN 37932

Distributed by: PETNET Solutions Inc.
810 Innovation Drive
Knoxville, TN 37932

PETNET Solutions

PN0002262 Rev. A

March 1, 2011

Why We Should Reduce Sedation in Pediatric MRI and What We Need to Do It

Robert J. Min, M.D., MBA

Chairman of Radiology, Weill Cornell Medical College; Radiologist in Chief, NewYork-Presbyterian Hospital; President, Weill Cornell Imaging at NewYork-Presbyterian, New York, NY, USA

With its excellent soft tissue contrast for distinguishing between normal and abnormal tissue, MRI remains one of the most powerful imaging tools we as clinicians have. In clinical practice, it can offer us information that truly can't be obtained any other way. And yet as powerful a tool as MRI is, it can be challenging to perform an MRI exam on some adults – and particularly on children*– without sedation. However, sedation itself poses its own risks.

When you give any medication to a patient, there is always the risk of an allergic or adverse reaction. In very rare cases, this can even result in death. Even if we discount these rare allergic reactions to sedation, any child or adult who receives sedation requires a longer recovery period after the exam. Patients may feel nauseated or groggy and they cannot rapidly return to normal activities. Among pediatric patients, these effects – and the risks associated with them – are further amplified.

Perhaps, the greatest risk to children is the risk of foregoing an important exam because of fear of sedation. As a parent myself and in speaking to other parents, I know this is a real fear. Some parents might withhold what might be a very valuable imaging exam, one that provides more and better clinical information, out of fear.

Over the years, there have been many attempts to reduce pediatric sedation in response to patient and parent anxieties. Practices have tried painting exam rooms and using decals to make exam rooms more child-friendly. Some imaging departments allow children to play music or watch videos to further distract them during their exams. To some degree, these programs are helpful.

As an industry, though, we could learn from pediatric dentists, who have made significant inroads to distracting their young patients and reducing their anxiety. For example, many dental practices allow children to pick a small toy after the exam, which leaves the child with a good memory for the next visit. That's a technique we don't typically use in imaging and one we should employ as part of a larger, more comprehensive program that addresses the anxieties and questions children and their parents have before the exam, during their visit, and, in many cases, after they leave.

By helping children understand what an MRI is, including what it looks like, what it sounds like, and what it does, I am convinced we can make a difference. I don't think we give 5- or 6-year-old children enough credit when it comes to their ability to understand and cooperate during an exam. With the right education before the exam, I am 100 percent convinced we can lower the rates of pediatric sedation.

That's what this new educational program strives to do. We are working to provide children and their parents with the tools and information they need to be more comfortable with an MRI exam – before they even come in for it. This can reduce patient and parental anxieties and limit the need for sedation for many children. In addition, reduction in sedation will eventually improve workflow efficiency and decrease costs. When a fun, educational program becomes part of routine imaging practice, positive results will follow – and not just in children. Adults could benefit from more and better education about what to expect from an MRI exam too.

We can – and should – work to reduce pediatric sedation in MRI. In many cases, it's the right thing to do for our patients, for their families, and for our practices.

*MR scanning has not been established as safe for imaging fetuses and infants under two years of age. The responsible physician must evaluate the benefit of the MRI examination in comparison to other imaging procedures.

Contact

Robert J. Min, M.D., MBA
Chairman of Radiology, Weill Cornell Medical College
Radiologist in Chief, NewYork-Presbyterian Hospital
President, Weill Cornell Imaging at NewYork-Presbyterian
525 East 68th Street
Starr 8a-37
New York, NY 10065
USA
Phone: +1 212-746-2520
rjm2002@med.cornell.edu

MRI Heroes Kit

In the USA we offer an MRI Heroes Kit to support pediatric imaging: Each MRI Heroes Kit includes an educational DVD; a mini-model of a Siemens MRI scanner; 100 copies of an educational Marvel Custom Solutions comic book featuring popular characters Captain America and Iron Man; 100 hero-themed capes; and 100 Captain America and Iron Man plush toys.

The educational video walks the patient through the process of an MRI exam via the experiences of a 10-year-old* girl who recently received a scan, detailing what pediatric patients and their parents can expect from the procedure. The video can be shown to patients and their parents on the facility's website as well as in the waiting room to help the child prepare for the exam.

The mini-model of a Siemens MRI system can be positioned in the hospital's play area and used by hospital staff to further educate children on the imaging process.

The Marvel Custom Solutions comic book explains an MR exam via an action-packed, visually compelling story and can be read to children by their parents or read by the child during a hospital visit.

The plush toy, which the young patient can hold during the exam, provides a fun way for hospital staff to reference the comic book storyline and interact with the child. The hero cape can be given to the child as a reward for completing the scan.

Should you be interested in the MRI Heroes Kit, please contact your local Siemens representative.

WIP, the product is currently under development and is not for sale in the US and in other countries.
Its future availability cannot be ensured.

How I do it: Renal Non-Enhanced MR Angiography (*syngo* NATIVE TrueFISP) in Pediatric Patients

Jie Deng, Ph.D.[1]; Marci Messina, RT(R)(MR)[1]; Gary McNeal, MS[2]; Xiaoming Bi, Ph.D.[3]; Brian Reilly, RT (R)[1]; Sheila Bero, BSRT (R)[2]; Shivraman Giri, Ph.D.[2]; Cynthia K. Rigsby, M.D.[1]

[1] Ann & Robert H. Lurie Children's Hospital of Chicago, Chicago, IL, USA
[2] Siemens Medical Solutions USA, Inc, Chicago, IL, USA
[3] Siemens Medical Solutions USA, Inc, Los Angeles, CA, USA

Background

The association between nephrogenic systemic fibrosis (NSF) and gadolinium-based (Gd) contrast agents has generated an active interest in the development and optimization of Non-Enhanced MR Angiography (NE-MRA) techniques. These techniques rely on physiologic processes, in conjunction with careful application of radio-frequency (RF) and gradient pulses, for maximizing the contrast between the desired vasculature and the rest of background.

syngo NATIVE TrueFISP was developed to optimize the conspicuity of renal arteries without administration of contrast, and is ideal to assess renal arteries in patients following kidney transplantation, impaired renal function, allergy to gadolinium based contrast agents, pregnant women, and neonates*. Renal NE-MRA aims to provide robust and high resolution MRA with maximal arterial signal and suppression of static tissue signal and venous flow. Figure 1 summarizes the principle of this sequence [1]. It utilizes 3D TrueFISP readout for bright-blood imaging. Background tissues are suppressed using one or more selective inversion pulses. To minimize respiratory motion-induced artifacts, the data acquisition has typically been synchronized to the respiratory cycle with respiratory gating using cross-pair navigator. A new alternative technique involves the use of respiratory bellows for respiratory gating because it is easier to setup than cross-pair navigator, and it also provides better and consistent image quality.

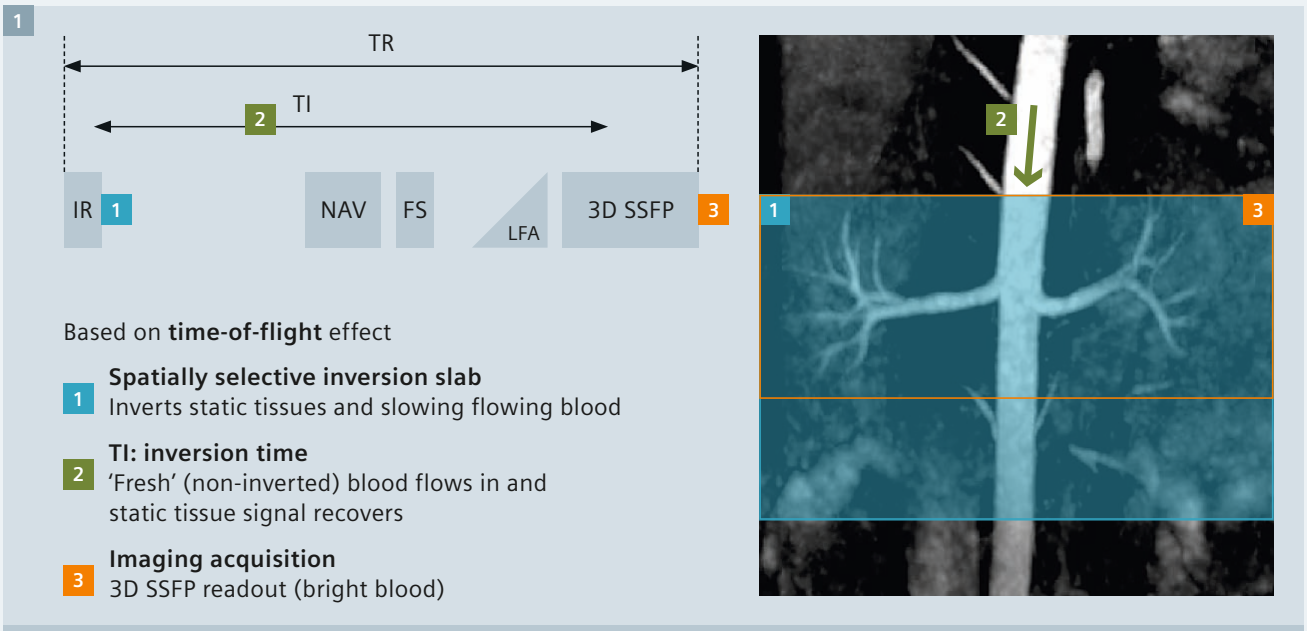

1 Basic principle of renal NE-MRA using *syngo* NATIVE TrueFISP.

NAV: respiratory navigator (optional); **FS:** fat saturation; **TR:** repetition time; **LFA:** 'linear flip angle' catalyzation for TrueFISP

Objectives

While an earlier article [2] offers many suggestions for protocol optimization in adult patients using *syngo* NATIVE TrueFISP, in this article we summarize our experience of imaging native and transplant renal arteries in pediatric* patients using this technique, and offer some additional hints and tricks for imaging patients of different ages.

Materials and methods

syngo NATIVE TrueFISP utilizes a slab of selective inversion pre-pulse with an inversion time (TI) to suppress signals from static tissues within the imaging volume, while enhancing arterial inflow. The inversion slab is asymmetric with reference to the imaging volume to reduce inflowing venous signal. In addition, the position of inversion slab relative to the imaging slab is critical to achieve optimal renal artery enhancement with minimal background and venous contamination. Figure 1 summarizes the basic principle of the default/original NATIVE TrueFISP that uses cross-pair navigator gating.

In the new approach, we propose the use of an alternative physiological gating method ('respiratory bellows without cardiac triggering') rather than the traditional method ('cross-pair navigator with cardiac triggering') for three reasons:

1. Positioning of the navigator cross-pair is not required, thereby increasing ease of use.
2. Positioning of the ECG electrodes is not required, thereby increasing ease of use.
3. Longer TI may be used for the inversion slab, thereby increasing the depth of penetration of the arterial signal into the FOV (better visualization of intra-renal arteries).

a. Patient setup: Place patient in a supine, head first position comforted with pillows and knee support cushions for best patient cooperation. Place the respiratory bellows (pictured in Figure 2) on the anterior surface of the patient's abdomen at a position where the inspiration and expiration waveforms are best visualized on the Physiological Monitoring Unit (PMU) display, then wrap the respiratory belt securely around the bellows to maintain its placement during the scan. Connect the respiratory tubing from the bellows into the ECG/Respiratory PERU unit. Since ECG triggering is not used in this technique, only the respiratory trigger signal must be monitored in the PMU display during this exam.

Triggering setup: Use respiratory bellows triggering with acquisition parameters as follows: Set TR/Acquisition Window = 2200 ms, Threshold = 35%, Trigger Delay = 0, Respiratory Phase = Expiration (Fig. 3). Note, if desired to further increase the depth of penetration of the arterial signal into the FOV, it may be necessary to slightly increase theTR/Acquisition Window in order to slightly increase the TI of the first inversion slab, but with a resulting slight loss of background suppression.

b. Imaging FOV setup: For coronal acquisitions center the imaging FOV on the renal arteries with L-R phase encoding – 100% phase oversampling mitigates lateral wrap from the abdomen (Fig. 4). For axial acquisitions center the imaging FOV on the renal arteries with A-P phase encoding – no phase oversampling is required (Fig. 4).

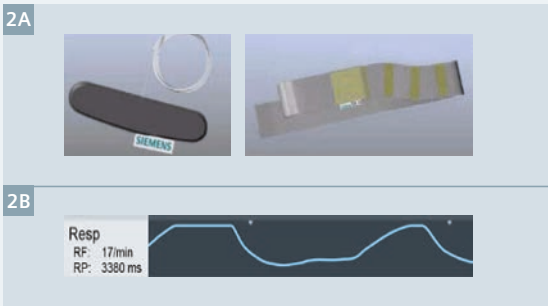

2 Respiratory bellows and the belt used for adjustment in patients **(2A)**. Signal detected by the physiologic monitoring unit **(2B)**.

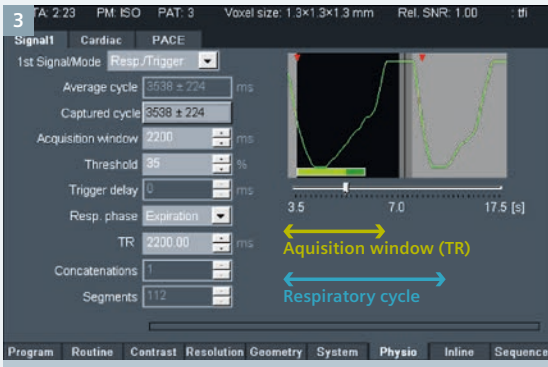

3 Settings on the physio card (for software version *syngo* MR D13) for the use of respiratory bellows.

*Siemens disclaimer: MR scanning has not been established as safe for imaging fetuses and infants less than two years of age. The responsible physician must evaluate the benefits of the MR examination compared to those of other imaging procedures.

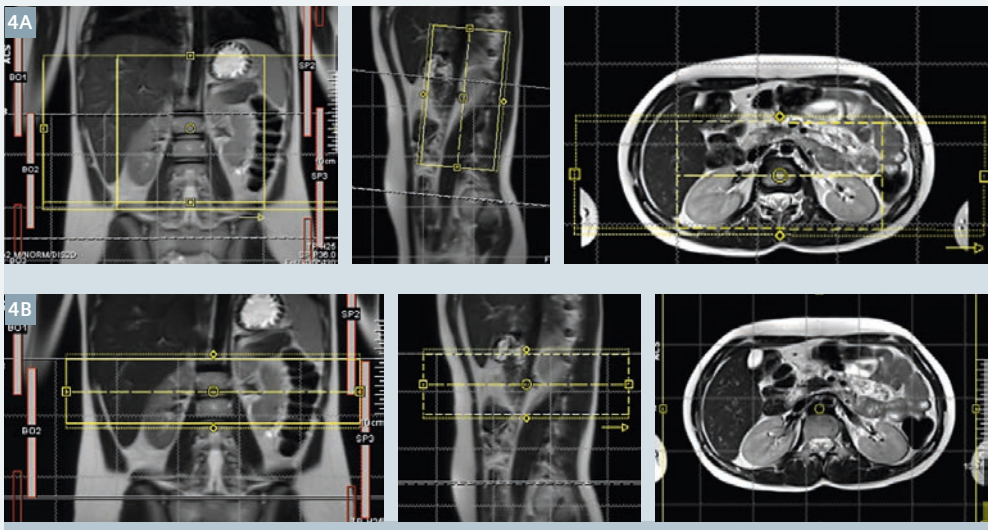

4 Centering the imaging field-of-view for coronal **(4A)** and axial **(4B)** acquisitions.

a. Inversion slab setup: The inversion slabs are setup identically for both coronal and axial acquisitions. The top edge of the first inversion slab (thickness = 150 mm, TI = 1100–1350 ms) is aligned to the top of the kidneys (blue band in Figure 5). The top edge of the second inversion slab (thickness = 100 mm and TI = 800 ms) is aligned to the bottom edge of the first slab (orange band in Fig. 6).

b. Use 'couple graphics' to link imaging FOV and both inversion slabs for fast setup.

At our site, imaging is performed on a 1.5T MRI scanner (MAGNETOM Aera). A body matrix coil is used on top of the respiratory bellows and combined with the posterior spine array coil. The imaging time for one plane acquisition is 3–4 minutes.

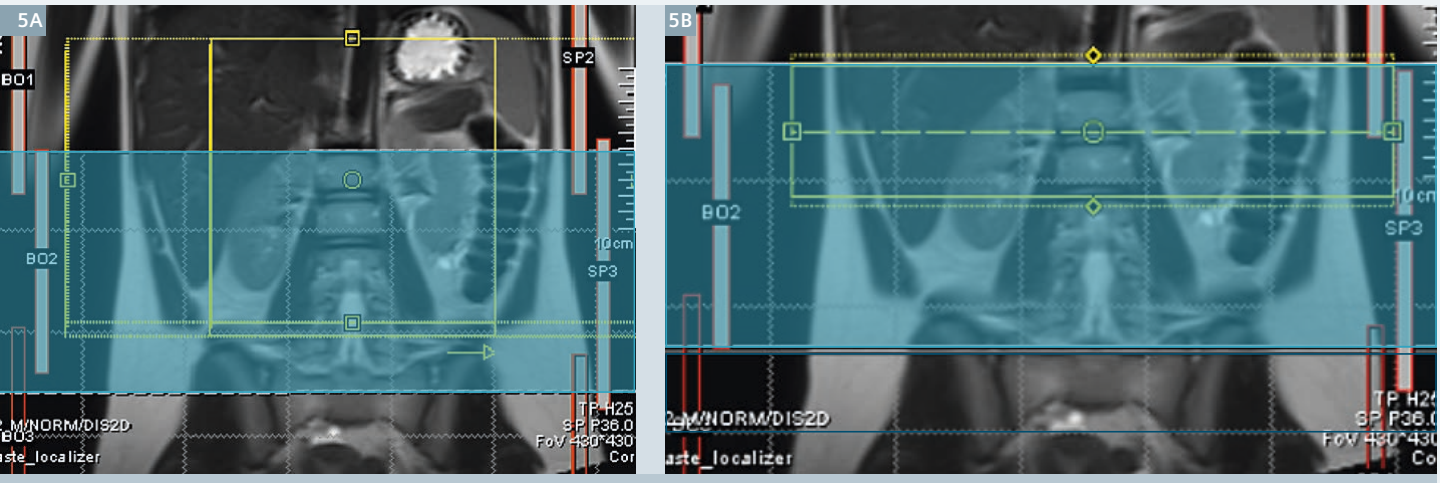

5 Positioning of the first inversion slab for coronal **(5A)** and axial **(5B)** acquisitions.
- Slab Thickness = 150 mm, inversion time (TI) = 1100–1350 ms
- Coronal acquisition: Inversion slab top aligns with the top of the kidney
- Axial acquisition: Inversion slab top aligns with the top of imaging volume

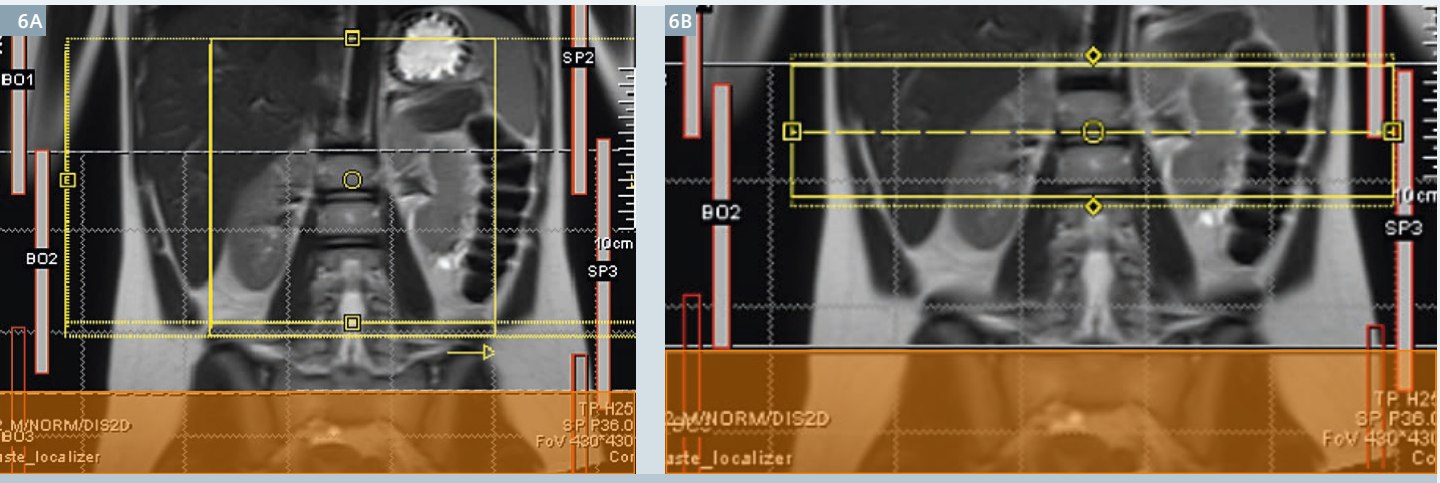

6 Positioning of the second inversion slab for coronal **(6A)** and axial **(6B)** acquisitions.
- Slab Thickness = 100 mm, inversion time (TI) = 800 ms
- Inferior to the first inversion slab to suppress venous signal from inferior vena cava
- Use 'couple graphics' to link imaging volume and both inversion slabs

Results

Figure 7 demonstrates 3D reconstructions of three different NATIVE TrueFISP acquisitions of a 16-year-old male with a kidney transplant. Images acquired with the novel method ('respiratory bellow without cardiac triggering', Fig. 7A, B) significantly improve image quality with superior delineation and integrity of renal arteries, principally due to longer TI (1200 ms) allowing deeper penetration of the arterial signal into the kidney, as compared to the traditional method ('cross-pair navigator with cardiac triggering', Fig. 7C) with much shorter TI (590 ms). In an 18-month-old* male with significant renal insufficiency and involuted left multicystic dysplastic kidney, images acquired by both respiratory and cardiac triggered NATIVE TrueFISP delineate the abdominal aorta and renal arteries with good vessel to background contrast with minimal respiratory motion and venous contamination. In this younger patient with a higher heart rate, the cardiac triggered acquisition provides smoother vessel signal by mitigating the pulsatile effect (Fig. 8B). In comparison, the respiratory triggered image (Fig. 8A) delineates more renal artery branches due to increased arterial inflow within longer TI (1100 ms). Shorter TI used in the cardiac triggered acquisition does not affect the arterial inflow as much as shown in the older patient (Fig. 7C), primarily due to the faster blood flow in younger patients.

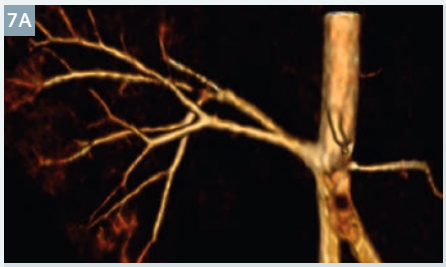

Respiratory trigger, coronal acquisition

TR/TI = 2200/1200 ms, TH = 1.3 mm
coronal FOV = 220 x 180,
matrix = 160 x 160

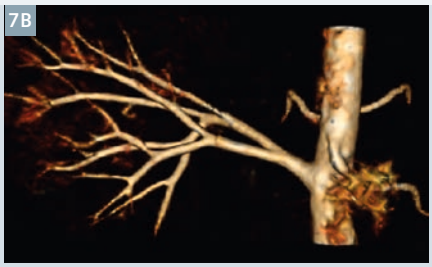

Respiratory trigger, axial acquisition

TR/TI = 2200/1200 ms, TH = 1.3 mm
axial FOV = 180 x 180,
matrix = 144 x 144

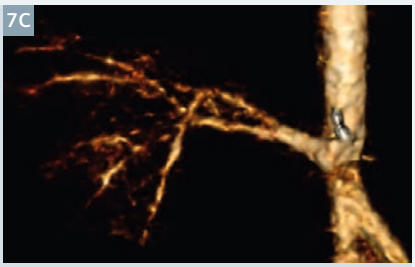

Cardiac trigger navigator, axial acquisition

TR/TI = 678/590 ms, TH = 1.2 mm
axial FOV = 256 x 320,
matrix = 184 x 240

7 16-year-old male with kidney transplant.
- Respiratory triggered images **(7A, B)** show significantly improved image quality compared to cardiac triggered image **(7C)**.
- Respiratory triggered image using axial plane acquisition **(7B)** provides better vessel delineation, integrity and smoothness, compared to coronal acquisition **(7A)** in this patient.

Respiratory trigger, axial acquisition

TR/TI = 2200/1100 ms, TH = 1.1 mm
FOV = 160 x 200, Matrix = 148 x 192

Cardiac trigger navigator, axial acquisition

TR/TI = 451/368 ms, TH = 1.1 mm
FOV = 160 x 200, Matrix = 148 x 192

8 18-month-old* male with renal insufficiency and right kidney mass and history of left multicystic dysplastic kidney with involution of the left kidney.
- Respiratory triggered image **(8A)** shows the most complete renal artery branches compared to the cardiac triggered image **(8B)**.
- For a young patient with fast blood flow, lower TI and cardiac triggering may help improve the vessel integrity and smoothness.

Figures 9 and 10 demonstrate 3D reconstructions of respiratory bellow triggered (TI 1350 ms) NATIVE True-FISP images of two different renal transplant patients. The axial acquisition (Fig. 9) demonstrates higher resolution, higher signal-to-noise ratio (SNR), and higher contrast-to-noise ratio (CNR) as compared to the coronal acquisition (Fig. 10), but with less coverage along the head to foot axis.

Conclusion

In this study, we have optimized the NATIVE TrueFISP renal NE-MRA protocol in pediatric* patients by using respiratory bellows without cardiac triggering method. Compared to the traditional method with cross-pair navigator and cardiac triggering, the new method allows longer effective TR and thus longer TI for deeper penetration of arterial inflow and therefore providesbetter visualization of intra-renal arterial signal. In addition, the use of inferior inversion slab further reduces the venous contamination. We have successfully implemented this protocol in our patients (5 month* to 19 years old) and have obtained robust and high resolution renal NE-MRA. We have noticed that in younger patients with higher heart rates or patients with unstable heart rates, the lack of cardiac triggering may cause vessel signal degradation, therefore, we recommend to use cardiac triggering with cross-pair navigator as an optional acquisition method in those patients.

9

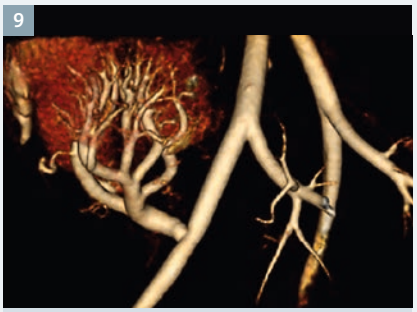

Respiratory trigger, axial acquisition

TR/TI = 2200/1350 ms, TH = 1.1 mm
FOV = 225 x 300, Matrix = 192 x 256

9 15-year-old* male s/p kidney transplant with a widely patent transplant renal artery and anastomosis between the transplant renal artery and the right external iliac artery.

10

Respiratory trigger, coronal acquisition

TR/TI = 2200/1350 ms, TH = 1.3 mm
FOV = 200 x 200, matrix = 144 x 144

10 8-year-old* male s/p kidney transplant.

References

1 Liu X, Berg N, Sheehan J, Bi X, Weale P, Jerecic R, Carr J. Renal transplant: nonenhanced renal MR angiography with magnetization-prepared steady-state free precession. Radiology. 2009 May;251(2):535-42.

2 Rick M et al. "How I do it: Non contrast-enhanced MR Angiography (*syngo* NATIVE). MAGNETOM Flash 3/2009.

*Siemens disclaimer: MR scanning has not been established as safe for imaging fetuses and infants less than two years of age. The responsible physician must evaluate the benefits of the MR examination compared to those of other imaging procedures.

Contact

Jie Deng, Ph.D., DABMP
MR Physicist, MR Safety Officer, Medical Imaging
Ann & Robert H. Lurie Children's Hospital of Chicago;
Research Assistant Professor, Radiology
Feinberg School of Medicine
Northwestern University
225 East Chicago Avenue, Box 9
Chicago, Illinois 60611-2605,
USA
Phone: +1 312.227.3394
Fax: +1 312.227.9786
jdeng@luriechildrens.org

The magazine of MR

MAGNETOM Flash

turns 60...

...and says thank you to all authors and readers.

With the first issue published in 1993 we are not celebrating our 60th birthday, but issue no. 60.
From the very beginning, MAGNETOM Flash was a cooperation between Siemens Healthcare and MAGNETOM users.
The first editor of the newspaper sized publication was Christine Harris, R.T. at Children's Hospital of Philadelphia, USA and the focus of the 'newsletter' was a communication network between Technologists and the Siemens Corporation. As the newsletter developed into a magazine the target group grew to include radiologists, physicists, cardiologists and researchers.
What did not change is the involvement of you - our readers. Being part of the MAGNETOM World, the community for all Siemens MR users worldwide, the magazine is affording you a platform to contribute and expand your knowledge.
We welcome your feedback, questions and comments – please contact us at **magnetomworld.med@siemens.com**.

www.siemens.com/magnetom-world – communications keeping you up-to-date.

Quiescent-Intervall Single-Shot Magnetic Resonance Angiography

Robert R. Edelman[1,2]; Shivraman Giri[3]; Eugene Dunkle[1]; Ioannis Koktzoglou[1,4]

[1] NorthShore University HealthSystem, Evanston, IL, USA
[2] Feinberg School of Medicine, Northwestern University, Chicago, IL, USA
[3] Siemens Medical Solutions USA, Inc., Chicago, IL, USA
[4] The University of Chicago Pritzker School of Medicine, Chicago, IL, USA

Introduction

More than 200 million people worldwide are afflicted by peripheral arterial disease (PAD) [1, 2]. Over the last decade, the incidence of PAD has risen by approximately 13% in high-income countries and 29% in low-income countries [3]. Patients with PAD have a high 10-year risk of death of 40%, 3-fold higher risk of all cause death and 6-fold higher risk of cardiovascular-related death than patients without PAD [4]. Accurate diagnosis is thus critical for disease management and for improving patient outcomes.

The availability of accurate non-invasive imaging tests has decreased the need for preoperative digital subtraction angiography (DSA) in the evaluation of PAD. The ankle brachial index (ABI) is an excellent screening test for hemodynamically significant PAD and can be performed in conjunction with Doppler waveform analysis and segmental pressure measurement in an effort to increase accuracy [5]. However, its sensitivity is low in elderly patients and those with diabetes [6]. Moreover, additional imaging is often needed to help plan for interventional procedures. Computed tomographic angiography (CTA) offers high spatial resolution and short scan times without the risks associated with DSA [7]. For ≥50% stenosis, the reported sensitivity of peripheral CTA is on the order of 89%-100%, with specificity reported at 92%-100% [8]. However, the clinical utility of peripheral CTA is diminished by the presence of vessel wall calcifications, which are associated with diabetes, heart dis-

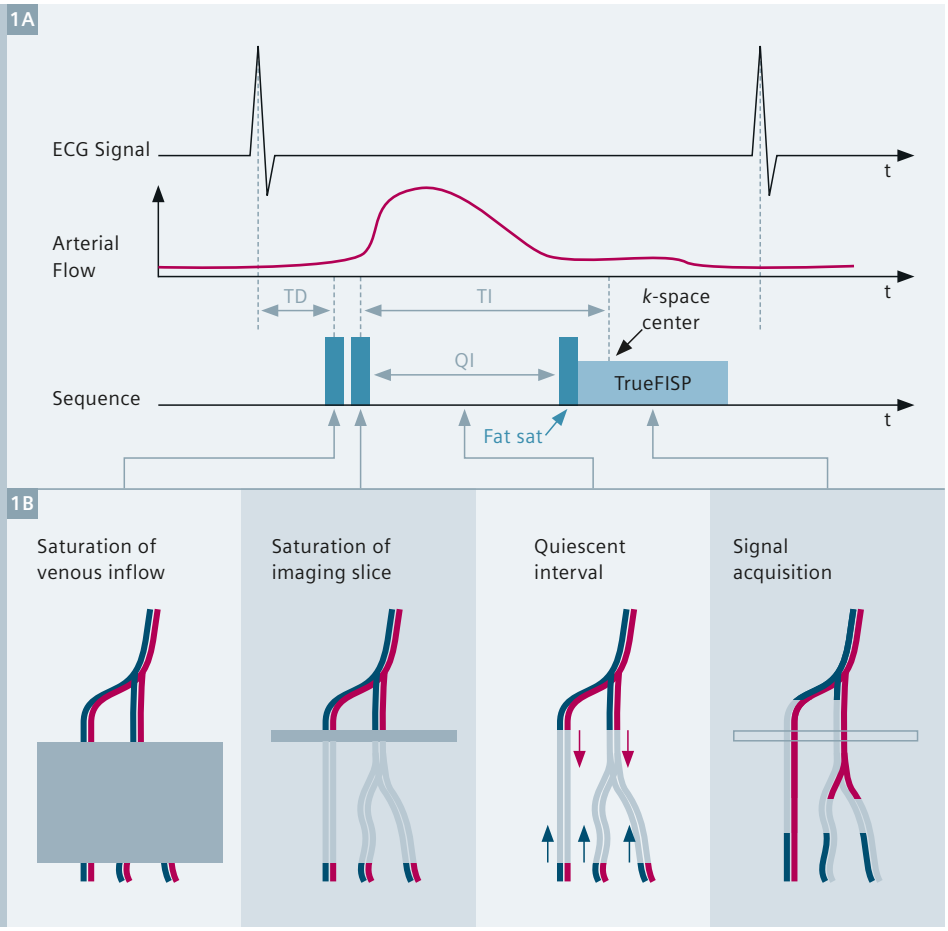

1 QISS* pulse sequence diagram **(1A, top)** and schematic of vasculature (**1B, bottom**) showing the effect of pulse-timings on signal manipulation to maximize arterial conspicuity. In-plane saturation and tracking venous saturation RF pulses are applied TD ~ 100 ms after the R-wave; these pulses suppress background and venous signal. Following a preset quiescent interval (QI) of 228 ms, during which unsaturated arterial blood flows into the imaging slice, a fat suppression RF pulse is applied, followed by single-shot TrueFISP readout. This process is repeated in subsequent heart-beats to acquire other slices, usually in foot-to-head direction. In the basic configuration used for survey examinations, one 3 mm-thick slice is acquired per RR interval with 1 x 1 mm in-plane spatial resolution.

ease, and advanced age [9]. CT angiography has the disadvantage of exposing patients to ionizing radiation and there is also the associated risk of contrast-induced nephropathy (CIN), which is of particular concern because nearly 40% of patients with PAD have significant renal dysfunction [10]. Contrast-enhanced magnetic resonance angiography (CEMRA) has also been shown to be highly accurate for the detection of stenoses ≥50% within the lower extremity arterial tree [11]. Unfortunately, the administration of gadolinium-based contrast agents in patients with severely impaired renal function is contraindicated due to the risk of nephrogenic systemic fibrosis (NSF) [12].

Non-enhanced MRA Techniques

Non-enhanced MRA (NEMRA, i.e. MRA without contrast agents) avoids the potential risks of NSF and CIN, as well as ionizing radiation. Two-dimensional time-of-flight NEMRA methods have been available for decades [13, 14]. However, lengthy acquisition times (typically approaching an hour or more) and image artifacts have limited their routine use in favor of contrast-enhanced techniques. Newer subtractive approaches for NEMRA of the peripheral arteries have been proposed which allow efficient depiction of arteries over large fields-of-view and suppress venous signal. These include ECG-gated subtractive 3D turbo spin echo (TSE) imaging such as fresh blood imaging (FBI) [15] and NATIVE SPACE (NATIVE = Non-contrast angiography of the arteries and veins; SPACE = Sampling perfection with application optimized contrast by using different flip angle evolution) [16], as well as variants predicated on 3D balanced steady-state free precession (bSSFP) imaging such as flow-sensitive dephasing [17]. Of these, subtractive TSE MRA techniques have the most clinical validation and are commercially available. However, subtractive TSE MRA is not robust due to its sensitivity to patient motion, pulse wave timing, and abnormal flow patterns [16].

The Quiescent-Intervall Single-Shot* (QISS) NEMRA technique was developed as a safer, simple 'push button' non-enhanced alternative to CTA and CEMRA (Fig. 1) [18]. Moreover, QISS MRA eliminates the need for point-of-service blood draws to determine eGFR and yields significant cost savings ($180 per study at our institution) compared with CEMRA by eliminating the MR contrast agent and injector kit. QISS offers several advantages over previously described NEMRA techniques (Fig. 2) [19]. It is highly robust with minimal sensitivity to patient motion and cardiac arrhythmias. It has the particular advantage of enabling a simple and efficient workflow, thereby eliminating the need for special technologist expertise.

*QISS is pending 510(k) clearance and is not commercially available in the US.

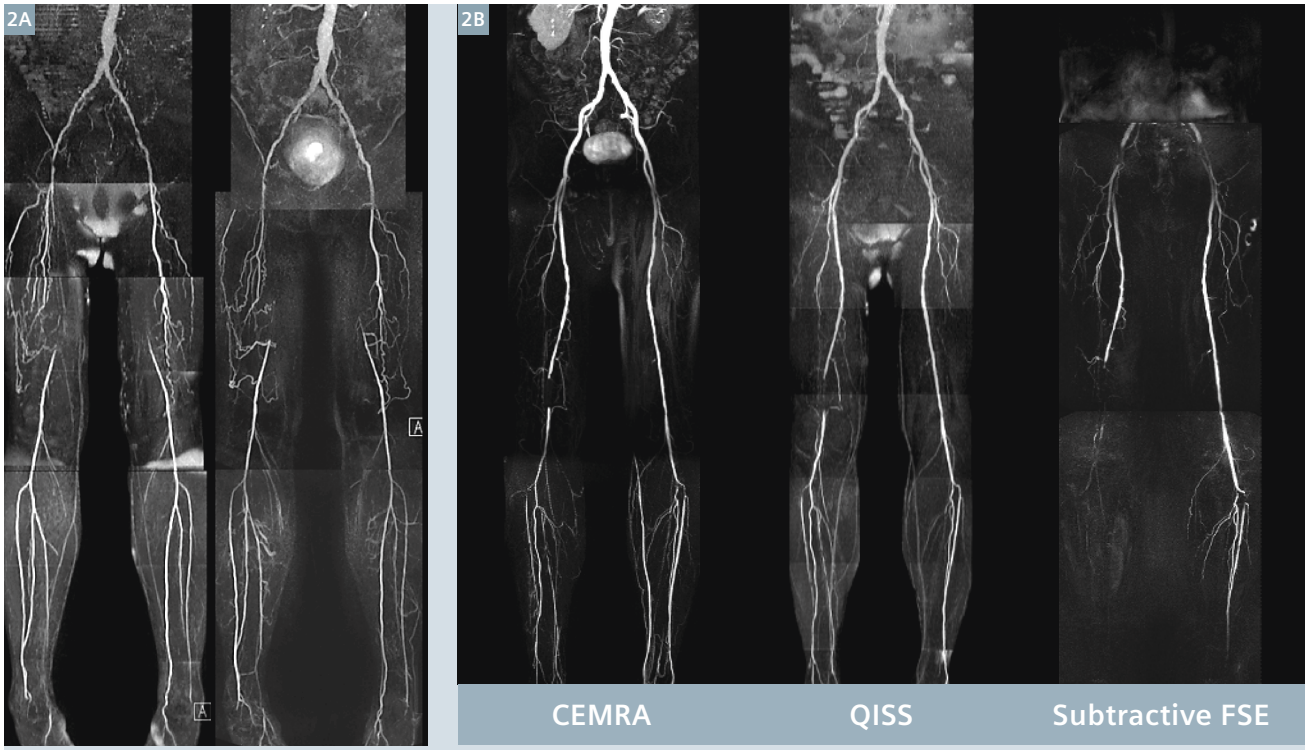

2 **(2A)** 91-year-old smoker with bilaterally occluded superficial femoral arteries (SFA). QISS MRA (left) and CEMRA (right) appear comparable. **(2B)** CEMRA, QISS, and subtractive TSE MRA (Native SPACE) in a patient with PAD. Multiple ≥50% stenoses in the right anterior and posterior tibial arteries and occlusion of the left posterior tibial artery are identified on CEMRA and QISS MRA. Subtractive TSE MRA shows extensive artifactual signal dropout in the abdomen, upper pelvis and right calf. (Signal dropout in the mid-right SFA is due to a stent.) *Adapted with permission from ref. 19*

Clinical Validation

QISS MRA has been evaluated at field strengths ranging from 1.5 Tesla to 7 Tesla*, with the reported accuracy at 1.5 Tesla and 3 Tesla generally approaching or matching that of CEMRA.[20-26] The technique has also been specifically evaluated in a diabetic patient population in whom CTA may be problematic due to the frequent presence of vascular calcifications and poor renal function.[27] Using CEMRA as the reference standard, QISS showed excellent diagnostic performance with sensitivity of 89.8%, specificity of 96.4%, positive predictive value of 92.4%, and negative predictive value of 95.0%. An example illustrating the advantage of QISS MRA over CTA for the evaluation of diabetic PAD patients is given in Figure 3.

*MAGNETOM 7T is ongoing research. All data shown are acquired using a non-commercial system under institutional review board permission. MAGNETOM 7T is still under development and not commercially available yet. Its future availability cannot be ensured.

QISS as scout and backup for CEMRA

Currently, many sites use a multi-station, multi-planar scout acquisition to plan the volume placements for stepping table CEMRA. This procedure can be cumbersome since the full extent of the arteries is not visible on the scout images. For such situations, QISS acquisition can potentially serve as a scout image for CEMRA; although it will take longer than the regular scout, it offers more complete and detailed visualization of arterial tree for CEMRA, providing diagnostic information in case of a technical failure with CEMRA. For instance, the patient might move between the time that the pre-contrast mask images and post-contrast images are acquired, resulting in misregistration artifact on the subtracted CEMRA images. Being a non-subtractive single shot technique with very short scan time (<1/3 second per slice), QISS is resistant to motion artifacts. Moreover, the timing for the CEMRA may be inaccurate, resulting in poor arterial opacification or venous overlap (e.g. due to asymmetric atherosclerotic disease causing slower flow on one side, or due to human error). In all these situations, QISS can be a fallback option to salvage patient exam despite non-diagnostic CEMRA (Fig. 4).

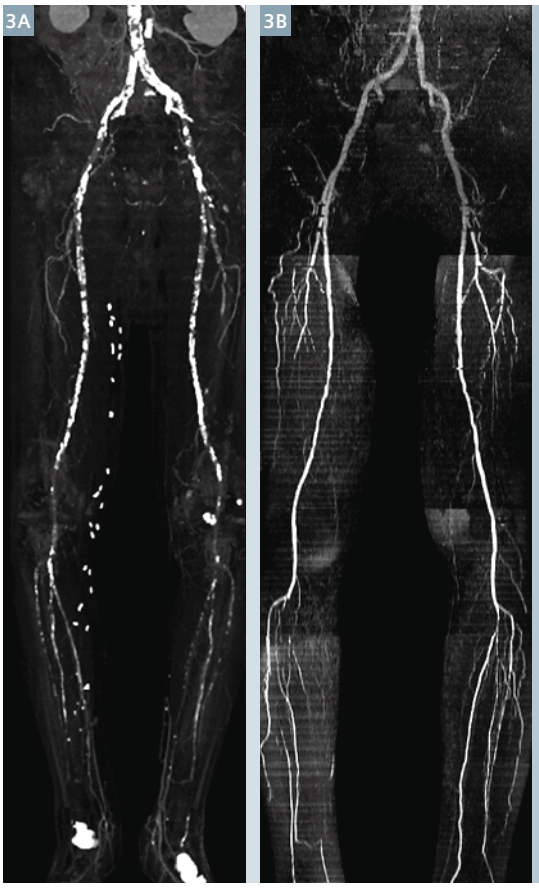

3 88-year-old male with claudication and type-2 diabetes. **(3A)** CTA; **(3B)** QISS MRA. The CTA was non-diagnostic due to the presence of extensive vascular calcifications. However, QISS MRA was completely unaffected by the vascular calcifications and demonstrated the patency of proximal vessels and occlusions of calf vessels. In this case, note that QISS MRA image quality was adequate despite the fact that the patient had atrial fibrillation. *Adapted with permission from ref. 20*

QISS at 3 Tesla

Until QISS, no NEMRA technique had proven effective at 3 Tesla, which is widely considered the optimal field strength for CEMRA. Imaging at 3 Tesla will be necessary to unlock the full clinical potential of NEMRA and to compete with the excellent spatial resolution provided by CTA. In order to take advantage of the large signal-to-noise ratio (SNR) boost at 3 Tesla, one must overcome challenges relating to high specific absorption rate (SAR) and worsened B_1 field homogeneity (Table 1).

Shortening the bSSFP shot length, which proportionately reduces RF power deposition, can ameliorate the impact of increased SAR at 3 Tesla. At 1.5 Tesla, we found that GRAPPA acceleration factors in excess of two degraded QISS image quality. Higher GRAPPA acceleration factors (3 to 4) can be used to reduce the shot length at 3 Tesla. With the SNR boost from the higher field strength, one can further reduce the shot length by increasing the sampling bandwidth (~962 Hz/pixel at 3 Tesla vs. 658 Hz/pixel at 1.5 Tesla). The higher sampling bandwidth has the further advantage of reducing bowel-related magnetic susceptibility artifacts in the pelvic region.

We have found that the combination of a GRAPPA factor of 3 and sampling bandwidth of 962 Hz/pixel are sufficient to permit a 90° flip angle to be maintained from the level of the feet through the mid-thigh level. However, this imaging strategy by itself is insufficient for the pelvic and abdominal regions, where SAR limitations are more pronounced due to larger body dimensions. Degradation of image quality from using a flip angle <90° is maximal in the pelvic region because of the additional impact of B_1 field inhomogeneity. Unfortunately, a flip angle less than 90° in the pelvis often

results in unilateral loss of arterial conspicuity with QISS MRA. One straightforward solution is to trigger to every other R-wave, which halves the time-averaged power deposition at the expense of doubling scan time. Since SAR limitations only come into play from the upper thigh region through the abdomen, triggering to every other R-wave is only used for the top three stations. Total scan time for a whole-leg study is increased by ~2-3 minutes (e.g. total scan time ~10 minutes**) which is still reasonable.

A final B_1 field-related issue is that the pre-scan image filters typically used to correct for RF coil-dependent signal intensity variations do not adequately normalize signal variations caused by B_1 field inhomogeneity at 3 Tesla. This signal variation will tend to obscure the arterial signal on a full-thickness MIP, even when the vessel is apparent on a thin MIP. The effectiveness of the pre-scan filter in the pelvis is impeded by noise amplification in the central portions of the body resulting from the use of a high GRAPPA acceleration factor. This limitation is largely avoided by using the 'broad' pre-scan filtering option. Figure 5 illustrates the image quality improvements that can be obtained when several pulse sequence optimizations are combined (e.g. high GRAPPA acceleration factor, high sampling bandwidth, FOCI venous suppression, triggering to every other R-wave for upper stations, and optimized image filtering).

Developing clinical applications

Although most clinical efforts using QISS MRA have been directed towards the lower-extremity peripheral arteries, there are several other areas where the technique appears promising. For instance, QISS MRA can be used to evaluate the arteries of the upper extremities and the veins of the lower extremities (Fig. 6). For imaging of the lower extremity veins, we typically place the traveling saturation pulse above the slice and turn off the in-plane saturation pulse (e.g. by setting the RF voltage to zero). Other potential applications include imaging of visceral arteries and veins, pulmonary vessels, and the extracranial carotid arteries. However, additional technical development and clinical validation will be needed for other vascular territories.

** This number indicates the image acquisition time, not including the time for frequency and shimming adjustments. These adjustments are performed once per station for every patient.

Table 1: Summary of challenges and solutions for 3T QISS

Challenges at 3T	Solutions
Increased SAR	• Shortened shot length using high GRAPPA acceleration factor (3-4) and high sampling bandwidth • Triggering to every other R-wave • QISS with FLASH readout
B_0 inhomogeneity	• Arterial spin labeled (ASL) QISS
B_1 inhomogeneity	• B_1-robust saturation RF pulses • FOCI inversion RF pulses • B_1-dependent image filtering • High permittivity pad

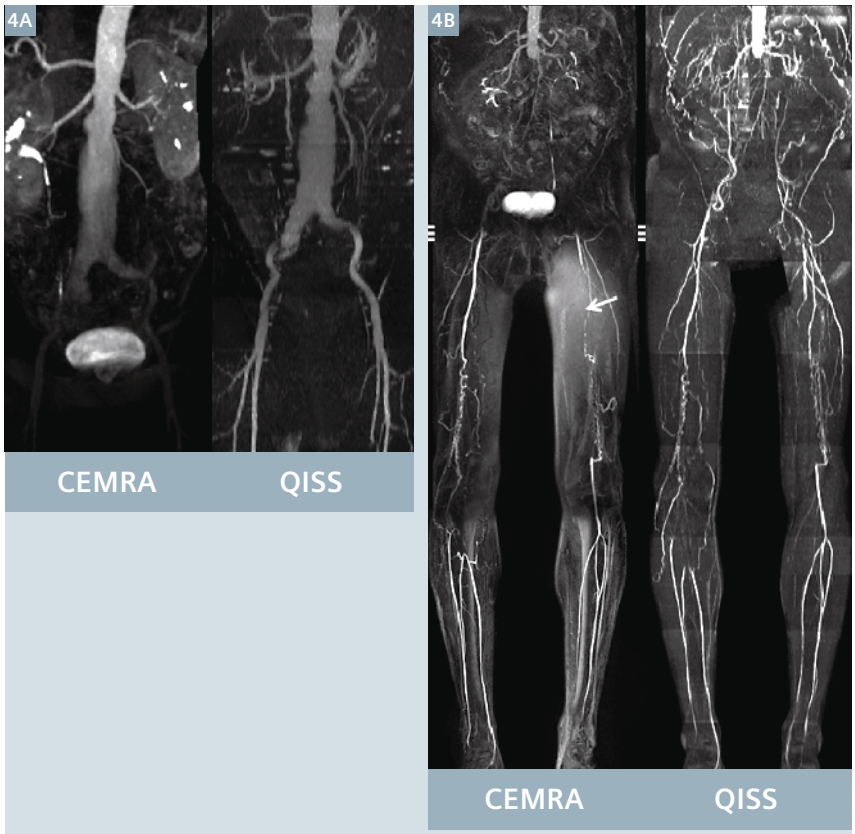

4 Cases where QISS MRA helped to salvage a non-diagnostic CEMRA.
(4A) Patient with an abdominal aortic aneurysm. Slow flow in the aneurysm delayed the contrast enhancement of the pelvic arteries, resulting in a non-diagnostic CEMRA exam. However, the pelvic arteries are well shown on the QISS scout study.
(4B) Patient with aorto-iliac and bilateral superficial femoral artery occlusive disease. Left leg motion caused misregistration artifact in part of the CEMRA (arrow), whereas the QISS scout images are diagnostic. *Adapted with permission from ref. 20*

Potential Pitfalls
Although QISS MRA has proven to be a robust imaging technique, there are potential limitations that should be kept in mind in order to avoid artifacts:

1. **Cardiac rhythm:** The default acquisition window for QISS is approximately 700 ms. In patients with medium or slow heart rates, one slice is acquired per RR interval. With rapid heart rates where the RR interval is less than 700 ms, one slice will be acquired every 2 RR intervals. It is possible to trigger to every RR interval, despite the fast heart rate, by reducing the acquisition window. This can be accomplished by slightly decreasing both the TD (in the special card, default value of 100 ms) and TI (in the contrast card, default value of 350 ms). However, if these values are reduced excessively then loss of flow signal may occur from inadequate inflow or data acquisition during the systolic phase of the cardiac cycle.

   In general, QISS is fairly insensitive to arrhythmias. However, with highly irregular heart rhythms (or with poor triggering due to an inadequate ECG signal), image quality may suffer. Work is currently under way to develop versions of QISS that do not require the use of ECG gating.

2. **Fat suppression:** QISS relies upon uniform fat suppression for optimal vessel depiction. In some areas where fat suppression is imperfect (e.g. groin area), a simple expedient is to edit out the affected region in the maximum intensity projection. However, in certain regions (e.g. the feet) it can be quite difficult to adequately shim so that fat suppression and hence QISS image quality may be suboptimal. For the pedal vessels, we have found that image quality is further improved by placing a small cushion between the top of each foot and the Peripheral Angio 36 coil, since having the coil touching the foot tends to impair the quality of the shim.

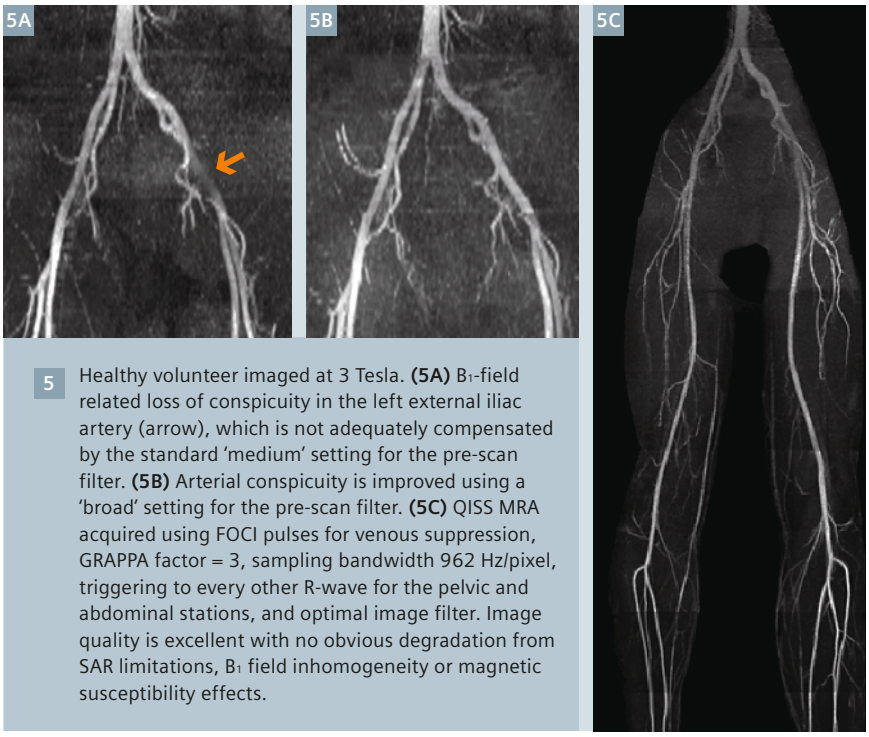

5 Healthy volunteer imaged at 3 Tesla. **(5A)** B_1-field related loss of conspicuity in the left external iliac artery (arrow), which is not adequately compensated by the standard 'medium' setting for the pre-scan filter. **(5B)** Arterial conspicuity is improved using a 'broad' setting for the pre-scan filter. **(5C)** QISS MRA acquired using FOCI pulses for venous suppression, GRAPPA factor = 3, sampling bandwidth 962 Hz/pixel, triggering to every other R-wave for the pelvic and abdominal stations, and optimal image filter. Image quality is excellent with no obvious degradation from SAR limitations, B_1 field inhomogeneity or magnetic susceptibility effects.

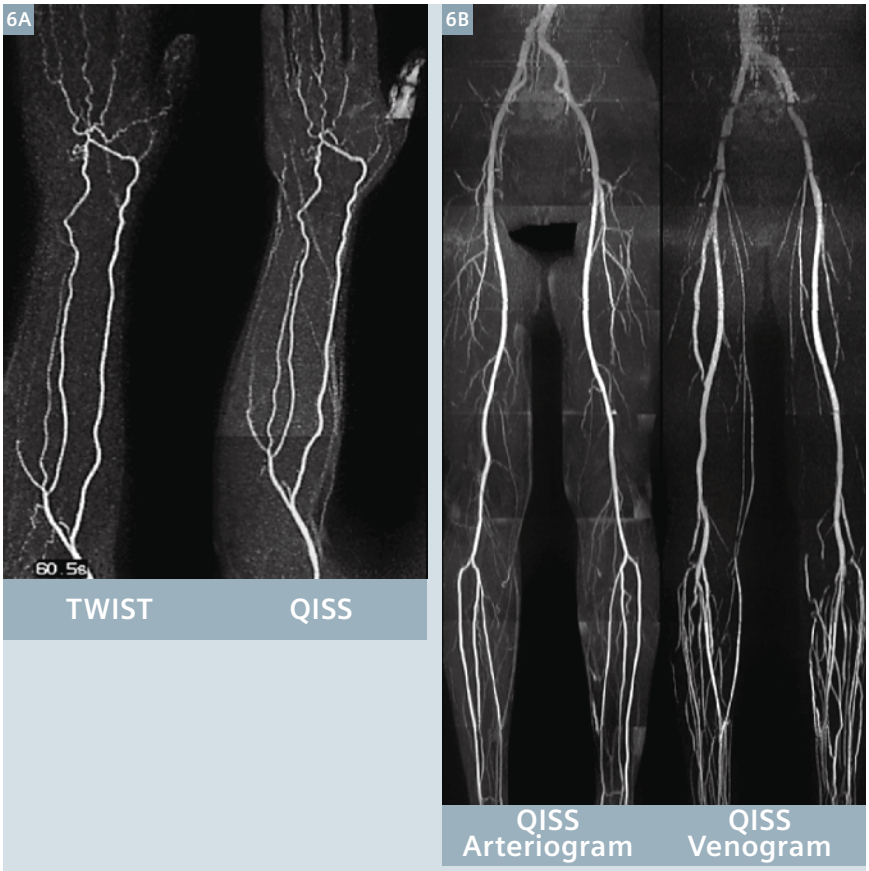

6 Developing potential future clinical applications for QISS MRA.
(6A) Healthy subject. QISS MRA (acquired with 1.2 mm thick slices) depicts the forearm arteries comparably to TWIST CEMRA.
(6B) Comparison of QISS arteriography (inferior saturation) with QISS venography (superior saturation).

3. **Susceptibility artifact:** The TrueFISP readout along with fat suppression makes QISS more sensitive to magnetic susceptibility artifacts (e.g. from joint prostheses or bowel gas) than CEMRA (which uses a 3D acquisition with short TE). Using a high readout bandwidth without fat suppression minimizes such artifacts.
4. **Flow direction:** The use of venous saturation impairs the ability of QISS to depict reversed arterial flow, particularly when the flow reversal extends over a long vessel segment. In cases where flow reversal is suspected, one may acquire an additional QISS data set using arterial saturation instead of venous saturation. These images will show reversed arterial flow (but will also show veins).
5. **Spatial resolution:** For most peripheral arterial segments, the default slice thickness of 3 mm with no slice overlap is sufficient to show stenotic disease. Thinner slices (e.g. 1.2 mm with 20% slice overlap) are helpful for avoiding partial volume averaging in horizontally oriented vessel segments (e.g. proximal anterior tibial artery) and for imaging small caliber vessels (e.g. in the foot).

Future Developments

1. **Alternative *k*-Space Trajectories:** The current implementation of QISS uses a Cartesian *k*-space trajectory. However, it is also possible to acquire QISS using a radial *k*-space trajectory [30]. There are potential advantages and disadvantages to a radial trajectory. One advantage for radial is that the number of views, and hence scan duration within each cardiac cycle, can be reduced almost arbitrarily with minimal impact on spatial resolution. This approach may be beneficial for imaging of patients with fast heart rates. However, the signal-to-noise ratio (SNR) is also reduced and radial streak artifacts may become objectionable if the number of views is excessively decreased. By using a golden view angle increment with a radial *k*-space trajectory, it becomes feasible to sample data throughout the cardiac cycle. One can then generate a cine series of time-resolved QISS images showing the progression of the arterial pulse wave within the arterial tree [31].
2. **Alternative Sampling Strategies:** Although the TrueFISP readout maximizes acquisition speed and SNR, using other pulse sequences for the readout can prove beneficial in certain circumstances. For instances, the use of a fast low angle shot (FLASH) readout in conjunction with a reduced flip angle excitation avoids SAR limitations at 3 Tesla. The use of an ultra-short TE readout might prove beneficial to reduce susceptibility artifacts around joint prostheses.
3. **Alternative Gating Strategies:** Currently, QISS images of the pelvis and abdomen are acquired using breath holding. In order to further enhance, patient comfort, it should be feasible to implement non-breathhold acquisitions by respiratory gating with a belt device, with a navigator technique applied to the anterior abdominal wall, or by self-gating [32].
4. **3D QISS:** Very thin slices (e.g. 0.3 mm can be obtained by using a thin-slab 3D implementation of the QISS technique. Although still early in development, the technique has the potential to exceed the spatial resolution available with CEMRA and nearly match that of CTA.

Conclusions

QISS MRA provides a robust, rapid, and easy-to-use technique for imaging of the peripheral arteries at both 1.5 and 3 Tesla. There is generally no need to tailor any of the imaging parameters for individual patients. Additionally it can serve as a backup for CEMRA, or function as a standalone technique. Despite similarities in the appearances of the projection angiograms, QISS and CEMRA are predicated on fundamentally different principles and care must be taken to avoid pitfalls specific to each technique. Future developments promise shorter scan times, reduced artifacts, and new clinical applications.

References

1. Leng GC, Lee AJ, Fowkes FG, Whiteman M, Dunbar J, Housley E, et al. Incidence, natural history and cardiovascular events in symptomatic and asymptomatic peripheral arterial disease in the general population. Int J Epidemiol. 1996 Dec;25(6):1172-81.
2. Selvin E, Erlinger TP. Prevalence of and risk factors for peripheral arterial disease in the United States: results from the National Health and Nutrition Examination Survey, 1999-2000. Circulation. 2004 Aug 10;110(6):738-43.
3. Hirsch AT, Duval S. The global pandemic of peripheral artery disease. Lancet. 2013 Oct 19;382(9901):1312-4. doi: 10.1016/S0140-6736(13)61576-7. Epub 2013 Aug 1.
4. Arain FA, Cooper LT. Peripheral Arterial Disease: Diagnosis and Management. Mayo Clin Proc. 2008;83(8):944-950.
5. Hirsch AT, Haskal ZJ, Hertzer NR, Bakal CW, Creager MA, Halperin JL, et al. ACC/AHA 2005 guidelines for the management of patients with peripheral arterial disease (lower extremity, renal, mesenteric, and abdominal aortic. J Am Coll Cardiol. 2006 Mar 21;47(6):1239-312.
6. Dachun Xu, Jue Li, Liling Zou, Yawei Xu, Dayi Hu, Pagoto SL, Yunsheng Ma. Sensitivity and specificity of the ankle-brachial index to diagnose peripheral artery disease: a structured review. Vasc Med. 2010 Oct;15(5):361-9. doi: 10.1177/1358863X10378376.
7. Hessel SJ, Adams DF, Abrams HL. Complications of angiography. Radiology. 1981; 138(2): 273-281.
8. Catalano C, Fraioli F, Laghi A, Napoli A, Bezzi M, Pediconi F, Danti M, Nofroni I, Passariello R. Infrarenal aortic and lower-extremity arterial disease: diagnostic performance of multi-detector row CT angiography. Radiology. 2004;231:555–563.
9. Ouwendijk R, Kock MC, van Dijk LC, van Sambeek MR, Stijnen T, Hunink MG. Vessel wall calcifications at multi-detector row CT angiography in patients with peripheral arterial disease: effect on clinical utility and clinical predictors. Radiology. 2006 Nov;241(2):603-8.
10. Tranche-Iparraguirre S, Marín-Iranzo R, Fernández-de Sanmamed R, Riesgo-García A, Hevia-Rodríguez E, García-Casas JB. Peripheral arterial disease and kidney failure: a frequent association. Nefrologia. 2012 May 14;32(3):313-20. doi: 10.3265/Nefrologia.pre2011.Nov.11172. Epub 2012 Jan 27.
11. Menke J, Larsen J. Meta-analysis: Accuracy of contrast-enhanced magnetic resonance angiography for assessing steno-occlusions in peripheral arterial disease. Ann Intern Med. 2010 Sep 7;153(5):325-34. doi: 10.7326/0003-4819-153-5-201009070-00007.

12. Prince MR, Zhang H, Morris M, MacGregor JL, Grossman ME, Silberzweig J, DeLapaz RL, Lee HJ, Magro CM, Valeri AM. Incidence of nephrogenic systemic fibrosis at two large medical centers. Radiology. 2008 Sep;248(3):807-16. doi: 10.1148/radiol.2483071863.
13. Koelemay MJ, Lijmer JG, Stoker J, Legemate DA, Bossuyt PM. Magnetic resonance angiography for the evaluation of lower extremity arterial disease: a meta-analysis. JAMA. 2001 Mar 14;285(10):1338-45.
14. Owen RS, Carpenter JP, Baum RA, Perloff LJ, Cope C.. Magnetic resonance imaging of angiographically occult runoff vessels in peripheral arterial occlusive disease. N Engl J Med. 1992 Jun 11;326(24):1577-1581.
15. Miyazaki M, Takai H, Sugiura S, Wada H, Kuwahara R, Urata J. Peripheral MR angiography: separation of arteries from veins with flow-spoiled gradient pulses in electrocardiography-triggered three-dimensional half-Fourier fast spin-echo imaging. Radiology. 2003 Jun;227(3):890-896. Epub 2003 Apr 17.
16. Lim RP, Hecht EM, Xu J, Babb JS, Oesingmann N, Wong S, Muhs BE, Gagne P, Lee VS. 3D nongadolinium-enhanced ECG-gated MRA of the distal lower extremities: preliminary clinical experience. J Magn Reson Imaging. 2008 Jul;28(1):181-189. doi: 10.1002/jmri.21416.
17. Fan Z, Sheehan J, Bi X, Liu X, Carr J, Li D. 3D noncontrast MR angiography of the distal lower extremities using flow-sensitive dephasing (FSD)-prepared balanced SSFP. Magn Reson Med. 2009 Dec;62(6):1523-32. doi: 10.1002/mrm.22142.
18. Edelman RR, Sheehan JJ, Dunkle E, Schindler N, Carr J, Koktzoglou I. Quiescent-interval single-shot unenhanced magnetic resonance angiography of peripheral vascular disease: technical considerations and clinical feasibility. Magn Reson Med. 2010;63:951–958.
19. Ward EV, Galizia MS, Usman A, Popescu AR, Dunkle E, Edelman RR. Comparison of quiescent inflow single-shot and native space for nonenhanced peripheral MR angiography. J Magn Reson Imaging. 2013;38:1531–1538.
20. Hodnett PA, Koktzoglou I, Davarpanah AH, Seanlon TG, Collins JD, Sheehan JJ, Dunkle E, Gupta N, Carr JC, Edelman RR. Evaluation of Peripheral Arterial Disease with Nonenhanced Quiescent-Interval Single Shot MR Angiography. Radiology. July 2011: 260(1):282-93. R01 HL096916; PMCID: PMC3121010
21. Klasen J, Blondin D, Schmitt P, Bi X, Sansone R, Wittsack HJ, et al. Nonenhanced ECG-gated quiescent-interval single-shot MRA (QISS-MRA) of the lower extremities: comparison with contrast-enhanced MRA. Clin Radiol. 2012 May;67(5):441-6. doi: 10.1016/j.crad.2011.10.014. Epub 2011 Dec 3.
22. Amin P, Collins JD, Koktzoglou I, Molvar C, Markl M, Edelman RR, Carr JC. Evaluating peripheral arterial disease with unenhanced quiescent-interval single-shot MR angiography at 3 T. AJR Am J Roentgenol. 2014 Apr;202(4):886-93. doi: 10.2214/AJR.13.11243. PMID: 24660721
23. Knobloch G, Gielen M, Lauff MT, Romano VC, Schmitt P, Rick M, et al. ECG-gated quiescent-interval single-shot MR angiography of the lower extremities: initial experience at 3 T. Clin Radiol. 2014 May;69(5):485-91. doi: 10.1016/j.crad.2013.12.006. Epub 2014 Mar 7. PMID:24613581.
24. Thierfelder KM, Meimarakis G, Nikolaou K, Sommer WH, Schmitt P, Kazmierczak PM, et al. Non-contrast-enhanced MR angiography at 3 Tesla in patients with advanced peripheral arterial occlusive disease. PLoS One. 2014 Mar 7;9(3):e91078. doi: 10.1371/journal.pone.0091078. eCollection 2014. PMID:24608937.
25. Hansmann J, Morelli JN, Michaely HJ, Riester T, Budjan J, Schoenberg SO, Attenberger UI. Nonenhanced ECG-gated quiescent-interval single shot MRA: image quality and stenosis assessment at 3 tesla compared with contrast-enhanced MRA and digital subtraction angiography. J Magn Reson Imaging. 2014 Jun;39(6):1486-93. doi: 10.1002/jmri.24324. Epub 2013 Oct 10. PMID:24338813.
26. Johst S, Orzada S, Fischer A, Schäfer LC, Nassenstein K, Umutlu L, et al. Sequence comparison for non-enhanced MRA of the lower extremity arteries at 7 Tesla. PLoS One. 2014 Jan 16;9(1):e86274. doi: 10.1371/journal.pone.0086274. eCollection 2014.
27. Hodnett PA, Ward EV, Davarpanah AH, Scanlon TG, Collins JD, Glielmi CB, Bi X, et al. Peripheral arterial disease in a symptomatic diabetic population: prospective comparison of rapid unenhanced MR angiography (MRA) with contrast-enhanced MRA. AJR Am J Roentgenol. 2011 Dec;197(6):1466-73. doi: 10.2214/AJR.10.6091. PMID:22109304.
28. Ordidge RJ, Wylezinska M, Hugg JW, Butterworth E, Franconi F. Frequency offset corrected inversion (FOCI) pulses for use in localized spectroscopy. Magn Reson Med. 1996;36(4):562-566.
29. Payne GS, Leach MO. Implementation and evaluation of frequency offset corrected inversion [FOCI) pulses on a clinical MR system. Magn Reson Med. 1997;38:828-833.
30. Edelman RR, Giri S, Dunkle E, Galizia M, Amin P, Koktzoglou I. Quiescent-inflow single-shot magnetic resonance angiography using a highly undersampled radial *k*-space trajectory. Magn Reson Med. 2013;70(6):1662-1668.
31. Koktzoglou I, Mistretta CA, Giri S, Dunkle EE, Amin P, Edelman RR. Simultaneous static and cine nonenhanced MR angiography using radial sampling and highly constrained back projection reconstruction. Magn Reson Med. 2013 Nov 11. doi: 10.1002/mrm.25008. [Epub ahead of print]
32. Larson AC, Kellman P, Arai A, Hirsch GA, McVeigh E, Li D, Simonetti OP. Preliminary investigation of respiratory self-gating for free-breathing segmented cine MRI. Magn Reson Med. 2005 Jan;53(1):159-68.

Contact

Robert R. Edelman, M.D.
Dept. of Radiology
NorthShore University HealthSystem
Feinberg School of Medicine
Northwestern University
Chicago, IL
USA
REdelman@northshore.org

Expert Talks

Don’t miss the talks of experienced and renowned experts on all aspects of MR imaging.

MRI Technology and Methodology: A Look into the Future

Peter Jezzard
University of Oxford (Oxford, UK)

Whole-Body MRI: Changing Cancer Patient Managment

Anwar R. Padhani
Mount Vernon Cancer Centre (London, UK)

Cartilage Evaluation

Darshana Sanghvi
Kokilaben Dhirubhai Ambani (Mumbai, India)

A 5 Minute Clinical Brain Protocol

Lawrence Wald
Massachusetts General Hospital (Boston, MA, USA)

Body MRI and Whole-Body Staging in Pediatric* Patients

Günther Schneider
Saarland University Hospital (Homburg, Germany)

Visit us at **www.siemens.com/magnetom-world**

Go to **Clinical Corner > Clinical Talks**

* MR scanning has not been established as safe for imaging fetuses and infants under two years of age.
The responsible physician must evaluate the benefit of the MRI examination in comparison to other imaging procedures.

QISS Non-Contrast MR Angiography: A Study of Three Cases with Peripheral Vascular Disease

Maria L. Carr[1]; Shivraman Giri[2]; Sven Zuehlsdorff[2]; Oisin Flanagan[4]; Heron E. Rodriguez[5]; Mark K. Eskandari[5]; Jeremy D. Collins[1]; Robert R. Edelman[3]; James C. Carr[1]

[1] Northwestern University, Department of Radiology, Feinberg School of Medicine, Chicago, IL, USA
[2] Siemens Medical Solutions USA, Inc., Chicago, IL, USA
[3] Northshore University HealthSystem, Evanston, IL, USA
[4] University of Toronto, Department of Medical Imaging, Ontario, Canada
[5] Northwestern Medicine, Division of Vascular Surgery, Chicago, IL, USA

Introduction

Peripheral arterial disease (PAD) is a common progressive vasculopathy that causes disabling symptoms in the lower extremities, such as diminished arterial pulses, intermittent claudication, rest pain, and can lead to tissue loss. PAD is a common manifestation of the atherosclerotic disease process, affecting from 12% to 14% of the general population [1]. CT angiography (CTA) and contrast-enhanced MR angiography (CEMRA) are the imaging approaches commonly used to evaluate PAD. Many of these patients suffer from renal dysfunction, thus making both CTA and CEMRA less useful due to concerns about contrast-induced nephropathy (CIN) with iodinated contrast or nephrogenic systemic fibrosis (NSF) with gadolinium-based agents [2], respectively. Quiescent-interval single-shot* (QISS) imaging employs a stack of 2D TrueFISP images to cover the entire lower extremity and has recently been described as a non-contrast MR angiography technique for assessment of the lower extremity vasculature that demonstrated clinical utility at 1.5T and 3T [3, 4]. In this article we review three cases with QISS MRA demonstrating the clinical utility of this non-contrast technique for lower extremity arterial evaluation.

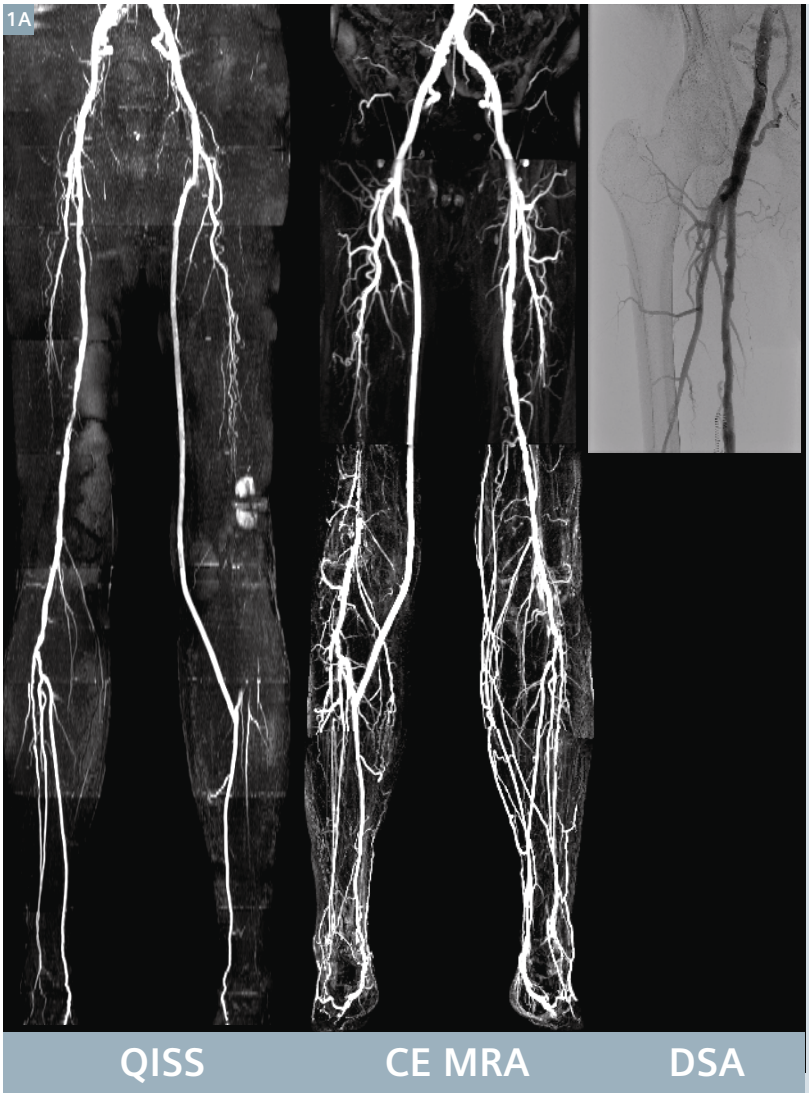

Case 1

A 67-year-old male with a history of diabetes mellitus, hypercholesterolemia, and hypertension presented with worsening symptoms of peripheral arterial disease. Five years ago he underwent arterial bypass surgery from the left common femoral artery to the posterior tibial artery with good results. He developed progressively worsening intermittent claudication in the right leg over the last year. His ankle brachial index was 0.62 in the right leg and 1.15 in the left leg. He initially underwent conservative management in a supervised exercise program with limited success. He was then referred for non-invasive imaging with contrast-enhanced MR angiography (CEMRA). His glomerular filtration rate at the time of the CEMRA was greater than 60 cc/min. He underwent a standard 2-injection hybrid CEMRA protocol of the pelvis and lower extremities, which consisted of time resolved TWIST of the calves followed by a timed stepping table, 4-station acquisition of the pelvis and lower extremities on a 3T MAGNETOM Skyra scanner. 0.2 mmol/kg of Gadopentetate dimeglumine was injected intravenously using a divided injection protocol. CEMRA demonstrated a patent left femoral-distal bypass graft and a focal stenosis in the right superficial femoral artery. There was significant venous contamination of the calf vessels bilaterally, more severe on the right, which precluded accurate assessment of the runoff vessels. A QISS non-contrast MRA exam, performed at the same imaging session just before the contrast injection, also showed a patent left femoral-distal bypass graft and a focal stenosis in the right superficial femoral artery. The runoff vessels were much better delineated by QISS and performed as well as TWIST and better than CEMRA in this region, with three-vessel runoff on the right and single-vessel runoff on the left via the left posterior tibial artery.

1B

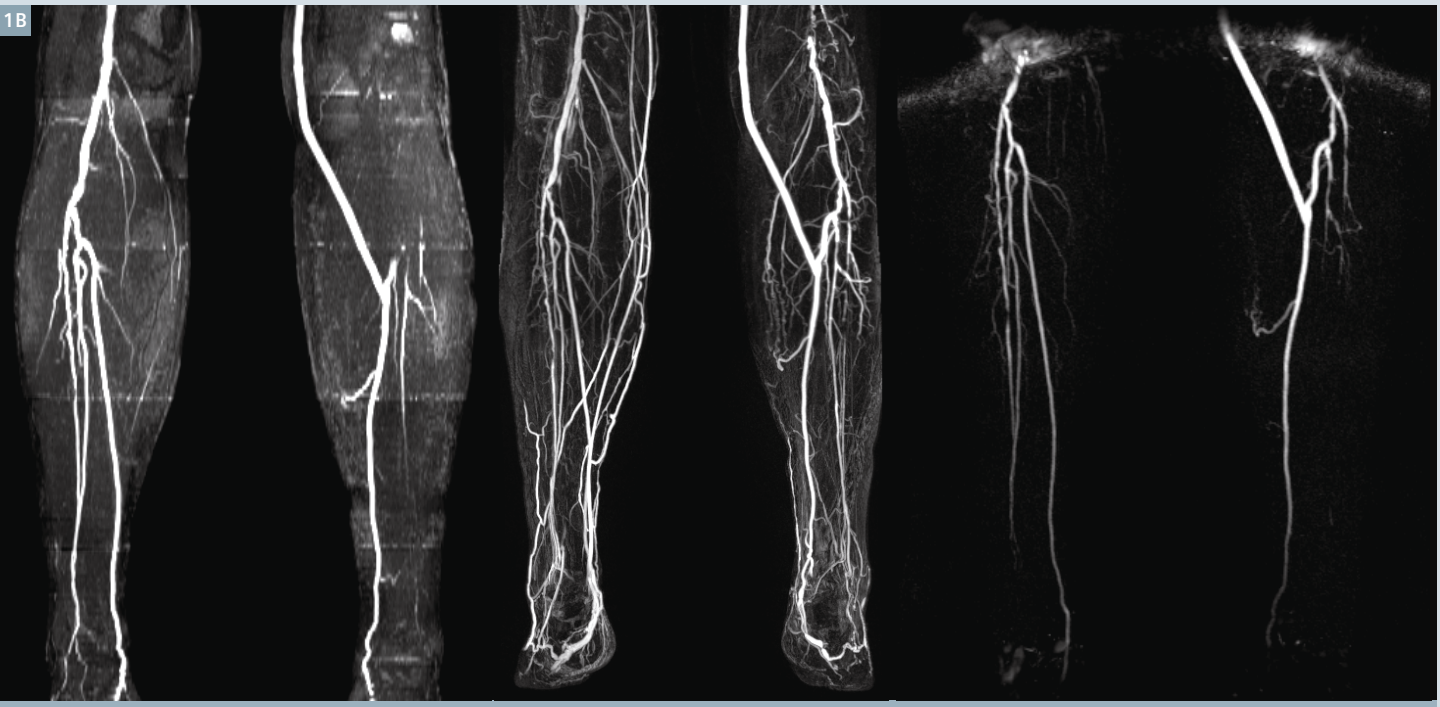

QISS CE MRA TWIST

* QISS is pending 510(k) clearance and is not commercially available in the US.

Case 2

A 79-year-old male with hypertension, prostate cancer, and ischemic cardiomyopathy status post coronary artery bypass surgery, presented with worsening bilateral intermittent calf claudication. He was unable to walk one block without pain. He initially underwent non-invasive vascular testing; however ankle brachial indices were found to be invalid due to extensive calcification in the runoff vessels. He then underwent CT angiography, which showed extensive calcification of his peripheral vasculature, notably of the calves, which limited assessment of stenosis severity of the infrapopliteal vessels.

The patient was referred for contrast-enhanced MRA, which confirmed CT findings with diffuse mild disease in the inflow and outflow segments and demonstrated bilateral moderate to severe tibial artery disease. Assessment of the left tibial vessels was limited by venous contamination, precluding evaluation of the distal anterior tibial and posterior tibial arteries. QISS MRA was performed for further assessment of the tibial vasculature, confirming patency of the bilateral posterior tibial and peroneal arteries, with occlusion of the anterior tibial arteries. There was perfect agreement between QISS MRA and CEMRA in the right calf, and QISS MRA was diagnostic in the left calf, demonstrating similar findings compared to CT angiography without the limitation of artifact from diffuse vascular calcificaitons. In particular, the left plantar arteries are patient on QISS MRA while the dorsalis pedis is seen to be occluded. Of note, the symmetric loss of signal noted in the pelvis and proximal thighs on QISS MRA is typical for 'striping' artifacts from intermittent ectopy resulting in misgating. The symmetry of this appearance reassures the reader that this represents artifact rather than real disease. If poor gating limits evaluation of a particular station, the station can be reacquired in just 45 seconds without the need to re-shim.

Case 3

An 86-year-old male with a history of cancer, hypertension and diabetes presented with left leg claudication. The patient had a history of renal dysfunction with eGFR < 30 ml/min/1.73 m^2, so contrast-enhanced MRA was not an option. The referring physician therefore ordered a non-contrast MRA. The QISS images showed a long left-sided superficial femoral artery occlusion with single-vessel runoff to the foot via the posterior tibial artery. On-table angiography in the operating room, using minimal amounts of contrast, confirmed the vascular findings and a bypass graft was placed. Therefore, this patient with severe renal dysfunction was diagnosed and treated without the need for a gadolinium-based contrast agent and minimal iodinated contrast.

Discussion

In this report, we described three cases that illustrate the potential utility of non-contrast MR angiography using QISS in the clinical setting. QISS MRA is a simple to use technique that provides excellent image quality with high diagnostic yield in relatively short acquisition times. Besides, QISS MRA can be an alternative to CEMRA, thereby resulting in significant cost savings by avoiding costs associated with gadolinium contrast administration and point of care eGFR testing. QISS protocol can be run in about half the time of a standard CEMRA runoff protocol leading to improved patient throughput. Since QISS is largely automated and image processing occurs inline, technologists can be attending to other tasks while scanning is taking place, leading to greater staff efficiency.

Traditionally, non-contrast MR angiography of the lower extremities relied on an ECG-gated 2D time of flight approach. However, this approach has the disadvantage of very long acquisition times and variable image quality, particularly in regions of disease and vessel tortuosity [5]. Newer approaches have focused on subtractive methods, using either fast spin echo [6] or balanced steady state free precession readouts [7]. These techniques depend on the variation in blood signal between systole and diastole. Both arteries and veins appear bright in diastole, whereas only veins are visible in systole. Therefore, a subtracted dataset can produce a pure arterial image. Unfortunately, this imaging technique can be unreliable and its complexity, e.g. the requirement to subtract two image sets and necessary patient specific adjustments reduces clinical utility and makes it challenging to use for technologists who do not have extensive experience with it.

The QISS technique acquires stacks of axial slices to cover the region of interest, which in the case of the peripheral vasculature is from pelvis to feet. Each image stack is acquired near the magnet isocenter in order to avoid artifacts from off-resonance effects. Each stack automatically undergoes inline maximum intensity projection (MIP) processing. Auto compose assembles these together at the end of the acquisition to produce a MIP of the entire peripheral vasculature. A key advantage of QISS is the simplicity of the acquisition technique and protocol set up, reducing dependence on experienced MR technologists. ECG leads are applied at the beginning of the test and the patient is placed supine, feet first with a peripheral vascular coil as with the usual runoff protocol. Since it is an axial acquisition, there is no time spent with setting up slices orientations and there is no risk to excluding regions of the vascular anatomy, as can occur with oblique coronal acquisitions tailored to the vascular anatomy to optimize the imaging time. The acquisition time is typically 8-10 minutes depending on heart rate. The images are acquired without operator intervention enabling the technologist to perform other tasks while scanning is taking place, and improving work efficiency. Moreover, since most of the image processing occurs inline, there is no need for advanced image analysis using other software algorithms or specialized post-processing staff.

Initial experience at 3T revealed two sporadic image quality issues in pelvic and abdominal stations: (1) Undesirable venous signal and (2) insufficient arterial conspicuity. These are possibly related to B_1-field inhomogeneity issues typically seen at higher field strengths. Subsequent patients were scanned using a modified version of QISS in which the venous contamination problem was addressed using an optimized FOCI adiabatic RF pulse for the Tracking Saturation pulse; arterial conspicuity was improved by scanning every other heartbeat for the top 3 stations covering pelvic and abdominal regions.

QISS MR angiography has been extensively validated in the medical literature, both at 1.5T and 3T. The initial paper by Hodnett et al. [8], which evaluated 53 patients at 1.5T in a two-center trial using both contrast-enhanced MRA and digital subtraction angiography as reference standards, found high sensitivities and specificities for QISS when compared to both CEMRA and DSA. In fact, QISS performed slightly better that CEMRA when compared to DSA in a patient subgroup and, also in this study, QISS performed well irrespective of renal function. In a second study of 25 patients with diabetes mellitus, QISS compared well to both CEMRA and DSA for detection of significant disease [4]. In another study comparing QISS to a non-contrast, ECG-gated 3D single shot fast spin echo pulse sequence in 20 patients, QISS demonstrated superior specificity and image quality, and was more robust in the abdominal and pelvic regions [9]. QISS MRA has also been extensively studied at 3T and results are similar to 1.5T showing high diagnostic accuracy and excellent image quality [10]. Recent technical advances promise to overcome limitations of B_1 field inhomogeneity and high power deposition, thereby further improving the performance at 3T.

Each of our cases demonstrates some of the advantages of QISS MRA.

Case 1 is of a diabetic patient who had previously undergone a left leg bypass graft. Stepping table contrast-enhanced MR angiography using a four-station approach on a 3T MAGNETOM Skyra resulted in venous contamination in the calf vessels due to suboptimal timing of contrast agent injection, precluding accurate evaluation. Early venous enhancement in this case was likely due to fast transit down the left leg due to the bypass graft and soft tissue inflammation in the right leg. Venous contamination is known to occur in up to 20% of cases using a single injection, stepping table CEMRA protocol. Several attempts to solve this problem for CEMRA include using a 2-injection protocol, where the calves are imaged first, or else attaching blood pressure cuffs on the thighs to slow venous return. Both approaches lengthen and complicate the protocol. Another solution is to use QISS as an alternative or adjunct to CEMRA. In our case, the QISS images clearly show the left sided bypass graft

and the calf vessels without any overlap of adjacent veins.

In case 2, non-invasive vascular testing was non-diagnostic due to heavily calcified vessels, which also impaired diagnosis by CT angiography. Most of the disease was confined to the infra-popliteal segments. QISS was comparable to CEMRA for depiction of the runoff vessels and both were superior to CTA.

In case 3, a patient with diabetes presented with left leg claudication but had renal dysfunction with an eGFR of 50 ml/min. The referring physician did not want to use either a MR or CT contrast agent, so that QISS MR angiography provided a helpful diagnostic solution. The QISS images showed a long left-sided superficial femoral artery occlusion with single vessel runoff to the foot, which was sufficient information for the vascular surgeon to plan arterial bypass.

In conclusion, QISS MR angiography is a robust, simple and reliable non-contrast technique that can be used at 1.5T and 3T. QISS MRA has been extensively evaluated in several studies, including diabetic patients in whom renal dysfunction and vascular calcifications are particularly common and infra-popliteal disease is usually more severe. QISS MRA should become the non-contrast MRA technique of choice in patients with renal dysfunction. It may be particularly suitable for diabetic patients or those already on dialysis where vascular calcification is particularly prevalent. Although QISS MRA is robust with an imaging protocol that can be run without patient-specific modifications, patients with frequent ectopy or irregular arrhythmias demonstrate symmetric mis-gating artifacts (Fig. 2) which can reduce image quality of QISS MRA. QISS MRA can also be employed as an alternative to CEMRA resulting in potential cost savings by avoiding the costs of the contrast agent and associated infusion paraphernalia, as well as by improving patient throughput.

References

1. Hiatt WR, Hoag S, Hamman RF. Effect of diagnostic criteria on the prevalence of peripheral arterial disease. The San Luis Valley Diabetes Study. Circulation 1995;91:1472-9.
2. Sadowski EA, Bennett LK, Chan MR, et al. Nephrogenic systemic fibrosis: risk factors and incidence estimation. Radiology 2007;243:148-57.
3. Edelman RR, Sheehan JJ, Dunkle E, Schindler N, Carr J, Koktzoglou I. Quiescent-interval single-shot unenhanced magnetic resonance angiography of peripheral vascular disease: Technical considerations and clinical feasibility. Magnetic resonance in medicine : official journal of the Society of Magnetic Resonance in Medicine / Society of Magnetic Resonance in Medicine 2010;63:951-8.
4. Hodnett PA, Ward EV, Davarpanah AH, et al. Peripheral arterial disease in a symptomatic diabetic population: prospective comparison of rapid unenhanced MR angiography (MRA) with contrast-enhanced MRA. AJR American journal of roentgenology 2011;197:1466-73.
5. Offerman EJ, Hodnett PA, Edelman RR, Koktzoglou I. Nonenhanced methods for lower-extremity MRA: a phantom study examining the effects of stenosis and pathologic flow waveforms at 1.5T. Journal of magnetic resonance imaging : JMRI 2011;33:401-8.
6. Lanzman RS, Blondin D, Schmitt P, et al. Non-enhanced 3D MR angiography of the lower extremity using ECG-gated TSE imaging with non-selective refocusing pulses--initial experience. RoFo : Fortschritte auf dem Gebiete der Rontgenstrahlen und der Nuklearmedizin 2010;182:861-7.
7. Lanzman RS, Schmitt P, Kropil P, Blondin D. [Nonenhanced MR angiography techniques]. RoFo : Fortschritte auf dem Gebiete der Rontgenstrahlen und der Nuklearmedizin 2011;183:913-24.
8. Hodnett PA, Koktzoglou I, Davarpanah AH, et al. Evaluation of peripheral arterial disease with nonenhanced quiescent-interval single-shot MR angiography. Radiology 2011;260:282-93.
9. Ward EV, Galizia MS, Usman A, Popescu AR, Dunkle E, Edelman RR. Comparison of quiescent inflow single-shot and native space for nonenhanced peripheral MR angiography. Journal of magnetic resonance imaging : JMRI 2013;38:1531-8.
10. Knobloch G, Gielen M, Lauff MT, et al. ECG-gated quiescent-interval single-shot MR angiography of the lower extremities: initial experience at 3 T. Clinical radiology 2014;69:485-91.

Contact

Maria L. Carr, RT.R (CT)(MR)
Project Research Manager
Department of Radiology
Northwestern University
Feinberg School of Medicine
737 N. Michigan Ave., Suite 1600
Chicago, IL 60611
USA
Phone: +1 312-926-5292
m-carr@northwestern.edu

Cardiac Dot Engine: Significant Time Reduction at Cardiac Magnetic Resonance Imaging

Jesús Ciro Pueyo, M.D., Ph.D.[1]; Paula García-Barquín, M.D.[1]; Laura Romina Zalazar, M.D.[1]; José Miguel Madrid, M.D.[1]; Jon Etxano, M.D.[1]; Efrén Ojeda, M.Sc.[2]; Óscar Fernández[3]

[1] Department of Radiology, Clínica Universidad de Navarra, Pamplona, Spain
[2] Siemens Healthcare, Erlangen, Germany
[3] Siemens Healthcare Getafe (Madrid), Spain

Introduction

Cardiac Magnetic Resonance (CMR) has rapidly developed and is now the technique of choice in the study of multiple heart diseases and an important tool for planning revascularization strategies in patients with coronary artery disease [1]. It allows the assessment of cardiac morphology and function. Therefore, it provides important information about tissue characterization by detecting the first steps of the ischemic cascade through perfusion sequences. An appropriate assessment of myocardial viability can be performed with delayed enhancement sequences [2].

However, CMR is not without certain limitations. Firstly, it requires skilled personnel with a good knowledge of cardiac anatomy and cardiac planes. Secondly, the scan times for CMR studies are substantially longer than for other types of study (with up to more than an hour on stress heart exams) and remain a limiting factor in the recruitment of patients suffering from claustrophobia.

In order to reduce CMR scan times, the Cardiac Dot Engine has been developed. It is a new software technology from Siemens Healthcare, which offers a review of CMR fully guided and suited to the needs of the patient.

The system guides you through a series of graphical illustrations selecting some anatomical reference points on the heart. The software then performs an automatic planning of the different cardiac planes without the need for user intervention. It also allows you to obtain superimposable slices in all sequences of the study, increasing confidence in our diagnoses [3].

Clinical experience

Our experience with the Dot software began in June 2013. To date, we have performed in our center over 272 CMR studies of which 60% are stress studies after administration of adenosine. All

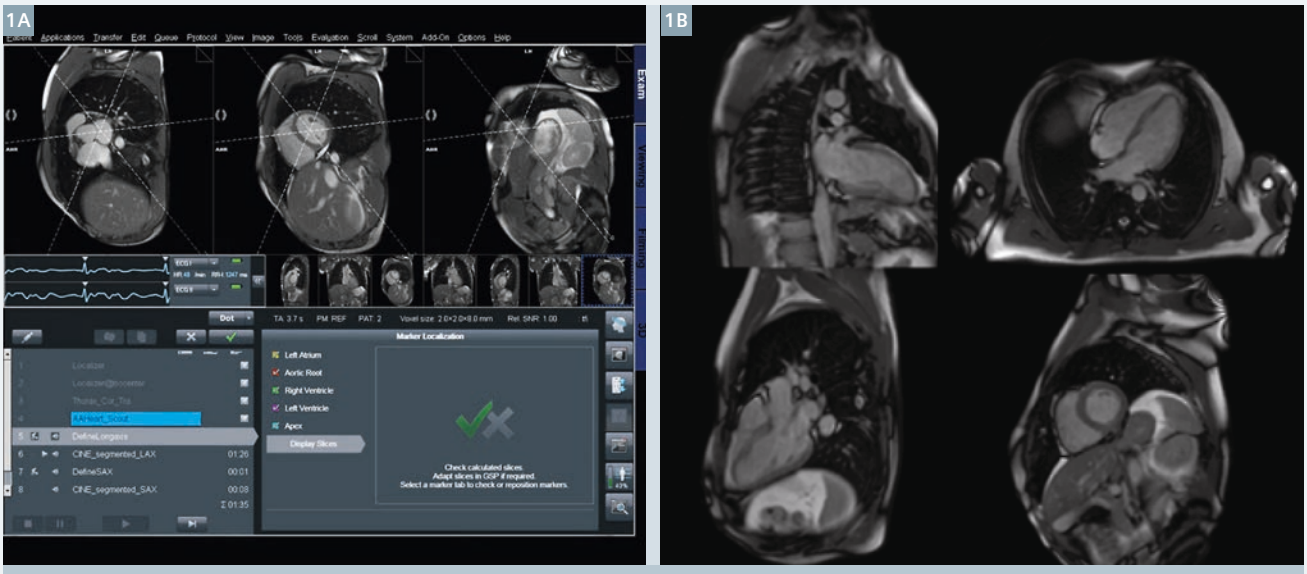

1 Automatic planning of the different cardiac axis with Cardiac Dot Engine.

studies have been performed under medical supervision and have been reproducible and high-quality diagnostic scans. During this time, we have observed a significant reduction of the average scan time.

We therefore proposed the following study to assess the time saved by using the Cardiac Dot Engine in both conventional and stress studies, compared to standard cardiac scans.

Materials and methods

Study design and patients
We have retrospectively reviewed a total of 194 patients consecutively between October 2012 and March 2014 with CMR studies performed at our Siemens 1.5T system (MAGNETOM Aera XQ) with an 18-channel body matrix coil.

For the correct categorization of the study we took into account some variables:

- First, the type of study of stress or conventional CMR. The technical specifications of both protocol studies are summarized in Table 1.
- Second, the use of Short Tau Inversion Recovery (STIR) sequences. We usually use this sequence for patients with suspected acute disease or suspicion of infiltrative heart disease.
- Third, the use of the Cardiac Dot Engine or conventional software.

Depending on the different variables, we obtained eight groups comparing the average scan time with the Cardiac Dot Engine and without it (conventional software).

The total examination time comprises the time from the beginning until the end of each scan.

The image quality of the studies has been assessed by a radiologist with over 20 years of experience on a 10-point scale (1 = poor to 10 = excellent).

The statistical analysis has been performed using a Student's T-test for independent samples to compare means. SPSS Statistics software 20.0 (IBM corporation, Armonk, NY, USA) has been used.

Table 1

Conventional CMR	Stress CMR
Localizer	Localizer
HASTE	HASTE
AAHeart-Scout	AAHeart-Scout
Function 4-chamber	Function 4-chamber
Dynamic rest (Gadovist® 0.1 mmol/kg, 4 ml/s)	Dynamic stress adenosine (Gadovist® 0.1 mmol/kg, 4 ml/s)
Function 2 + 3-chamber	Function 2 + 3-chamber
Function short-axis	Function short-axis
Delayed enhancement	Delayed enhancement
	Dynamic rest (Gadovist® 0.1 mmol/kg, 4 ml/s)

Specifications of both study protocols (stress and conventional CMR) performed at our Siemens 1.5T MAGNETOM Aera XQ.

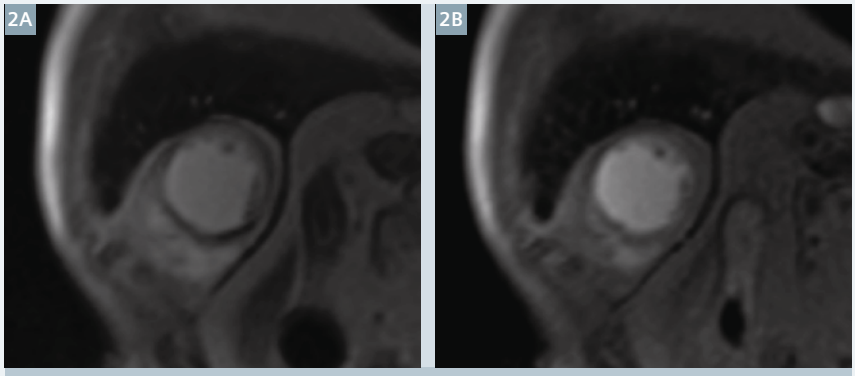

2 MR images show positive findings on stress study in a 53-year-old man with chest pain. The inferolateral wall stress-induced perfusion shows a defect **(2A)** that corresponds with a stenosis involving the left circumflex artery (LCX), disappearing in the dynamic perfusion study **(2B)**.These findings were confirmed on subsequent invasive angiography with successful coronary stenting of the stenosis.

Results

The image quality of all studies obtained a result between 9 and 10.

For conventional CMR studies with STIR sequences (58 patients) statistically significant differences in the average examination time using the Cardiac Dot Engine (t = 39.1 min +/- 12.1) have been observed, reducing the average examination time by 26.5 minutes compared to examination times using conventional software (t = 65.6 min +/- 14.1) (P = .003).

For stress CMR studies with STIR sequences (27 patients) a statistically significant decrease of the examination time has been observed with a reduction of 19.7 minutes (t = 45.11 min +/- 14.7) using the Cardiac Dot Engine compared to (t = 64.9 min +/- 7.8) examination times using conventional software (P = .001).

Furthermore, for CMR studies without STIR sequences (31 patients) a significant mean reduction of the examination time of 15.5 minutes has been found, which has been also statistically significant (t = 57.7 min +/- 14.7) compared to (t = 42.2 min +/- 16.1) (P= .001).

Stress CMR studies without STIR sequences (78 patients) have also shown mean examination times of (t = 44.6 min +/- 16.8) using the Cardiac Dot Engine compared to (t = 65.1 min +/- 22.3) using the conventional software, which means a time reduction of 20.4 min (P = .002) (Table 2).

Discussion and limitations

Our study is not without limitations.

First of all, it is a retrospective study, which has inherent disadvantages.

There are also independent variables that may alter the average examination time. For example, at the time of infusion of adenosine, as a rule, there is a cardiologist present. The mean arrival time of the cardiologist is (t = 4.8 min +/- 7.1), which introduces a considerable delay.

There may also be glitches that force the study to be repeated, although this is very rare. This process, however, rarely extends beyond 5 minutes.

Another factor that may have extended the examination times at the beginning of this study is the universal training of all MRI personnel. It has been observed that during the initial learning phase, after the introduction of the Cardiac Dot Engine, the average examination times have been longer than afterwards. However, once the basic handling of the Dot Engine has been learned, the Cardiac Dot Engine has a fast learning curve without requirement of highly specialized technologists.

Conclusion

The Cardiac Dot Engine introduces patient benefit by providing systematically reproducible and efficient studies that consistently reduce examination time, resulting in increased efficiency, reduced costs and improved patient satisfaction without ever sacrificing high-quality diagnostic images.

Table 2

Time reduction in cardiac magnetic resonance

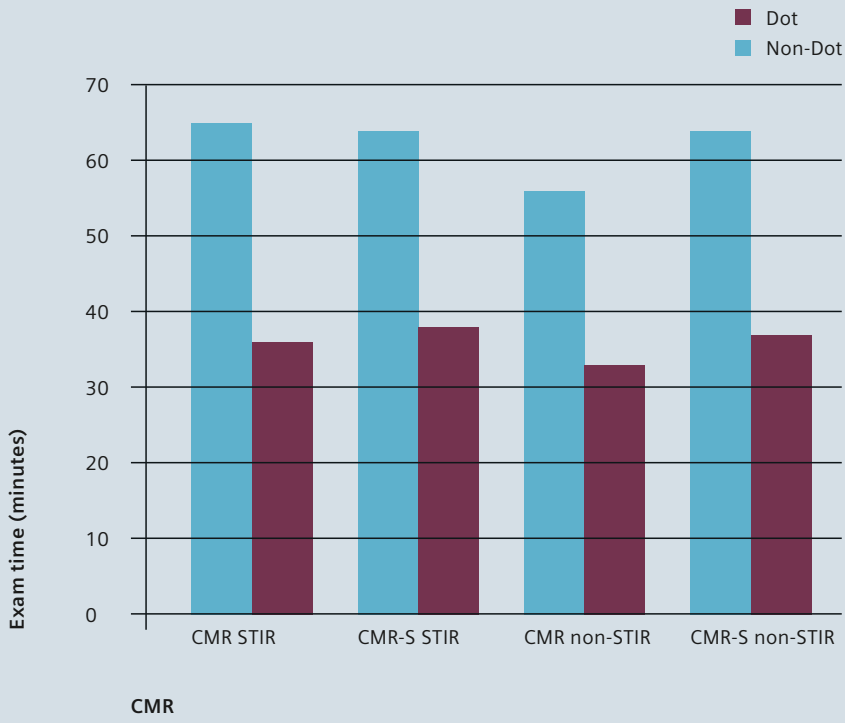

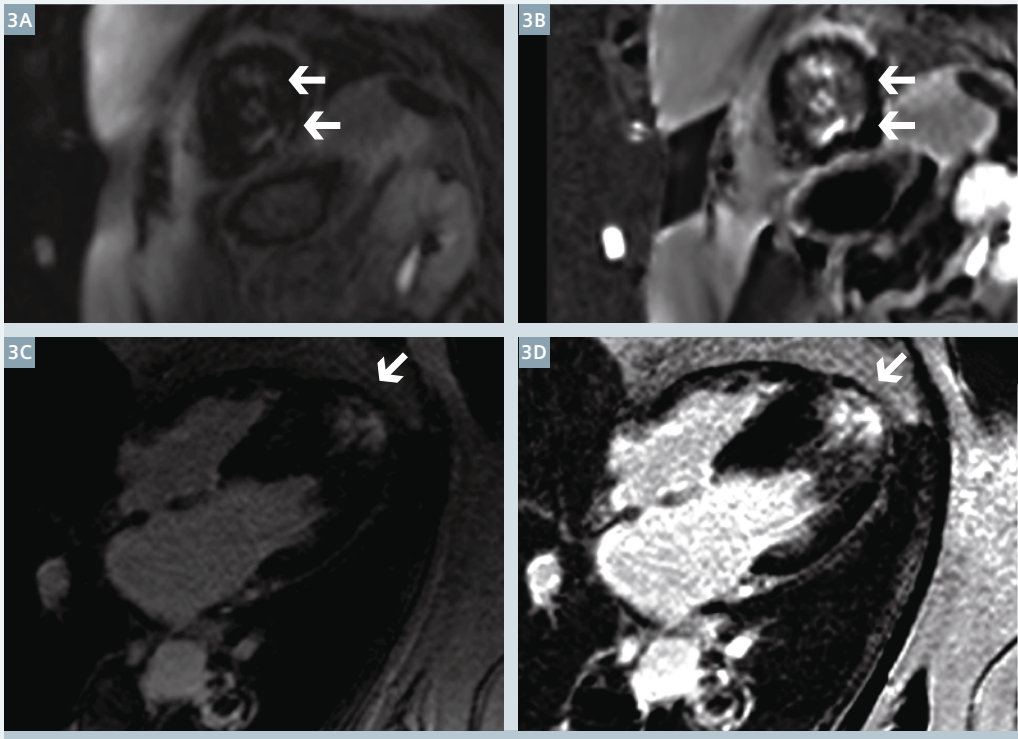

3 Short axis **(3A, B)** and four-chamber-view **(3C, D)** demonstrates hypertrophic changes as well as delayed contrast enhancement in the apex in a 43-year-old man with hypertrophic cardiomyopathy.

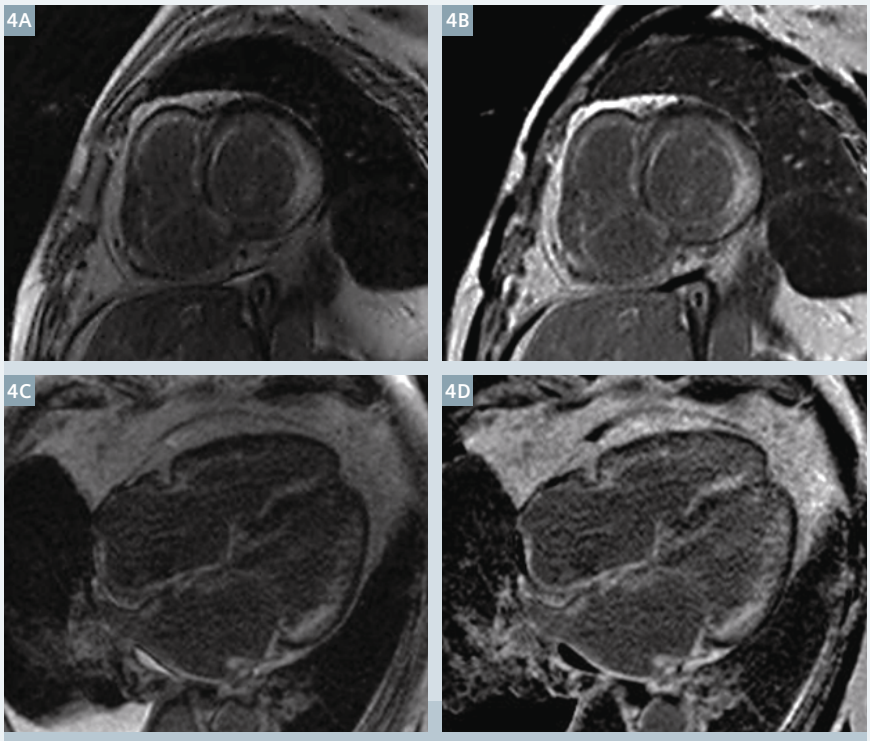

4 Delayed enhancement in the short axis **(4A, B)** and four-chamber-view **(4C, D)** reveals the presence of a diffuse patchy enhancement pattern, very suggestive of cardiac amyloidosis in a patient with congestive heart failure. A cardiac biopsy confirmed the diagnosis.

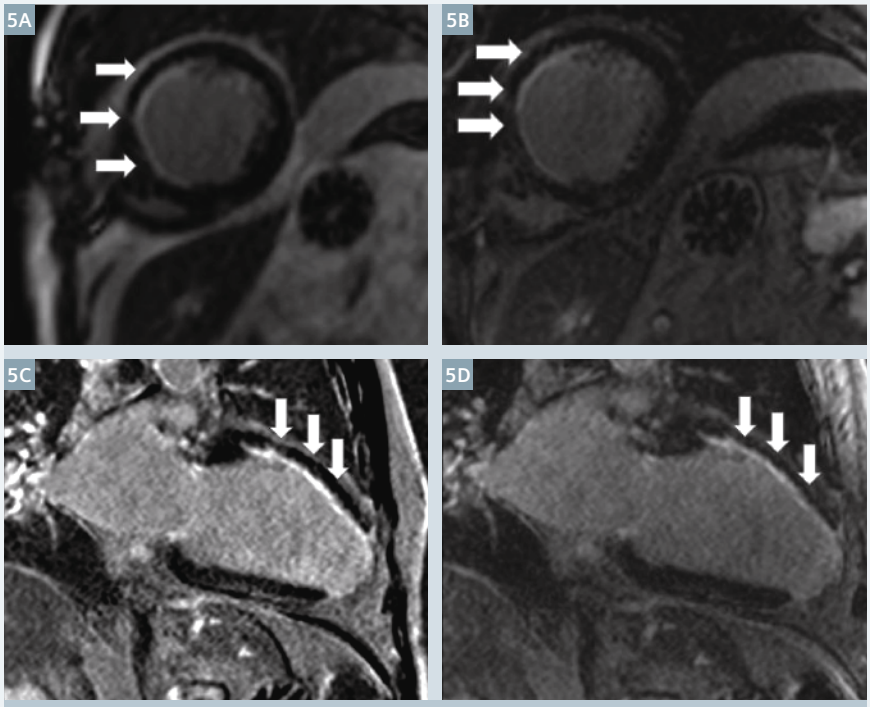

5 **(5A, B)** Short axis and **(5C, D)** two-chamber-view of delayed enhancement sequences. Arrows point to the septal wall of this patient, showing a severe subendocardial hyperenhancement that represents the region of myocardial infarction in the territory of left anterior descending (LAD) and the left circumflex artery (LCX).

Acknowledgements

The authors would like to thank all the members of the Cardiac MRI team from the Clínica Universidad de Navarra (CUN) and the MRI nurses for their valuable participation, helpfulness and support during the study, and also a very important acknowledgment to our colleagues from Siemens Healthcare, especially Efrén Ojeda, for his continuous support and contribution.

References

1 McMurray JJ, Adamopoulos S, Anker SD, Auricchio A, Böhm M, Dickstein K et al. ESC guidelines for the diagnosis and treatment of acute and chronic heart failure 2012. Eur J Heart Fail. 2012 Aug;14(8):803-69.

2 Montalescot G, Sechtem U, Achenbach S, Andreotti F, Arden C, Budaj A et al. 2013 ESC guidelines on the management of stable coronary artery disease: the Task Force on the management of stable coronary artery disease of the European Society of Cardiology. Eur Heart J. 2013 Oct;34(38):2949-3003.

3 Moenninghoff C, Umutlu L, Kloeters C, Ringelstein A, Ladd ME, Sombetzki A et al. Workflow efficiency of two 1.5 T MR scanners with and without an automated user interface for head examinations. Acad Radiol. 2013 Jun;20(6):721-30.

Contact

Jesús Ciro Pueyo, M.D., Ph.D.
Department of Radiology
Clínica Universidad de Navarra
Av. Pio XII, 36
31008 Pamplona
Spain
Phone: +34 948255400
Fax: +34 948296500
jpueyo@unav.es

How Modules of Imaging Sequences Fit Together: An Overview of Recent Advances in MR Imaging

Jamie Ho Xiu Mei; Chan Ling Ling; Helmut Rumpel

Department of Diagnostic Radiology, Singapore General Hospital, Singapore

Abstract

The past decade has seen a vast number of new MRI sequences and a great deal of development of protocols, so that we are left with the question: Does the MRI terrain lend itself to complexity? The answer is no. MRI sequences are made of modules on image contrast and image acquisition. The purpose of this short reprise is to compile the well-established methods based on this modular approach together with recent advances in MRI. This will take away the mystery of seemingly complex MRI sequences.

An MRI sequence can be expressed as a series of time events. For instance, in conventional imaging, a Spin Echo sequence refers to a timed series comprising *excitation – refocussing – readout* and a Gradient Echo sequence refers to a timed series of *excitation – dephasing – readout*. These sequences are then repeated along the phase encoding direction. In a more generalised term this comprises the steps of *excitation – phase encoding – frequency encoding*. The image contrast relies mainly on TR and TE in a conventional sense.

Fast imaging is achieved through a transformation of this sequence. The sequence is now an ordered list of events: *Preparation – evolution – detection*, this initial idea dating back to 1990 by Haase et al. [1]. The first part of such a sequence prepares for image contrast whilst the second creates the contrast, and these evolve over time. This is followed by a detection part, which can yield the spatial resolution in one go, or even over a time course.

In the last decade, 'The many combinations of MRI' [2] for structural and functional images rich in contrast have entered clinical routine. In this article, we attempt a classification of these MR techniques based on the concept of *preparation – evolution – detection* with the following subcategories of:

- Inversion Recovery prepared sequences
- Spin Echo / Gradient Echo prepared sequences
- Subtraction imaging
- Double preparation-evolution approaches

as shown in Table 1.

Contrast: Preparation – Evolution

The term *'Preparation'* refers to preparation for T1, T2, and T2* contrast. *'Evolution'* over time allows the spin system to change.

- T1 effects are achieved by inversion of the longitudinal magnetization, which can be in a non-selective manner, spatially-selective, or frequency-selective. The time to inversion recovery of T1 is used for nulling either lipid (STIR/SPAIR), CSF (FLAIR) or background signal in non-contrast MR angiography. Note that in the frequency-selective mode (SPAIR), only the signal-of-interest, e.g. lipid or silicone, follows this scheme of inversion recovery, hence leaving the water signal undisturbed for optimal signal-to-noise ratio. Other applications of TI effects include enhancement in contrast differentiation between grey matter and white matter (MPRAGE, MP2RAGE) or in-flow time in ASL.
- T2 contrast is generated by a Spin Echo preparation module. Its TE period can be used for T2 contrast preparation or encoding of diffusion (diffusion-weighted imaging).
- T2* weighting during a Gradient Echo sequence serves as a contact time for water in blood to exchange with deoxy- or meth-haemoglobin/ hemosiderin deposits, to detect haemorrhagic lesions, or with oxy/ deoxy-haemoglobin to produce BOLD contrast in fMRI, or to assess liver and cardiac iron overload.
- No contrast preparation: The FLASH sequence can produce PD/T1/T2*-weighted tissue contrast depending on the acquisition parameters, whilst TrueFISP exhibits an intrinsic T1/T2 contrast.

Table 1

Body region	MRI technique/ application	Magnetization prepared contrast	Preparation	Evolution	Detection
Inversion-recovery prepared sequences					
Brain	FLAIR [3–5]	nulling of CSF	non-selective inversion	T1 recovery	TSE/HASTE/EPI/ FLASH
Spine, skull base	STIR [6]	nulling of lipid	non-selective inversion	T1 recovery	TSE/HASTE/EPI/ FLASH
Breast/ Any body region	SPAIR [7]	nulling of lipid	fat-selective inversion	T1 recovery	TSE/HASTE/EPI/ FLASH
Brain	MPRAGE [8]	GM-to-WM contrast	non-selective inversion	T1 recovery	T1 recovery
Vascular	Non-CE MRA [9–10]	nulling of background signal	spatially selective inversion	T1 recovery	TrueFISP
Spin Echo / Gradient Echo prepared sequences					
Brain, spine, body	DWI/DTI [11]	diffusion weighting	Spin Echo	time interval	EPI/HASTE
Vascular	CE MRA [12–14]	T2* weighting	Gradient Echo	long TE	EPI
Brain	fMRI [12]	T2* weighting	Gradient Echo	long TE	EPI
Subtraction imaging					
Brain	ASL [15–18]	tagging	off-centre non-selective inversion	inflow time	EPI/GRASE
Vascular	Non-CE MRA [10]	bright blood contrast	ECG trigger	trigger delay	SPACE
Double preparation-evolution approaches					
Brain	MP2RAGE [19–20]	nulling of WM	non-selective inversion	T1 recovery	3D-FLASH
		GM-to-WM contrast			
Cardiac	Dark-blood cardiac MRI [21–22]	nulling of viable myocardium	selective saturation	T1 recovery	TrueFISP
		nulling of blood	non-selective inversion		
Body	Whole-body DWI [23–24]	TI – nulling of lipid	fat-selective inversion	T1 recovery	EPI
		diffusion weighting	Spin Echo	time interval	

Table 1 comprises MRI applications for neuro, cardiac, musculoskeletal, and body imaging with magnetization prepared contrast. The sequences are subdivided into modules of *preparation – evolution – detection*: The first expresses preparing for contrast, the second allows the magnetization to change, and the third performs the image. The modules under the detection part are in most instances interchangeable.

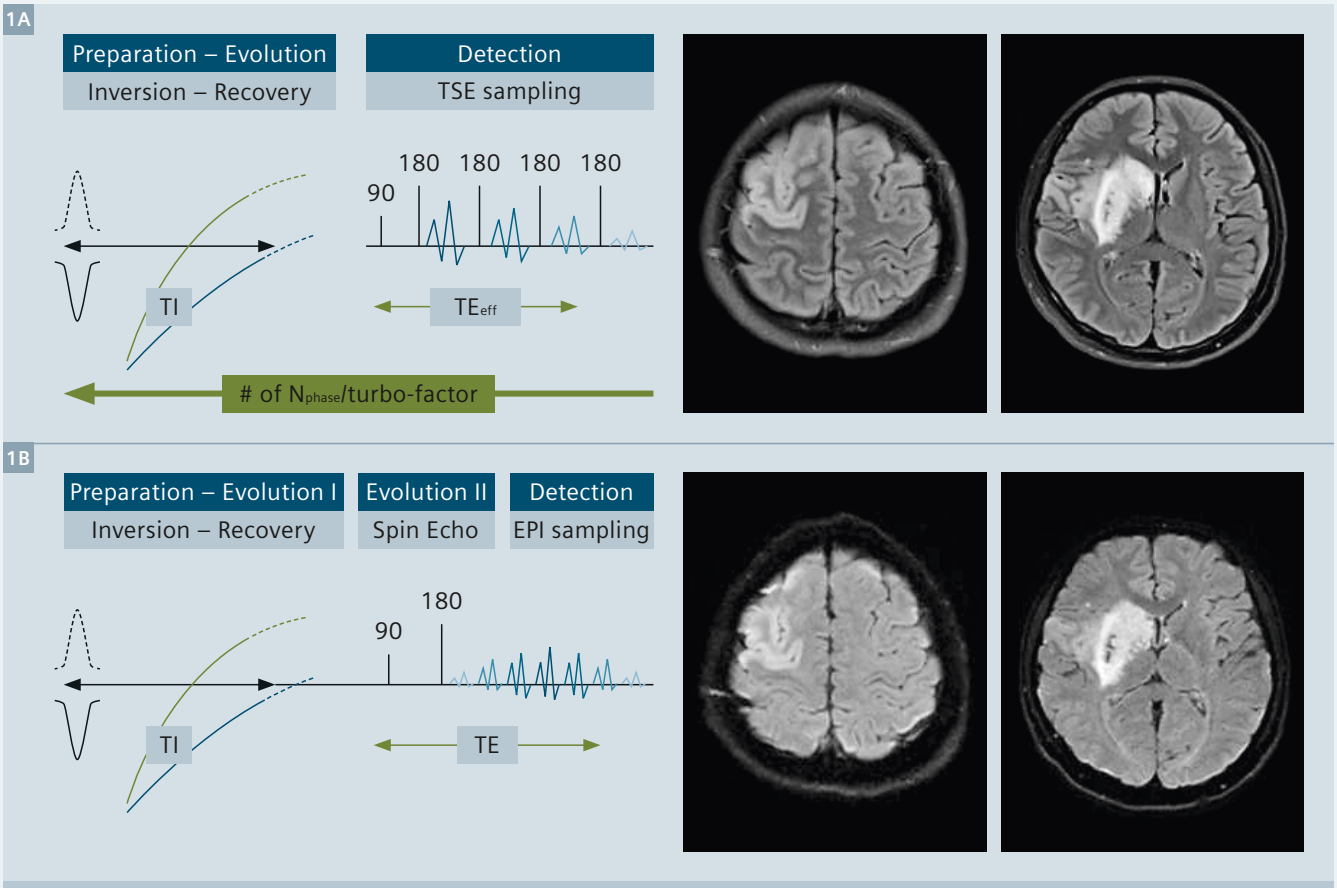

1 Comparison of TSE-FLAIR and EPI-FLAIR of the brain in a patient with subacute stroke. **(1A)** TSE-FLAIR with oversimplified pulse-sequence scheme. The entire sequence of inversion-recovery-sampling is repeated for each segment with TR 7000 ms, TE_{eff} 132 ms, TI 2100 ms. **(1B)** EPI-FLAIR with inversion-recovery first, followed by a Spin Echo preparation module, followed by EPI sampling with TR 10000 ms, TE 88 ms, TI 2300 ms. The lesion conspicuity is comparable between the two sequences, although there is some loss of sharpness in EPI-FLAIR (1B) with a significant shorter acquisition time of TA = 1:20 min compared to that for TSE-FLAIR (TA = 2:50 min). (3T MAGNETOM Skyra)

Imaging: Detection (Read-out)

Longitudinal or transverse magnetization?

A Gradient Echo or Spin Echo preparative module creates transverse magnetization. The read-out train in EPI directly uses this prepared transverse magnetization. However – unlike EPI – FLASH and TrueFISP are imaging techniques that require a separate excitation for each line of *k*-space. The prerequisite is the preparation of longitudinal magnetization. This is achieved using a 90° flip-back pulse at the end of the *preparation – evolution* period.

One-time contrast preparation

Even though the contrast preparation occurs at one time point, the contrast created decays and changes during the entire detection period, and is thus determined by the speed of readout and *k*-space traversal. In other words, the detection period should be of the same order of magnitude as the lifetime of the state of a magnetization-prepared contrast. Acquisition of the entire image after a single preparation-evolution period is primarily achieved by real-time imaging based on EPI or TrueFISP, followed by FLASH and HASTE, all providing 'singleshot' imaging but in the order of one-tenths to hundreds of milliseconds per image.

Repeated contrast preparation

When the lifetime (durability) of the state of a magnetization prepared contrast does not match with a reasonable detection period, then segmentation in the phase dimension is required. In this scenario, multiple preparation-evolution periods are executed, one for each segmentation step. This is especially the case for TSE/SPACE as the acquisition time is relatively long, even for high turbo-factors. However, for each segmentation step, preparation – evolution – detection periods are separated in the same way as in the single-shot approach. The EPI sequence carries the additional option of segmentation in the readout dimension, which shortens the inter-echo time compared to shortening of the echo-train length for segmentation in the phase dimension. Otherwise, the concept of repeated contrast preparation is the same.

Repeated contrast preparation sequences are normally combined with methods for motion correction with either prospective acquisition correction PACE [25], or real-time correction using ECG and respiratory-

Continued on page 87.

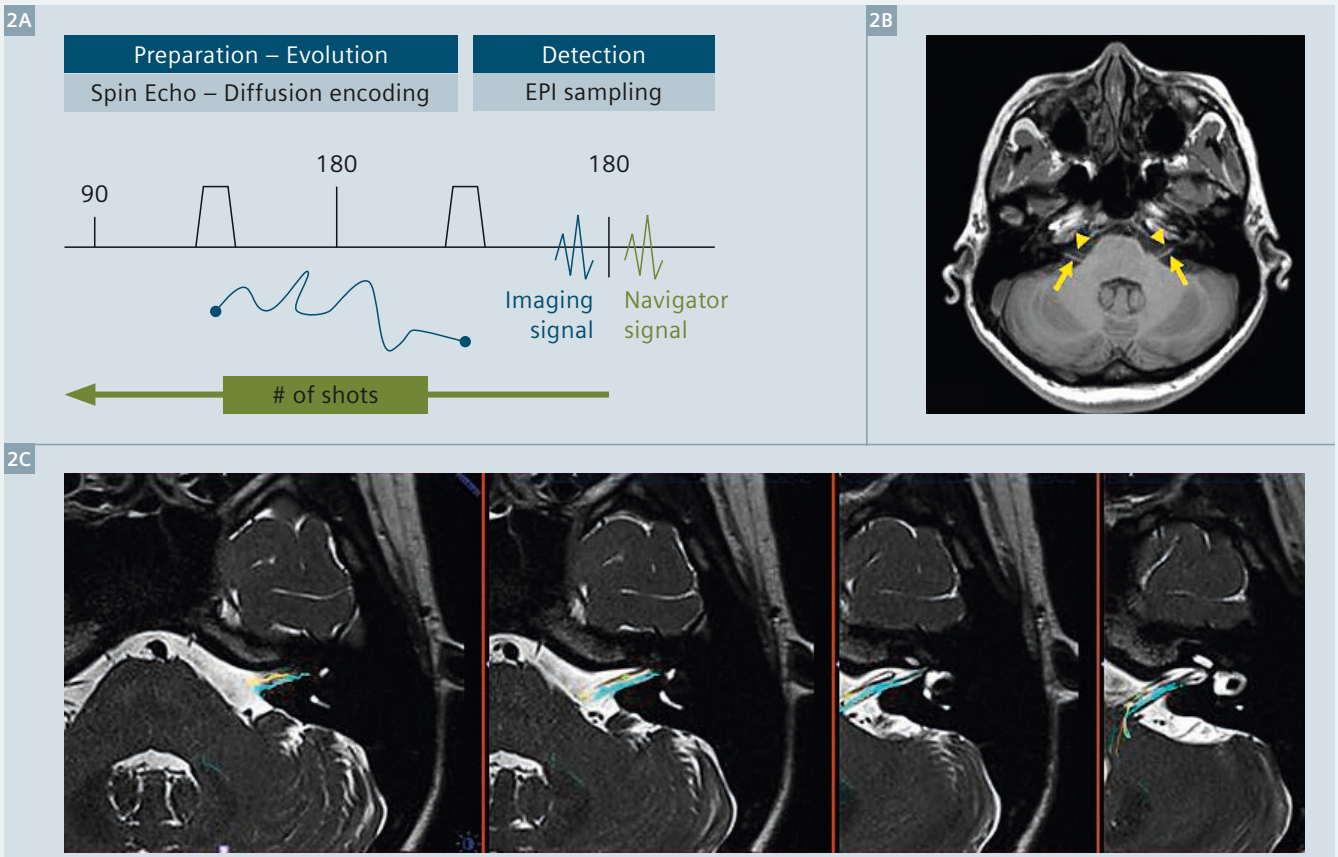

2 DTI-RESOLVE [26] **(2A)** Scheme of diffusion-weighted read-out segmented echo-planar imaging. The entire sequence of slice selective excitation-encoding of diffusion-sampling is repeated for each read-out segment. An illustrative example of the effect of read-out segmentation in reducing susceptibility artefacts is shown for the facial nerve: **(2B)** Axial T1-weighted image of the cisternal portion of the cranial nerves CN7 (arrow head) and CN8 (arrow). CN7 is exceedingly fine (~1 mm diameter) and in very close proximity (1-2 mm) to CN8. The cisternal portion of nerve is subject to distortion by CSF pulsation from the basilar artery. **(2C)** Tractography of the 7-8th CN complex using the *syngo*.via DTI software of four consecutive slices, based on nine read-out segments per image of 0.8 mm in-plane resolution. (3T MAGNETOM Skyra)

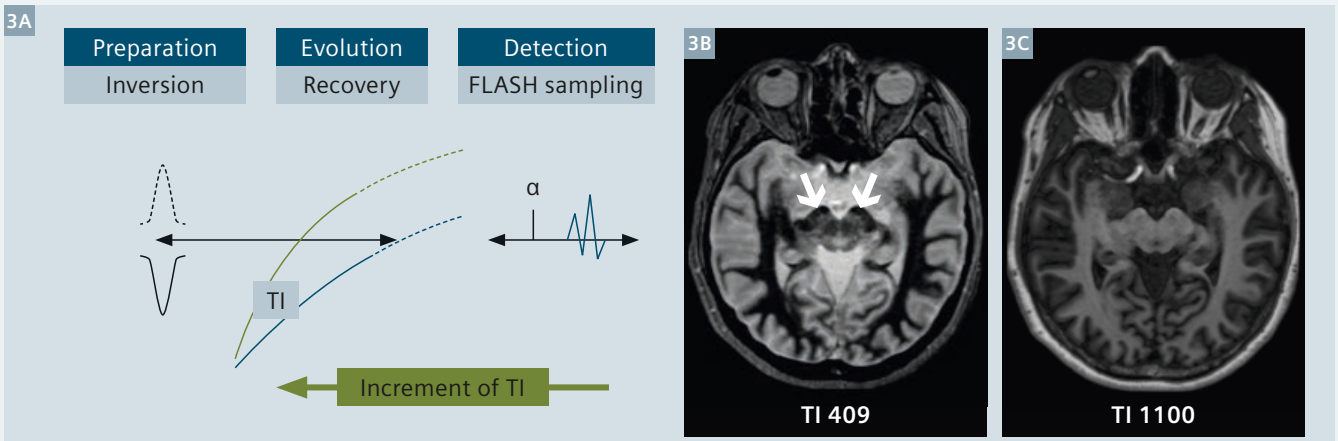

3 MP2RAGE of the midbrain. TR 5000 ms, TE 3 ms, TI 409 ms and 1100 ms; **(3A)** the shorter TI nulls white matter yielding superior contrast of substantia nigra, **(3B)** the longer TI provides grey matter / white matter contrast. (3T MAGNETOM Skyra)

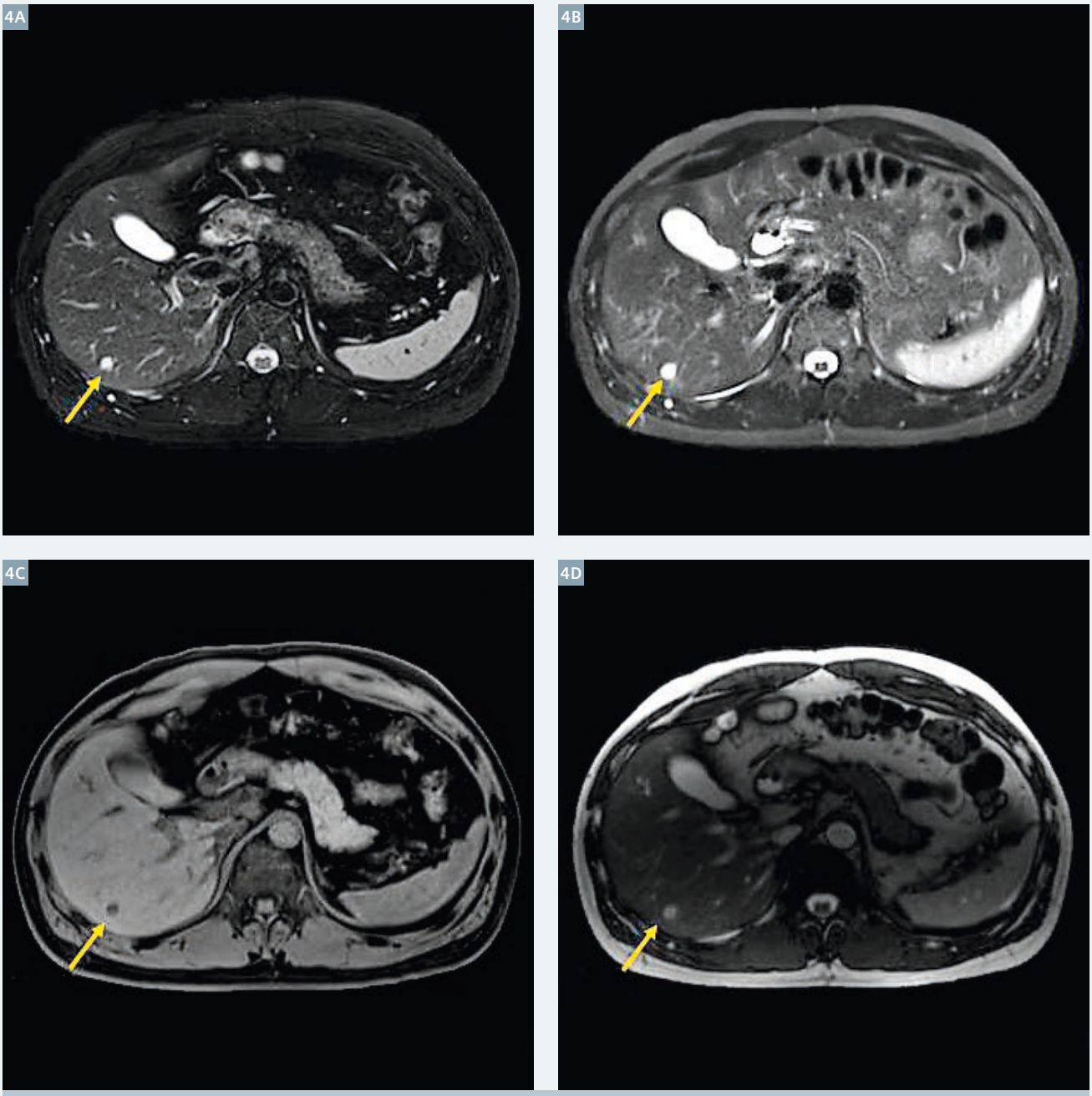

4 Breathhold liver imaging with decreasing acquisition time **(4A)** T2 TSE (four breathholds of 19 seconds each with 10 seconds break: TA = 2:04 min), **(4B)** inversion-recovery HASTE (three breathholds of 23 seconds each with 8 seconds break: TA = 1:35 min), **(4C)** FLASH (one breathhold of 15 sec), and **(4D)** TrueFISP (one breathhold of 15 sec) of a tiny hepatic lesion in segment 7 compatible with a haemangioma (arrow). In comparing the image lesion conspicuity, TSE shows a high lesion-to-background contrast, and best lesional-liver contrast in HASTE but concomitant T2 blurring overestimating the lesion size. Note the sub-optimal predominantly T1-weighted contrast of lesion in FLASH, improved T2-weighting contrast on TrueFISP. (1.5T MAGNETOM Aera)
Reprinted with permission from: Rumpel H, Chan LL (2015) Pitfalls in Diagnostic Radiology: Chapter 3 Magnetic Resonance Imaging. Editor: WCG Peh Springer Heidelberg Germany, ISBN 978-3-662-44168-8.

gating. These methods allow data acquisition only if the patient's position falls within an acceptance window i.e. the operator decides on the range of diaphragm positions or the stage of the cardiac cycle allowed in this window. For fast imaging of about 30 seconds or less, the image acquisition can be performed within a single breathhold window or in multiple breathhold windows if patients experience difficulties in maintaining even a short breathhold. Figure 4 is a pictorial of four different breathhold scans.

Conclusion

With the current status of the magnetic resonance technique, there is no general solution to fast imaging. Instead, this goal is achieved through various strategies, each well respected in its own niche. *Preparation – evolution – detection* is an expedient way of representing the versatile convertibility of imaging techniques.

Table 1 pulls together cornerstones of fast imaging strategies in achieving time-efficient acquisitions, each with its associated magnetization prepared contrast. Complementary combinations with different detection modules serve to avoid pitfalls and resolve artefacts in specific examinations. If, for example, the typical problems such as susceptibility-induced signal losses in EPI or sensitivity to off-resonance effects (balanced SSFP) compromise the quality of an image of interest, the appropriate module under the detection part can be readily changed while keeping the magnetization prepared contrast.

References

1 Haase A (1990) Snapshot FLASH MRI. Applications to T1, T2, and chemical shift imaging. MRM 13: 77-89.

2 MRI: The Basics (2010) 3rd edition, by Ray Hashemi H, Bradley WG Jr, Lisanti CJ. The many combinations of MRI.

3 Filippi M, Rocca MA, Wiessmann M et al (1999) A Comparison of MR Imaging with Fast-FLAIR, HASTE-FLAIR, and EPI-FLAIR Sequences in the Assessment of Patients with Multiple Sclerosis. AJNR Am J Neuroradiol 20:1931–1938.

4 Meshksar A, Villablanca JP, Khan R et al (2014) Role of EPI-FLAIR in Patients with Acute Stroke: A Comparative Analysis with FLAIR. AJNR Am J Neuroradiol doi: 10.3174/ajnr.A3786.

5 Nael K, Khan R, Johnson K et al (2013) How I do it: Acute stroke protocol in 6 minutes. MAGNETOM Flash 55: 44-50.

6 Rossa JS (1999) Newer Sequences for Spinal MR Imaging: Smorgasbord or Succotash of Acronyms? AJNR 20: 361-373.

7 Lee YS, Low CK, Rumpel H (2011) STIR vs SPAIR in Breast Imaging: a Case-Based Discussion MAGNETOM Flash 46: 54-55.

8 Deichmann R, Good CD, Josephs O, Ashburner J, Turner R 2000 Optimization of 3-D MP-RAGE Sequences for Structural Brain Imaging. NeuroImage 12: 112–127.

9 Morita S, Masukawa A, Suzuki K (2011) Unenhanced MR Angiography: Techniques and Clinical Applications in Patients with Chronic Kidney Disease. RadioGraphics 31: 13–33.

10 Rick M, Kaarmann K, Weale P et al (2009) How I do it: Non Contrast-Enhanced MR Angiography (*syngo* NATIVE). MAGNETOM Flash 42: 18-23.

11 Hagmann P, Jonasson L, Maeder P (2006) Understanding Diffusion MR Imaging Techniques: From Scalar Diffusion-weighted Imaging to Diffusion Tensor Imaging and Beyond. RadioGraphics 26: 205-223.

12 Chavhan GB, Babyn PS, Thomas B et al (2009) Principles, Techniques, and Applications of T2*-based MR Imaging and Its Special Applications. Radiographics 29: 1433–1449.

13 Laub G, Kroeker R (2006) *Syngo* TWIST for DynamicTime-Resolved MR Angiography MAGNETOM Flash 34: 92-95.

14 Natsuaki Y, Kroeker R, Laub G et al (2013) Advancements in the ECG-Gated Contrast-Enhanced MR Angiography MAGNETOM Flash 53: 32-39 and Khan SN, Natsuaki Y, Tao W et al (2013) Contrast-Enhanced MRA in Practice: Tips and Caveats. MAGNETOM Flash 53: 40-54

15 Petcharunpaisan S, Ramalho J, Castillo M (2010) Arterial spin labeling in neuroimaging. World J Radiol 28: 384–398.

16 Detre JA (2008) Arterial Spin Labeled Perfusion MRI. MAGNETOM Flash 38: 6-9.

17 Feinberg DA, B. Kiefer B, Johnson G. (1995) GRASE improves spatial resolution in single shot imaging. Magn Reson Med 33: 529–33.

18 Feinberg DA, Günther M (2009) Cerebral Blood Flow Imaging with 3D GRASE ASL Sequence Increases SNR and Shortens Acquisition Time MAGNETOM Flash 42: 62-69.

19 Marques J P, Kober T, Krueger G et al (2010) MP2RAGE, a self bias-field corrected sequence for improved segmentation and T(1)-mapping at high field. Neuroimage 49:1271-1281.

20 Tanner M, Gambarota G, Kober T et al (2012) Fluid and White Matter Suppression With the MP2RAGE Sequence. JMRI 35:1063-1070.

21 Rehwald WG, Salerno M, Chen EL et al (2007) Dark Blood Delayed Enhancement in Humans By Double Preparation and Gradient-Echo or Turbo-Spin-Echo Readout. Proc Intl Soc Mag Reson Med.

22 Rehwald WG, Salerno M (2007) Dark-Blood Delayed Enhancement Imaging: New Developments in the Imaging of Myocardial Viability MAGNETOM Flash 36: 110-116.

23 Padhani AR, Koh DB, Collins DJ (2011) Whole-Body Diffusion-weighted MR Imaging in Cancer: Current Status and Research Directions. Radiology 261: 700-718.

24 Doring T, Strecker R, da Silva M et al. (2013) New features of *syngo* MR D13 for improved whole-body diffusion weighted imaging. MAGNETOM Flash 55: 12-14.

25 Thesen S, Heid O, Mueller E, Schad LR (2000) Prospective acquisition correction for head motion with image-based tracking for real-time fMRI. Magn Reson Med 44: 457-465.

26 Porter DA, Heidemann RM (2009) High resolution diffusion-weighted imaging using readout-segmented echo-planar imaging, parallel imaging and a two-dimensional navigator-based reacquisition. Magn Reson Med 62:468–475.

27 Chavhan GB, Babyn PS, Bhavin G et al (2008) Steady-state MR imaging sequences: physics, classification, and clinical applications. Radiographics 28:1147-1160.

Contact

Helmut Rumpel, Ph.D.
Department of Diagnostic Radiology
Singapore General Hospital
helmut.rumpel@sgh.com.sg

"The best way to predict the future is to invent it."

Theodore Edward Hook, 1825

Magnetic Resonance Imaging at Siemens: A success story

Ingo Zenger; Antje Hellwich

Siemens Healthcare, Erlangen, Germany

In 1983 the first Siemens MRI system bearing the MAGNETOM name was installed at Mallinckrodt Institute of Radiology, in St. Louis, Missouri, USA. That was thirty years ago.

Today MAGNETOM systems feature our integrated Tim coil technology; our unique Dot scanning software; our applications, which continue to set trends in imaging; and naturally also the design of our MRI systems, which makes scans increasingly efficient for MAGNETOM users and increasingly patient-friendly. Let's take a look back and see how we got there.

1 The very first MAGNETOM system in 1983.

Making the invisible visible

On November 8, 1895, Wilhelm Conrad Röntgen revolutionized the field of medical diagnostics when he discovered X-rays. Over time, researchers developed other imaging methods to help doctors diagnose disease: Computed tomography, ultrasound, and nuclear medicine all use different techniques, each one supplying especially good images for specific scans. In the second half of the 20th century, scientists also began researching the fundamentals of a technology that turned out to be outstanding for medical imaging purposes: Magnetic resonance imaging (MRI).

In 1946, two physicists independently discovered the principle of magnetic resonance: Felix Bloch and Edward Mills Purcell showed that atomic nuclei in a magnetic field tilt when they are excited by a high-frequency electromagnetic field. If this high-frequency field is switched off, the atoms release the energy they have absorbed and return to their original state. By making this discovery, Block and Purcell laid the technical foundations for magnetic resonance imaging. It was an accomplishment for which they shared the Nobel Prize in Physics in 1952.

In 1950, Erwin Hahn proved that atomic nuclei generate an echo – a 'spin echo' – when they are influenced with two high-frequency pulses. But magnetic resonance remained a slow and imprecise method until 1968, when a group of researchers from Zurich made groundbreaking

Innovation track

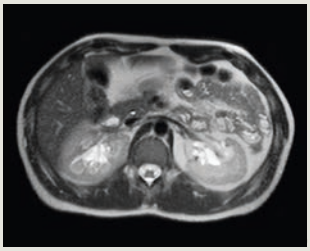

First passive direct magnetic shielding

1984

progress in enhancing its sensitivity. Richard Ernst, Weston Anderson, and Kurt Wüthrich improved the pulse excitation and used a new method to analyze the resonance signal. This made magnetic resonance technology about a thousand times faster and significantly more sensitive. Ernst went on to receive the Nobel Prize in Chemistry in 1991 for this achievement.

In the years that followed, magnetic resonance imaging became an important analytical method suitable for solids, liquids, and gases – until, in 1971, Raymond Damadian showed that it could also be used to distinguish between tumors and healthy tissue. Modern MRI technology is considered to have been born in 1973, when chemist Paul C. Lauterbur and physicist Sir Peter Mansfield were the first to make it possible to visualize a fluid-filled object. The two men together received the Nobel Prize in Medicine in 2003 for their groundbreaking work in developing MRI technology.

Early history at Siemens

Siemens recognized the new method's potential and displayed great interest in research and development involving this technology. Engineers at the Siemens research lab used magnetic resonance to study the qualities of plastics back in 1959. In 1965, the company hired a man who would play a significant role in shaping the development of MRI in the years to come: The physicist Alexander Ganssen (Fig. 2). Ganssen became intrigued by magnetic nuclear resonance while still a student, and remained true to this passion for the rest of his life. At Siemens, his research focused on MR techniques for medical diagnostics. He developed a system that was built in 1966 and patented a year later: The world's first unit that used magnetic resonance to measure a patient's blood flow at the carotid artery or arm.

On February 1, 1978 Siemens began to develop an MRI system. Alexander Ganssen engaged physicist Arnulf Oppelt to manage the project and the team built the first MRI prototype: A 0.1-tesla system with a magnet already able to fit a person's whole body. This magnet was ordered from Oxford Instruments Ltd. – later to become Siemens Magnet Technologies. This experimental system (Fig. 3A) was completed in a wooden shed built specifically for the purpose (Fig. 4). To avoid disrupting the magnetic field, the building was constructed without any magnetic parts – not even a single steel nail. Even so, the researchers still struggled with issues: The power supply to the magnet fluctuated, and since the frequency of the nuclear resonance was in the same range as that of radio waves, the physicists received shortwave broadcasts instead of MRI signals in the evening. To solve this problem, they built a Faraday cage around the magnet to shield it (Fig. 3B).

2

2 Alexander Ganssen, around 1954.

3A

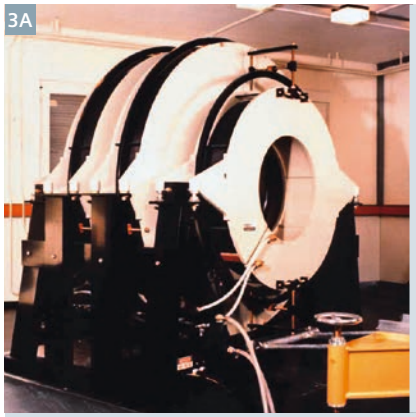

3B

3 **(3A)** Air-cooled 0.1 Tesla magnet, 1978.
(3B) 0.1T magnet with Faraday cage, 1979.

1989

First actively shielded 1T system

1993

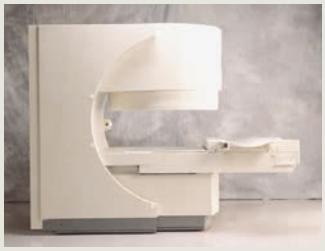

First open MR 0.2T system

In 1979, Oppelt's team looked around for a suitable test object, ultimately deciding on a green bell pepper (Fig. 5), since "It would definitely hold still, it was big enough to stand in for a human organ, and you could also cut it open to ascertain the similarity between the potential image and its anatomy." The team's research soon brought further successes. The first image of a human skull followed just a few months later, in March 1980 (Fig. 6). Ganssen himself volunteered for the scan, which took only eight minutes – already significantly shorter than the amount of time needed to scan the bell pepper just a few months before.

In September 1980 the first few patients were scanned using an MRI system (Fig. 8). The early scanning process was not very comfortable for the test subjects, who had to crawl into the magnet – which was a very tight fit – on a wooden board.

Over the course of the year in 1981, the engineers significantly enhanced the MRI system's image quality. A second pilot unit was built, this time with a field strength of 0.2T. Ernst Zeitler, a radiologist in Nuremberg, Germany, used the new system to scan his patients. By then, the images were so good that tumors in the head or abdomen and changes in the brains of patients with multiple sclerosis could be localized. "The potential that MRI technology had for diagnostic purposes was clear in 1981, when we saw the first tumor in a head scan," Oppelt says.

It wasn't long before the superconducting magnets made it possible to achieve higher field strengths, and the third pilot system reached 0.5T. Soon after Siemens began developing 1.5T magnets.

In early 1983, the time had come: At Hannover Medical School, Germany, Siemens installed the first MRI system to be tested in a clinical setting to ensure that it was suitable for day-to-day clinical use. The system's centerpiece was an oil-cooled, normally conductive 0.2T magnet. The testing went so well that Siemens ramped up product development efforts, establishing the new Magnetic Resonance Business Unit within the Medical Technology Division. Not long after that Siemens installed the first 0.35T MAGNETOM system at the Mallinckrodt Institute of Radiology, in St. Louis, MO, USA (Fig. 9). This made Siemens one of the first providers worldwide to offer magnetic resonance imaging for clinical applications.

The first MAGNETOM systems were available in different field strengths (0.35, 0.5 and 1.5 tesla). Once the system had been set up in the shielded MRI room, the magnet was cooled to minus 269 degrees Celsius using liquid nitrogen and liquid helium and then charged with electricity. After that, no further electrical power to the magnet was needed, and the power supply was permanently cut off. The helium and nitrogen, however, slowly evaporated, so regular replenishments were necessary – the first MAGNETOM systems used about two liters of nitrogen and half a liter of helium per hour (Fig. 10). Today's advanced MAGNETOM systems rely on 'zero helium boil-off' technology, which allows MRI systems to keep running in normal operation without using up any helium.

In December 1983, Klinikum Charlottenburg, a hospital operated by Freie

4

4 The wooden building used as the first MRI research lab, Erlangen, 1979.

5

5 MR image of a green bell pepper, November 1979.

6

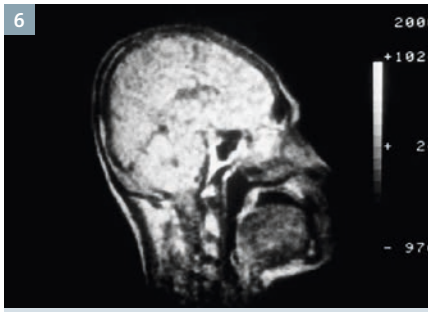

6 Alexander Ganssen's head, 1980. 128 matrix, 8 minutes.

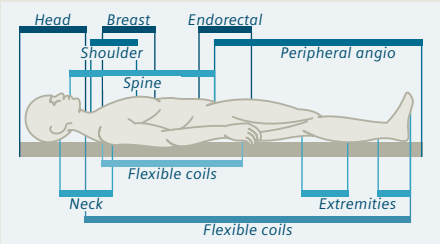

1997

First integrated Panoramic Array Coil concept for whole body imaging

2001

MAGNETOM World

The MRI community consisting of internet platform, MAGNETOM Flash magazine and MAGNETOM World Summits

Universität Berlin, became the first university medical center in Germany to receive an MRI system with superconducting magnets from Siemens (Fig. 11). From then until June 1984, Siemens shipped 14 MAGNETOM systems to destinations all over the world. That same month, the U.S. Food and Drug Administration granted the MAGNETOM its final approval for the U.S. market. In 1986, Siemens became the first manufacturer of MRI systems to win approval for 1.5-tesla systems in Japan.

7 Arnulf Oppelt with the 0.1T MRI prototype, 1981.

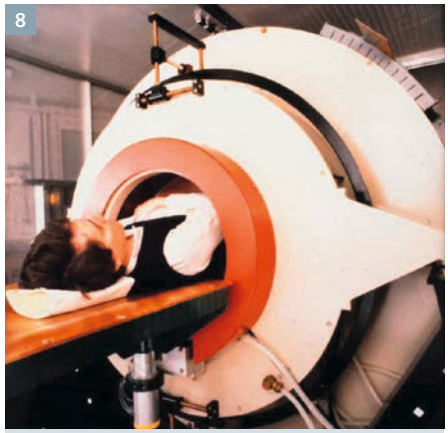

8 A whole-body scan using the pilot system, 1980.

9 The first MAGNETOM, St. Louis, 1983.

10 Replenishing helium in the early 80s.

11 Klinikum Charlottenburg, operated by Freie Universität Berlin, 1983.

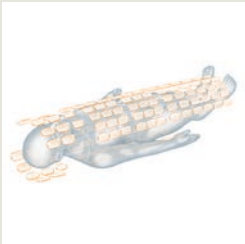

New Technology Tim RF and coil technology

2003

2004

First Open Bore (70 cm) system

12 Magnet shielding, 1984.

13 Actively shielded 1T MAGNETOM 42 SPE.

The magnets used in the first MRI systems lacked any shielding for the magnetic field and therefore could only be installed in rooms measuring at least 40 m². So Siemens developed a superconducting magnet with a stray field about five times smaller. This design, found nowhere else in the world, shielded the magnetic field through 'self shielding', where a cage-shaped shield conducted the stray field back to the magnet. These magnets required only a quarter of the space. Many of the changes that rooms had previously needed in order to accommodate an MRI system were no longer necessary, cutting installation costs (Fig. 12).

In 1989, Siemens launched a 1.0-tesla system with an actively shielded magnet, the MAGNETOM 42 SPE (Fig. 13). Active shielding means that in addition to the coils that generate the magnetic field, there are also coils installed on the magnet itself, which weaken the magnetic field toward the outside – where no magnetic field is needed for imaging purposes. It was followed in 1991 by an MRI system with an actively shielded 1.0-tesla whole-body magnet operated via an intuitive user interface similar to that of a PC: The MAGNETOM Impact (Fig. 14).

Even as these performance gains were being made, Siemens was also introducing a number of technological innovations that unlocked new diagnostic possibilities, shortened scan times, and reduced power consumption. As early as 1985, the company was able to cut scanning time nearly in half by using a 'half-Fourier imaging'. In this measurement technique, only about half the data was determined through direct measurements, while the other half was reconstructed mathematically.

14 MAGNETOM Impact, 1991.

Open and standardized

By the early 1990s, MRI had become an integral part of everyday clinical practice. In 1992, the standard was 20 patients in eight hours. However, some patients felt uncomfortable

2009

New Technology
Dot workflow engines
and Tim 4G

15 Using the MAGNETOM Open to monitor an operation at Cleveland University in 1994.

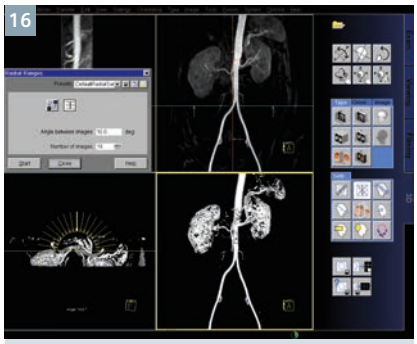

16 Angiography with *syngo*, 2001.

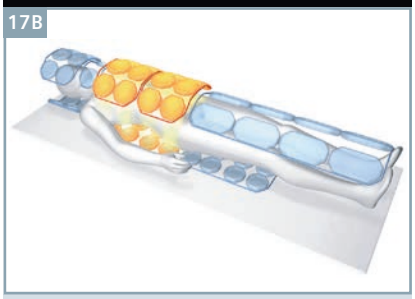

17 **A, B:** Whole-body imaging with Tim (Total imaging matrix).

when they were moved into the MRI system's narrow bore. In 1993, Siemens succeeded in making MRI accessible to everyone by introducing the first truly open MRI system, the MAGNETOM Open.

The 0.2T MAGNETOM Open even made it possible to monitor patients during surgery (Fig. 15).

The software used for the Siemens MRI systems in the 1990s was structured similarly to PC software, so it was already much more intuitive to use than the software for the first MRI systems. However, MRI and CT or other imaging systems from the same manufacturer had always used different software interfaces – which operators had to learn individually. Around the turn of the 21st century, Siemens became the first medical technology manufacturer to craft a standardized user interface for all of its systems: *syngo* software (Fig. 16). When a hospital or medical practice purchases a new system from Siemens, the learning curve for staff is much shorter.

From then on, all imaging systems from Siemens featured standardized operation.

In late 2003, Tim – the Total imaging matrix – revolutionized MRI (Fig. 17). The centerpiece of Tim technology is the completely innovative HF coils that collect data based on a matrix concept.

Whole-body scans without changing coils and without repositioning the patient finally came true. Tim makes it possible to produce images of the entire body from head to toe in a single pass, since the matrix coils cover all areas of the body at the same high level of detail. Scanning the entire body is possible in about twelve minutes for patients as much as 2.05 meters tall.

Tim represents tremendous technological progress in image quality, significantly lower patient preparation time, and shorter scanning times, but it also has additional advantages for operators and patients. Patient comfort is also

2010

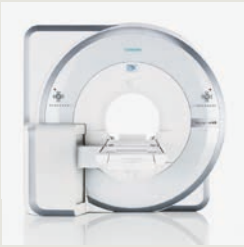

First MR-PET Biograph mMR

2011

First parallel transmit application: Tim TX TrueShape

18 MAGNETOM Espree, the world's first 1.5-tesla system with a 70-centimeter open bore.

enhanced by light-weight coils: At just 950 grams, the body matrix coil is lighter than some winter bed comforters. Tim technology allows patients to be positioned feet first for almost all scans – a big relief for many patients, since it means the head can stay outside the tube. Siemens combined all of these features in the MAGNETOM Avanto, which was commissioned for clinical operation at University Hospital Tübingen, Germany on November 25, 2003.

A few months later, Tim technology, working in tandem with optimization of components such as the magnet, gradient system, and receiver electronics, enabled another milestone in magnetic resonance imaging: The MAGNETOM Espree was the world's first 1.5-tesla system with a 70-centimeter opening (Fig. 18). This allowed invasive procedures and gave obese patients unrestricted access to high-field MRI for the first time.

*QISS is pending 510(k) clearance and is not commercially available in the US.

Biograph mMR	first simultaneous acquired MR-PET images across all body regions
FLASH	fast imaging
PACE	inline motion correction for fMRI
ASL	non-contrast MRI perfusion
AutoAlign	standardized, reproducible patient scan positioning
SWI	new insights with susceptibility-weighted imaging
DTI task card	easy visualization of fiber tracks
SPACE	high-speed TSE imaging in 3D
TrueFISP cine	excellent blood-tissue contrast and cardiac function
Inline Dynamic Signal	fully automated myocardial perfusion analysis incl. motion correction and quantification of myocardial first pass perfusion with Cardiac Dot Engine
Delayed Enhancement	visualization of myocardial scar and fibrosis
Inline VF	inline analysis of ventricular function
TWIST	low-dose time resolved MR Angiography with high resolution in space and time
QISS*	non-CE MR Angiography technology
Cardiac Dot Engine	standardizes Cardiovascular MR examinations with workflow guidance and automation
Tissue4D	pharmakokinetic modeling of dynamic studies
TimCT	moving table whole-body MR imaging
TWIST-VIBE	always the right contrast in dynamic liver MRI
StarVIBE	free-breathing contrast-enhanced body imaging
GRAPPA	small FOVs with parallel imaging in *k*-space
WARP	minimizing artifacts from metal implants
MapIt	quantitative cartilage characterization
Phoenix	drag and drop protocol sharing
Inline	motion correction and analysis such as MIPs and ADC maps on the fly
Dot Engines	automated and personalized scanning for each body region

19 Leading applications developed together with our international collaboration partners.

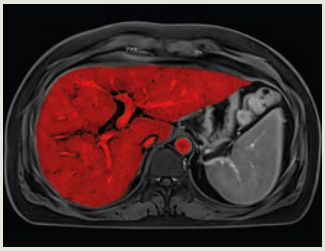

FREEZEit
body imaging

Innovation drives our success

2014

Siemens engineers have since worked on technologies and software that further improve and support Tim technology. The *syngo* software has received numerous new MRI applications that further enhance comfort and convenience, expand the range of scanning options (Fig. 19).

Healthcare providers face mounting pressure to work on a cost-optimized basis while also offering the very best in diagnosis and treatment. Technological innovations and enhanced productivity play a large role in achieving this balance. In 2009, Siemens launched the fourth generation of Tim technology (Tim 4G) as well as Dot – Day optimizing throughput – technology (Fig. 20). Dot simplifies workflows, thereby boosting productivity by as much as 30 percent. It uses images and text to guide operators step by step through the scanning process, even during complex scans.

Another technological breakthrough from Siemens has unlocked completely new views of the inside of the human body in 2010: The Biograph mMR system combines MRI and PET (Fig. 21). These two methods have different strengths, and they supply complementary information on diseases.

On the journey from fundamental research in the wooden shed to world market leadership in MRI technology, Siemens has grown around the globe. With production sites in Erlangen (Germany), Oxford (UK), Shenzhen (China) and Joinville (Brazil) Siemens has all the technology and capabilities needed to build state-of-the-art MRI systems entirely from a single source. The sites work seamlessly together on research and development. Ongoing investments give rise to numerous innovations that add to the product family and are adjusted to meet the needs of the various markets Siemens serves. At all of the locations, the superior standard of quality that applies to development and production activities is supplemented by consulting and other services for customers from all over the world.

This retrospective shows the impressive development of this technology from the early days to the first commercial steps and right through to today's technology and market leadership.

Many innovations from Siemens have changed the world. With MRI, we have been unlocking new possibilities for 30 years now – what we once dreamed about is now reality. And today's dreams will become tomorrow's reality.

Further reading

If you are interested in the whole story of MRI development at Siemens, please visit

www.siemens.com/magnetom-world > Publications > MR Basics

where you will find a 43-page booklet with many more images and all the details on 30 years of innovation at Siemens.

20 Screenshot of a Dot Engine.

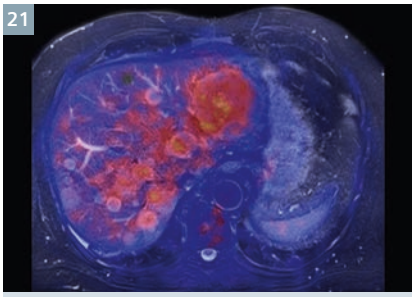

21 Molecular MR image generated with Biograph mMR at TU Munich, Germany in 2011.

22 Since 2001 the MAGNETOM World offers a platform to meet, discuss and exchange valuable information with your peers.

Siemens Healthcare Publications

Our publications offer the latest information and background for every healthcare field. From the hospital director to the radiological assistant – here, you can quickly find information relevant to your needs.

MAGNETOM Flash
Everything from the world of magnetic resonance imaging.

SOMATOM Sessions
Everything from the world of computed tomography.

Imaging Life
Everything from the world of molecular imaging innovations.

AXIOM Innovations
Everything from the world of interventional radiology, cardiology, and surgery.

Heartbeat
Everything from the world of sustainable cardiovascular care.

Medical Solutions Online
The online version includes additional video features and greater depth to the articles in the printed healthcare leadership magazine. Read online at:
www.siemens.com/medical-solutions

For current and past issues and to order the magazines, please visit
www.siemens.com/healthcare-magazine

The entire editorial staff at Seoul National University, College of Medicine and at Siemens Healthcare extends their appreciation to all the radiologists, technologists, physicists, experts and scholars who donate their time and energy – without payment – in order to share their expertise with the readers of MAGNETOM Flash.

MAGNETOM Flash – Imprint

© 2014 by Siemens AG,
Berlin and Munich,
All Rights Reserved

Publisher:
Siemens AG
Medical Solutions
Business Unit Magnetic Resonance,
Karl-Schall-Straße 6, D-91052 Erlangen,
Germany

Guest Editor:
Professor Jeong Min Lee
Chief Radiologist of the section of Abdominal Radiology and Nonvascular Intervention at the Department of Radiology, Seoul National University, College of Medicine, Seoul, Korea.

Editor-in-chief: Antje Hellwich
(antje.hellwich@siemens.com)

Editorial Board: Wellesley Were;
Ralph Strecker; Sven Zühlsdorff, Ph.D.;
Gary R. McNeal, MS (BME);
Peter Kreisler, Ph.D.

Production: Norbert Moser, Siemens AG, Medical Solutions

Layout: Agentur Baumgärtner,
Friedrichstraße 4, D-90762 Fürth,
Germany

Printer: G. Peschke Druckerei GmbH,
Taxetstrasse 4,
D-85599 Parsdorf b. Munich,
Germany

Note in accordance with § 33 Para.1 of the German Federal Data Protection Law: Despatch is made using an address file which is maintained with the aid of an automated data processing system.

MAGNETOM Flash is sent free of charge to Siemens MR customers, qualified physicians, technologists, physicists and radiology departments throughout the world. It includes reports in the English language on magnetic resonance: diagnostic and therapeutic methods and their application as well as results and experience gained with corresponding systems and solutions. It introduces from case to case new principles and procedures and discusses their clinical potential. The statements and views of the authors in the individual contributions do not necessarily reflect the opinion of the publisher.

The information presented in these articles and case reports is for illustration only and is not intended to be relied upon by the reader for instruction as to the practice of medicine. Any health care practitioner reading this information is reminded that they must use their own learning, training and expertise in dealing with their individual patients. This material does not substitute for that duty and is not intended by Siemens Medical Solutions to be used for any purpose in that regard. The drugs and doses mentioned herein are consistent with the approval labeling for uses and/or indications of the drug. The treating physician bears the sole responsibility for the diagnosis and treatment of patients, including drugs and doses prescribed in connection with such use. The Operating Instructions must always be strictly followed when operating the MR system. The sources for the technical data are the corresponding data sheets. Results may vary.

Partial reproduction in printed form of individual contributions is permitted, provided the customary bibliographical data such as author's name and title of the contribution as well as year, issue number and pages of MAGNETOM Flash are named, but the editors request that two copies be sent to them. The written consent of the authors and publisher is required for the complete reprinting of an article.

We welcome your questions and comments about the editorial content of MAGNETOM Flash. Please contact us at magnetomworld.med@siemens.com.

Manuscripts as well as suggestions, proposals and information are always welcome; they are carefully examined and submitted to the editorial board for attention. MAGNETOM Flash is not responsible for loss, damage, or any other injury to unsolicited manuscripts or other materials. We reserve the right to edit for clarity, accuracy, and space. Include your name, address, and phone number and send to the editors, address above.

MAGNETOM Flash is also available on the internet:

www.siemens.com/magnetom-world

SIEMENS

MAGNETOM Flash

The Magazine of MRI

Issue Number 5/2014 | RSNA Edition

Not for distribution in the US

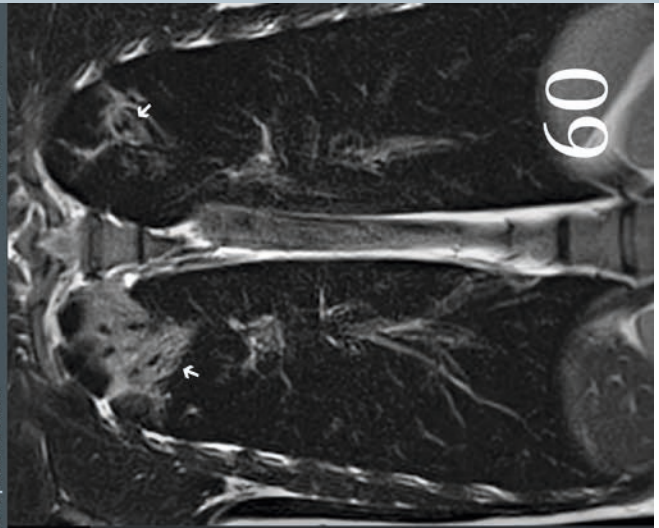

60

Athletic Pubalgia and Core Injury
Page 24

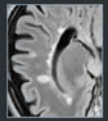

'White Dots' on Cranial MRI: MS and Differential Diagnosis
Page 32

30 Years of Innovation at Siemens
Page 88

Please enter your business address

Institution

Department

Function

Title

Name

Street

Postal Code

City

State

Country

MR system used

Please include me in your mailing list for the following Siemens Healthcare customer magazine(s):

- ☐ Medical Solutions
- ☐ MAGNETOM Flash
- ☐ SOMATOM Sessions
- ☐ AXIOM Innovations

Stay up to date with the latest information

Register for:

E-mail

Please print clearly!

☐ Yes, I consent to the above information being used for future contact regarding product updates and other important news from Siemens.

☐ unsubscribe from info service

→ **Visit www.siemens.com/magnetom-world**
for case reports,
clinical methods,
application tips,
talks and much more
clinical information.

SUBSCRIBE NOW!

– and get your free copy of future MAGNETOM Flash! Interesting information from the world of magnetic resonance – gratis to your desk. Send us this postcard, or subscribe online at **www.siemens.com/MAGNETOM-World**

Siemens AG
Healthcare
Magnetic Resonance
Antje Hellwich – Marketing
P.O. Box 32 60
D-91050 Erlangen
Germany

MAGNETOM Flash

On account of certain regional limitations of sales rights and service availability, we cannot guarantee that all products included in this brochure are available through the Siemens sales organization worldwide. Availability and packaging may vary by country and is subject to change without prior notice. Some/All of the features and products described herein may not be available in the United States.

The information in this document contains general technical descriptions of specifications and options as well as standard and optional features which do not always have to be present in individual cases, and which may not be commercially available in all countries. Due to regulatory reasons their future availability cannot be guaranteed. Please contact your local Siemens organization for further details.

Siemens reserves the right to modify the design, packaging, specifications, and options described herein without prior notice. Please contact your local Siemens sales representative for the most current information.

Note: Any technical data contained in this document may vary within defined tolerances. Original images always lose a certain amount of detail when reproduced.

Not for distribution in the US

Global Business Unit

Siemens AG
Medical Solutions
Magnetic Resonance
Henkestraße 127
DE-91052 Erlangen
Germany
Phone: +49 9131 84-0
www.siemens.com/healthcare

Local Contact Information

Asia/Pacific:
Siemens Medical Solutions
Asia Pacific Headquarters
The Siemens Center
60 MacPherson Road
Singapore 348615
Phone: +65 6490 6000

Canada:
Siemens Canada Limited
Healthcare
1550 Appleby Lane
Burlington, ON L7L 6X7, Canada
Phone +1 905 315-6868

Europe/Africa/Middle East:
Siemens AG, Healthcare
Henkestraße 127
91052 Erlangen, Germany
Phone: +49 9131 84-0

Latin America:
Siemens S.A., Medical Solutions
Avenida de Pte. Julio A. Roca No 516, Piso
C1067 ABN Buenos Aires, Argentina
Phone: +54 11 4340-8400

USA:
Siemens Medical Solutions USA, Inc.
51 Valley Stream Parkway
Malvern, PA 19355-1406, USA
Phone: +1 888 826-9702

Global Siemens Headquarters

Siemens AG
Wittelsbacherplatz 2
80333 Muenchen
Germany

Global Siemens Healthcare Headquarters

Siemens AG
Healthcare
Henkestraße 127
91052 Erlangen
Germany
Phone: +49 9131 84-0
www.siemens.com/healthcare

Order No. A91MR-1000-110C-7600 | Printed in Germany | CG MR 2516 111420. | © 11.14, Siemens AG

www.siemens.com/magnetom-world